# Ultra-broadband frequency generation in a cavity confined Raman medium

**CHRISTOPHER ROSE**

Materials and Physics Research Centre

School of Computing, Science and Engineering

University of Salford, Salford, UK

Submitted in Partial Fulfilment of the Requirements
of the Degree of Doctor of Philosophy,
September 2013

# Abstract

Throughout the past few decades, science has progressed towards the ability to probe many extremely fast processes and a large amount of research has been aimed at the area of few-femtosecond pulse generation. This thesis describes the generation of coherent broadband radiation through two-colour pumping of molecular hydrogen confined to a unidirectional ring cavity, and the subsequent synthesis of high peak power and few-femtosecond pulses. A set of normalised semi-classical field equations are derived in Bloch form describing the process of ultra-broadband multi-frequency Raman generation or UMRG, and a 3-wave gain suppression analysis is derived from a subset of the plane wave UMRG field equations which describes gain suppression within the ring cavity in terms of both medium and cavity parameters. The gain suppression analysis is further generalised to include finite levels of linear two-photon frequency detuning of the pump beams. Simulations of the plane wave ultra-broadband multi-frequency Raman (UMRG) equations show that a broad frequency spectrum of mutually coherent sideband can be generated. The inverse Fourier transform of spectra generated in this way yields a train of high power near Fourier limited pulses in the time domain which can range from a few-femtoseconds in duration to tens of attoseconds with repetition rates equal to the Raman transition frequency. Pulses synthesised in this way are limited only by the level of medium dispersion, the reflection bandwidth of the chosen coupling mirror and the chosen Raman medium. Simulations of the transverse UMRG equations within the ring cavity geometry have shown ring cavity enhanced UMRG to be resilient to transverse effects such as finite beam width, beam diffraction and the transverse beam separation of the applied pump beams.

# Acknowledgements

I would like to begin by thanking my supervisor Dr. Graham McDonald for his help, wisdom and support throughout both my undergraduate degree and throughout the duration of my PhD research. Graham has helped me through the transition from undergraduate degree to postgraduate PhD research which can be daunting step when you realise no matter how much you already know there are still vast amounts left to learn. He has shared his vast knowledge and experience freely and added some humour along the way. It has been a pleasure witnessing a great mind at work over the past few years therefore I would like to thank him for the many hours of enlightening meetings which would often leave me scratching my aching head but heading in the right direction.

I would like to thank the entire Salford Physics department for putting up with me for over six years and producing an entirely enjoyable and entirely unique experience. Though many of the staff deserve special mention here I will restrict myself to giving special thanks to Dr. James Christian who has taken the time to share his vast knowledge (and Matlab experience) and has made himself available for any questions which I might have. It has been a pleasure knowing him and witnessing his unique insight into the world of physics.

I couldn't possibly write these acknowledgements without thanking my entire family for their support throughout my undergraduate degree and PhD. I would like to specifically thank my mother Karen Rose for her unwavering support throughout my life, and i would also like to thank my Grandparents Ronald and Barbara Hitchen for allowing me to invade their home (and Garage) over the duration of my PhD.

I would also like to take this opportunity to thank my father David Rose who is the hardest working and kindest person I have ever known. He wanted nothing more than for his sons to achieve their goals, have success in life and most of all be happy. I went to university to make my father proud but unfortunately he lost his battle with cancer before he could see me graduate. So in memory of my father I have chosen to include a portion of the wording on his memorial plaque and in doing so dedicate this thesis to him.

**"Dave, a husband, a father, a son, a brother, a fighter, a legend. Sleep well our hero"**

He touched many people's lives and lives on in their thoughts.

# List of parameters

$\epsilon$ - Total electric field

$j$ - Integer denoting the index of each Raman sideband

$E_j$ - Un-normalised complex electric field amplitudes

$A_j$ - Normalised complex electric field amplitudes

$V_j$ - Components of the perturbing potential

$a_j$ - Amplitude of trial eigensolutions

$R_j$ - Cavity mirror reflectivity

$\omega_j$ - Sideband frequency

$\Delta k_j$ - Wave vector mismatch of each component of the total electric field

$\Delta_j$ - Mistuning of each frequency component

$\gamma_j$ - A set of normalised mistuning which account for dispersion and off axis sideband growth

$d_j$ - Set of diffraction terms for each component of the electric field

$L_D^j$ - Diffraction length of each frequency component

$L_R$ - Raman scattering gain length

$\omega_R$ - Raman transition frequency

$\omega_P$ - Half width of a reference Gaussian beam

$\varepsilon$ - Stokes shift parameter

$t$ - Retarded time coordinate

$\tau$ - Normalised time coordinate

$T_1$- Phenomelogical relaxation time describing population decay

$T_2$- Phenomelogical relaxation time describing dephasing of the dipole moment

$t_p$- Width of the pump pulse in the time domain

$T_{cav}$ - Time for light to complete one cavity transit

$c$ - The speed of light

$z$ - Spatial variable

$Z$ - Gain length product

$Z_c$ - Cavity length

$n$ - Integer denoting the index of each molecular energy level

$|n\rangle$ - Set of eigenvalues

$W_n$ - Frequency of each molecular energy level

$H_0$ - Unperturbed Hamiltonian

$\rho$ - Density matrix

$p$ - Dipole moment operator

$c_n$ - Components of the wavefunction

$H_{12}, H_{21}, H_{11}, H_{22}$ - Components of the two state Schrodinger equation

$\alpha_{ik}$ - Polarizability

Ω - The two-photon Rabi frequency

$I$ - The total intensity of the electric field

$I_0$ - Initial intensity of the pump

$\delta\omega$ - Linear detuning from resonance

$\delta$ - Normalised linear detuning

Δ - Total detuning including both linear and nonlinear

$u, v, w$ - The components of the Bloch vector

$\langle p \rangle$ - The molecular polarisation

$P$ - The macroscopic polarisation

$q$ - Medium excitation variable

$g$ - Gain parameter

$m$ - Integer corresponding to the $m'th$ cavity transit

$\alpha$ - Linear loss coefficient

$\emptyset$ - Pump mistuning from cavity resonance

$K_m^{\pm}$ - Gain parameter for the $m'th$ cavity transit

$C_{jS}$ , $C_{jA}$ $j = 1,2$ - Components of the gain suppression analysis general solutions

# List of figures

Figure 7c - Inverse Fourier transform profile of a spectrum generated by a symmetrically pumped cavity with a short cavity length and a finite level of linear detuning

Figure 7d - Inverse Fourier transform profile of a spectrum generated by a cavity with a short cavity length zero linear detuning and a non-unity pump ratio

Figure 7e - Reflectivity profile for a typical commercially available broadband dielectric output coupling mirror

Figure 7f - Inverse Fourier transform profile of a spectrum generated by a symmetrically pumped cavity with a short cavity length and zero linear detuning, generated when employing the reflectivity profile given in figure 7e

Figure 7g - Inverse Fourier transform profile of a spectrum generated by a symmetrically pumped cavity containing atmospheric Nitrogen. A short cavity length, zero linear detuning and the reflectivity profile given in figure 7e are employed

Figure 7h - Inverse Fourier transform profile of a spectrum generated by a symmetrically pumped cavity containing atmospheric Nitrogen. A very short cavity length, zero linear detuning and the reflectivity profile given in figure 7e are employed

Figure 7i - Inverse Fourier transform profile of a gigawatt intensity pulse generated in the cavity when employing a large pump intensity generated by a pulsed Nd:YAG laser and employing molecular Hydrogen as the medium

Figure 7j - Inverse Fourier transform profile of a gigawatt intensity pulse generated in the cavity when employing a large pump intensity generated by a pulsed Nd:YAG laser and employing atmospheric Nitrogen as the medium

# CHAPTER 1

## Introduction

Throughout the past few decades, scientific research has progressed towards the ability to probe many extremely fast processes which can have timescales ranging from a few femtoseconds to a few hundred attoseconds in duration. For example the Bohr model of atomic hydrogen predicts the period of the ground state electron orbit to be $\sim 100$as. Many fast molecular processes such as those utilised in the field of femtochemistry (1) have been revealed by mode-locked lasers which can produce pulses on the femtosecond timescale. The field of attoscience is of particular interest due to the availability of high power few-femtosecond pulses which can be used to generate attosecond pulses via the process of high harmonic generation. Attosecond pulses have made the observation of ultra-fast processes such as electron dynamics in matter possible such as the real-time observation of electron tunnelling in atoms (2).

Several theoretical and experimental investigations have been undertaken regarding the synthesis of high intensity few-femtosecond pulses. Such methods fall under two main categories: high harmonic generation and molecular modulation. Each method relies on the generation of an extremely broad frequency bandwidth to support the synthesis of attosecond pulses. The need for a large number of frequency components is implied by the well known Fourier bandwidth theorem. Wherein any wave phenomenon that occurs over a time period $\Delta t$ has to possess a spread of frequencies $\Delta f$ satisfying

$$\Delta t \approx \frac{1}{\Delta f}.$$

## 1.1 Ti:sapphire lasers

The first tuneable laser based on the titanium doped sapphire laser medium was operated for the first time in 1982 (3). Ti:sapphire has become one of the most widely used and commercially available transition metal doped gain medium for a tuneable laser. Ti:sapphire possesses a large tuning range from 660 - 1180 nm and a broad range of lasers can be used to pump the medium in the green spectral region. Hence Ti:sapphire lasers can be pumped with Argon-ion lasers or frequency doubled Nd:YAG lasers. Nd:YAG lasers have seen large power gains in recent years using multiple laser head technology and have become widely available in both scientific labs and industry.

Ti:sapphire is well suited to coherent broadband light generation and the synthesis of short pulses and several methods for achieving such pulses have been demonstrated. Active mode locking by an acousto-optic modulator can produce pulses as short as 1.3 picoseconds (4) and other mode locking techniques have produced pulses approaching 200 femtoseconds. However the shortest pulses have been generated using the process of self mode locking (5, 6).

In recent years few femtosecond pulses have been readily achieved through the use of Ti:sapphire gain media (7) and much focus has been moved towards increasing the repetition rate of Ti:sapphire lasers. Reference (8) reports results for a prismless femtosecond Ti:sapphire ring laser where 5.9 femtosecond pulses were generated at a repetition rate of 2.12GHz and each pulse had an average power of 0.95W for 7.5W of pump power. Higher repetition rates of up to 5GHz have also been reported by other authors (9). These types of laser configuration rely on the nonlinear mechanism of Kerr lensing for mode-locking and the synthesis of femtosecond pulses.

The availability of broadband femtosecond pulses at such high repetition rates are particularly useful sources of optical frequency combs for application in the field of optical frequency metrology and atomic clocks (10). Other key applications of such broadband few femtosecond lasers include high resolution molecular spectroscopy,

holography, Terahertz generation, high harmonic generation (11) and as light sources for the generation of attosecond pulses.

## 1.2 High harmonic generation

The process of high harmonic generation has been used to generate pulses which have been recorded to be as short as 80 *as* (12) and are composed of frequencies within the ultraviolet and x-ray regions of the frequency spectrum (13, 14). High harmonic generation occurs when highly intense femtosecond pulses of infra red wavelength ( $e.g\ \lambda = 1.45\ \mu m\ (15)$) are focused in an atomic or molecular medium, causing the emission of higher order harmonics. High harmonics are generated when an electron is dragged away from the core of an atom / molecule in a fraction of an optical cycle. The electron then undergoes a large amplitude oscillation therefore gaining a large kinetic energy. The subsequent re-collision of the electron with the atom / molecule can cause the emission of higher energy photons. Various orders of harmonic frequencies can be generated through the variation of electron trajectories within the medium. A more in depth description of the process of high harmonic generation is given in references (16, 17). High harmonic generation has been shown to be capable of generating bandwidths suitable for the synthesis of pulses of attosecond duration. Pulses generated using this method usually have a low total energy due to the process having a low efficiency of around $< 10^{-6}$ (13). The maximum attainable bandwidth is determined by the cut-off frequency of the medium which is related to the maximum amount of energy which can be extracted from an electron re-collision $(18)$. Several other schemes employing temporal gratings have been proposed to increase the conversion efficiency of high harmonic generation and to reduce the requirements on the required duration of the applied driving pulses ($\sim 5fs$) needed to generate isolated attosecond pulses [19-28].

A powerful method for confining the process of ultra-short pulse generation to a single event involves the use of a modulating polarisation (19). This technique exploits the dependence of the high harmonic generation on the polarisation of the pulses used to drive the light – matter interaction. Such dependence can be exploited using a pulse that is elliptically polarised in its wings and linearly polarised around the peak of the pulse (20). This can lead to the production of isolated attosecond pulses.

The conversion efficiency of this method strongly depends on the length of the input pulses used to generate the extreme ultraviolet radiation, where longer pulse durations decrease the conversion efficiency. The addition of a second harmonic field reduces the requirements of the duration of the applied driving pulse. When the relative phase between the two laser harmonics is optimised, the synthesis of attosecond pulses has been shown to take place once for every optical cycle of the applied field (20). Researchers have reported high photon fluxes and conversion efficiencies of $6 \text{ x } 10^{-6}$ employing this method (22).

A two colour method for generating attosecond pulses was proposed in 2007 by Merdji and co-workers (23) and was later demonstrated by researchers in 2009 (15). This method employs the use of a fundamental near infra-red pulse ($\lambda = 1.45\ \mu m$) along with a detuned second harmonic ($\lambda = 0.8\ \mu m$) pulse (15), which can be generated by a near infra-red tuneable optical parametric amplifier (24, 25). Researchers observed that the harmonic conversion efficiency for two-colour excitation was much larger than in experiments using a single frequency pulse, which suggested that the detuned second harmonic was responsible for increasing conversion efficiency (24, 25).

Takahashi and co-workers [28] also recently showed that longer driving pulses ($\sim 30 fs$) can drive the generation of broadband spectra around the cut-off spectral region (the medium dependant region where harmonic generation typically stops). This reduces the requirements on the driving pulse durations required to produce an attosecond pulse (26, 27). The advantage of using this method is that medium

ionisation is reduced and conversion efficiencies of around $10^{-5}$ can be achieved. Therefore high intensity attosecond pulses can be synthesised in a neutral gas (28).

The above methods of high harmonic generation are capable of producing low energy attosecond pulses consisting of frequencies in the extreme ultraviolet and soft x-ray regions. The low pulse energies occur because the process of generating very high order harmonics is inefficient.

## 1.3 Raman scattering

The field of attoscience would benefit from higher power femtosecond pulses with a spectral range in the visible to ultraviolet. Such pulses could be used to explore electronic resonances in molecules and would present the opportunity for several new measurement methods and experiments to be investigated such as high resolution molecular spectroscopy. There would be the additional benefit of a wide and varied selection of optical components readily available for use in the visible and ultraviolet range of the spectrum.

A number of schemes aimed at the generation of short pulses in the visible to ultraviolet spectral range have been under development since the late 1990's (29-32). These schemes employ Raman scattering in a medium composed of molecules oscillating in phase. This involves a modulation of the refractive index of the medium which drives multiple Raman sidebands as the field propagates through the medium (33, 34). This offers the possibility of a much more efficient conversion of pump light into a broadband spectrum and the synthesis of high intensity pulses. Molecular modulation offers the possibility of generating high energy few-femtosecond pulses, which could be suitable pump sources for high harmonic generation.

A Raman active medium such as molecular hydrogen under the influence of a strong electromagnetic field can undergo two-photon inelastic scattering (Raman scattering). After the interaction of an incident laser photon of frequency $\omega_0$ and a molecule the scattered photon has a lower frequency $\omega_{-1}$ and is known as a first Stokes photon. The frequency difference between the original laser photon and the scattered photon is equal to the frequency separation of the rotational or vibrational molecular energy levels of the molecule $\omega_R$, which is known as the Raman transition frequency. The energy lost by the original laser photon is absorbed by the molecule and leaves it in an excited state. Further interaction between laser photons and the excited molecule can also produce a scattered photon with a higher frequency $\omega_1$ known as an anti-Stokes photon. Figure 1a demonstrates the four wave mixing process required to generate anti-Stokes photons in a Raman medium.

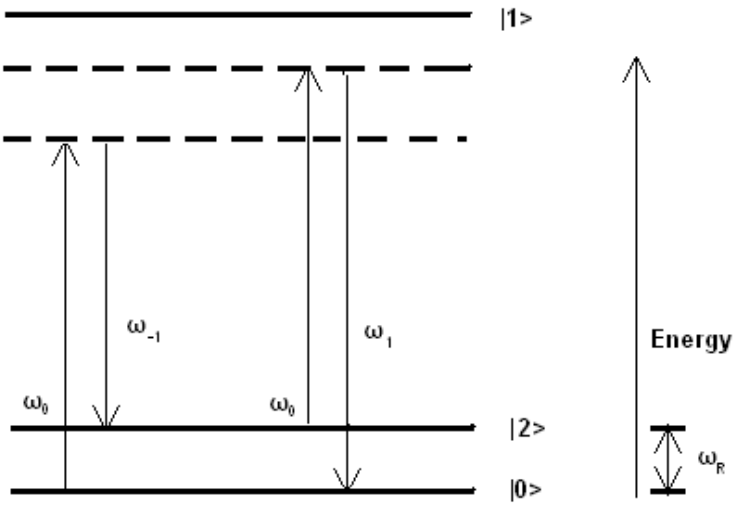


**Figure 1a – The molecular energy levels 0 and 2 are separated by the Raman frequency $\omega_R$. The generation of anti-Stokes photons is a four wave mixing process. The Raman medium gains energy from Stokes scattering in the form of an optical phonon. This excess energy can be released when the incident laser interacts with the excited molecular energy level. In this case the scattered photon is of higher frequency (energy).**

The frequencies generated through this process take the form:

$$\omega_j = \omega_0 + j\omega_R$$

where $j = \ldots -3, -2, -1, 0, 1, 2, 3 \ldots$ indicates the order of the sideband. Negative integers label the Stokes frequencies and positive integers label the anti-Stokes frequencies, $\omega_0$ is the frequency of the incident pump photon. Each frequency within the spectrum is separated by the frequency of the exploited Raman transition $\omega_R$ of the medium.

When large laser intensities are employed the Raman process can cascade which leads to the generation of a large number of frequency components separated by the Raman transition frequency (35). Researchers have demonstrated that the efficiency of Raman scattering can be improved by the introduction of a seed amplitude at the first Stokes frequency (36-42). This reduces the pump intensities required for the generation of higher order radiation because stimulated scattering increases the level of the seed and allows it to act as a pump source for higher orders of Stokes radiation.

Bi-harmonic pumping and symmetric pumping [43, 44] have been shown to increase the efficiency of Raman scattering and can produce many orders of Stokes and anti-Stokes sideband radiation. Bi-harmonic pumping requires that the applied pump laser and Stokes seed have similar levels of intensity, and symmetric pumping requires that they also possess the same temporal shape, polarisation and propagate collinearly. The frequencies of the applied laser fields are chosen such that their frequency difference equals the transition frequency of the Raman medium $\omega_R$.

The application of two laser fields produces a coherent molecular oscillation which modulates the incident laser fields to produce a broad frequency comb of Raman sidebands (45, 46, 47).

The above techniques can generate very large bandwidths which can span the entire ultraviolet, visible and near infrared range of the spectrum (45, 46, 47) and are suitable for the generation of ultra-short pulses (39). Broadband Raman spectra

are of great interest due to their potential application in inertial confinement fusion, where broadband laser- plasma interactions could reduce the growth rates of laser-plasma driven instabilities which inhibit plasma heating (29). Spreading the applied laser energy across a large spectrum inhibits the growth of parasitic processes whilst maintaining a high level of energy transfer to the plasma (30, 48). Broadband spectra have also triggered advances in precision measurements (49) and optical frequency metrology (50), laser-gas based sensing (51) and the characterisation of molecules (52).

## 1.4 Optical micro-resonators

Another emerging branch of physics relating to the generation of broadband spectra utilises the confinement of light within optical micro-resonator / micro-cavity structures to generate broad frequency combs. Such structures trap light in small volumes through the mechanism of total internal reflection or distributed Bragg reflection (or a mixture both) and can support a spectrum of optical modes which depend on the shape and size of the cavity structure. Typical, rotationally symmetric, micro-structures have radii from $1\ \mu m$ to $100\ \mu m$ and can be fabricated from a wide range of materials.

A large number of micro resonator / micro-cavity geometries have been explored for various applications, such as the microsphere (53), microtorus (54), microdisk (55), quadrupolar micro-resonator (56), micropillar (57) and photonic crystal defect micro-cavities (58). It is critical to produce micro-structures with a small modal volume, V, and a high quality factor, Q. The quality factor is defined as the ratio of energy stored to energy dissipated by the resonator / cavity. The ratio Q/V determines the strength of the light-matter interactions within the micro-structure, and this value needs to be maximised for the generation of broad spectra. The simultaneous requirements of high Q and small V have however been found to be contradictory, as the Q-factor decreases exponentially as the micro-structures decrease in size.

Micro-structures can generate broad spectra through a combination of parametric interactions (59) and non-degenerate four-wave mixing (60). Two conditions have to be satisfied before parametric interactions are observed. Firstly, momentum has to be conserved (61) within the cavity and, secondly, the energy of the system has to be conserved, hence only specific levels of medium dispersion are allowed. However, providing that dispersion is minimised the generated spectrum can contain phase coherent sidebands with equidistant frequency spacing. The frequency spacing of the sidebands is determined by the specific dimensions of each micro-cavity which controls the frequency of the allowable cavity modes. Broadband frequency combs, high intra-cavity intensities and high efficiencies have been demonstrated using optical micro-cavities (62, 63, 65).

## 1.5 Development of the theory of Raman scattering

The work presented within this thesis investigates the cavity confinement of a Raman active medium. The equations of multi-wave stimulated Raman scattering derived by Hickman and Bischel (66) will be used to simulate how such a system evolves in terms of medium (such as dispersion) and cavity (such as boundary condition) parameters. Before going into further detail regarding the Raman cavity system it is worthwhile to review the historical development of the theory of Raman scattering.

The inelastic scattering of light was predicted in 1923 by Adolf Smekal (67) and later discovered on 28 February 1928 by C.V. Raman (68, 33) who received the Nobel Prize in 1930 after a series of investigations into the molecular diffraction of light. The inelastic scattering process which he discovered was entitled Raman scattering.

There has been a large amount of research aimed towards characterising the generation of Stokes and anti-Stokes radiation under a variety of conditions. In 1963, Y.R. Shen and N. Bloembergen (69) published a detailed account of the theory of stimulated Raman scattering. They described the effect classically as the result of

light waves coupling to optical phonons within a material and offered a qualitative description of experimental results published around that time.

Many theoretical investigations (70 , 71) relating to the Raman effect had great success describing experimental observations of stimulated Raman scattering, though they only considered the interaction between a limited number of frequency components. Usually only the pump, first Stokes and first anti-Stokes components were considered. These simple theories neglected the population dynamics of the molecules within the system by making the assumption that most of the molecules remained in the ground state which is a valid approximation for most Raman active media.

In 1978, V. Wilke and W. Schmidt (72) observed the efficient production of high order anti-Stokes radiation. This could not be explained by the existing theories of stimulated Raman scattering and, in 1981, a paper entitled Efficient frequency conversion by stimulated Raman scattering was published (70). This new theory showed that the generation of high order anti-Stokes waves arose as a natural consequence of casting the problem in a multi-wave form, which included all possible frequency components. Such initial works dealt with the problem in the limit of small molecular excitation. This limited the ability to accurately describe the conversion efficiencies of anti-Stokes generation when compared with experimental data.

The multi-wave approach was generalised in 1986 by Hickman, Paisner and Bischel (73) to describe higher-order Stokes and anti-Stokes frequency components arising from input pulses strong enough to induce significant molecular excited state populations. This new theory was also later extended by Hickman and Bischel (66) to include off axis wave vector mismatch.

Several papers have been published which discuss results generated using the theory derived by Hickman and Bischel, for both steady state (no transient evolution of the molecular excitation) and transient (the molecular excitation evolves in time) systems (31 , 32, 74). Bandwidths greater than the width of the pump frequency have been predicted (31).

Several authors have proposed parameter regimes which maximise the bandwidth for different types of Raman media such as molecular hydrogen and nitrogen (29, 30, 66, 70, 74). Bandwidths of approaching 150 sidebands (of intensity comparable to the pump beam) have been predicted in air at atmospheric pressure through the exploitation of the $J = 8 \rightarrow 10$ rotational transition of atmospheric $N_2$. McDonald *et al* determined that resonant symmetric pumping techniques were optimal for the generation of large bandwidths in air. There two pump beams of equal intensity, matching temporal shape and linear polarisation (30, 43) were employed. The frequencies of the pump beams were specifically chosen to have a frequency difference resonant with the Raman transition (32).

## 1.6 Thesis content

The work presented in this thesis describes the generation of coherent broadband spectra in a cavity confined Raman medium such as hydrogen and atmospheric nitrogen. The contents of this thesis are as follows:

CHAPTER 2 - The semi-classical ultra broadband multi-frequency Raman (UMRG) envelope equations are derived in Bloch form and normalised.

CHAPTER 3 + 4- A three wave gain suppression analysis is derived which describes a subset of the UMRG equations in terms of linear general solutions. The analysis is extended to include intra-cavity pump depletion, and then each gain suppression model is compared to the results of numerical simulations, for a large range of parameters. The points at which the analysis breaks down are discussed in terms of non-parametric sideband growth. The analysis is further extended in chapter 5 to include finite levels of linear detuning.

CHAPTER 5 - Multi-frequency simulations of the cavity system, with a single pump beam, are performed. The growth of bandwidth, total intensity and medium excitation amplitude are characterised for finite levels of dispersion. The gain suppression analysis derived in chapter 4 is shown to describe the results of the multi-frequency simulations in certain parameter regimes.

CHAPTER 6- Multi-frequency simulations are performed with symmetric pumping applied at the cavity boundary. Large bandwidths are shown to be generated and are described in terms of parametric and non-parametric growth mechanisms. Specific parameter regimes which optimise bandwidth growth are also discussed.

CHAPTER 7 - Femtosecond pulses are synthesised from results of multi-frequency simulations. The pulse power densities, energies and durations are given in physical units. Results are also presented which model realistic coupling mirror reflection profiles (with limited reflection bandwidths).

CHAPTER 8 + 9 - The transverse UMRG equations are modelled and the results of multi-frequency simulations are presented. The roles of beam diffraction, finite transverse structure and transverse beam separation are considered in detail for both the (1+1)D and (1+2)D UMRG equations.

CHAPTER 10 - The effects of linear and nonlinear detuning are discussed with specific emphasis on (1+1)D transverse UMRG.

# CHAPTER 2

# Derivation of the UMRG equations

Throughout this chapter the ultra-broadband multi-frequency Raman equations (UMRG) will be derived. The UMRG equations were originally developed to explain large conversion efficiencies and bandwidths generated in experiments conducted on various Raman media (73). They describe the growth of Raman spectra in terms of the molecular dynamics of the medium (66), and show that large conversion efficiencies arise as a direct consequence of deriving the equations in terms of an infinite number of plane waves. The derivation given in reference (73) will be followed but steps omitted from the original derivation will be included. Particular emphasis is placed on the derivation of the Bloch equations from the density matrix.

## 2.1 Semi-classical theory of multi-wave stimulated Raman scattering

We wish to find a set of solutions to the nonlinear wave equation (2.1). These solutions will describe a set of plane waves travelling through a Raman active medium such as molecular hydrogen or molecular nitrogen. The envelope equations derived in this chapter will be normalised in accordance with the normalisation process used within reference (66). This final form of the envelope equations will be used in all simulations and analyses within this thesis.

The one dimensional nonlinear wave equations is;

$$\left[\frac{\partial^2}{\partial z^2} - \frac{1}{c^2}\frac{\partial^2}{\partial t^2}\right]\epsilon(z,t) = \frac{4\pi}{c^2}\frac{\partial^2 P}{\partial t^2}, \tag{2.1}$$

where the electric field $\epsilon$ is of the form

$$\epsilon(z,t) = \sum_j E_j(z,t)cos\left[\omega_j(t_{lab} - {}^{z}/_{c}) + \emptyset_j\right], \tag{2.2}$$

and the frequencies $\omega_j$ are defined by

$$\omega_j = \omega_0 + j\omega_R \,, \tag{2.3}$$

where $j$ is an integer which defines each Stokes or anti-Stokes index, and $\omega_R$ is the exploited Raman transition frequency of the medium. The difference frequency between any two adjacent waves can drive the transition between molecular energy levels. The oscillating polarisation created in this process takes the form of *P* within equation (2.1). The right hand side of equation (2.1) acts as the source term which can generate further higher order frequency sidebands. The macroscopic polarisation of the medium *P* will be obtained from the quantum-mechanical density matrix which describes the molecule/field interaction, and will be described in terms of Bloch-vectors of the two-photon Bloch equations (75).

The wavefunction of a single hydrogen molecule under the influence of the field given in (2.2) will be considered and the time dependent wavefunction will be written as a set of zero-field eigenfunctions. The coefficients of the wavefunction will be obtained and all equations will be written in terms of the longitudinal distance *z* and the retarded time frame $t = t_{lab} - {}^{z}/_{c}$.

We can begin by assuming that the energies $\hbar W_n$ and eigenfunctions $|n\rangle$ of the unperturbed Hamiltonian $H_0$ are known, therefore solutions to the time dependant Schrödinger equation can be obtained:

$$(H_0 + V)\psi = i\hbar \frac{d\psi}{dt} \tag{2.4}$$

where,

$$V = -p\epsilon \tag{2.5}$$

and $p$ is the electronic dipole-moment operator. The perturbing potential can be described as a sum of potentials occurring with frequencies $\omega_j$

$$V = -\frac{1}{2} p \sum_j V_j e^{i\omega_j t} + c.c. \tag{2.6}$$

and

$$V_j = E_j e^{i\phi_j} \quad . \tag{2.7}$$

The solution to equation (2.4) can be expanded

$$\psi = \sum_n^\infty c_n e^{-iW_n t}|n\rangle \tag{2.8}$$

where n = 1,2 are the indices corresponding to the 0 and 1 vibrational or rotational energy levels of the molecule. We will assume that n = 3,4,.. refer to the vibrational / rotational energy levels on higher electronic transitions. Through the substitution of equation (2.8) into equation (2.4) we can obtain a set of coupled equations for $c_n$.

Substituting equation (2.8) into equation (2.4) gives,

$$V\sum_{n=1}^\infty c_n e^{-iW_n t}|n\rangle = i\hbar\frac{dc_n}{dt}e^{-iW_n t}|n\rangle \tag{2.9}$$

and projecting equation (2.9) onto the eigenstate $\langle k||$ and re-arranging gives,

$$i\hbar\frac{dc_k}{dt} = \langle k|V|n\rangle\sum_n^\infty c_n e^{-iW_n t + iW_k t}. \tag{2.10}$$

Making the substitution $k = n, n = n'$ equation (2.10) becomes

$$i\hbar\frac{dc_n}{dt} = -\frac{1}{2}\sum_{n'=1}^\infty c_{n'}p_{nn'}\sum_j(V_j e^{i(\omega_j + W_{nn'})t} + V_j^* e^{-i(\omega_j - W_{nn'})t}) \ , \tag{2.11}$$

where $p_{nn'} = \langle n|p|n'\rangle$ and $W_{nn'} = W_n - W_{n'}$ , where $W_{nn'}$ represents the frequency difference between the energy levels $n$ and $n'$.

## 2.2 The two state Schrödinger equation

We can now consider the specific case of $n = 1,2$ and $p_{12} = 0$ where the rotational / vibrational levels 1 and 2 are taken to be on the same electronic state, and therefore possess no dipole interaction. We will also choose to neglect all terms except $p_{1n}$and $p_{n2}$ because only the interactions between the 1,2 and $n^{th}$ levels are required. With these stipulations equation (2.11) can be partially

uncoupled. Higher energy states are eliminated by applying the adiabatic approximation where the interaction between the molecule and laser is taken to be far off resonance and will not affect the higher electronic states. Therefore the population in these states will be constant and its possible to solve for $c_n$ (where $n = 3,4,5 \ldots$) in terms of $c_1$and $c_2$.

This solution is valid when the time dependence of $c_1$ and $c_2$ is small compared to other time dependant terms in equation (2.11). In this limit,

$$c_n = -\frac{1}{2\hbar}\sum_{n'=1}^{2} c_{n'} p_{nn'} \sum_j \left( \frac{-V_j e^{i(\omega_j + W_{nn'})t}}{\omega_j + W_{nn'}} + \frac{V_j^* e^{-i(\omega_j - W_{nn'})t}}{\omega_j - W_{nn'}} \right). \tag{2.12}$$

Substituting equation (2.12) into equation (2.11) for n = 1,2 and keeping only terms which do not oscillate at a high frequency such as a laser frequency leads to equations for $\frac{\partial c_1}{\partial t}$ and $\frac{\partial c_2}{\partial t}$.

For example, selecting $n = 1, n' = 3$ in equation (2.11),

$$i\hbar \frac{dc_1}{dt} = -\frac{1}{2} c_3 p_{13} \sum_j (V_j e^{i(\omega_j + W_{13})t} + V_j^* e^{-i(\omega_j - W_{13})t}) \tag{2.13}$$

and substituting equation (2.12) gives

$$i\hbar \frac{dc_1}{dt} = -\frac{1}{4\hbar} p_{13} c_1 p_{31} \sum_j \left(V_j e^{i(\omega_j + W_{13})t} + V_j^* e^{-i(\omega_j - W_{13})t}\right) \left( \frac{-V_j e^{i(\omega_j + W_{31})t}}{\omega_j + W_{31}} + \frac{V_j^* e^{-i(\omega_j - W_{31})t}}{\omega_j - W_{31}} \right) - \frac{1}{4\hbar} p_{13} c_2 p_{32} \sum_j \left(V_j e^{i(\omega_j + W_{13})t} + V_j^* e^{-i(\omega_j - W_{13})t}\right) \left( \frac{-V_j e^{i(\omega_j + W_{32})t}}{\omega_j + W_{32}} + \frac{V_j^* e^{-i(\omega_j - W_{32})t}}{\omega_j - W_{32}} \right) , \tag{2.14}$$

$$i\hbar \frac{dc_1}{dt} = -\frac{1}{4\hbar} p_{13} c_1 p_{31} \sum_j \left( -\frac{V_j V_j^*}{\omega_j + W_{31}} + \frac{V_j V_j^*}{\omega_j - W_{31}} \right) - \frac{1}{4\hbar} p_{13} c_1 p_{32} \sum_j \left( -\frac{V_j V_{j-1}^*}{\omega_j + W_{32}} + \frac{V_j V_{j-1}^*}{\omega_j - W_{32}} \right) . \tag{2.15}$$

Repeating the above process for n = 4,5,6,.. gives the full equations for $\frac{\partial c_1}{\partial t}$ and $\frac{\partial c_2}{\partial t}$ which can be written in matrix form:

$$i\hbar \frac{\partial}{\partial t}\begin{bmatrix} c_1 \\ c_2 \end{bmatrix} = \begin{bmatrix} H_{11} & H_{12} \\ H_{21} & H_{22} \end{bmatrix}\begin{bmatrix} c_1 \\ c_2 \end{bmatrix} \tag{2.16}$$

and the components of the two-level Schrödinger equation are given as

$$\begin{aligned} H_{11} &= -\tfrac{1}{4}\textstyle\sum_j^{\infty} \alpha_{11}\, V_j V_j^* \ , \\ H_{12} &= -\tfrac{1}{4}\textstyle\sum_j^{\infty} \alpha_{12}\, V_j V_{j-1}^* \\ H_{21} &= H_{12}^* \ , \\ H_{22} &= -\tfrac{1}{4}\textstyle\sum_j^{\infty} \alpha_{22}\, V_j V_j^* \ , \end{aligned} \tag{2.17}$$

where the polarizability is given as,

$$\alpha_{ik} = \tfrac{1}{\hbar}\textstyle\sum_{n=3}^{\infty} p_{in} p_{nk}\left[\frac{1}{W_{ni}-\omega_j} + \frac{1}{W_{nk}+\omega_j}\right]. \tag{2.18}$$

The dependence of $\alpha_{ik}$ on $\omega_j$ is small when the frequencies are far from resonance with the higher electronic levels. For the selected medium (molecular hydrogen) $\alpha_{ik}$ are taken here to be constants. The summations within equations (2.17) can be defined as

$$\Omega = \frac{\alpha_{12}}{2\hbar}\textstyle\sum_j V_j V_{j-1}^* \ , \tag{2.19}$$

$$I = \textstyle\sum_j V_j V_j^* \ . \tag{2.20}$$

Where $I$ is the total incoherent intensity of the electric field in the system and $\Omega$ is identified as the two-photon Rabi frequency. The latter is the frequency of oscillation for the molecular transition of the two-state system and is associated with the strength of the coupling between the molecular transition and the interacting electric field. The two-state Schrodinger equation can be described in terms of the components of the optical Bloch vector $(u, v, w)$, and the Bloch equations can be derived following the standard method (75, 76) which we will now follow.

## 2.3 The optical Bloch equations and density matrix

The optical Bloch equations are a system of equations which describe the resonance behaviour of quantum systems where only two energy levels are interacting. This makes them a useful tool for gaining insight into the physical properties which couple quantum systems to electromagnetic fields. The optical Bloch equations can be derived from the components of the density matrix for the two-state system:

$$\rho = \begin{bmatrix} \rho_{11} & \rho_{12} \\ \rho_{21} & \rho_{22} \end{bmatrix}, \tag{2.21}$$

where the components are defined as

$$\rho_{11} = c_1 c_1^* \tag{2.22}$$

$$\rho_{12} = \rho_{21}^* = c_1 c_2^* e^{iW_{21}t} \tag{2.23}$$

$$\rho_{22} = c_2 c_2^* . \tag{2.24}$$

To include detuning from resonance we make the following transformation

$$c_2 = \bar{c}_2 e^{i\delta\omega t} \ , \tag{2.25}$$

where $\delta\omega = W_{21} - \omega_R$ is the detuning. The components of the density matrix then become

$$\rho_{11} = c_1 c_1^* \tag{2.26}$$

$$\rho_{12} = \rho_{21}^* = c_1 \bar{c}_2^* e^{iW_{21}t - i\delta\omega t} \tag{2.27}$$

$$\rho_{22} = \bar{c}_2 \bar{c}_2^* . \tag{2.28}$$

Equation (2.16) is also modified by the above transformation, and takes the form

$$i\hbar \frac{\partial c_1}{\partial t} = H_{11} c_1 + H_{12} \bar{c}_2 \tag{2.29}$$

$$-i\hbar \frac{\partial \bar{c}_2^*}{\partial t} = H_{12} c_1^* + (H_{22} + \hbar\delta\omega)\bar{c}_2^* . \tag{2.30}$$

Taking the time derivative of the density matrix component (2.27) and substituting, equations (2.29) and (2.30) give

$$\frac{\partial \rho_{12}}{\partial t} = \frac{i}{\hbar}(H_{22} - H_{11} + \hbar\delta\omega)\rho_{12} + \frac{i}{\hbar}(\rho_{11} - \rho_{22})H_{12}e^{i(W_{21}-\delta\omega)t} + i(W_{21} - \delta\omega)\rho_{12}\,. \tag{2.31}$$

One can eliminate the exponential term within equation (2.31) through the introduction of a slowly varying quantity $\sigma_{12}$defined by

$$\rho_{12} = \sigma_{12}e^{i(W_{21}-\delta\omega)t}. \tag{2.32}$$

Equation (2.31) can now be rewritten in terms of this slowly varying quantity

$$\frac{\partial \sigma_{12}}{\partial t} = \frac{i}{\hbar}(H_{22} - H_{11} + \hbar\delta\omega)\sigma_{12} - \frac{1}{T_2}\sigma_{12} + \frac{i}{\hbar}(\rho_{11} - \rho_{22})H_{12}\,, \tag{2.33}$$

where $T_2$ is a phenomenological relaxation time. The addition of relaxation times to the density matrix equations of motion are well justified in reference (76). In a closed system the population of the upper energy level would decay due to spontaneous emission. The relaxation time (or dephasing time) $T_2$ describes how the oscillation of the molecular dipole moment decays.

Equation (2.33) can be written in terms of the intensity and two-photon Rabi frequency

$$\frac{\partial \sigma_{12}}{\partial t} = -i\left(\left(\frac{\alpha_{22}-\alpha_{11}}{4\hbar}\right)I + \delta\omega\right)\sigma_{12} - \frac{1}{T_2}\sigma_{12} - \frac{i}{2}(\rho_{11} - \rho_{22})\Omega\,. \tag{2.34}$$

Defining $\sigma_{12} = \frac{1}{2}(u - iv)$ , $\Omega = \Omega_R + i\Omega_I$ and splitting equation (2.34) into its real and imaginary components gives

$$\frac{\partial u}{\partial t} = -\Delta v - \frac{u}{T_2} - \Omega_I(\rho_{22} - \rho_{11}) \tag{2.35}$$

$$\frac{\partial v}{\partial t} = \Delta u - \frac{v}{T_2} - \Omega_R(\rho_{22} - \rho_{11})\,, \tag{2.36}$$

where the detuning is given by

$$\Delta = \left(\left(\frac{\alpha_{22}-\alpha_{11}}{4\hbar}\right)I + \delta\omega\right). \tag{2.37}$$

Taking the derivatives of equations (2.26) and (2.28) gives

$$\frac{\partial \rho_{11}}{\partial t} = \frac{i}{\hbar}(H_{21}\sigma_{12} - H_{12}\sigma_{21}) + \frac{\rho_{22}}{T_1} \tag{2.38}$$

$$\frac{\partial \rho_{22}}{\partial t} = \frac{i}{\hbar}(H_{12}\sigma_{21} - H_{21}\sigma_{12}) - \frac{\rho_{22}}{T_1}, \tag{2.39}$$

where $\sigma_{21} = \sigma_{12}^{*}$ and $T_1$ is also a phenomenological relaxation time which has been included in the standard way to define the decay of the population of the upper energy state, and in turn the population gain of the lower energy state due to spontaneous emission. Defining the population difference $w = \rho_{22} - \rho_{11}$ and using equations (2.38) and (2.39) one can define the equation of motion for the population difference as

$$\frac{\partial w}{\partial t} = \Omega_R v + \Omega_I u - \frac{w - w_0}{T_1}, \tag{2.40}$$

where $w_0$is the initial population difference, which accounts for the fact that the initial population difference of the molecule in thermal equilibrium can have some value other than -1.

Hence the complete set of optical Bloch equations are given as

$$\begin{aligned} \frac{\partial u}{\partial t} &= -\Delta v - \frac{u}{T_2} - \Omega_I w \\ \frac{\partial v}{\partial t} &= \Delta u - \frac{v}{T_2} - \Omega_R w \\ \frac{\partial w}{\partial t} &= \Omega_R v + \Omega_I u - \frac{w - w_0}{T_1}. \end{aligned} \tag{2.41}$$

The Bloch equations fully illustrate the coupling of the molecule and optical field in terms of a 3-vector with three real components $(u, v, w)$. The goal of describing the quantum system for molecular hydrogen was to find an explicit form for the polarisation induced by the potential (2.6); this polarisation can then be inserted into the nonlinear wave equation (2.1) and yield a set of envelope equations defining the amplitudes $V_j$.

## 2.4 The molecular polarisation

The polarisation can be obtained from

$$\langle p \rangle = \langle \psi(t)|p|\psi(t)\rangle \tag{2.42}$$

$$\langle p \rangle = \sum_{n=3}^{\infty} c_1 c_n^* p_{n1} e^{iW_{n1}t} + \bar{c}_2 c_n^* p_{n2} e^{i(W_{n2}+\delta\omega)t} + c_n c_1^* p_{1n} e^{iW_{1n}t} + c_n \bar{c}_2^* p_{2n} e^{i(W_{2n}-\delta\omega)t}. \tag{2.43}$$

Using equations (2.12) and (2.18), equation (2.43) can be reduced to

$$\langle p \rangle = \left[\alpha_{12} c_1^* \bar{c}_2 V_j e^{i\omega_{j-1}t} + \alpha_{21}^* c_1^* \bar{c}_2 V_j^* e^{-i\omega_{j+1}t} + \alpha_{21} \bar{c}_2^* c_1 V_j e^{i\omega_{j+1}t} + \alpha_{12}^* \bar{c}_2^* c_1 V_j^* e^{-i\omega_{j-1}t}\right]. \tag{2.44}$$

Multiplying the polarisation by the number density of the molecules $N$ initially in the ground state gives the macroscopic polarisation $P$ which can be written in terms of the Bloch vector.

$$P = \frac{1}{4}(u + iv) N \alpha_{12} \sum_j \left(V_j e^{i\omega_{j-1}t} + V_j^* e^{-i\omega_{j+1}t}\right) + c.c. \tag{2.45}$$

The macroscopic polarisation represents how the ensemble of quantum systems acts under the influence of the applied field given by equation (2.2). This polarisation can be substituted into equation (2.1). The field amplitudes $V_j$ are taken to be slowly varying (only first derivatives are retained) and the differential operator is expressed in the coordinates $z$ and retarded time (73). By equating each frequency components coefficient we can obtain a set of coupled differential equations describing the field amplitudes:

$$\frac{\partial V_j}{\partial z} = \frac{\omega_j \pi N \alpha_{12}}{c}\left[V_{j+1}(v - iu) - V_{j-1}(v + iu)\right]. \tag{2.46}$$

## 2.5 Wave vector mismatch

The above field equation (2.46) can be further generalised to include longitudinal wave vector mismatch $\Delta k_j$ which allows for wave vectors to differ from the value $k_j^0 = \frac{\omega_j}{c}$ which characterises on axis propagation in a medium with no dispersion.

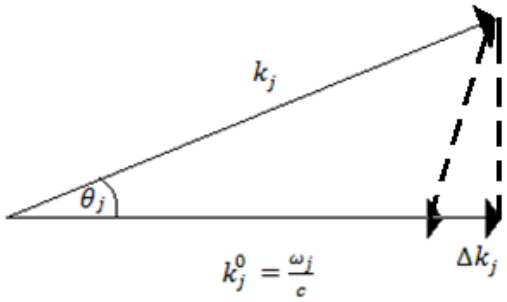


**Figure 2a – The z component of the wave vector differs from the dispersionless case.**

As demonstrated by Figure 1a, the wave vector mismatch takes the form

$$\Delta k_j = k_j \cos\theta_j - \frac{\omega_j}{c} \quad . \tag{2.47}$$

For small cone angles, $\Delta k_j$ can be approximated by

$$\Delta k_j = k_j - \frac{\omega_j}{c} \ . \tag{2.48}$$

The introduction of wave vector mismatch leads to the electric field given in equation (2.2) taking a new form

$$\epsilon(z,t) = \sum_j E_j(z,t) cos\left[\omega_j(t_{lab} - {}^{z}/_{c}) - \Delta k_j z + \emptyset_j\right] \ . \tag{2.49}$$

Under the expansion (2.49) the envelope field equations (2.46) becomes generalised through the incorporation of mismatch terms which account for the effects of off axis propagation or refractive index phase contributions when all the optical fields propagate collinearly.

$$\frac{\partial V_j}{\partial z} = -i\Delta k_j V_j + \frac{\omega_j \pi N \alpha_{12}}{c}\left[V_{j+1}(v - iu) - V_{j-1}(v + iu)\right] \ . \tag{2.50}$$

The mismatch term on the right hand side of equations (2.50) can be eliminated through the introduction of ansatz

$$V_j(z,t) = F_j e^{-i\Delta k_j z}, \tag{2.51}$$

$$\frac{\partial F_j}{\partial z} = \frac{\omega_j \pi N \alpha_{12}}{c}\left[F_{j+1}(v-iu)e^{-i(\Delta k_{j+1}-\Delta k_j)z} - F_{j-1}(v+iu)e^{i(\Delta k_j - \Delta k_{j-1})z}\right]. \tag{2.52}$$

The medium excitation $q(z,t)$ can be defined as

$$v + iu = q(z,t)e^{-i(\Delta k_0 - \Delta k_{-1})z}\ , \tag{2.53}$$

and the mistuning can be identified as

$$\Delta_{\mathrm{j}} = \left(\Delta k_j - \Delta k_{j-1}\right) - (\Delta k_0 - \Delta k_{-1}). \tag{2.54}$$

Implementing equations (2.53) and (2.54) yields the field equations for $F_j(z,t)$

$$\frac{\partial F_j}{\partial z} = \frac{\omega_j \pi N \alpha_{12}}{c}\left[q^* F_{j+1} e^{-i\Delta_{\mathrm{j}+1} z} - q F_{j-1} e^{i\Delta_{\mathrm{j}} z}\right]. \tag{2.55}$$

## 2.6 Medium dynamics

The time evolution of the medium excitation can be analysed using equations (2.41) where

$$\frac{\partial(v+iu)}{\partial t} = -\frac{1}{T_2}(v+iu) - i\Delta(v+iu) - (\Omega_R + i\Omega_I)w\ , \tag{2.56}$$

and substituting equation (2.53) gives

$$\frac{\partial q}{\partial t} = -\left(\frac{1}{T_2} + i\Delta\right)q - \Omega \mathrm{e}^{\mathrm{i}(\Delta k_0 - \Delta k_{-1})z} w\ , \tag{2.57}$$

where the detuning is now given as

$$\Delta = \left(\frac{\alpha_{22}-\alpha_{11}}{4\hbar}\right)\sum_j F_j F_j^* + \delta\omega\ . \tag{2.58}$$

Through the use of equations (2.19), (2.51) and (2.54) one can re-write equation (2.57) in terms of the field components $F_j$ and mistuning $\Delta_j$

$$\frac{\partial q}{\partial t} = -\left(\frac{1}{T_2} + i\Delta\right) q - w\frac{\alpha_{12}}{2\hbar}\sum_j F_j F_{j-1}^* e^{-i\Delta_j z} \ . \tag{2.59}$$

The dynamics of the population difference can also be described in terms of the field components $F_j$ and the medium excitation $q$ by using equation (2.41) and (2.53) which gives

$$\frac{\partial w}{\partial t} = \frac{1}{2}\left(iq\frac{\alpha_{21}}{2\hbar}\sum_j F_j^* F_{j-1} e^{i\Delta_j z} + (i\Omega_I Im|q| + + i\Omega_R Re|q|)e^{-i(\Delta k_0 - \Delta k_{-1})z}\right) - \frac{w-w_0}{T_1}. \tag{2.60}$$

## 2.7 The UMRG equations

If the medium is taken to be relatively unpopulated, i.e. $w = -1$ and $\frac{\partial w}{\partial t} = 0$ the governing equations of the Raman system become

$$\frac{\partial F_j}{\partial z} = \frac{\omega_j \pi N \alpha_{12}}{c}\left[q^* F_{j+1} e^{-i\Delta_{j+1} z} - q F_{j-1} e^{i\Delta_j z}\right]$$

$$\frac{\partial q}{\partial t} = -\left(\frac{1}{T_2} + i\Delta\right) q + \frac{\alpha_{12}}{2\hbar}\sum_j F_j F_{j-1}^* e^{-i\Delta_j z} \tag{2.61}$$

$$\Delta = \left(\frac{\alpha_{22} - \alpha_{11}}{4\hbar}\right)\sum_j F_j F_j^* + \delta\omega \ ,$$

where equations (2.61) are known as the Ultra-broadband Multi-frequency Raman Generation equations (UMRG equations).

The normalised form of equations (2.61) are given as

$$\frac{\partial A_j}{\partial Z} = \frac{\omega_j}{2\omega_0}\left[P^* A_{j+1} e^{-i\gamma_{j+1} Z} - P A_{j-1} e^{i\gamma_j Z}\right]$$

$$\left(\frac{T_2}{t_p}\right)\frac{\partial P}{\partial \tau} = -(1 + i\delta)P + \sum_j A_j A_{j-1}^* e^{-i\gamma_j Z}, \tag{2.62}$$

$$\delta = T_2\left(\mathrm{I}_0\left(\frac{\alpha_{22} - \alpha_{11}}{4\hbar}\right)\sum_j A_j A_j^* + \delta\omega\right).$$

The parameter $\gamma_j = \frac{\Delta_j}{gI_0}$ is the normalised mistuning which defines the level of medium dispersion for the $j^{th}$ frequency component, $Z = gI_0 z$ is the gain-length product where g is the steady -state gain coefficient and $I_0$ is the intensity of the pump. $\tau = \frac{t}{t_p}$ is time normalised by the pump pulse width $t_p$.

The normalisation process undertaken in reference (32) can be found in Appendix A. Equations (2.62) form a complete set of multi-wave (parametrically and non parametrically coupled) envelope equations, where each field component is linked to every other field in the system through multiple four-wave interactions.

The steady state form of equations (2.62) are given as

$$\frac{\partial A_j}{\partial Z} = \frac{\omega_j}{2\omega_0}\left[P^* A_{j+1} e^{-i\gamma_{j+1}Z} - P A_{j-1} e^{i\gamma_j Z}\right]$$

$$P = \frac{1}{(1+i\delta)} \sum_j A_j A_{j-1}^* \, e^{-i\gamma_j Z} \qquad (2.63)$$

$$\delta = T_2 \left(I_0 \left(\frac{\alpha_{22}-\alpha_{11}}{4\hbar}\right) \sum_j A_j A_j^* + \delta\omega\right).$$

Generally, the steady state UMRG equations need to be numerically integrated and only the specific case of zero mistuning, $\gamma_j = 0$, offers analytical solutions (such solutions will not be discussed here).

Unless otherwise specified the results throughout this thesis are presented for a cavity containing molecular hydrogen at 1 atmosphere of pressure where the transition of interest is the S(1) rotational transition. The pump laser frequency is taken to be $\frac{\omega_0}{2\pi c} = 18900\ cm^{-1}$, and the transition frequency is taken to be $\frac{\omega_R}{2\pi c} = 587\ cm^{-1}$. The gain of the exploited transition will be taken to be 0.2 *GWcm*$^{-1}$ and the dephasing time $T_2$ is taken to be approximately *2 ns* (74).

The UMRG equations can also be derived in such a way as to include transverse dimensions where the electric field envelope is of the form

$$\epsilon(x', y', z, t) = \sum_j E_j(x', y', z, t) cos\left[\omega_j(t_{lab} - {}^{Z}/_{c}) - \Delta k_j z + \emptyset_j\right]. \tag{2.65}$$

In this case the normalised steady state transverse multi-frequency Raman equations take the form given in reference (78)

$$\frac{\partial A_j}{\partial Z} - i d_j \nabla_{\mathrm{T}}^2 A_j = \frac{\omega_j}{2\omega_0}\left[P^* A_{j+1} e^{-i\gamma_{\mathrm{j}+1} Z} - P A_{j-1} e^{i\gamma_{\mathrm{j}} Z}\right]$$

$$P(x, y) = \frac{1}{(1+i\delta)} \sum_j A_j A_{j-1}^* \, e^{-i\gamma_{\mathrm{j}} \mathrm{Z}} \tag{2.66}$$

$$\delta = T_2 \left(\mathrm{I}_0 \left(\frac{\alpha_{22} - \alpha_{11}}{4\hbar}\right) \sum_j A_j A_j^* + \delta\omega\right).$$

Where $\nabla_{\mathrm{T}}^2$ is the scaled transverse Laplacian, which is scaled by the half width of a reference Gaussian beam, $\omega_P$. The parameter $d_j$ is a set of diffraction terms which characterise the diffraction of each frequency component of the total electric field. In Reference (78) the diffraction terms are normalised to the width of a reference Gaussian beam in which case the set of diffraction terms are equal to

$$d_j = \frac{L_R}{4L_D^j}. \tag{2.67}$$

Where $L_R$ is the stimulated Raman scattering gain length

$$L_R = \frac{1}{\mathrm{g I}_0}, \tag{2.68}$$

and $L_D^j$ is the diffraction length of each frequency component of the electric field

$$L_D^j = \frac{\omega_j {\omega_P}^2}{2c}. \tag{2.69}$$

The combination of equations (2.68) and (2.69) means that the diffraction terms have the same normalisation as the normalised spatial length $Z$.

The implementation of the UMRG equations is carried out using various numerical schemes such as Runge Kutta methods (79, 80, 81) and finite difference schemes such as Crank-Nicolson methods (82, 83) and ADI methods (84). A detailed account of each specific method and their implementation can be found in appendix B.

## 2.8 Cavity UMRG

The theoretical work presented throughout this thesis characterises the growth of broadband frequency spectra in a Raman medium confined within a unidirectional ring cavity. The ring cavity consists of four mirrors at $45^{\circ}$ angles and confines the Raman medium. Three of the mirrors are taken to be broadband with unity reflectivity and the final mirror is a partially transmitting coupling mirror.

The constant wave (CW) multi-frequency Raman equations derived in chapter 2 are used to simulate the growth of broadband Raman spectra within the cavity. The system is initially pumped adiabatically at the pump, $\omega_0$, and first Stokes, $\omega_{-1}$, frequencies (two-colour pumping) and the Raman equations are numerically integrated over the cavity length, $Z_c$. At the end of each cavity transit the amplitude of each frequency component is subject to a bulk mirror reflectivity and further pumping at the pump and first Stokes frequencies.

Throughout a cavity transit each frequency component is assumed to be subject to a total phase shift of $4\pi$ through reflections at each mirror surface. The case of limited bandwidth mirrors will be covered in chapter 8. A basic diagram of the cavity geometry is given in figure 2b.

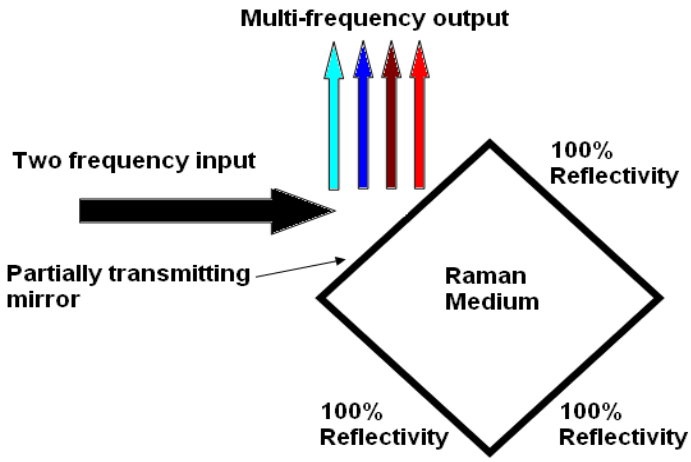


**Figure 2b – Raman cavity geometry, the amplitudes generated within the Raman medium are subject to pumping and loss at the final cavity mirror.**

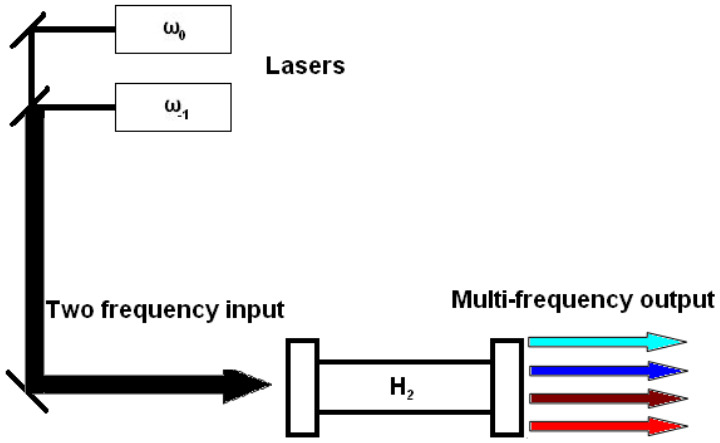


**Figure 2c– Diagram of the basic setup for symmetric pumping of molecular hydrogen (77).**

Typical non-cavity Raman experiments can produce multiple Raman sideband frequencies through molecular modulation induced by pumping at both a pump frequency $\omega_0$ and first Stokes sideband frequency $\omega_{-1}$. Such non-cavity Raman experiments can be capable of generating several sideband frequencies ($\sim 30$ in the case of molecular hydrogen) which are suitable for the synthesis of femtosecond pulses. A basic diagram for symmetrically pumped molecular hydrogen is given in figure 2c.

# CHAPTER 3

## The Gain suppression analysis

It has been shown both theoretically (69) and experimentally (84) that in the presence of dispersion (wave-vector mismatch) the first Stokes and anti-Stokes sidebands experience exponential gain which is proportional to the level of dispersion. In the case of zero dispersion (phase-matched condition) the gain is suppressed and the parametric coupling between the waves leads to the termination of their growth (through the depletion of the medium excitation).

Gain suppression can be shown to occur mathematically by considering a 3-wave subset of the UMRG envelope equations (first Stokes, pump and first anti-Stokes sidebands). The substitution of a trial plane wave solution reduces the envelope equations to an eigenvalue equation, which is quadratic with respect to the gain parameter. The complex roots of the eigenvalue equation can then be used to find general solutions which describe the growth of the sideband amplitudes.

Before undertaking the analysis of the full multi-wave UMRG equations, and characterising the growth of the Stokes and anti-Stokes bandwidth within the ring cavity system, it is instructive to look at the dynamics of a simpler 3-wave subsystem which consists of the first Stokes, pump and first anti-Stokes components $(j = -1,0,1)$. All higher order sidebands are taken to be zero amplitude and do not contribute to the evolution of the 3-wave system.

Throughout this chapter a 3-wave parametric gain suppression analysis will be derived, which extends the original work presented by Shen and Bloembergen (69) to include cavity boundary conditions (periodic boundary pumping and loss), and also the effects of pump depletion and a finite Stokes shift $\varepsilon = \frac{\omega_R}{\omega_0}$. In these gain suppression analyses only a single pump, at the $j = 0$ frequency, is considered.

We seek here approximate linear solutions to the UMRG equations (2.62) which will describe the gain of the Stokes amplitude.

The governing envelope equations (steady-state) for the 3-wave Raman system, without a cavity, are given by equation (2.63) as

$$\frac{dA_{-1}}{dZ} = \frac{1}{2}(1-\varepsilon)\left[|A_0|^2 A_{-1} + A_0^2 A_1^* e^{i\gamma_1 Z}\right] \tag{3.1}$$

$$\frac{dA_0}{dZ} = \frac{1}{2}[A_0(|A_1|^2 - |A_{-1}|^2)] \tag{3.2}$$

$$\frac{dA_1}{dZ} = -\frac{1}{2}(1+\varepsilon)\left[|A_0|^2 A_1 + A_0^2 A_{-1}^* e^{i\gamma_1 Z}\right], \tag{3.3}$$

where the Stokes shift parameter $\varepsilon = \frac{\omega_R}{\omega_0}$.

Assuming zero pump depletion, $\frac{dA_0}{dZ} = 0$, and denoting for the m$^{th}$ cavity round trip in the medium $A_0^2 = A_{0,m}^2 = \left|A_{0,m}\right|^2 e^{i2\theta_m}$

where $\theta_m = \arg\left[A_{0,m}\right]$, and similarly $A_{-1} = A_{-1,m}$ and $A_1 = A_{1,m}$. Equations (3.1) and (3.3) become

$$\frac{dA_{-1,m}}{dZ} = \frac{|A_{0,m}|^2}{2}(1-\varepsilon)\left[A_{-1,m} + A_{1,m}^* e^{i\gamma_1 Z + i2\theta_m}\right] \tag{3.4}$$

$$\frac{dA_{1,m}}{dZ} = -\frac{|A_{0,m}|^2}{2}(1+\varepsilon)\left[A_{1,m} + A_{-1,m}^* e^{i\gamma_1 Z + i2\theta_m}\right]. \tag{3.5}$$

These sidebands are assumed to be subject to a lumped loss at a coupling mirror of amplitude reflectivity $R_j$ for the field $A_j$:

$$A_{-1,m+1}(Z=0) = R_{-1}A_{-1,m}(Z=L)$$

$$A_{1,m+1}(Z=0) = R_1 A_{1,m}(Z=L).$$

For the undepleted pump model, one could model the intra-cavity pump field through

$$A_{0,m+1} = A_0 + A_{0,m}R_0 e^{-\alpha L + i\emptyset} \quad , m = 1,2,3 \ldots , \tag{3.6}$$

where $\alpha$ includes any linear loss, $L = Z_c$ is the cavity length, $R_0$ is the pumps (amplitude) cavity mirror reflectivity and $m$ is the transit number. $\alpha$ defines any linear loss within the cavity and $\emptyset$ defines any pump mistuning from cavity resonance.

For the undepleted model the evolution of the pump may be treated as a geometric series, since

$m = 1, \quad A_{0,m} = A_0$

$m = 2, \quad A_{0,m} = A_0 + A_0 R_0 e^{-\alpha L + i\emptyset} = A_0(1 + R_0 e^{-\alpha L + i\emptyset})$

$m = 3, \quad A_{0,m} = A_0 + R_0 e^{-\alpha L + i\emptyset} A_0\left(1 + R_0 e^{-\alpha L + i\emptyset}\right) = A_0\left(1 + R_0 e^{-\alpha L + i\emptyset} + (R_0 e^{-\alpha L + i\emptyset})^2\right)$ , etc.

Thus, the series can be defined as

$$A_{0,m} = \sum_{j=1}^{m} A_0 (R_0 e^{-\alpha L + i\emptyset})^{j-1} = \frac{A_0(1 - R_0^m e^{-m(\alpha L + i\emptyset)})}{(1 - R_0 e^{-\alpha L + i\emptyset})} .$$

There are two cases of interest defined by this model such as the resonant high-finesse limit, where $R_0 e^{-\alpha L} = 1$, and the case of $R_0 e^{-\alpha L} < 1$. The high finesse case causes the pump to grow as $mA_0$, while for any value of finite cavity loss the series converges. Convergence depends on the inequality $\left|R_0\ e^{-(\alpha L + i\emptyset)}\right| < 1$ (i.e. the modulus is less than unity).

It is convenient to conjugate the Stokes field equation, so that the model now takes the form

$$\frac{dA_{-1,m}}{dZ} = \frac{|A_{0,m}|^2}{2}(1 - \varepsilon)\left[A_{-1,m} + A_{1,m}^* e^{i\gamma_1 Z + i2\theta_m}\right] \tag{3.7}$$

$$\frac{dA_{1,m}^*}{dZ} = -\frac{|A_{0,m}|^2}{2}(1 + \varepsilon)\left[A_{1,m}^* + A_{-1,m} e^{-i\gamma_1 Z - i2\theta_m}\right] . \tag{3.8}$$

These equations pose an eigenvalue problem with a periodic set of eigenfunctions, $A_{-1,m}$, $A_{1,m}^*$, and eigenvalues $K_m^{\pm}$ which permit general solutions to be constructed.

We seek trial eigensolutions of the form:

$$A_{-1,m}(Z) = a_{-1,m}e^{\left[\left(K_m+i\frac{\gamma_1}{2}\right)Z+i\theta_m\right]} \tag{3.9}$$

$$A^*_{1,m}(Z) = a^*_{1,m}e^{\left[\left(K_m-i\frac{\gamma_1}{2}\right)Z-i\theta_m\right]}. \tag{3.10}$$

Introducing the trial eigensolutions into equations (3.7) and (3.8) gives.

$$a_{-1,m}\left(K_m + i\frac{\gamma_1}{2}\right) = \frac{|A_{0,m}|^2}{2}(1-\varepsilon)\left[a_{-1,m} + a^*_{1,m}\right] \tag{3.11}$$

$$a^*_{1,m}\left(K_m - i\frac{\gamma_1}{2}\right) = -\frac{|A_{0,m}|^2}{2}(1+\varepsilon)\left[a^*_{1,m} + a_{-1,m}\right]. \tag{3.12}$$

This can be expressed in matrix form,

$$\begin{bmatrix} K_m + i\frac{\gamma_1}{2} - \frac{|A_{0,m}|^2}{2}(1-\varepsilon) & -\frac{|A_{0,m}|^2}{2}(1-\varepsilon) \\ \frac{|A_{0,m}|^2}{2}(1+\varepsilon) & K_m - i\frac{\gamma_1}{2} + \frac{|A_{0,m}|^2}{2}(1+\varepsilon) \end{bmatrix} \begin{matrix} a_{-1,m} \\ a^*_{1,m} \end{matrix} = \begin{matrix} 0 \\ 0 \end{matrix} \tag{3.13}$$

Taking the determinant of the coefficient matrix to determine non-trivial sideband solutions gives:

$$K_m^2 + \left(|A_{0,m}|^2\varepsilon\right)K_m + \frac{{\gamma_1}^2}{4} + i\frac{|A_{0,m}|^2\gamma_1}{2} = 0, \tag{3.14}$$

which has complex solutions:

$$K_m^{\pm} = -\frac{|A_{0,m}|^2\varepsilon}{2} \pm \frac{1}{2}\sqrt{\left(|A_{0,m}|^2\varepsilon\right)^2 - 4\left(\frac{\gamma_1}{4} + i\frac{|A_{0,m}|^2\gamma_1}{2}\right)}. \tag{3.15}$$

Splitting equation (3.15) into its real and imaginary components yields,

$$K_m^{\pm} = Re[K_m^{\pm}] + iIm(K_m^{\pm}),$$

$$Re[K_m^{\pm}] =$$

$$-\frac{|A_{0,m}|^2\varepsilon}{2} \pm \frac{1}{2\sqrt{2}}\left[\left(|A_{0,m}|^4\varepsilon^2 - \gamma_1^2\right) + \sqrt{\left(|A_{0,m}|^4\varepsilon^2 - \gamma_1^2\right)^2 + 4|A_{0,m}|^4{\gamma_1}^2}\right]^{\frac{1}{2}} \quad (3.16)$$

$$Im[K_m^{\pm}] = \mp \frac{1}{2\sqrt{2}}\left[-\left(|A_{0,m}|^4\varepsilon^2 - \gamma_1^2\right) + \sqrt{\left(|A_{0,m}|^4\varepsilon^2 - \gamma_1^2\right)^2 + 4|A_{0,m}|^4{\gamma_1}^2}\right]^{\frac{1}{2}}, \quad (3.17)$$

where $Re[K_m^{\pm}]$ parameterises the growth (or attenuation) of the eigenmodes of the Raman sidebands within the cavity. The imaginary component is linked to the phase evolution of the eigenmodes of each sideband.

General solutions to the envelope equations can be written as a linear combination of eigensolutions with coefficients $C_{ks,m}$and $C_{ka,m}$ (where $k = 1,2$)

$$A_{-1,m}(Z) = \left(C_{1s,m}e^{K_m^+ Z} + C_{2s,m}e^{K_m^- Z}\right)e^{i\frac{\gamma_1}{2}Z + i\theta_m} \quad (3.18)$$

$$A_{1,m}^*(Z) = \left(C_{1a,m}e^{K_m^+ Z} + C_{2a,m}e^{K_m^- Z}\right)e^{-i\frac{\gamma_1}{2}Z - i\theta_m}\ . \quad (3.19)$$

The cavity boundary conditions then determine the form of the coefficients involved in the general solutions. Setting $Z = 0$ in equations (3.18) and (3.19) gives

$$A_{-1,m}(0) = \left(C_{1s,m} + C_{2s,m}\right)e^{i\theta_m} \quad (3.20)$$

$$A_{1,m}^*(0) = \left(C_{1a,m} + C_{2a,m}\right)e^{-i\theta_m}\ . \quad (3.21)$$

Taking the $Z$-derivative of equations (3.18) and (3.19) and equating the results to equations (3.7) and (3.8) respectively and setting $Z = 0$

$$\left(K_m^+ + i\frac{\gamma_1}{2}\right)C_{1s,m}e^{i\theta_m} + \left(K_m^- + i\frac{\gamma_1}{2}\right)C_{2s,m}e^{i\theta_m} = \frac{|A_{0,m}|^2}{2}(1-\varepsilon)\left[A_{-1,m}(0) + A_{1,m}^*(0)e^{i2\theta_m}\right] \quad (3.22)$$

$$\left(K_m^+ - i\frac{\gamma_1}{2}\right)C_{1a,m}e^{-i\theta_m} + \left(K_m^- - i\frac{\gamma_1}{2}\right)C_{2a,m}e^{-i\theta_m} = -\frac{|A_{0,m}|^2}{2}(1+\varepsilon)\left[A_{1,m}^*(0) + A_{-1,m}(0)e^{-i2\theta_m}\right].$$

(3.23)

Substituting equation (3.20) into equation (3.22) and re-arranging gives

$$\frac{\left[2K_m^+ + i\gamma_1 - |A_{0,m}|^2(1-\varepsilon)\right]}{|A_{0,m}|^2(1-\varepsilon)}C_{1s,m} + \frac{\left[2K_m^- + i\gamma_1 - |A_{0,m}|^2(1-\varepsilon)\right]}{|A_{0,m}|^2(1-\varepsilon)}C_{2s,m} = A_{1,m}^*(0)e^{i\theta_m},$$

(3.24)

while substituting equation (3.21) into equation (3.23) and re-arranging gives

$$\frac{\left[2K_m^+ - i\gamma_1 + |A_{0,m}|^2(1+\varepsilon)\right]}{|A_{0,m}|^2(1+\varepsilon)}C_{1a,m} + \frac{\left[2K_m^- - i\gamma_1 + |A_{0,m}|^2(1+\varepsilon)\right]}{|A_{0,m}|^2(1+\varepsilon)}C_{2a,m} = -A_{-1,m}(0)e^{-i\theta_m}.$$

(3.25)

The derivatives of equations (3.18) and (3.19) equated to equations (3.7) and (3.8), when $Z = 0$ gives

$$\left(K_m^+ + i\frac{\gamma_1}{2}\right)C_{1s,m}e^{K_m^+ + i\frac{\gamma_1}{2}Z + i\theta_m} + \left(K_m^- + i\frac{\gamma_1}{2}\right)C_{2s,m}e^{K_m^- + i\frac{\gamma_1}{2} + i\theta_m} = \frac{|A_{0,m}|^2}{2}(1-\varepsilon)\left[A_{-1,m} + A_{1,m}^*e^{i\gamma_1 Z + i2\theta_m}\right]$$

(3.26)

$$\left(K_m^+ - i\frac{\gamma_1}{2}\right)C_{1a,m}e^{K_m^+ - i\frac{\gamma_1}{2}Z - i\theta_m} + \left(K_m^- - i\frac{\gamma_1}{2}\right)C_{2a,m}e^{K_m^- - i\frac{\gamma_1}{2} - i\theta_m} = -\frac{|A_{0,m}|^2}{2}(1+\varepsilon)\left[A_{1,m}^* + A_{-1,m}e^{-i\gamma_1 Z - i2\theta_m}\right].$$

(3.27)

The substitution of equations (3.18) and (3.19) into both equations (3.26) and (3.27) gives

$$\left[\left(K_m^+ + i\frac{\gamma_1}{2}\right)C_{1s,m} - \frac{|A_{0,m}|^2}{2}(1-\varepsilon)\left(C_{1s,m}+C_{1a,m}\right)\right]e^{(K_m^+ - K_m^-)Z} = \frac{|A_{0,m}|^2}{2}(1-\varepsilon)\left(C_{2s,m}+C_{2a,m}\right) - \left(K_m^- + i\frac{\gamma_1}{2}\right)C_{2s,m} \tag{3.28}$$

$$\left[\left(K_m^+ - i\frac{\gamma_1}{2}\right)C_{1a,m} + \frac{|A_{0,m}|^2}{2}(1+\varepsilon)\left(C_{1s,m}+C_{1a,m}\right)\right]e^{(K_m^+ - K_m^-)Z} = -\frac{|A_{0,m}|^2}{2}(1+\varepsilon)\left(C_{2s,m}+C_{2a,m}\right) - \left(K_m^- - i\frac{\gamma_1}{2}\right)C_{2a,m}\ . \tag{3.29}$$

Taking the derivative of equations (3.28) and (3.29) and setting Z = 0 gives

$$(K_m^+ - K_m^-)\left[\left(K_m^+ + i\frac{\gamma_1}{2}\right)C_{1s,m} - \frac{|A_{0,m}|^2}{2}(1-\varepsilon)\left(C_{1s,m}+C_{1a,m}\right)\right] = 0 \tag{3.30}$$

$$(K_m^+ - K_m^-)\left[\left(K_m^+ - i\frac{\gamma_1}{2}\right)C_{1a,m} + \frac{|A_{0,m}|^2}{2}(1+\varepsilon)\left(C_{1s,m}+C_{1a,m}\right)\right] = 0\ . \tag{3.31}$$

When $K_m^+ \neq K_m^-$ , re-arranging equation (3.30) or (3.31) gives the ratio

$$\frac{C_{1a,m}}{C_{1s,m}} = \frac{2K_m^+ + i\gamma_1 - |A_{0,m}|^2(1-\varepsilon)}{|A_{0,m}|^2(1-\varepsilon)}\ , \tag{3.32}$$

and comparing equation (3.32) to equation (3.25), with use of equation (3.20) one finds the ratio of the complementary components

$$\frac{C_{2a,m}}{C_{2s,m}} = \frac{2K_m^- + i\gamma_1 - |A_{0,m}|^2(1-\varepsilon)}{|A_{0,m}|^2(1-\varepsilon)}\ . \tag{3.33}$$

The use of relations (3.20) and (3.25) then yields equations for $C_{1s,m}$ and $C_{2s,m}$

$$C_{1s,m} = \frac{|A_{0,m}|^2(1-\varepsilon)A_{1,m}^*(0)e^{i\theta m} + \left[|A_{0,m}|^2(1-\varepsilon) - 2K_m^- - i\gamma_1\right]A_{-1,m}(0)e^{-i\theta m}}{2\left(K_m^+ - K_m^-\right)} \ ,$$

(3.34)

$$C_{2s,m} = \frac{|A_{0,m}|^2(1-\varepsilon)A_{1,m}^*(0)e^{i\theta m} + \left[|A_{0,m}|^2(1-\varepsilon) - 2K_m^+ - i\gamma_1\right]A_{-1,m}(0)e^{-i\theta m}}{2\left(K_m^- - K_m^+\right)} \ .$$

(3.35)

The above expressions fully define the mode coefficients involved in the gain suppression analysis for an undepleted pump.

Setting the Stokes shift $\varepsilon = 0$, transit number $m = 0$ and $|A_{0,m}|^2 = 1$ recovers the results of the gain suppression analysis of Shen and Bloembergen (69).

## 3.1 The depleted pump model

In later sections, where predictions made by the gain suppression analysis are compared to results from numerical simulations, it is found that the undepleted pump model accurately describes the evolution of the first Stokes and anti-Stokes amplitudes for cavity configurations with relatively short cavity lengths, small initial Stokes seed and low coupling mirror reflectivity. When parameters are selected to include moderate cavity lengths, larger initial seed amplitudes or higher levels of cavity mirror reflectivity, it is found that there are increased levels of pump depletion within the Raman medium. These trends are expected because larger initial Stokes seed amplitudes and longer interaction lengths lead to more developed evolution of the Stokes and anti-Stokes amplitudes. Similarly, higher cavity reflectivity increases the amplitudes of the (nonlinearly) interacting waves. The undepleted pump analysis thus fails to capture these effects. To provide a more complete picture of the wave dynamics it is worth including the effect of intra-

cavity pump depletion in a form other than the general linear loss mechanisms described by $\alpha$ in equation (3.6).

Taking into account the envelope equation for the pump amplitude (equation (3.2))

$$\frac{dA_0}{dZ} = \frac{1}{2}[A_0(|A_1|^2 - |A_{-1}|^2)]$$

it can be seen that an increase in the Stokes ($j = -1$) amplitude leads to a decrease in the amplitude of the pump. For short cavity lengths the right hand side of equation (3.2) can be taken to be zero. This is equally so for low initial Stokes seeds. However, this simplification does not apply when the initial level of the Stokes amplitude, or cavity length, is appreciable.

To extend the range of accuracy of this cavity gain suppression analysis, one can to find a solution to equation (3.2) and express this in terms of the general solutions given by the gain suppression analysis. Such a solution can be easily obtained by writing the envelope equation for the intra-cavity pump amplitude in the following form

$$\frac{dA_{0,m}}{dZ} = f(Z)A_{0,m}\,, \tag{3.36}$$

and the function $f(Z)$ is defined as

$$f(Z) = \frac{1}{2}\left[\left(\left|A_{1,m}\right|^2 - \left|A_{-1,m}\right|^2\right)\right]\,. \tag{3.37}$$

Re-arranging equation (3.36) gives

$$\frac{dA_{0,m}}{A_{0,m}} = f(Z)dZ\,, \tag{3.38}$$

and after integration

$$\left[\ln A_{0,m}\right]_{A_{0,m}(0)}^{A_{0,m}(Z')} = \left[\int f(Z)dZ\right]_0^{Z=Z'}\,. \tag{3.39}$$

This yields a formal solution for the pump amplitude

$$A_{0,m}(Z') = A_{0,m}(Z'=0)e^{\left[\int_{Z=0}^{Z=Z'} f(Z)dZ\right]}\,. \tag{3.40}$$

The function $f(Z)$ can be evaluated using the general solutions for the first Stokes and anti-Stokes amplitudes and its integration can be safely handled via the

trapezium rule. The inclusion of pump depletion extends the validity of the gain suppression analysis to a larger range of parameters. This is demonstrated later in Figure 3a, where a stronger agreement between the depletion model and numerical results is illustrated.

## 3.2 The small dispersion regime

As expressions can be complicated, it is worth deriving approximate solutions to the gain suppression analysis. The case of particular interest is the case of small dispersion, and it will be shown throughout the following analysis that cavity pumping masks the effects of dispersion through suppression of the Stokes gain.

The small dispersion regime is of particular interest because for all but the most extreme choice of initial conditions cavity pumping supports the inequality $\gamma_1^2 \ll \varepsilon^2 \left|A_{0,m}\right|^2$ (where the chosen level of normalised dispersion is much smaller than the pump intensity multiplied by the Stokes shift).

A simple form of the gain parameter can be obtained using the above inequality and the Taylor expansion $\sqrt{1+x} = 1 + {}^{x}/_{2} - {}^{x^2}/_{8}$.

Equation (3.16) can be written as

$$Re[K_m^{\pm}] = -\frac{\left|A_{0,m}\right|^2 \varepsilon}{2} \pm \frac{1}{2\sqrt{2}}\left[\left(\left|A_{0,m}\right|^4 \varepsilon^2 - \gamma_1^2\right) + \sqrt{\left|A_{0,m}\right|^8 \varepsilon^4 - 2\gamma_1^2 \left|A_{0,m}\right|^4 \varepsilon^2 + 4\left|A_{0,m}\right|^4 {\gamma_1}^2}\right]^{\frac{1}{2}}$$

where the term $\gamma_1^4$ has been dropped due to its very small value.

Dividing the term within the square root by a factor of $\left|A_{0,m}\right|^8\varepsilon^4$ gives

$$Re[K_m^{\pm}] = -\frac{\left|A_{0,m}\right|^2\varepsilon}{2} \pm \frac{1}{2\sqrt{2}}\left[\left(\left|A_{0,m}\right|^4\varepsilon^2 - \gamma_1^2\right) + \left|A_{0,m}\right|^4\varepsilon^2\sqrt{1+\left(\frac{4\gamma_1^2/\varepsilon^2 - 2\gamma_1^2}{\left|A_{0,m}\right|^4\varepsilon^2}\right)}\right]^{\frac{1}{2}}, \tag{3.41}$$

and applying the Taylor expansion to the second order gives

$$Re[K_m^{\pm}] = -\frac{\left|A_{0,m}\right|^2\varepsilon}{2} \pm \frac{1}{2\sqrt{2}}\left[\left(\left|A_{0,m}\right|^4\varepsilon^2 - \gamma_1^2\right) + \left|A_{0,m}\right|^4\varepsilon^2\left(1+\frac{2\gamma_1^2}{\left|A_{0,m}\right|^4\varepsilon^4} - \frac{\gamma_1^2}{\left|A_{0,m}\right|^4\varepsilon^2} - \frac{2\gamma_1^4}{\left|A_{0,m}\right|^8\varepsilon^8} - \frac{\gamma_1^4}{2\left|A_{0,m}\right|^8\varepsilon^4} + \frac{2\gamma_1^4}{\left|A_{0,m}\right|^8\varepsilon^6}\right)\right]^{\frac{1}{2}}, \tag{3.42}$$

which can be rewritten as

$$Re[K_m^{\pm}] = -\frac{\left|A_{0,m}\right|^2\varepsilon}{2} \pm \frac{1}{2\sqrt{2}}\left[2\left|A_{0,m}\right|^4\varepsilon^2 - 2\gamma_1^2\left|A_{0,m}\right|^4\varepsilon^2 - 2\gamma_1^2 + 2\frac{\gamma_1^2}{\varepsilon^2} - \frac{2\gamma_1^4}{\left|A_{0,m}\right|^4\varepsilon^6} + \frac{\gamma_1^4}{2\left|A_{0,m}\right|^4\varepsilon^2} - \frac{2\gamma_1^4}{\left|A_{0,m}\right|^4\varepsilon^4}\right]^{\frac{1}{2}}. \tag{3.43}$$

After dropping terms proportional to $\gamma_1^4$ a simple equation for the real component of the gain parameter is found to be

$$Re[K_m^{\pm}] = -\frac{\left|A_{0,m}\right|^2\varepsilon}{2} \pm \frac{1}{2}\sqrt{\left|A_{0,m}\right|^4\varepsilon^2 - \gamma_1^2\left|A_{0,m}\right|^4\varepsilon^2 + \frac{\gamma_1^2}{\varepsilon^2}}, \tag{3.44}$$

and following the same method , an expression for the imaginary component of the gain can also be found to be

$$Im[K_m^{\pm}] = \mp\frac{\gamma_1^2}{\varepsilon^2}. \tag{3.45}$$

Equations (3.44) and (3.45) offer a few insights into cavity gain suppression. Firstly there is always a small dispersion dependent contribution to the Stokes phase from the imaginary component of the gain parameter. Secondly, when large pump intensities build up as a result of cavity pumping the real component of the positive

gain approaches an amplitude of $[K_m^{\pm}] \approx 0$ , which is the gain experienced with zero dispersion.

The above results indicate that in the extreme limit that $m \to \infty$ and $\gamma_1^2 \ll \varepsilon^2 \left|A_{0,m}\right|^2$ equations (3.18) and (3.19) become the zero dispersion gain equations, given as

$$Re[K_m^{\pm}] \approx -\frac{\left|A_{0,m}\right|^2 \varepsilon}{2} \pm \frac{\left|A_{0,m}\right|^2 \varepsilon}{2}, \tag{3.46}$$

$$Im[K_m^{\pm}] = \mp \frac{\gamma_1^2}{\varepsilon^2} \approx 0 . \tag{3.47}$$

Hence the positive and negative Stokes gains are given as,

$$K_m^{+} = 0 , \tag{3.48}$$

$$K_m^{-} = -\left|A_{0,m}\right|^2 \varepsilon . \tag{3.49}$$

Using the above expressions for the gain parameters and equations (3.34), (3.35) and (3.18), a simple expressions for the first Stokes amplitude can be found to be

$$A_{-1,m}(Z) = A_{-1,m}(0) e^{i\frac{\gamma_1}{2}Z + 2i\theta_m} + \frac{(1-\varepsilon)}{2\varepsilon} A_{1,m}^{*}(0) \left( e^{i\frac{\gamma_1}{2}Z + 2i\theta_m} - e^{\left(-\left|A_{0,m}\right|^2 \varepsilon + i\frac{\gamma_1}{2}\right)Z + 2i\theta_m} \right) + \frac{(1-\varepsilon)}{2\varepsilon} A_{-1,m}(0) \left( e^{i\frac{\gamma_1}{2}Z} - e^{\left(-\left|A_{0,m}\right|^2 \varepsilon + i\frac{\gamma_1}{2}\right)Z} \right) - i\frac{\gamma_1 A_{-1,m}(0)}{2\left|A_{0,m}\right|^2 \varepsilon} \left( e^{i\frac{\gamma_1}{2}Z} - e^{\left(-\left|A_{0,m}\right|^2 \varepsilon + i\frac{\gamma_1}{2}\right)Z} \right) . \tag{3.50}$$

In the limit of small $Z$ the Taylor expansion $e^x \approx 1 + x$ can be applied and equation (3.50) reduces to,

$$A_{-1,m}(Z) = A_{-1,m}(0) e^{2i\theta_m} + \frac{i\gamma_1 A_{-1,m}(0)}{2} \left(e^{2i\theta_m} - 1\right) Z + \frac{(1-\varepsilon)}{2} \left|A_{0,m}\right|^2 \left[ A_{1,m}^{*}(0) e^{2i\theta_m} - A_{-1,m}(0) \right] Z . \tag{3.51}$$

The above expression can be further simplified by specifying that $\theta_m = 0$, in which case the expression for the growth of the Stokes amplitude becomes

$$A_{-1,m}(Z) = A_{-1,m}(0) + \frac{(1-\varepsilon)}{2}\left|A_{0,m}\right|^2\left[A^*_{1,m}(0) - A_{-1,m}(0)\right]Z\,, \tag{3.52}$$

and similarly an equation for the anti-Stokes amplitude can be found to be

$$A^*_{1,m}(Z) = A^*_{1,m}(0) - \frac{(1+\varepsilon)}{2}\left|A_{0,m}\right|^2\left[A^*_{1,m}(0) + A_{-1,m}(0)\right]Z\,. \tag{3.53}$$

Equations (3.52) and (3.53) specify the growth of each sideband amplitude during each cavity transit in the limit, $\to \infty$ . They can also be recognised as the amplitude equations for the zero dispersion regime (zero positive gain).

Defining the cavity boundary conditions to be

$$A_{-1,m+1}(0) = A_{-1,m}(Z)R_0\,,$$

$$A^*_{1,m+1}(0) = A^*_{1,m}(Z)R_0\,,$$

and

$$A_{0,m} = \sum_{j=1}^{m} A_0(R_0)^{j-1}$$

allows recurrence relations to be constructed from equations (3.52) and (3.53), given as

$$A_{-1,m+1}(Z) = \left[A_{-1,m}(Z) + \frac{(1-\varepsilon)}{2}\left|A_{0,m}\right|^2\left[A^*_{1,m}(Z) - A_{-1,m}(Z)\right]Z\right]R_0 \tag{3.54}$$

$$A^*_{1,m+1}(Z) = \left[A^*_{1,m}(Z) - \frac{(1+\varepsilon)}{2}\left|A_{0,m}\right|^2\left[A^*_{1,m}(Z) + A_{-1,m}(Z)\right]Z\right]R_0\,. \tag{3.55}$$

The above relations show that each cavity transit depends on the final amplitudes of the preceding cavity transit. This gives rise to a series of terms ($(m+1)$ terms) which decrease in amplitude as the number of cavity transits is increased, forming a convergent series. Two specific cases of interest arise as $m \to \infty$, the choice of $R_0 = 1$ and $R_0 < 1$. In the first case the Stokes and anti-Stokes intensities reach a steady state and further cavity transits (and cavity pumping) produce no further sideband growth, and in the second case the intensities reach their maximum level and then decrease after each further cavity transit in proportion to $R_0^2$, where $|A_{-1}|^2 \to 0$ and $|A_1|^2 \to 0$.

The above equations apply specifically to the small dispersion regime $\gamma_1^2 \ll \varepsilon^2 \left|A_{0,m}\right|^2$ as $m \to \infty$. When larger levels of dispersion are considered extra terms (proportional to the level of dispersion) also contribute to the growth of sidebands. However the final results, at large $m$, and in the limits of $R_0 = 1$ and $R_0 < 1$ remain consistent with the analysis given above. Figures 4a and 4b provide examples of Stokes growth within the cavity when $R_0 = 1$ and $R_0 < 1$ respectively.

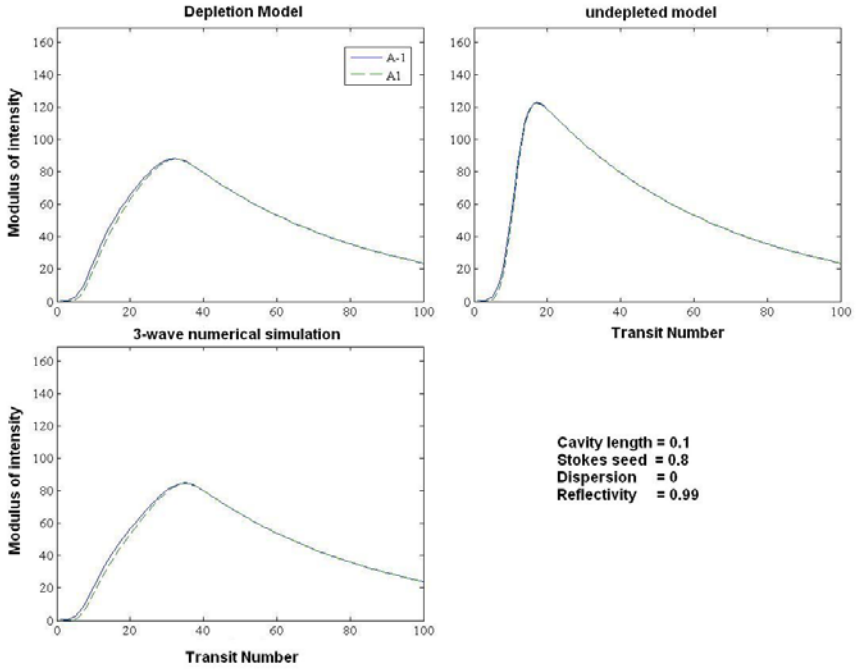


**Figure 3a – When the chosen value of reflectivity is less than unity the Stokes (solid line) and anti-Stokes (dashed line) intensities reach their maximum level and then decrease with every further cavity transit by a factor of $R_0^2$.**

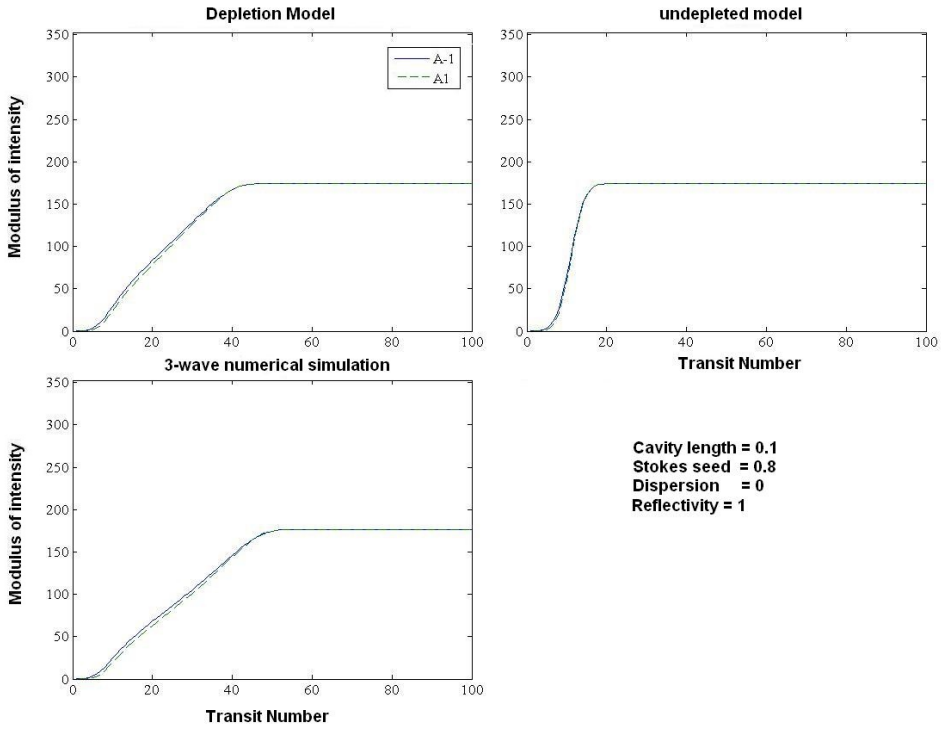


**Figure 3b – When the chosen value of reflectivity is unity the Stokes (solid line) and anti-Stokes (dashed line) intensities reach a fixed level. Further cavity transits give rise to no additional growth.**

Through the selection of a specific parameter regime the gain suppression analysis has provided simple equations which characterise the growth of the first Stokes and anti-Stokes sidebands within the cavity. Equation (3.44) implies that cavity pumping leads to gain suppression within the cavity.

## 3.3 The gain parameter $K^{\pm}$

The results of the previous section indicated that gain suppression occurs within the cavity system because of pumping. This will now be considered in more detail, starting with the variation of the gain parameter with respect to dispersion for non-cavity UMRG.

Gain suppression in non-cavity UMRG has been well documented in reference (25). In the absence of dispersion ($\gamma_1 = 0$) gain is fully suppressed, while for finite values of dispersion the level of gain becomes positive and increases with increasing levels of dispersion. Looking at equations (3.41) and (3.42) for the first transit only ($m = 0$) the results from reference (25) can be recovered. Figure 3c shows the evolution of the real component of $K_0^+$ which is the exact curve given for the non-cavity UMRG system (for $H_2$).

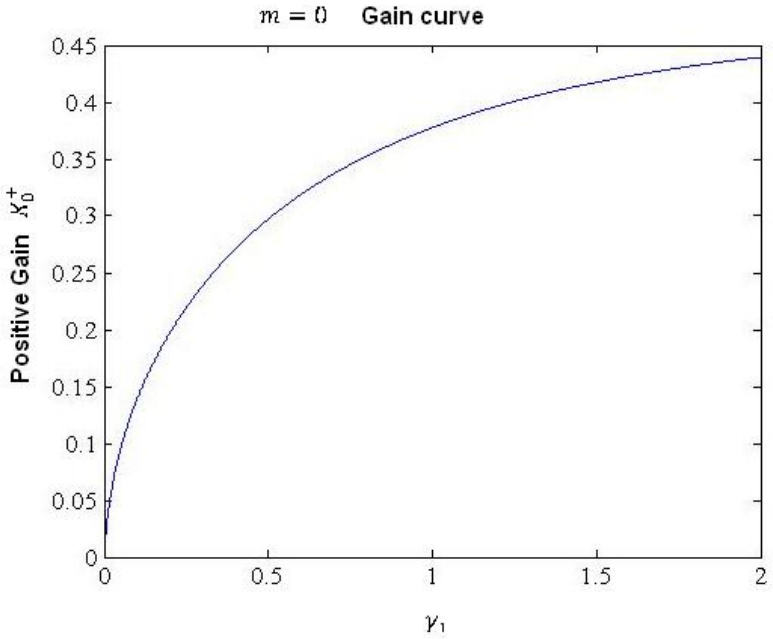


**Figure 3c – The $m = 0$ Gain curve is the same gain curve for the non-cavity UMRG gain suppression analysis, as found in reference (25) for $H_2$. For this particular figure the range of values for the dispersion has been extended past the range explored in reference (25).**

When considering the gain in the cavity system it can be recognised from equations (3.16) that the level of gain is determined not only by the level of dispersion and Stokes shift but also cavity pumping.

Figure 3d shows how the Stokes gain decreases as the pump intensity builds up within the cavity. In the case of the undepleted pump model the gain decreases geometrically to a fixed value which depends on both the level of dispersion which specifies the initial gain and the choice of cavity mirror reflectivity which determines the final pump amplitude. These results agree with equation (3.44) which indicates that the real positive gain decreases towards zero as the pump intensity builds up within the cavity.

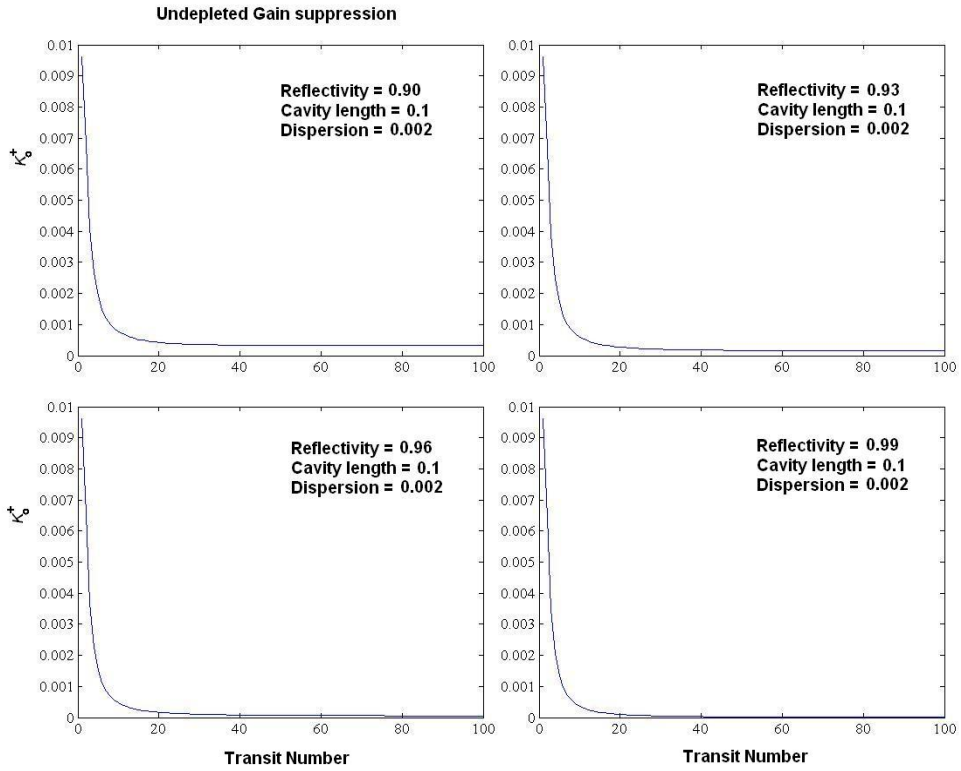


**Figure 3d – Positive ( $K_m^+$) gain curves for the undepleted pump model for increasing values of cavity mirror reflectivity. The selection of higher values of reflectivity leads to a greater decrease in the amount of positive gain over a number of cavity transits. The gain decreases in proportion to the growth of the pump intensity.**

When the depleted pump gain suppression model is taken into account the level of pump depletion affects the growth of the gain parameter. The results of figure 3e show that increasing amounts of pump depletion (proportional to the level of the Stokes and anti-Stokes intensities) slows down cavity gain suppression, and can significantly alter the shape of the gain curve. When pump depletion is taken into account the Stokes and anti-Stokes sidebands experience a greater level of parametric gain for a large number of cavity transits.

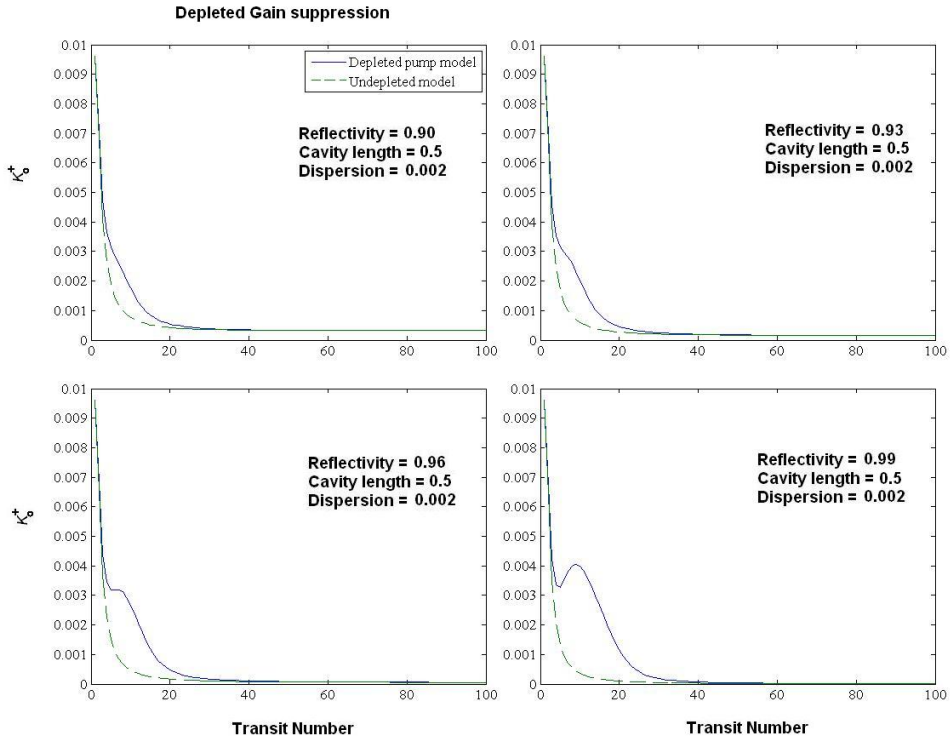


**Figure 3e – Positive ( $K_m^+$) gain curves for the undepleted (dashed line) and depleted (solid line) pump models for increasing values of cavity mirror reflectivity. A significant amount of pump depletion offsets the loss of positive Stokes gain incurred by boundary pumping.**

## 3.4 Gain suppression vs numerical simulations

Throughout this section the results given by both the undepleted and depleted pump gain suppression models will be compared to results achieved by the numerical integration of the initial system of equations (3.1), (3.2) and (3.3). A broad range results are provided in Appendix C which demonstrate the accuracy of the depleted and undepleted pump analysis. The results are given for a range of initial Stokes seeds, coupling mirror reflectivity and cavity lengths.

Since the gain suppression analysis represents a linear approximation of the nonlinear equations (3.1 and 3.3) it will not provide suitable results over certain ranges of parameters. The analysis is expected to break down at points where the chosen parameter regime produces large (nonlinearly interacting) Stokes and anti-Stokes amplitudes, and when terms contributing to non-parametric growth in the UMRG equations become large.

The results of the analysis will now be compared to results of numerical simulations to yield insight into the points at which the gain suppression analysis begins to break down. The parameter regimes of interest are cavity length, dispersion and Stokes seed amplitude.

Figures 3f, 3g and 3h represent the ranges of parameters for which the gains suppression analysis applies, which cover dispersion, Stokes seed amplitude and coupling mirror reflectivity respectively. These figures take the form of contour plots where the red and blue regions represent strong levels of agreement and strong levels of disagreement respectively. The measure of agreement is that the ratio of the Stokes intensity predicted by the gain suppression analysis to the value given by numerical integration of the UMRG equations should fall within the range, $0.9 > 1 < 1.1$.

Together figures 3f,3g and 3h indicate that the gain suppression analysis breaks down when combinations of large levels of dispersion, large initial Stokes seeds, high values of coupling mirror reflectivity and moderate to long cavity lengths are employed. These results indicate that strong disagreement between the analysis and simulations exist when parameter regimes are chosen which lead to the generation of large sideband amplitudes. In the case of simulations of the UMRG equations, the Stokes and anti-Stokes amplitudes are nonlinearly interacting, and when the amplitudes become large enough the results of the simulations differ from those of the linear gain suppression analysis.

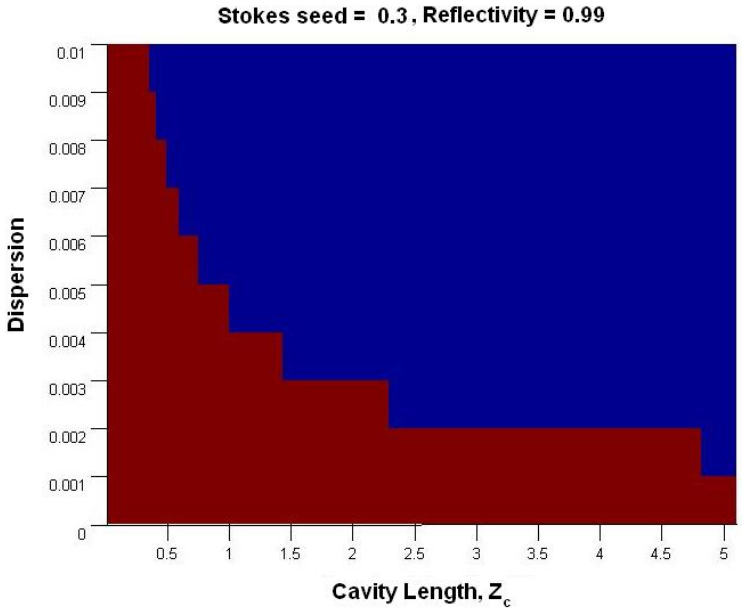


**Figure 3f – This figure demonstrates the accuracy of the gain suppression analysis for a range of cavity lengths and values of dispersion. The red are indicates where the analysis fully agrees with the numerical simulations, and the blue section indicates strong disagreements.**

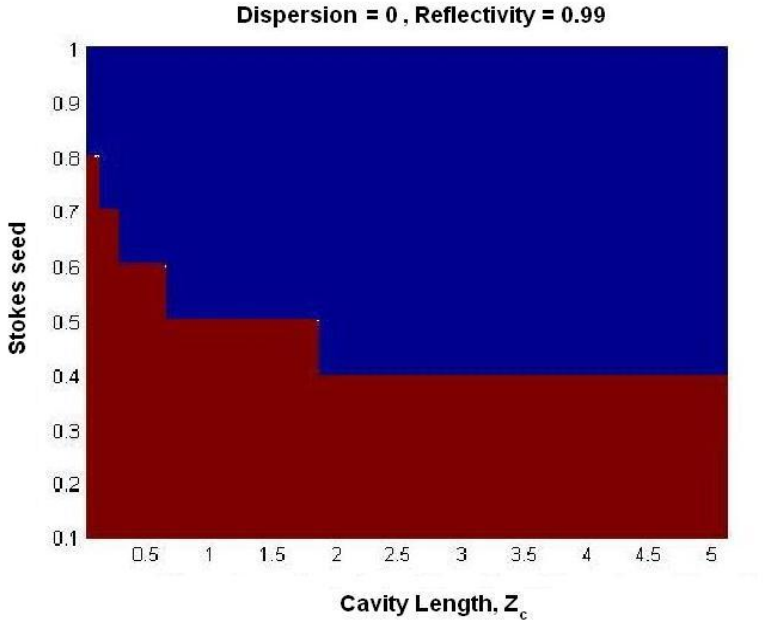


**Figure 3g – This figure demonstrates the accuracy of the gain suppression analysis for a range of cavity lengths and levels of initial Stokes seed. The red are indicates the where the analysis fully agrees with the numerical simulations, and the blue section indicates strong disagreements.**

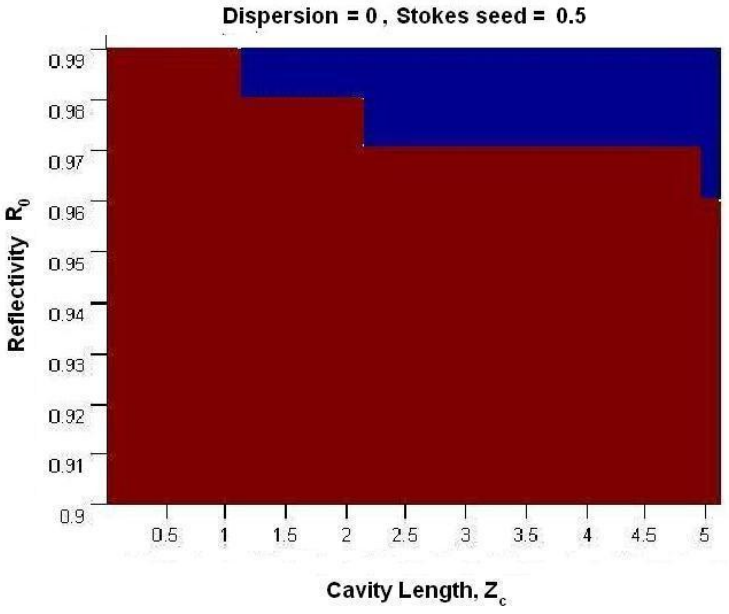


**Figure 3h – This figure demonstrates the accuracy of the gain suppression analysis for a range of values of cavity length and Reflectivity. The red indicates the where the analysis fully agrees with the numerical simulations, and the blue section indicates strong disagreements.**

If a combination of finite levels of dispersion and long cavity lengths is considered. Such as the ranges considered in figure 3f. The affects of non-parametric terms contributing to sideband growth in the UMRG equations also needs to be considered. The agreement between the numerical results and gain suppression analysis can begin to differ when non-parametric terms begin to drive the growth of the sideband amplitudes

The effects of non-parametric growth can be characterised by considering the extreme limit of long cavity length and a high level of dispersion. In this case the integral of the second term on the right hand side of equation (3.1) effectively gives

$$\int A_0^2 A_1^* e^{i\gamma_1 Z}\, dZ = 0. \tag{3.56}$$

Equation (3.56) holds true when $\gamma_1 z$ causes exponential terms to oscillate rapidly. In this limit the equation effectively has an average of zero and equations (3.1 and 3.3) reduce to

$$\frac{dA_{-1}}{dZ} = \frac{1}{2}(1-\varepsilon)[|A_0|^2 A_{-1}]\,, \tag{3.57}$$

$$\frac{dA_1}{dZ} = -\frac{1}{2}(1+\varepsilon)[|A_0|^2 A_1]\,. \tag{3.58}$$

Where equations (3.57 and 3.58) are governed by non-parametric terms and describe the extreme case of high dispersion and long cavity lengths. The gain suppression analysis fails to describe the UMRG equations in this limit.

It has been made clear that the accuracy of the gain suppression restricts its use to parameter regimes which include short cavity lengths, small to moderate initial Stokes seed amplitudes and small to moderate levels of dispersion. In these regimes Stokes and anti-Stokes growth is approximately linear (in terms of the numerical simulations) and non-parametric growth is minimised (in the case of finite dispersion). It will be shown in later chapters, that the above parameter regimes are optimal for bandwidth growth in the symmetrically pumped multi-wave analysis.

# CHAPTER 4

## Gain suppression analysis with finite linear detuning

The effect of the two-photon detuning present in equations (2.63) has so far been ignored. The detuning is given as:

$$\delta = T_2\left(\mathrm{I}_0\left(\frac{\alpha_{22}-\alpha_{11}}{4\hbar}\right)\sum_j A_j A_j^* + \delta\omega\right), \tag{4.1}$$

and has both linear and nonlinear components.

This section of the thesis will extend the framework of the previous gain suppression analysis to include the linear two-photon detuning from Raman resonance.

The linear detuning is given as:

$$\delta\omega = W_{21} - (\omega_0 - \omega_{-1}) = W_{21} - \omega_R. \tag{4.2}$$

The governing envelope equations for the 3-wave Raman system are obtained from equations (2.63):

$$\frac{dA_{-1}}{dZ} = \frac{(1-\varepsilon)}{2(1-i\delta)}\left[|A_0|^2 A_{-1} + A_0^2 A_1^* e^{i\gamma_1 Z}\right]$$

$$\frac{dA_0}{dZ} = \frac{1}{2(1-i\delta)}\left[A_0^* A_{-1} A_1 e^{-i\gamma_1 Z} + |A_1|^2 A_0\right] - \frac{1}{2(1+i\delta)}\left[A_0^* A_{-1} A_1 e^{-i\gamma_1 Z} + |A_{-1}|^2 A_0\right] \tag{4.3}$$

$$\frac{dA_1}{dZ} = -\frac{(1+\varepsilon)}{2(1+i\delta)}\left[|A_0|^2 A_1 + A_0^2 A_{-1}^* e^{i\gamma_1 Z}\right].$$

Employing a similar method to the one applied in the last chapter a gain suppression analysis for finite detuning can be derived, where equations for the gain $K_m^{\pm}$ and general solutions to the above envelope equations can be found:

$$K_m^{\pm} = -\frac{(1+i\delta)|A_{0,m}|^2\varepsilon}{D} \pm (\propto_R + i \propto_I) \quad , \tag{4.4}$$

where $D = 1 + \delta^2$ and

$$\propto_R$$

$$= \frac{1}{\sqrt{2}}\left[\left(\frac{(1-\delta^2)\left|A_{0,m}\right|^4\varepsilon^2}{D^2} + \frac{2\gamma_1\left|A_{0,m}\right|^2\delta}{D} - \gamma_1^2\right)\right.$$

$$\left. + \sqrt{\left(\frac{(1-\delta^2)\left|A_{0,m}\right|^4\varepsilon^2}{D^2} + \frac{2\gamma_1\left|A_{0,m}\right|^2\delta}{D} - \gamma_1^2\right)^2 + \frac{4\left|A_{0,m}\right|^4\left(\varepsilon^2\left|A_{0,m}\right|^2\delta - D\gamma_1\right)^2}{D^4}}\right]^{\frac{1}{2}},$$

$$\propto_I$$

$$= \frac{1}{\sqrt{2}}\left[-\left(\frac{(1-\delta^2)\left|A_{0,m}\right|^4\varepsilon^2}{D^2} + \frac{2\gamma_1\left|A_{0,m}\right|^2\delta}{D} - \gamma_1^2\right)\right.$$

$$\left. + \sqrt{\left(\frac{(1-\delta^2)\left|A_{0,m}\right|^4\varepsilon^2}{D^2} + \frac{2\gamma_1\left|A_{0,m}\right|^2\delta}{D} - \gamma_1^2\right)^2 + \frac{4\left|A_{0,m}\right|^4\left(\varepsilon^2\left|A_{0,m}\right|^2\delta - D\gamma_1\right)^2}{D^4}}\right]^{\frac{1}{2}}.$$

(4.5)

Splitting equation (4.4) into its real and imaginary components yields:

$$K_{\bar{m}}^{\pm} = Re[K_{\bar{m}}^{\pm}] + iIm[K_{\bar{m}}^{\pm}]\,,$$

$$Re[K_{\bar{m}}^{\pm}] = \frac{1}{2}\left[-\frac{\left|A_{0,m}\right|^2\varepsilon}{D} \pm \propto_R\right] \tag{4.6}$$

$$Im[K_{\bar{m}}^{\pm}] = \frac{1}{2}\left[-\frac{\delta\left|A_{0,m}\right|^2\varepsilon}{D} \mp \propto_I\right]\,, \tag{4.7}$$

where $Re[K_{\bar{m}}^{\pm}]$ is linked to the growth (or attenuation) of the Raman sidebands within the cavity. The general solutions for equations (4.3) are given as:

$$A_{-1,m}(Z) = \left(C_{1s,m}e^{K_{\bar{m}}^{+}Z} + C_{2s,m}e^{K_{\bar{m}}^{-}Z}\right)e^{i\frac{\gamma_1}{2}Z + i\theta_m} \tag{4.8}$$

$$A_{1,m}^{*}(Z) = \left(C_{1a,m}e^{K_{\bar{m}}^{+}Z} + C_{2a,m}e^{K_{\bar{m}}^{-}Z}\right)e^{-i\frac{\gamma_1}{2}Z - i\theta_m}\,. \tag{4.9}$$

Where the constants are given as:

$$\frac{C_{1a,m}}{C_{1s,m}} = \frac{\left(2K_m^+ + i\gamma_1\right)D}{\left|A_{0,m}\right|^2(1-\varepsilon)(1+i\delta)} - 1 \quad , \tag{4.10}$$

$$\frac{C_{2a,m}}{C_{2s,m}} = \frac{\left(2K_m^- + i\gamma_1\right)D}{\left|A_{0,m}\right|^2(1-\varepsilon)(1+i\delta)} - 1 \quad , \tag{4.11}$$

$$C_{1s,m} = \frac{\left|A_{0,m}\right|^2\left(\frac{(1-\varepsilon)(1+i\delta)}{D}\right)A_{1,m}^*(0)e^{i\theta m} + \left[\left|A_{0,m}\right|^2\left(\frac{(1-\varepsilon)(1+i\delta)}{D}\right) - 2K_m^- - i\gamma_1\right]A_{-1,m}(0)e^{-i\theta m}}{2\left(K_m^+ - K_m^-\right)} \quad , \tag{4.12}$$

$$C_{2s,m} = \frac{\left|A_{0,m}\right|^2\left(\frac{(1-\varepsilon)(1+i\delta)}{D}\right)A_{1,m}^*(0)e^{i\theta m} + \left[\left|A_{0,m}\right|^2\left(\frac{(1-\varepsilon)(1+i\delta)}{D}\right) - 2K_m^+ - i\gamma_1\right]A_{-1,m}(0)e^{-i\theta m}}{2\left(K_m^- - K_m^+\right)} \quad . \tag{4.13}$$

The full derivation of the finite detuning gain suppression analysis is similar to the zero detuning derivation given in chapter 4, therefore the derivation of the finite detuning analysis will only be provided in Appendix D. By setting $\delta = 0$ in the above expressions one recovers the zero detuning analysis derived in chapter 3.

The form of the pump envelope equation from equations (4.3) complicates the use of a depleted pump analysis because it would need to be solved numerically, therefore only the undepleted model is considered in the following analysis. The code used to generate the results of the gain suppression analysis, for both the current chapter and chapter 3, is given in Appendix E.

## 4.1 The small dispersion regime

As the above expressions can be complicated it is again worth considering approximate solutions to the finite detuning gain suppression analysis, where the case of interest is the small dispersion regime.

In the case of small dispersion and in the limit that $m \to \infty$, the dispersion of the medium can be assumed to be small enough that the inequality $\gamma_1^2 \ll \epsilon^2 \left|A_{0,m}\right|^4$ holds true.

Recalling equations (4.5) and (4.6) the real component of the gain is defined as:

$$Re[K_m^{\pm}] = \frac{1}{2}\left[-\frac{\left|A_{0,m}\right|^2 \varepsilon}{D} \pm \propto_R\right]$$

$$\propto_R =$$

$$\frac{1}{\sqrt{2}}\left[\left(\frac{(1-\delta^2)\left|A_{0,m}\right|^4 \varepsilon^2}{D^2} + \frac{2\gamma_1 \left|A_{0,m}\right|^2 \delta}{D} - \gamma_1^2\right) + \sqrt{\left(\frac{(1-\delta^2)\left|A_{0,m}\right|^4 \varepsilon^2}{D^2} + \frac{2\gamma_1 \left|A_{0,m}\right|^2 \delta}{D} - \gamma_1^2\right)^2 + \frac{4\left|A_{0,m}\right|^4 \left(\varepsilon^2 \left|A_{0,m}\right|^2 \delta - D\gamma_1\right)^2}{D^4}}\right]^{\frac{1}{2}} .$$

(4.14)

The second group of terms on the right hand side of equation (4.14) can be defined as:

$$S = \left(\frac{(1-\delta^2)\left|A_{0,m}\right|^4 \varepsilon^2}{D^2} + \frac{2\gamma_1 \left|A_{0,m}\right|^2 \delta}{D} - \gamma_1^2\right)^2 + \frac{4\left|A_{0,m}\right|^4 \left(\varepsilon^2 \left|A_{0,m}\right|^2 \delta - D\gamma_1\right)^2}{D^4} , \qquad (4.15)$$

and after some re-arranging:

$$S = \varepsilon^4 \left|A_{0,m}\right|^8 \left(\frac{(1-\delta^2)}{D^2} + \frac{2\gamma_1 \delta}{D\varepsilon^2 \left|A_{0,m}\right|^2} - \frac{\gamma_1^2}{\left|A_{0,m}\right|^4 \varepsilon^2}\right)^2 + \frac{4\varepsilon^4 \left|A_{0,m}\right|^8 \left(\delta - D\frac{\gamma_1}{\varepsilon^2 \left|A_{0,m}\right|^2}\right)^2}{D^4} .$$

(4.16)

Expanding the terms in equation (4.16) and dropping terms including $\frac{\gamma_1^2}{\varepsilon^2}$ gives:

$$S = \varepsilon^4 \left|A_{0,m}\right|^8 \left[ \frac{(1-\delta^2)^2}{D^4} + \frac{4{\gamma_1}^2\delta^2}{D^2\varepsilon^4\left|A_{0,m}\right|^4} + \frac{4\gamma_1\delta(1-\delta^2)}{D^3\varepsilon^2} + \frac{4\left(\delta^2 + D^2\frac{{\gamma_1}^2}{\varepsilon^4\left|A_{0,m}\right|^4} - \frac{2D\delta\gamma_1}{\varepsilon^2\left|A_{0,m}\right|^2}\right)}{D^4} \right], \tag{4.17}$$

and neglecting terms which include $\frac{\gamma_1^2}{\varepsilon^4\left|A_{0,m}\right|^4}$ reduces equation (4.17) to:

$$S = \frac{\varepsilon^2\left|A_{0,m}\right|^4}{D}\left[1 - \frac{4\gamma_1\delta}{\varepsilon^2\left|A_{0,m}\right|^2}\right]^{\frac{1}{2}}. \tag{4.18}$$

Equation (4.14) can now be re-written using (4.18) as:

$$\propto_R = \frac{\varepsilon\left|A_{0,m}\right|^2}{D}, \tag{4.19}$$

hence the real component of the gain takes the form:

$$Re[K_m^{\pm}] = \frac{\left|A_{0,m}\right|^2\varepsilon}{2D}(-1 \pm 1). \tag{4.20}$$

Equation (4.20) has the same form as (4.46) and is in fact the zero dispersion form of the gain parameter. Following the same procedure yields an equation describing the evolution of the imaginary component of the gain parameter:

$$Im[K_m^{\pm}] = \frac{\delta\left|A_{0,m}\right|^2\varepsilon}{2D}(-1 \mp 1). \tag{4.21}$$

The finite levels of detuning leads to the attenuation of both the real and imaginary components of the gain by a factor of $D = 1 + \delta^2$. $Im[K_m^{+}]$ is also modified by a factor of $\delta$ hence the chosen sign of the detuning changes the sign of the phase of each sideband.

As with the non-cavity case the zero dispersion gain equations arise from gain suppression as a result of cavity pumping. This occurs in a way analogous to that of the zero detuning analysis.

## 4.2 The gain parameter $K^{\pm}$

The evolution of the gain parameter under the influence of linear detuning will now be discussed. Taking equation (4.4) for the first transit ($m = 0$) the variation of the initial Stokes gain for various levels of detuning can be shown.

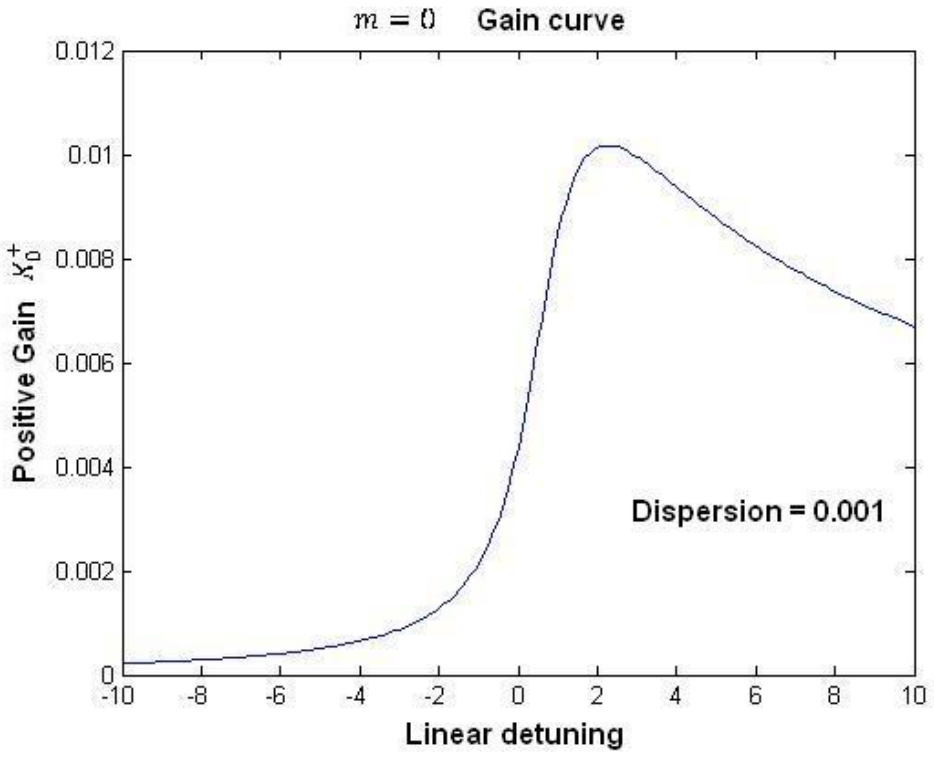


**Figure 4a – The introduction of linear detuning changes the initial value of the positive gain asymmetrically, positive detuning increases the gain, and negative detuning decreases the gain, this figure also shows maximum gain at a particular value of positive linear detuning.**

Figure 4a demonstrates that the introduction of detuning can have a large impact on the amount of gain experienced by the Stokes and anti-Stokes amplitudes. The peak of the curve given in figure 4a suggests that an optimal level of detuning exists which maximises the real component of the positive gain parameter. Figure 4b shows how the maximum Stokes gain when ($m = 0$) evolves for a range of values of dispersion and linear detuning.

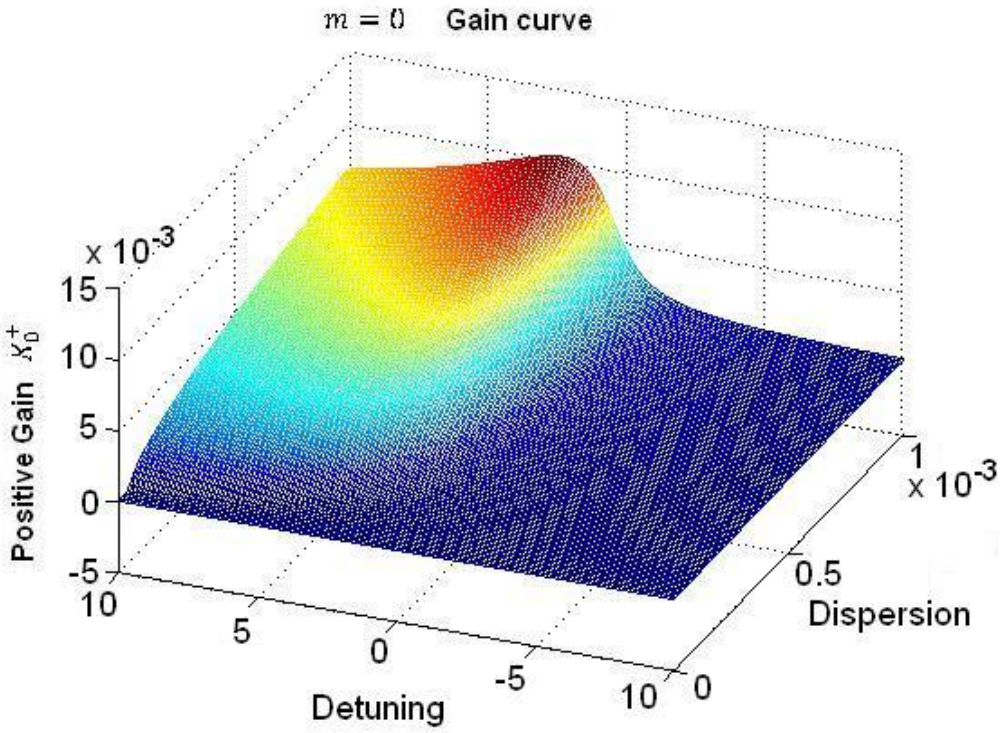


**Figure 4b – The real component of the positive gain has a maximum value when there is a positive linear detuning, the amount of detuning required to have maximum initial gain depends on the amount of medium dispersion. Hence for a non cavity system an optimum level of detuning could be selected to maximise the Stokes gain.**

The choice of ($m = 0$) is equivalent to a non cavity system, and the results within figure 4b, suggests that in the absence of a cavity the parametric gain of the Stokes and anti-Stokes amplitudes could be maximised through the selection of an optimal value of linear detuning. The value of the detuning required to maximise gain depends on the chosen level of dispersion.

When considering the gain in terms of the cavity system, equations (4.4) and (4.5) include terms where the detuning and dispersion parameters are scaled by the pump intensity. Therefore after each cavity transit the growth of the pump intensity moves the peak value of the parametric gain to larger values of detuning (because the intensity increases). In the case of a cavity the Stokes gain can only be maximised for the first cavity transit, after which cavity pumping moves the gain off its peak value. Figure 4c provides an example of the peak gain shift produced by pumping.

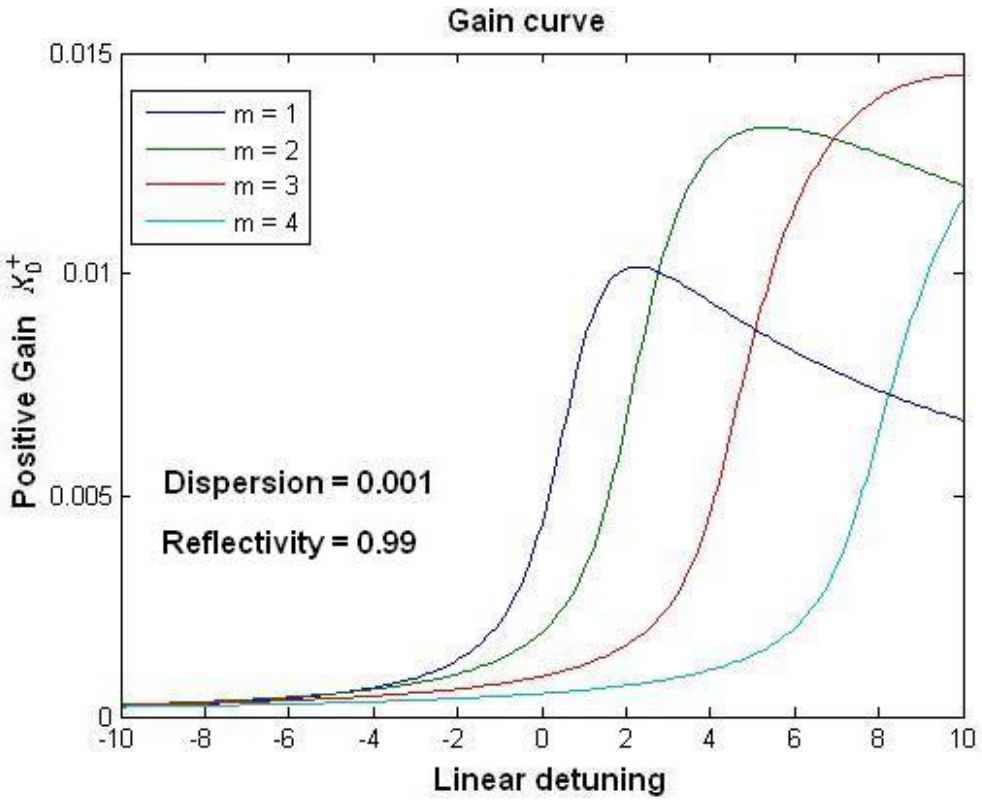


**Figure 4c – The real component of the positive gain. This figure demonstrates that for increasing numbers of cavity transits the maximum positive gain peak shifts towards higher levels of positive detuning. To achieve maximum gain in the cavity system the detuning would have to change in proportion to the increasing pump intensity.**

## 4.3 The Stokes and anti-Stokes sidebands

The results of the zero detuning and finite detuning gain suppression analyses can now be compared. Figure 4d shows the Stokes intensity for the zero detuning case and figure 4e shows the intensity when there is a finite positive detuning.

.

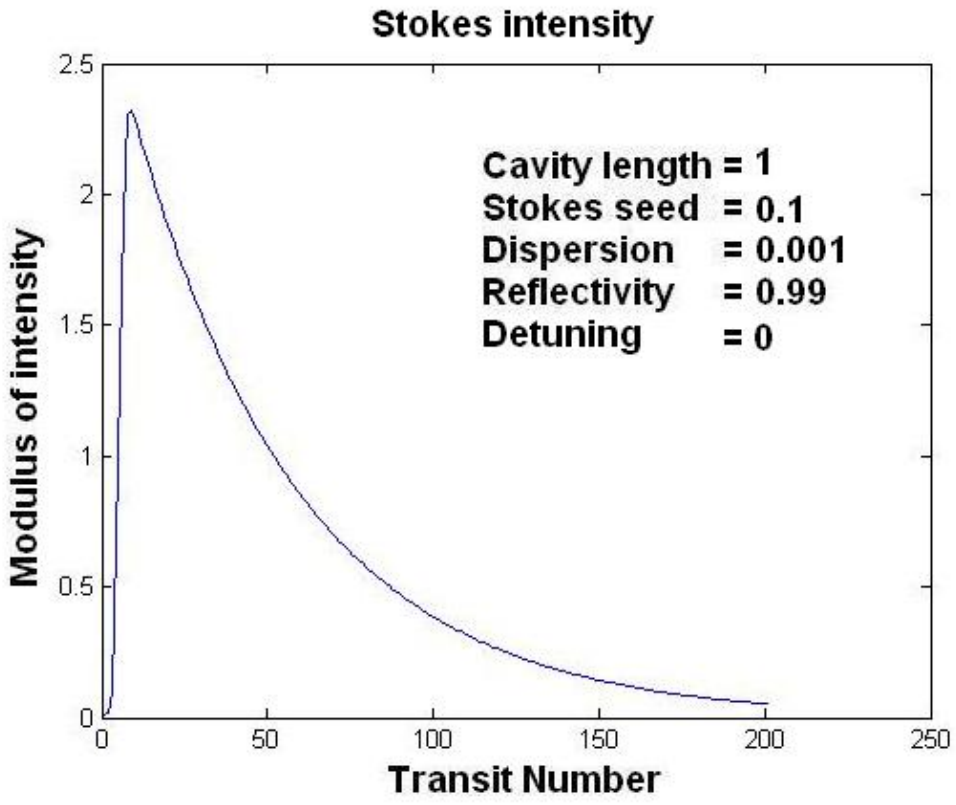


**Figure 4d – The growth of the normalised Stokes intensity with zero detuning.**

When a positive level of detuning is employed the maximum Stokes intensity generated in the cavity is greater than the intensity generated when the level of detuning is zero. This implies an increased level of parametric gain over the initial stages of sideband growth. This coincides with the gain curve shown in figure 4a and 4c which show a positive level of linear detuning leads to an increased level of initial gain which decreases with each cavity transit.

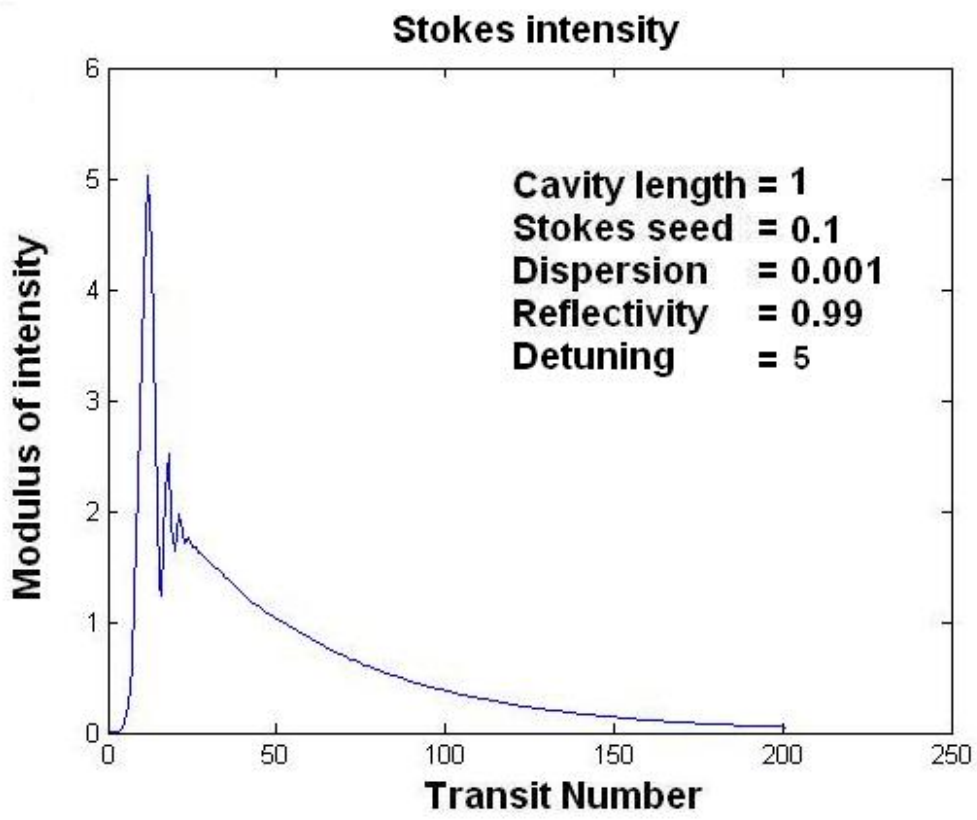


**Figure 4e – The growth of the normalised Stokes intensity when a positive level of detuning is employed. There is a large initial intensity build-up which then decreases over many cavity transits; the long term level of intensity decreases in a way which corresponds with the zero detuning results given in figure 4d.**

The long term growth of the Stokes intensity given in figure 4e resembles the zero dispersion case given in figure 4d where the growth of the pump intensity drives the gain parameter towards zero (mimicking the zero dispersion regime). It is clear from figure 4e that even when a finite level of detuning is applied the Stokes intensity converges to a maximum value (recall the recurrence relations from chapter 3). In the case of figure 4d and 4e the coupling mirror reflectivity, $R_0 < 1$, causes the intensity to eventually decrease to zero as $m \to \infty$.

The results of the finite detuning analysis indicate that a finite level of detuning contributes to the growth of sidebands within the cavity, where in the presence of finite detuning the Stokes and anti-Stokes amplitudes are subject to large levels of gain during their initial growth.

Both the finite and zero-detuning analysis indicate that as $m \to \infty$ any initial level of Stokes gain is suppressed by pumping and the growth of the Stokes and anti-Stokes amplitudes converges to a maximum value, after which the amplitudes can either decrease in proportion to the coupling mirror reflectivity or remain at a constant value (constant only for unity reflectivity mirrors).

The results of the gain suppression analysis indicate that a cavity system with only a single applied pump will be unsuitable for the generation of large bandwidths or synthesis of short pulses.

# CHAPTER 5

## Non-cavity UMRG and the ring cavity with a single pump

We can begin the analysis of full multi-frequency simulations of UMRG by first considering the growth of bandwidth in symmetrically pumped hydrogen without a cavity. Results will be presented later in this chapter which characterise bandwidth generation in the ring cavity with only a single pump at the $\omega_0$ frequency and an initial seed (equal in amplitude to the pump) at the first Stokes frequency, $\omega_{-1}$, which will be applied at the start of the first cavity transit. The growth of bandwidth within the cavity will then be compared to the results of the gain suppression analysis given in chapter 3. Finally examples of pulses synthesised from frequency spectra generated by both non-cavity and cavity UMRG will be characterised and compared.

Many authors have presented work describing the non-cavity plane wave and transient UMRG equations for a range of parameters (29, 30, 66, 70, 74). For the purpose of this thesis, results will be provided which generalise the growth of the frequency bandwidth, total intensity and medium excitation for the cases of zero and finite dispersion.

It has already been shown that a non-cavity system is capable of generating bandwidths containing approximately 30 new frequency components for both zero and finite levels of dispersion (30, 74), and for particular levels of dispersion the bandwidth can be optimised to reach levels of approximately 35 frequency components of comparable intensity. Figure 5a gives examples of the bandwidth growth for both zero and a finite level of dispersion.

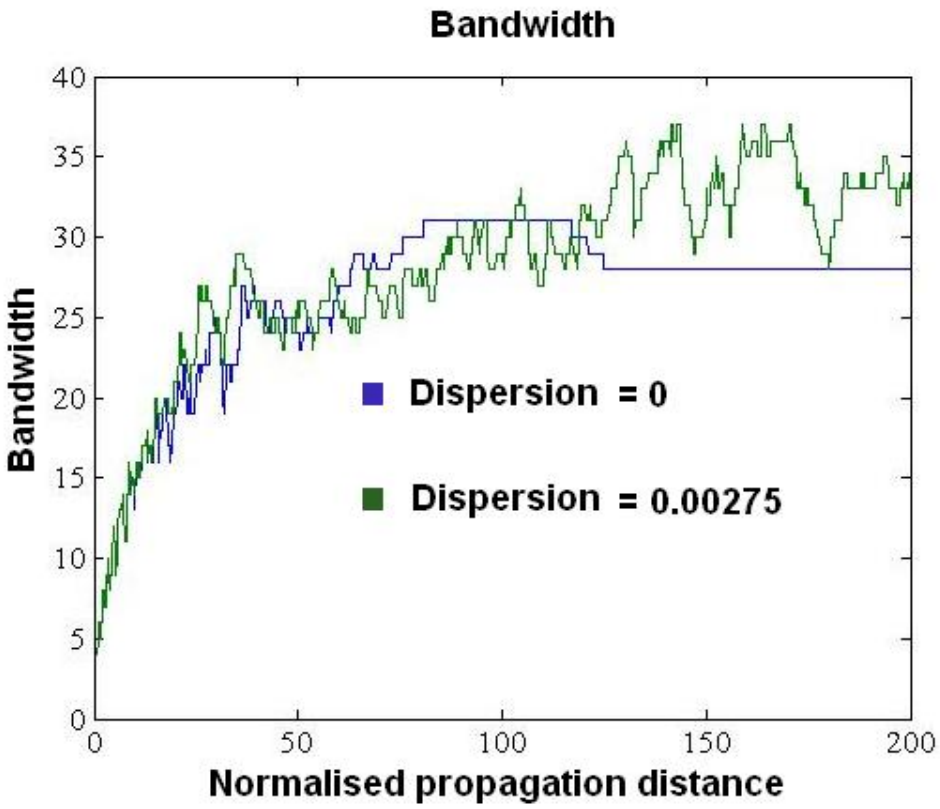


**Figure 5a – This figure shows the growth of bandwidth for both zero dispersion and finite dispersion. For a normalised dispersion of 0.00275 there is a noticeable increase in the amount of bandwidth.**

When there is no dispersion, the bandwidth generated by the non-cavity system can reach a stable level, and the point at which the bandwidth stabilises coincides with the depletion of the medium excitation amplitude. Depletion occurs when contributions of the Stokes and anti-Stokes wings of the spectrum to the medium excitation are approximately equal in magnitude and opposite in sign.

When a finite level of dispersion is employed, sideband growth can be further amplified by parametric gain, which arises as a consequence of non-zero wave vector mismatch between sidebands, and can lead to the generation of greater bandwidth. In the case of finite dispersion, the medium excitation amplitude is never fully depleted and the system does not reach a stable level of bandwidth. Figure 5a provides an example of the levels of bandwidth generated for zero

dispersion and a finite level of dispersion. In the case of finite dispersion a greater, but unstable, level of bandwidth can be achieved.

The growth of each frequency component of the Raman spectra is driven by both parametric and non-parametric processes. When a large level of dispersion is employed the maximum bandwidth can be restricted by non parametric growth (72); an example of this is given later in figure 5d.

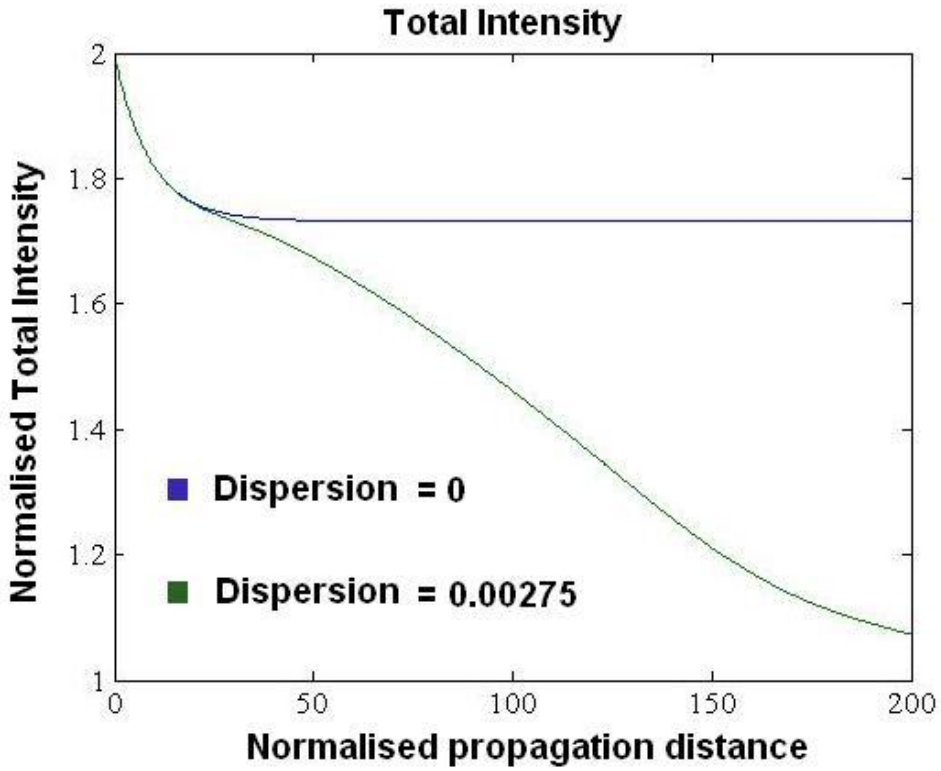


**Figure 5b – This figure shows how the intensity varies over propagation through the medium. When there is no dispersion the intensity reaches a stable level; When a finite level of dispersion is present the total intensity continues to decrease with increasing propagation distance.**

The total intensity of the multi-frequency spectrum is found to decrease with increasing propagation length. In the case of zero dispersion the intensity levels out at a fixed value, and the point at which the intensity reaches a steady state also coincides with the depletion of the medium excitation amplitude.

However, when a finite level of dispersion is employed, the intensity no longer reaches a fixed level and continues to decrease with increasing propagation length. This indicates a continuation of sideband growth, see figure 5b. This coincides with the higher bandwidths observed in figure 5a.

As previously discussed, when there is no dispersion, parametric generation of sidebands drives the medium excitation amplitude to zero ($P$ from equations (2.63)). This occurs because the total contribution to the medium excitation, made by the Stokes and anti-Stokes wings of the spectrum, cancel each other out. This is best described in terms of the first Stokes sideband, pump and first anti-Stokes sideband. In the case of zero dispersion, the anti-Stokes sideband amplitude grows $\pi$ out of phase with the Stokes amplitude, and when the Stokes and anti-Stokes amplitudes reach similar magnitudes their contributions to the medium excitation cancel out. Hence the medium excitation is driven to zero and sideband growth stops.

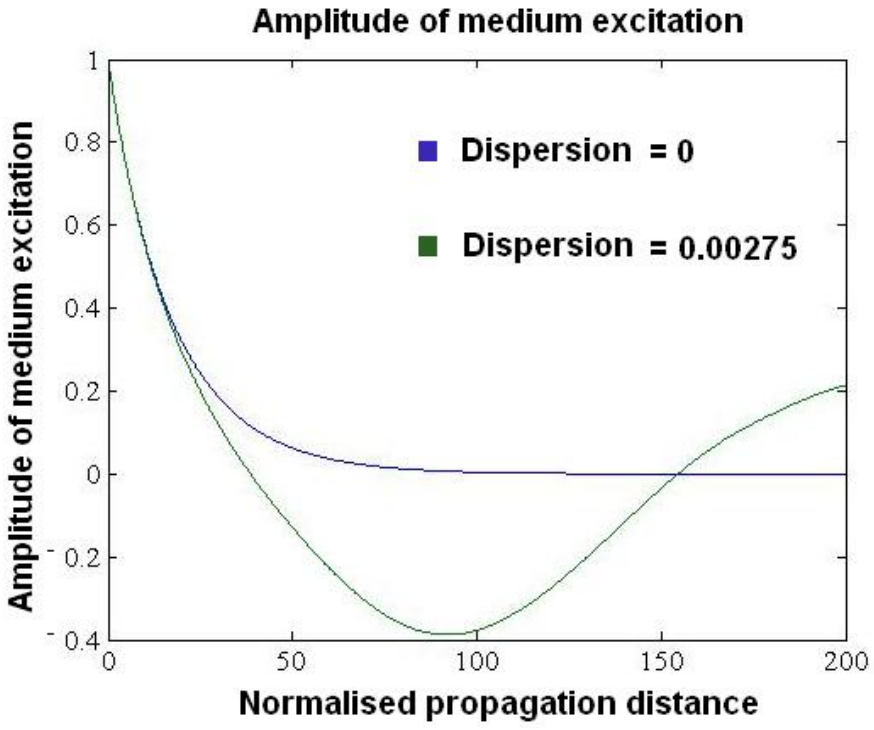


**Figure 5c – This figure shows how the medium excitation variable $P$ evolves as the spectrum propagates through the medium for two values of normalised dispersion.**

When a finite level of dispersion is introduced the growth of the medium excitation changes significantly. This occurs because dispersion alters the phase of each sideband and means that sidebands, which would usually grow with opposite phases, no longer provide cancelling contributions to the medium excitation.

Changes in sideband phase contributions manifest themselves as oscillations in the medium excitation amplitude, such as the oscillation shown in figure 5c. The non-zero medium excitation amplitude causes the generation of higher bandwidth levels, and a corresponding drop in intensity of the multi-frequency spectrum, as shown in figures 5a and 5b.

## 5.1 Large levels of dispersion and long propagation lengths

When large levels of dispersion are considered (or low levels of dispersion and long propagation lengths) non-parametric terms inherent in equations (2.63) dominate the growth of the Raman spectra and lead to cascaded Raman scattering.

Figure 5d provides an example of the growth of the frequency spectrum when a Stokes cascade occurs. The cascade process is detrimental to the growth of anti-Stokes sidebands and therefore limits the overall bandwidth (72). When a Stokes cascade occurs, only two frequency components of appreciable intensity occur at any one point in space, and as the spectrum propagates through the medium the flow of energy moves towards lower frequency sidebands. The rapid re-distribution of the pump energy into the Stokes wing of the spectrum means that no anti-Stokes sidebands of appreciable intensity can form, though some anti-Stokes radiation does exist at a very small level.

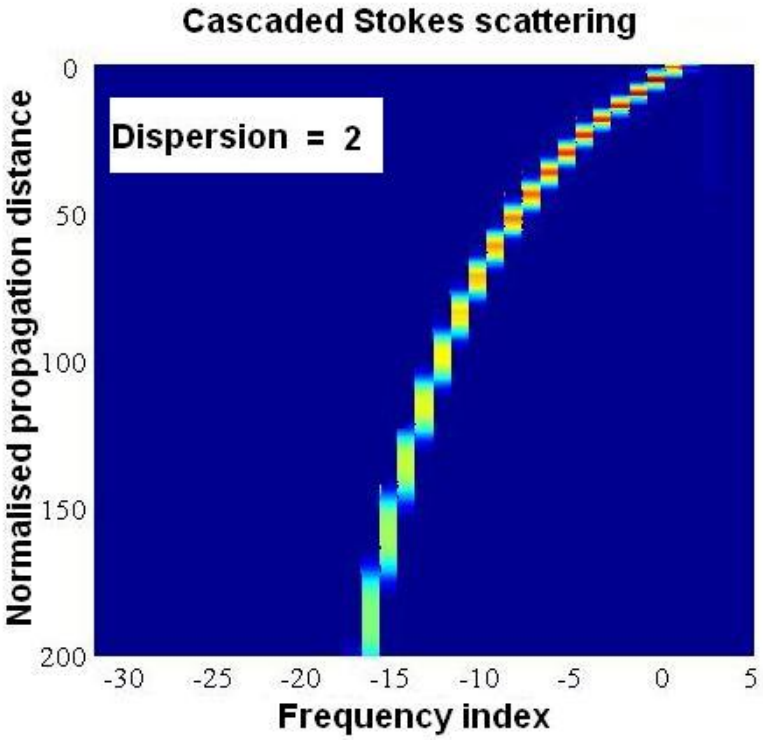


**Figure 5d – Cascaded Stokes scattering occurs for large levels of normalised dispersion (or very long propagation distances). The frequency index defines the order of the Stokes radiation i.e. -1 indicates the first Stokes sideband, -2 the second and so on.**

## 5.2 The ring cavity with a single pump

Results will now be presented which generalise the growth of the frequency spectrum in a cavity with only one pump beam at the $\omega_0$ frequency which is re-introduced at the beginning of every cavity transit. An initial seed amplitude will be applied at the first Stokes frequency at the beginning of the first cavity transit, and will possess an amplitude equal to that of the pump. The coupling mirror is taken to be partially transmitting (as described in chapter 3) and the amplitude of each frequency component of the total electric field will experience the same reflectivity i.e. the mirror has a uniform reflectivity over the entire frequency range of the simulations.

At short normalised cavity lengths the bandwidth generated using a single pump cavity is similar in the case of zero dispersion, and for small levels of dispersion. In both cases the bandwidth initially grows to a level similar to that of the non cavity system and after further cavity transits the bandwidth dies away, as shown in figure 5e. These results bear a resemblance to the results obtained by the gain suppression analysis in chapter 3; this will be described in more detail in section 5.5.

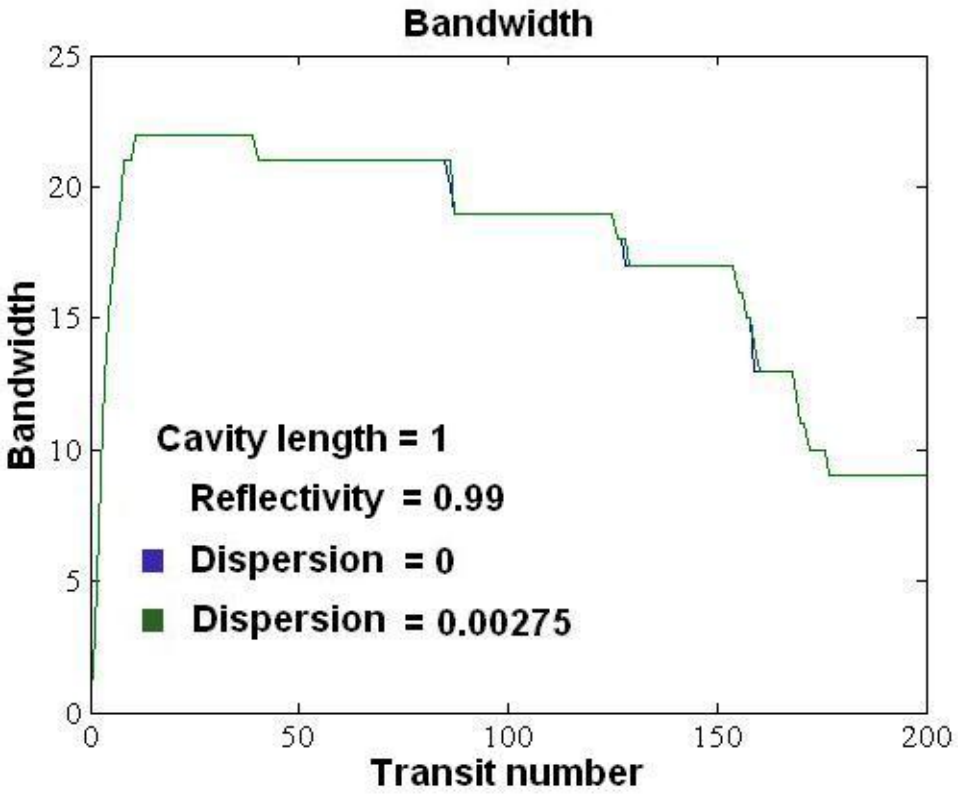


**Figure 5e – The bandwidth generated by a single pump cavity drops off with as the number of cavity transits increases. The evolution of the bandwidth is similar for both zero dispersion and low levels of dispersion.**

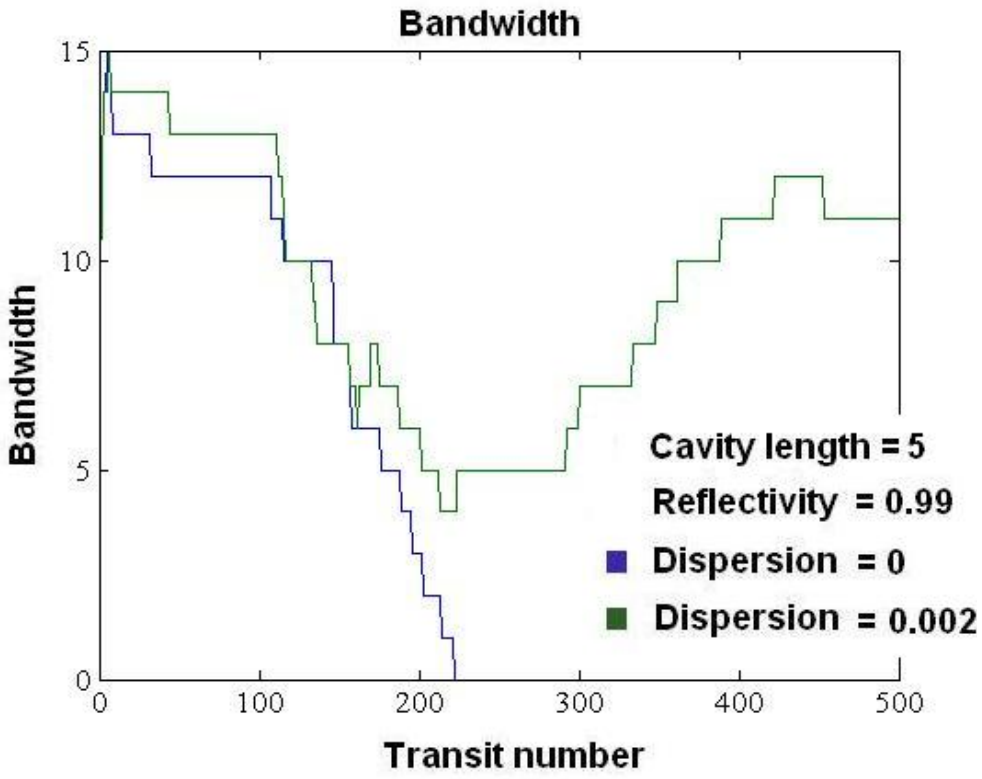


**Figure 5f – At longer normalised cavity lengths finite levels of dispersion can support the growth of a higher level of bandwidth than the zero dispersion case.**

If longer normalised cavity lengths and finite levels of dispersion are employed, larger levels of bandwidth such as those shown in figure 5f can be achieved. In this case the medium excitation amplitude drives the growth of new sidebands and remains undepleted, the medium excitation amplitude will be discussed in detail in section 5.3. The above result indicates that certain parameter regimes, which include long cavity lengths and non-zero levels of dispersion, can support the generation of multiple sidebands. Sidebands generated in these regimes can reach intensities which are far greater than the initial pump intensity.

## 5.3 Medium excitation in the ring cavity

We have already discussed the growth of bandwidth within the ring cavity in terms of the medium excitation amplitude. For short normalised cavity lengths, the medium excitation amplitude evolves in a similar way to that of the non cavity system, where the excitation amplitude is eventually depleted by the growth of new sidebands. In this case the sidebands possess phases which drive the depletion of the medium excitation amplitude.

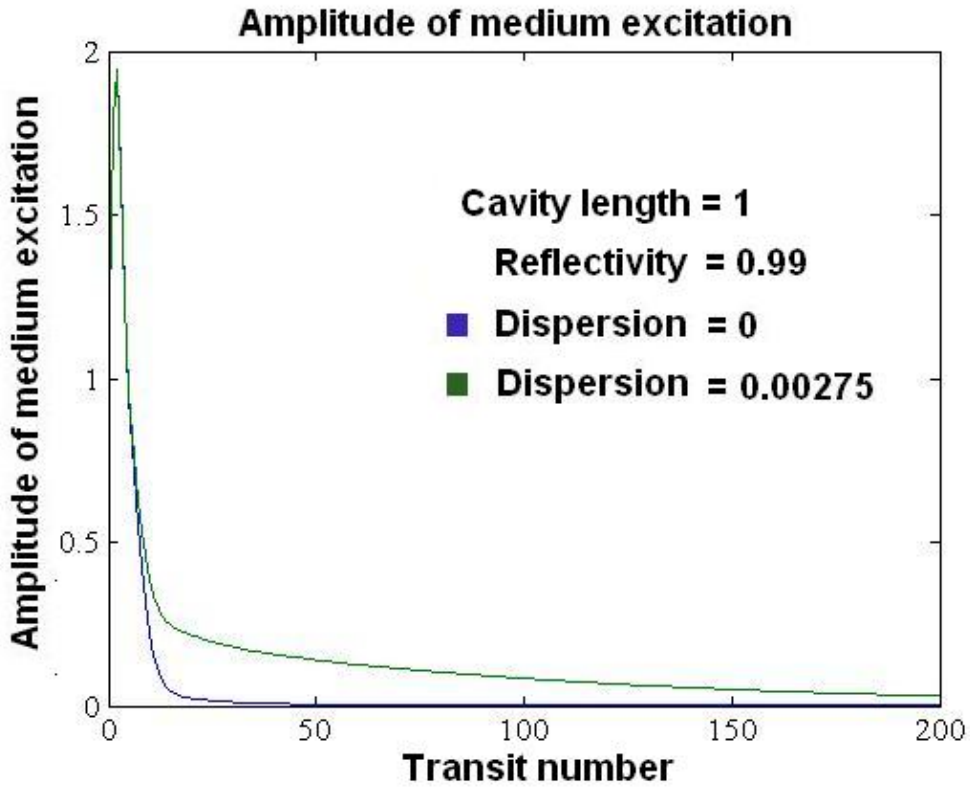


**Figure 5g – The medium excitation amplitude drops with increasing cavity transits. Finite dispersion offsets the depletion of the excitation amplitude.**

Figure 5g shows that for both zero dispersion and a small level of dispersion the medium excitation amplitude can be driven to zero. In the case of finite dispersion the depletion of the medium excitation occurs at a much slower rate because of the dispersion related phases of the sidebands.

If longer cavity lengths are employed the amplitude of the medium excitation can grow to large levels, such as those shown in figure 5h. Large levels of medium excitation occur because of non-cancelling contributions to the medium excitation amplitude, and the large pump amplitudes achieved by cavity pumping. The medium excitation amplitude drives the growth of sideband and is linked to the increased levels of bandwidth shown in figure 5f.

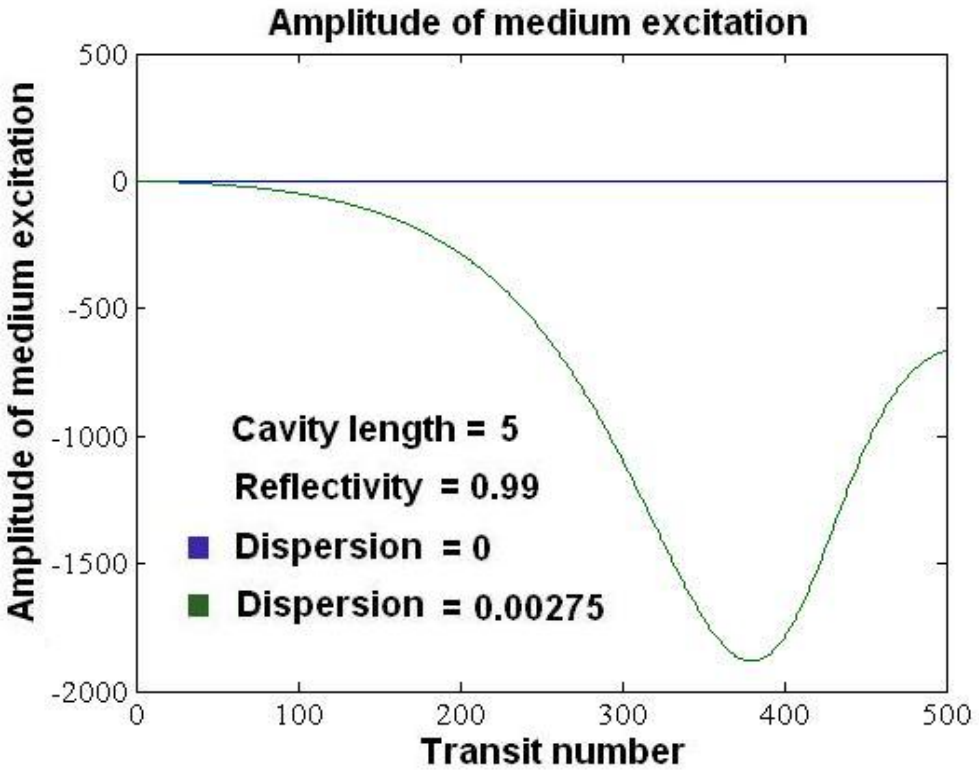


**Figure 5h – A finite level of dispersion and a longer cavity length causes the medium excitation to increase with an increasing number of cavity transits.**

## 5.4 Sideband phase

Throughout the previous sections the sideband phases have been discussed with respect to the growth of frequency bandwidth and the level of the medium excitation amplitude. Therefore the phase evolution of both the first Stokes and anti-Stokes sidebands, under the influence of finite levels of normalised dispersion, will now be discussed.

The phase angles of Stokes and anti-Stokes sidebands can be affected by finite levels of medium dispersion, and as previously discussed the sideband phases can control the level of the medium excitation amplitude. Figures 5i and 5j give examples of how the phase angle of the first Stokes and anti-Stokes sidebands can change in the presence of a finite level of dispersion.

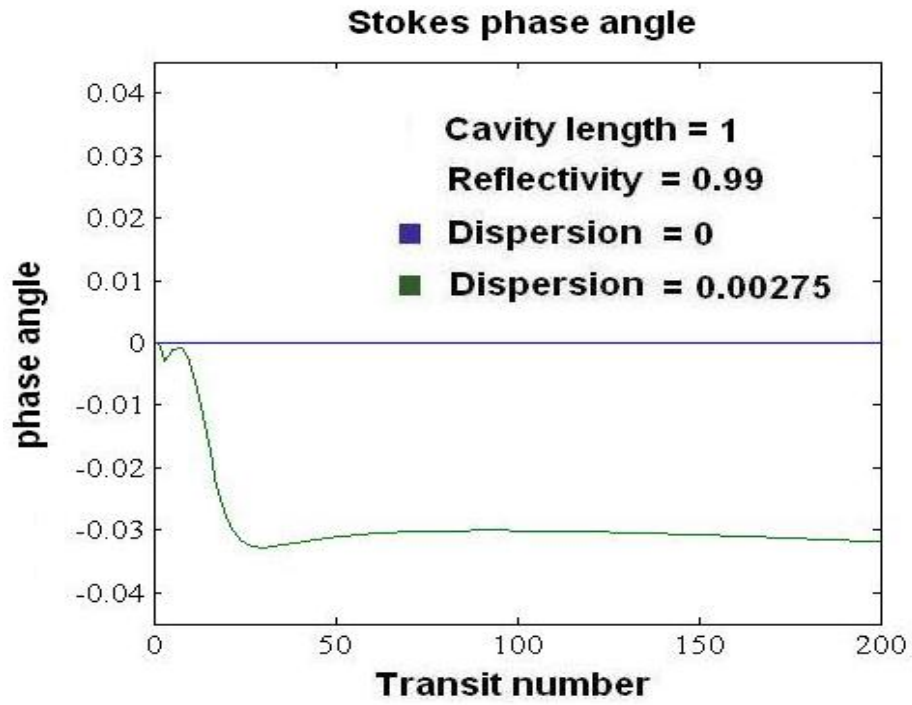


**Figure 5i – A finite level of dispersion changes the phase angle of the Stokes sideband and therefore its contribution to the medium excitation amplitude. At short normalised cavity lengths there is only a small difference in the phase angles given by both zero and finite dispersion.**

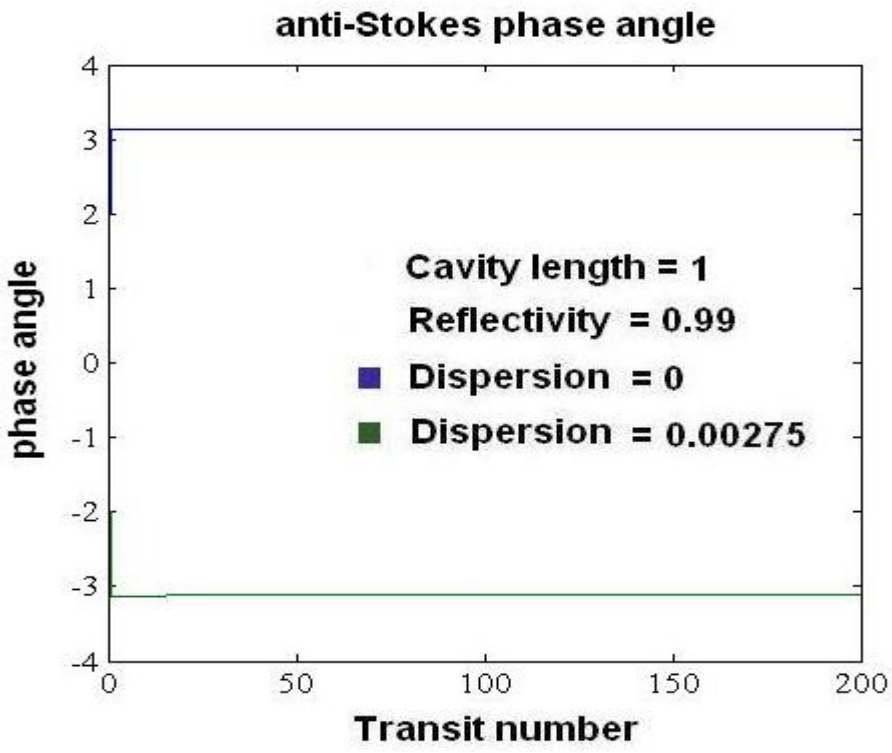


**Figure 5j – In the case of zero dispersion the anti-Stokes phase angle is $\pi$. The level of dispersion given in this figure causes the anti-Stokes sideband to grow with a phase angle of approximately $-\pi$.**

From both figures 5i and 5j it is clear that finite levels of medium dispersion introduce phase changes to the sidebands, and for the particular parameter regime employed in figures 5i and 5j both the Stokes and anti-Stokes sidebands possess negative phase. When sidebands share the same phase it implies that their contributions increase the medium excitation. This contributes to the growth of the large excitation amplitude shown in figure 5h and the increased levels of bandwidth shown in figure 5f.

The results presented in this chapter have so far indicated that the cavity (with only a single pump) is unable to maintain a high level of bandwidth, unless the chosen parameter regime allows the phase of each sideband to evolve in such a way as to sustain the medium excitation amplitude over a large number of cavity transits. It will be shown in section 5.6 that the spectra generated in these parameter regimes are unsuitable for the synthesis of ultra-short pulses.

## 5.5 The gain suppression analysis and multi-frequency simulations

The results of multi-wave simulations of the single pump cavity, employing a short normalised cavity length, can be further explained using the results of gain suppression analysis derived in chapter 3.

The main results of the gain suppression analysis indicated that for most choices of initial parameters, which include short cavity lengths or small levels of dispersion, the parametric gain is eventually decreased by a geometrically increasing pump intensity. The results also showed that in the limit, $m \to \infty$ (after many cavity transits), and when the coupling mirror reflectivity is less than unity, such that $R_j = R_0 < 1$, each sideband reaches a peak level and then depletes as a function of $R_0^{2m}$ towards zero intensity. Examples of the evolution of the Stokes intensity given by the 3-wave gain suppression analysis were given in figure 3j and examples which cover wider parameter ranges can be found in appendix C.

When considering multi-wave simulations of the single pump cavity the results show a clear resemblance to the results of the 3-wave gain suppression analysis. There is a link between increasing the level of dispersion and the Stokes sideband reaching higher peak intensity. This can be attributed to an increased level of parametric gain over the first few cavity transits. Figure 5k gives an example of the growth of the first Stokes sideband in relation to increasing levels of normalised dispersion.

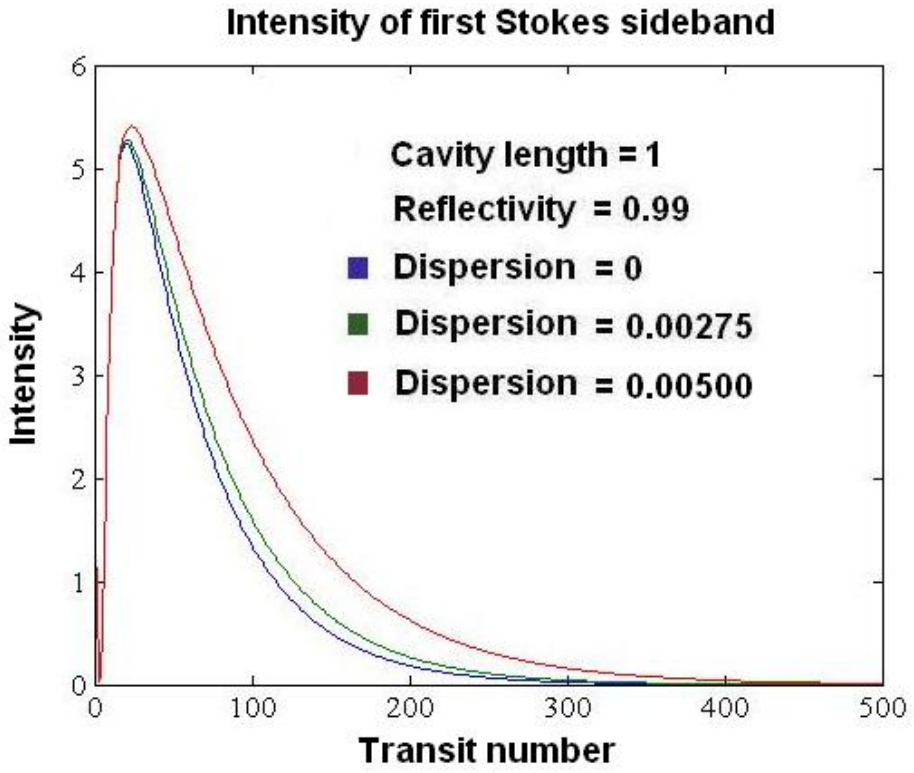


**Figure 5k – multi-wave simulations show that increasing the level of dispersion increases the growth of the first Stokes sideband intensity. For any level of dispersion the intensity reaches a peak value and then decreases as a function of cavity mirror reflectivity toward zero intensity.**

The Stokes intensity profiles given figure 5k indicate that the gain suppression analysis can describe the growth characteristics of amplitudes in the multi-wave results, providing that the parameter choice falls within the small dispersion, short cavity regime.

## 5.6 The Fourier synthesis of pulses

The results given for non-cavity UMRG indicated that for certain parameter regimes bandwidths can be generated which are suitable for the synthesis of trains of low intensity few femtosecond pulses. Figure 5l gives an example of a typical pulse given by the inverse Fourier transform of the Raman spectra generated by a non-cavity system at an optimal (but relatively long) normalised propagation distance of $Z = 100$. It is clear that the frequency spectrum used to synthesise this pulse suffers from poor phase matching between sidebands, hence the pulse has a high average power.

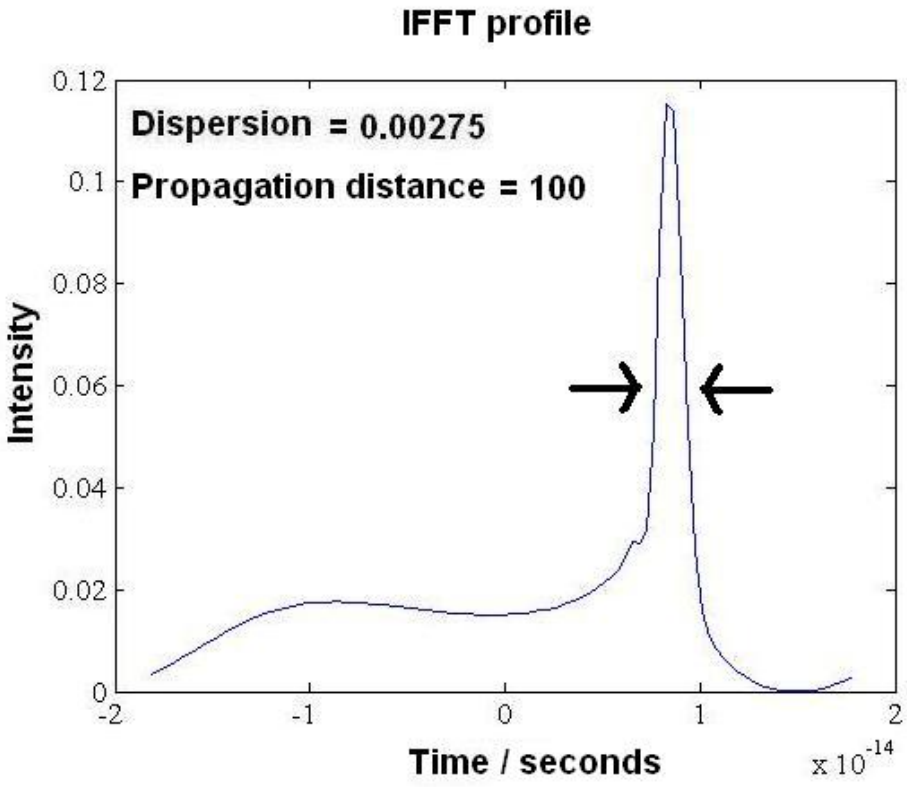


**Figure 5l – IFFT pulse profile. The arrows indicate a half peak pulse width of 1.75 femtoseconds. The pulse energy is spread over the entire width of the time domain indicating poor phase matching between the sidebands. The pulse intensity is given in arbitrary units.**

In the case of the cavity system the results of figure 5f have shown that for the right choice of parameters, such as finite levels of dispersion and relatively long cavity lengths, the cavity system can generate bandwidths containing multiple sidebands. However, the level of bandwidth is achieved at the expense of phase matching between sidebands. Figure 5m gives an example of a pulse generated by a single pump cavity with a moderate normalised cavity length and finite dispersion.

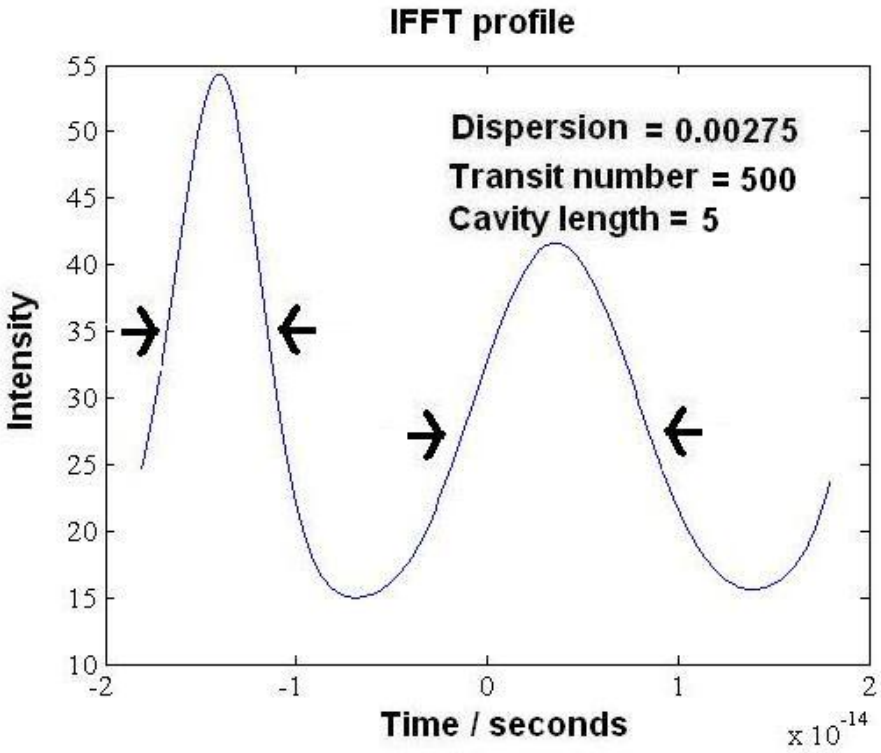


**Figure 5m – IFFT pulse profile. The single pump cavity produces two pulses over one cycle. The pulses have time spans of approximately 7.5 femtoseconds and 10 femtoseconds, with a separation of approximately 20 femtoseconds between peaks. Both peaks have normalised intensities which are several times greater than that of the initial pump intensity at $\omega_0$.**

It is clear from the results given in figure 5m that poor phase matching between the components of the frequency spectrum leads to the synthesis of pulses of long durations with a high average intensity.

These results presented in this chapter all point to the fact that the single pump cavity is unsuitable for the efficient generation of femtosecond pulses, when only a single pump beam is employed. To increase the efficiency of sideband generation, and improve phase matching between sidebands, it is necessary to consider symmetric pumping at the pump and first Stokes frequencies.

# CHAPTER 6

## Sideband generation in the ring cavity with two applied pump beams

Symmetric pumping of the cavity system will now be explored. Pump beams will be employed at the pump, $\omega_0$, and first Stokes frequency, $\omega_{-1}$, which are introduced at the start of each cavity transit. The end cavity mirror is taken to be partially transmitting with a uniform reflectivity over the entire frequency range covered by the simulations. Throughout this chapter simulations of the cavity system will be quantified in terms of bandwidth and the total intensity of the multi-frequency spectrum, and parameters which can optimise bandwidth generation will be discussed, such as dispersion, linear detuning and the ratio of applied pump amplitudes.

The results presented in this chapter will cover only a single value of cavity mirror reflectivity (amplitude), $R_j = 0.99$. Simulations including finite reflection bandwidth cavity mirrors (of varying configuration) will be discussed in chapter 7.

Before considering any particular parameter regimes it is worth describing how cavity pumping and losses can affect the overall growth of bandwidth. The loss mechanism arises as a consequence of the partially transmitting input / output coupling mirror, and there is also a characteristic drop in intra-cavity intensity associated with frequency conversion within the Raman medium. It is clear that defining a non unity value of cavity mirror reflectivity sets a limit on the maximum achievable intra-cavity intensity.

The efficiency of cavity pumping depends on the phases of the pump and first Stokes amplitudes at the end of each cavity transit, because interference between the applied pump beams and the intra-cavity amplitudes (at the same frequencies) can be destructive and decrease the efficiency of cavity pumping.

## 6.1 Zero dispersion

The results presented in chapter 5 indicated that the total amount of frequency bandwidth can be restricted by the choice of cavity length and level of dispersion. The generation of multiple sidebands could only be achieved through the use of finite levels of dispersion and long cavity lengths, and such parameter regimes give rise to strong levels of non-parametric growth and poor phase matching between sidebands, meaning that the resulting frequency spectrum was unsuitable for the generation of high power few-femtosecond pulses.

The introduction of pumping of the first Stokes sideband can be shown to increase the levels of bandwidth generated in the cavity by a significant amount. Figure 6a shows bandwidth growth within the cavity for a range of cavity lengths, with zero medium dispersion and zero linear detuning.

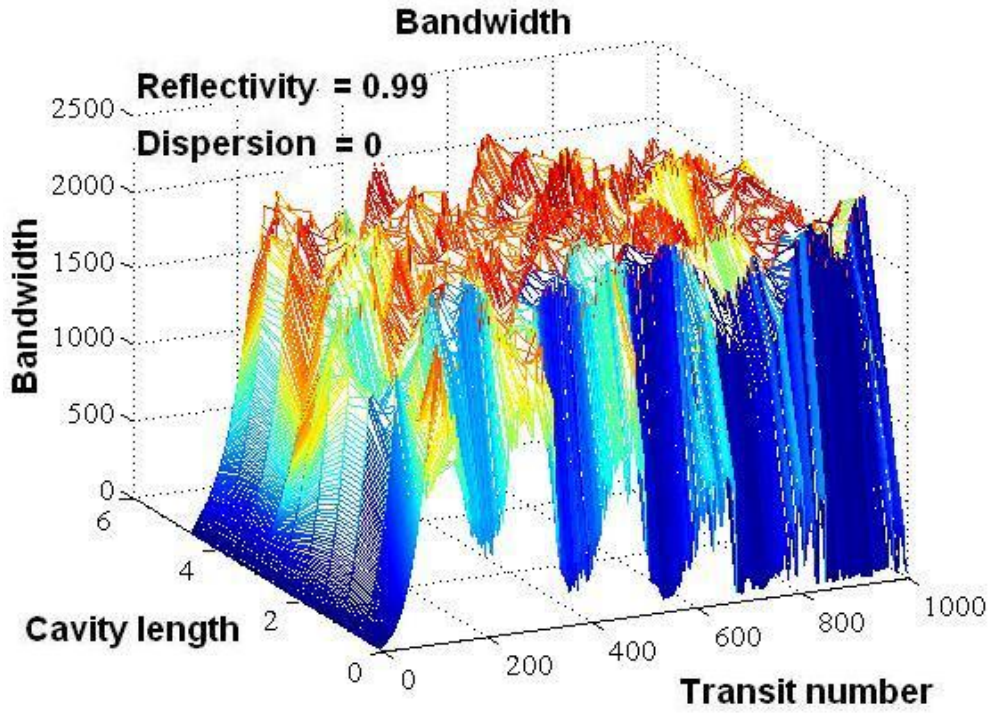


**Figure 6a – When there is no dispersion the symmetrically pumped cavity is capable of generating very large bandwidths. The choice of cavity mirror reflectivity limits the maximum achievable bandwidth.**

When there is no dispersion, and the coupling mirror reflectivity is close to unity, very large bandwidths can be generated. The large levels of bandwidth shown in figure 6a occur because sidebands are generated parametrically during each cavity transit, and the maximum value of bandwidth is only restricted by the chosen value of coupling mirror reflectivity. If $R_j = 1$ then the level of bandwidth is only limited by the frequency range of the simulation and can grow indefinitely.

Figure 6b gives an example of the bandwidth generated when the normalised cavity length is relatively short ($Z_c = 0.1$). The bandwidth initially reaches a high level, over a number of the cavity transits, but then eventually decreases to a much smaller level, which is approximately equal to the level of bandwidth obtained in the non-cavity case. The final bandwidth after a very large number of cavity transits contains mainly Stokes sidebands, which contain most of the intensity of the spectrum. The intensity data given in figure 6c corresponds to the bandwidth data given in figure 6b, and demonstrates that after a large number of cavity transits the intensity contained within the Stokes wing of the spectrum contains over double the intensity of the anti-Stokes wing.

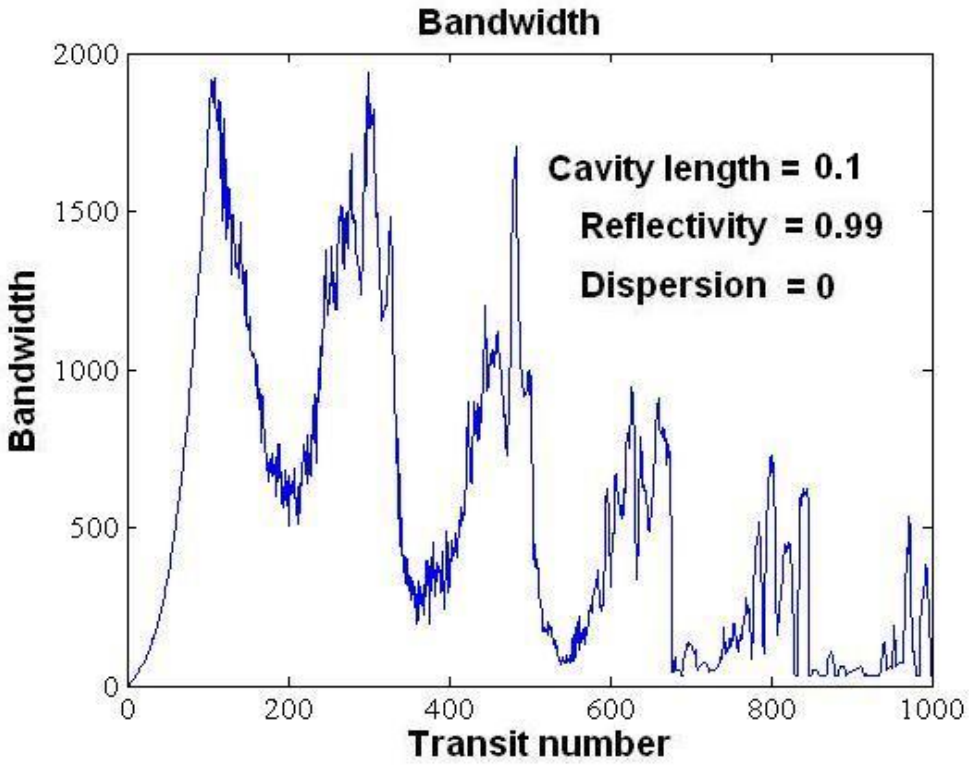


**Figure 6b – At short cavity lengths the symmetrically pumped cavity will not maintain a high level of bandwidth. Most of the pump energy is transferred to the Stokes wing of the spectrum and the anti-Stokes sidebands are depleted leading to a drop bandwidth.**

The results of figures 6b and 6c share similarities with the results of chapter 5, and demonstrate that the addition of a second pump beam allows the cavity to generate a reasonable number of sidebands (approximately equal to the non-cavity case) which possess a large intensity. There is an underlying process which causes the majority of the pump energy to be transferred into the Stokes wing of the spectrum, which restricts the overall bandwidth. This will be discussed in detail in section 6.5.

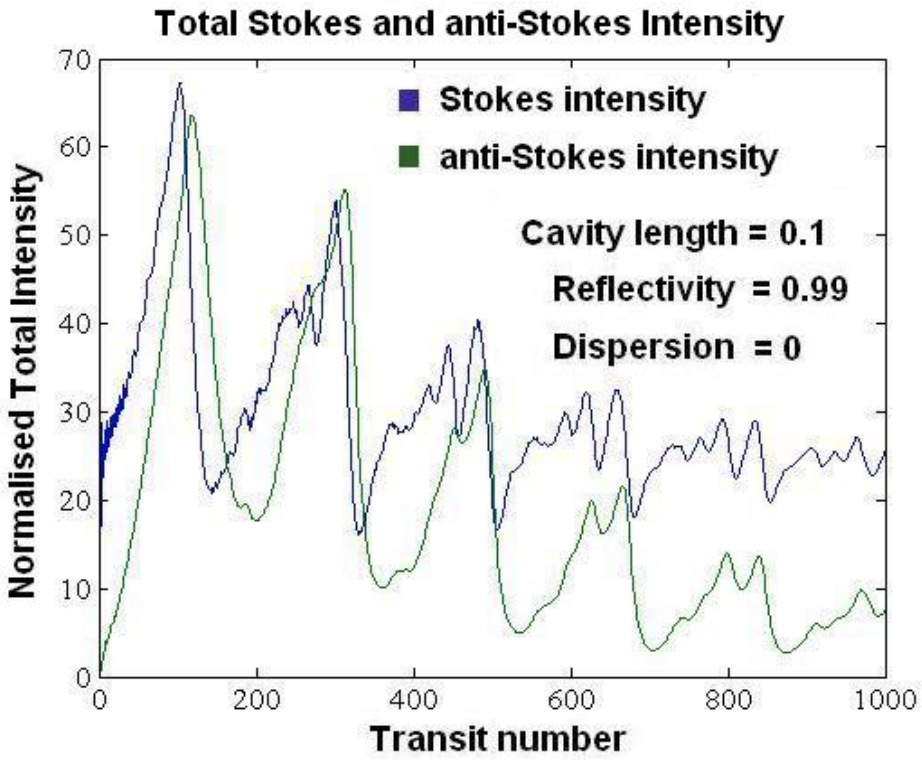


**Figure 6c – At short cavity length the intensity of the spectrum is initially evenly distributed between the Stokes and anti-Stokes wings of the spectrum. After many cavity transits the Stokes wing of the spectrum contains the largest level of intensity.**

When moderate to large normalised cavity lengths are considered, a high level of bandwidth can be maintained through symmetric pumping (see figure 6a). Figure 6d gives a specific example of the large levels of bandwidth which can be achieved at longer cavity lengths. Figure 6e represents the intensity data corresponding to figure 6d and shows an even distribution between each wing of the frequency spectrum.

The intensity contained within the Stokes and anti-Stokes wings of the spectrum are much greater when longer cavity lengths are employed. Generally longer cavity lengths (in the case of zero dispersion) allow a more even distribution of the applied pump energy. Therefore greater levels of intensity can be achieved in higher order sidebands, rather than the majority of the intensity remaining at lower order sidebands (close to the pump frequency). The overall bandwidth, in the case of figure 6d, is only limited by intensity losses at the cavity mirror.

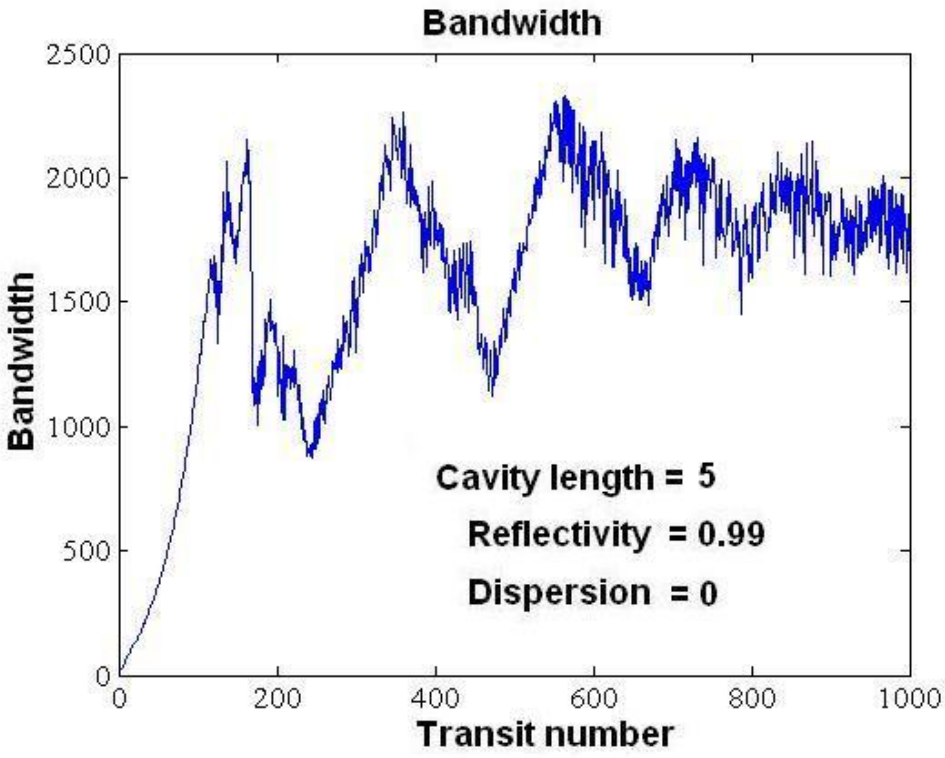


**Figure 6d – At long cavity lengths a large amount of bandwidth can be generated and maintained. The bandwidth is only limited by the overall loss of intensity in the system due to sideband growth and cavity mirror losses.**

The results, in the case of zero dispersion, indicate that large numbers of sidebands can be generated through symmetric pumping techniques, and with the right selection of cavity length an even distribution of energy between each wing of the spectrum can be achieved (see figures 6d and 6e). The large numbers of sidebands and high intensities offer the possibility of generating high intensity sub-femtosecond pulses. Examples of pulses generated in the cavity will be discussed in chapter 7.

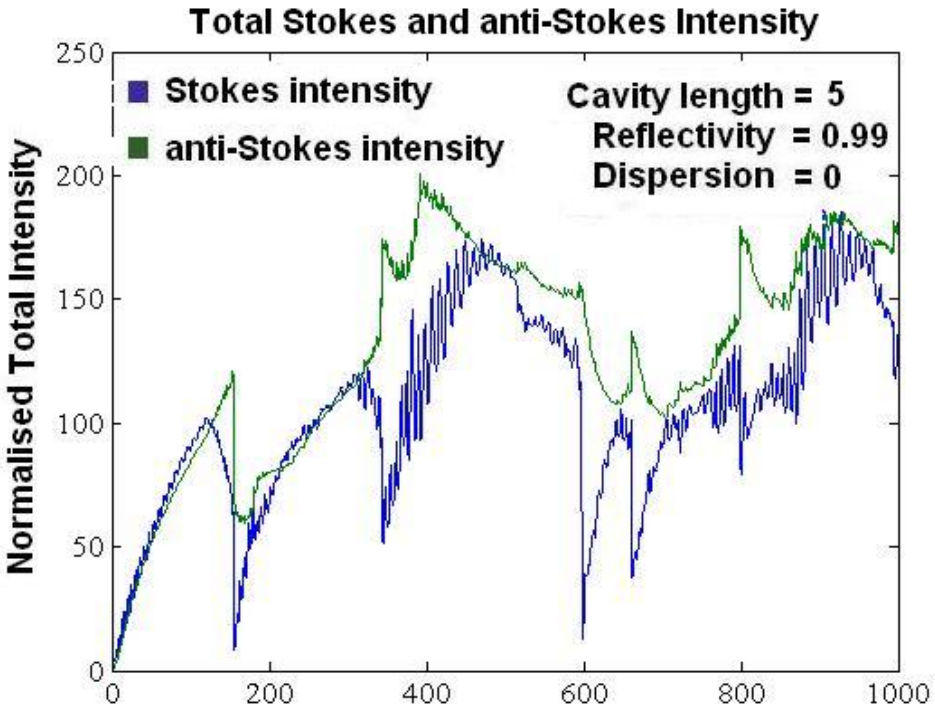


**Figure 6e – At longer cavity lengths the intensity in the cavity is more evenly distributed between Stokes and anti-Stokes sidebands. The intensity reaches its peak value after $\sim 400$ cavity transits.**

## 6.2 Finite levels of medium dispersion

Finite levels of dispersion must now be considered, and its effect on bandwidth growth discussed. The introduction of a finite level of dispersion requires that the effects of non-parametric growth need to be considered. The growth of high order (high frequency) sidebands can be particularly sensitive to finite levels of dispersion because of the frequency dependence of the refractive index of the medium, where higher frequency sidebands are subject to large levels of dispersion.

As with the zero dispersion case, short cavity lengths will first be considered. When the cavity length is relatively short, the bandwidth grows in a way similar to the zero dispersion case, where the bandwidth grows to a large peak value and then eventually drops to a low level after a number of cavity transits. The main difference between the zero and finite dispersion results, given in figures 6b and 6f

respectively, is that the peak level of bandwidth is much higher in the zero dispersion results.

When longer cavity lengths are considered (in the finite dispersion regime), large levels of bandwidth can be achieved which persist over a large number of cavity transits. Bandwidths containing up to $500$ frequency components, such as the bandwidth shown in figure 6g, can be achieved. However, the peak level of bandwidth is much smaller than the zero dispersion equivalents (recall figure 6d).

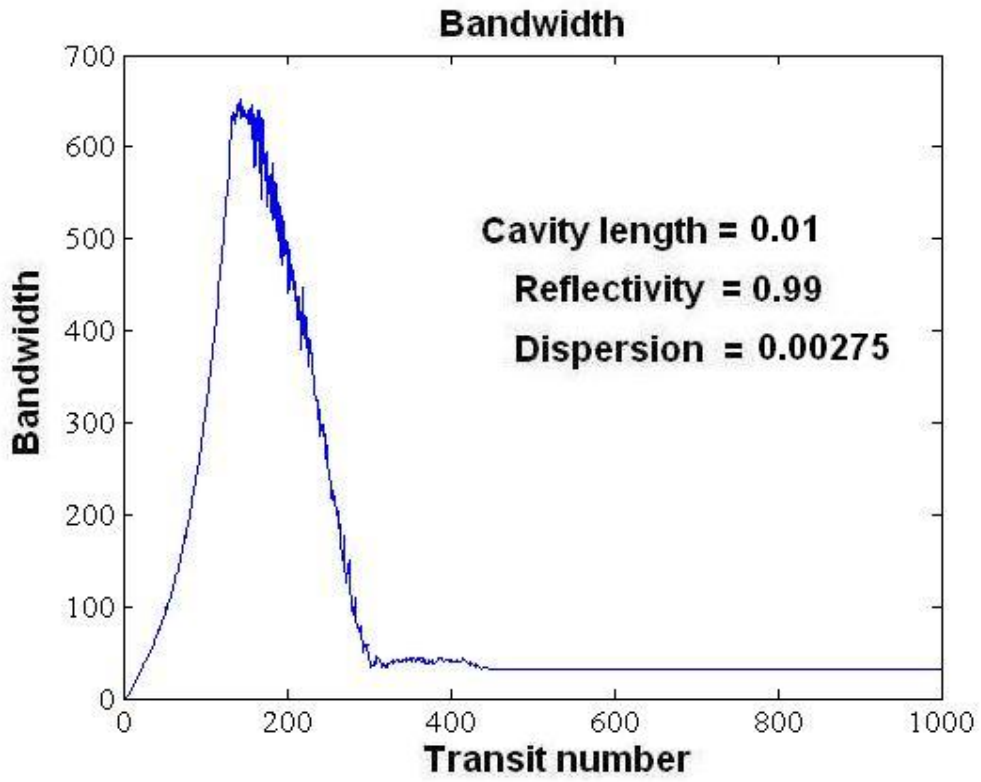


**Figure 6f – At very small normalised cavity lengths and finite dispersion the bandwidth growth is similar to that of the zero dispersion case where large bandwidth is initially generated which drops off with increasing numbers of cavity transits.**

The limitation of the peak bandwidths, shown in figures 6g and 6h, can be explained by considering the non-cavity results given in chapter 5 for the large dispersion regime. The results demonstrated how the Raman envelope equations have a strong dependence on the product of cavity length and dispersion, and in the limit of large dispersion the UMRG equations can be reduced to a form consisting solely of non-parametric terms, and describe the formation of a Stokes cascade.

Hence in the limit of large dispersion and long propagation distances the UMRG equations (2.63) describing sideband growth become:

$$\frac{\partial A_j}{\partial Z} = \frac{\omega_j}{2\omega_0} A_j \left[ \left| A_{j+1} \right|^2 - \left| A_{j-1} \right|^2 \right] \quad . \tag{6.1}$$

Equation (6.1) has solutions of the form:

$$A_j = \exp\left( \frac{\omega_j}{2\omega_0} \left[ \left| A_{j+1} \right|^2 - \left| A_{j-1} \right|^2 \right] Z \right) . \tag{6.2}$$

Equation (6.2) indicates that sidebands grow exponentially in proportion to the intensity of a higher order sideband, and are attenuated in proportion to the intensity of a lower order sideband. Hence in the limit of large dispersion the energy of the spectrum flows towards the lowest possible sideband frequency. It is also clear from the form of equation (6.2) that non-parametric sideband growth can occur independently of the level of medium excitation.

If we consider the Cauchy type dispersion equation from appendix B we can recognise the fact that high order anti-Stokes sidebands experience larger levels of dispersion than the rest of the spectrum. The limits of bandwidth growth, such as those shown in figures 6f, 6g and 6h, can be described in terms of Stokes cascading.

When any combination of dispersion and cavity length is considered, a high order anti-Stokes sideband will exist which experiences a level of dispersion large enough to cause the sideband to grow non-parametrically. This sideband represents the point at which bandwidth stops growing, because any energy transferred to this sideband (in the early stages of a cavity transit) will cascade back into the lower frequency components of the spectrum. The interplay between parametric sideband growth and Stokes cascading from higher frequencies manifests itself as oscillations in the bandwidth growth shown in figures 6g and 6h. Figure 6h clearly identifies the point made above by demonstrating the relationship between longer normalised cavity lengths and decreased levels of bandwidth.

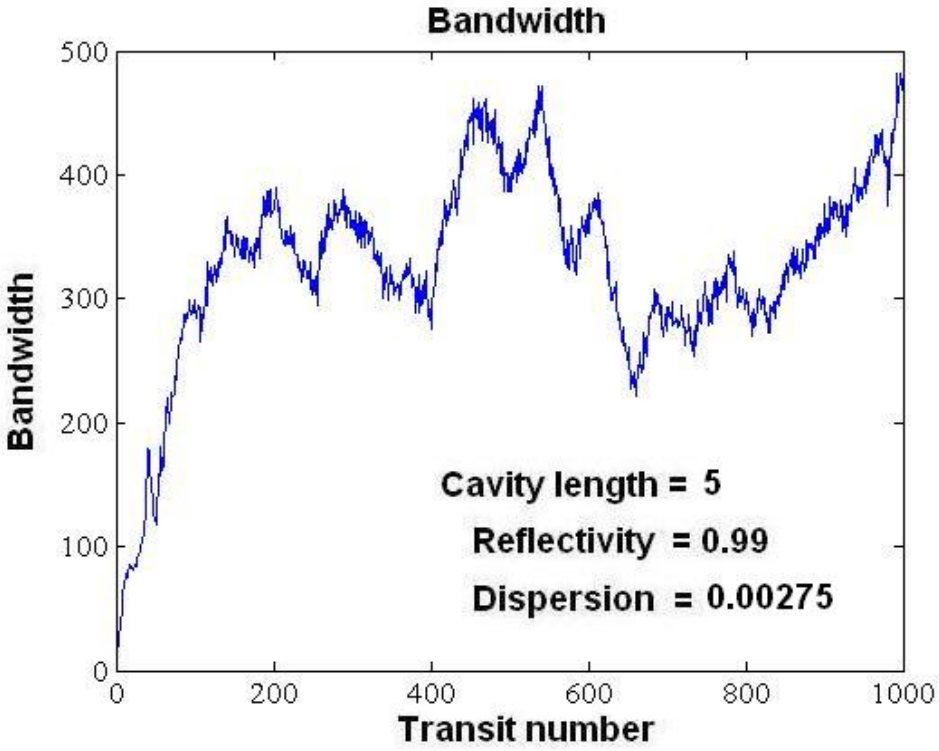


**Figure 6g – At long cavity lengths the maximum bandwidth is limited by the level of dispersion.**

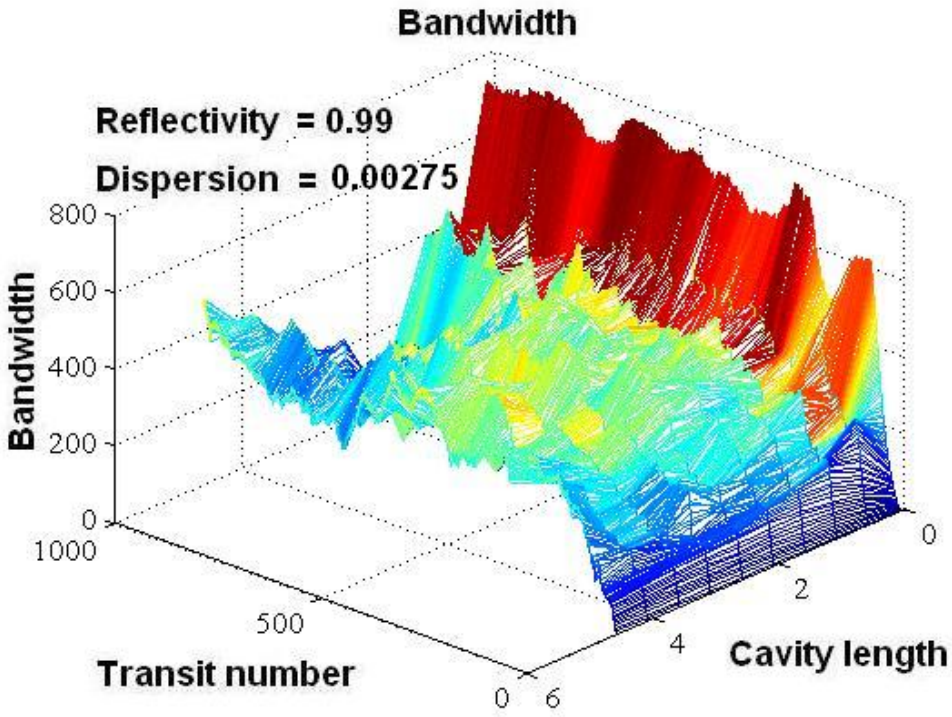


**Figure 6h – Shorter cavity lengths produce the largest bandwidths when there is a finite level of dispersion.**

It is also clear from 6h that an optimal cavity length exists ($Z_c = 0.1$) which maximises the level of bandwidth generated by the cavity.

## 6.3 Finite levels of linear detuning.

In chapter 4 the finite detuning gain suppression analysis provided results which showed finite levels of detuning can increase the peak intensities of the sidebands.

If the medium excitation amplitude from equation (2.63) is considered, it can be recognised that the medium excitation amplitude is scaled by a factor of $\frac{1}{(1+i\delta)}$. In this case any level of detuning decreases the level of the medium excitation amplitude. The results of simulations indicate that the bandwidth can be optimised through the selection of specific levels of linear detuning. The results also indicate that for most parameter regimes any selection of positive detuning can increase the overall level of bandwidth. Generally the level of detuning required to optimise the bandwidth depends on the chosen cavity length. Figure 6i provides results for a range of linear detunings for a normalised cavity length of $Z_c = 2$ and finite dispersion.

Figure 6i indicates that when finite levels of linear detuning are employed the bandwidth generated by the cavity can be significantly increased above the levels generated without linear detuning, and at the specific level of $\delta = 0.2$ the cavity produces its peak level of bandwidth. It is also clear that employing larger levels of detuning enables bandwidths to be generated which are only slightly less than the peak value. Figure 6j provides results for a range of linear detunings for a normalised cavity length of $Z_c = 0.01$ with a finite level of dispersion. The peak level of bandwidth of the cavity can be generated by a range of detunings, where $0.035 < \delta < 0.2$.

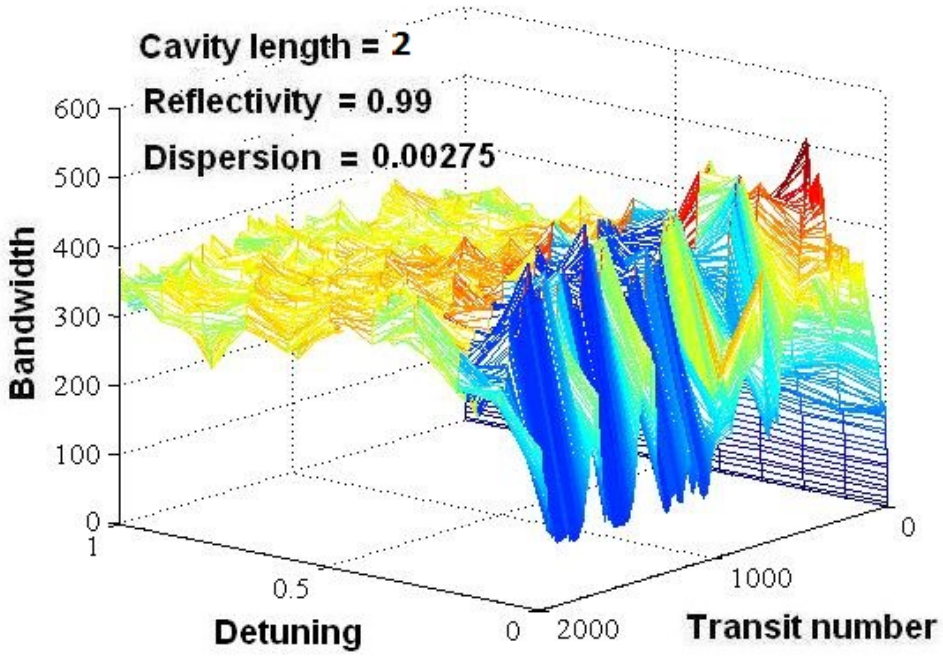


**Figure 6i – Finite levels of detuning increase the bandwidth generated by the cavity and there exists an optimal level of detuning for the chosen cavity length.**

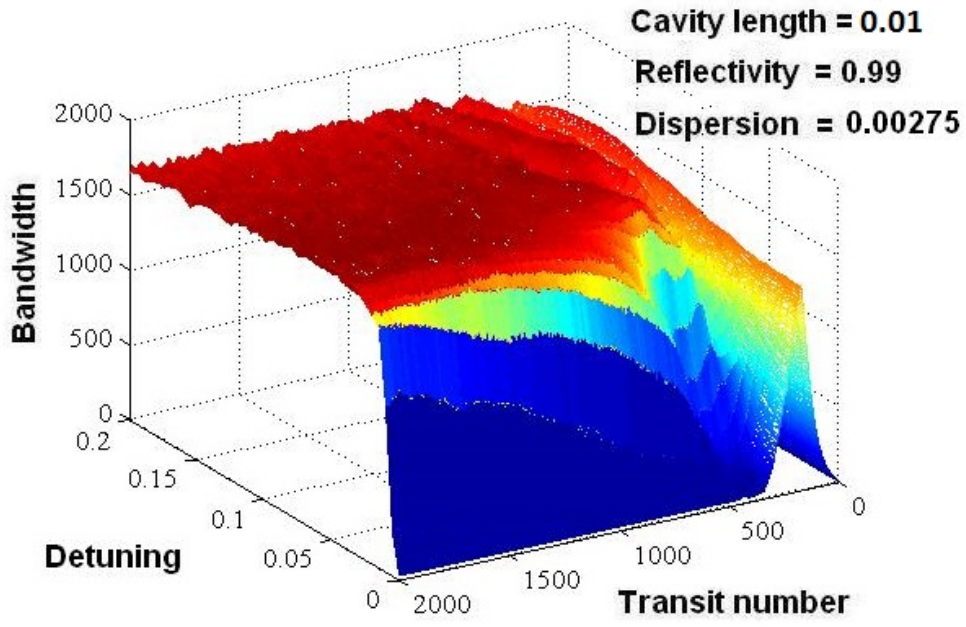


**Figure 6j – Finite levels of detuning allow large bandwidths to be generated when short normalised cavity lengths are used. Like figure 6i an optimum level of linear detuning exists.**

The results given in figure 6j are for the same range of detunings as figure 6i but for a much shorter normalised cavity length. These results also suggest that the cavity system can be optimised by a finite level of linear detuning. In the case of figure 6j the increase in bandwidth level, due to finite levels of detuning, can be much greater than the increase shown in figure 6i, and bandwidths can be achieved which are over fifty times larger than the bandwidths obtained for zero linear detuning.

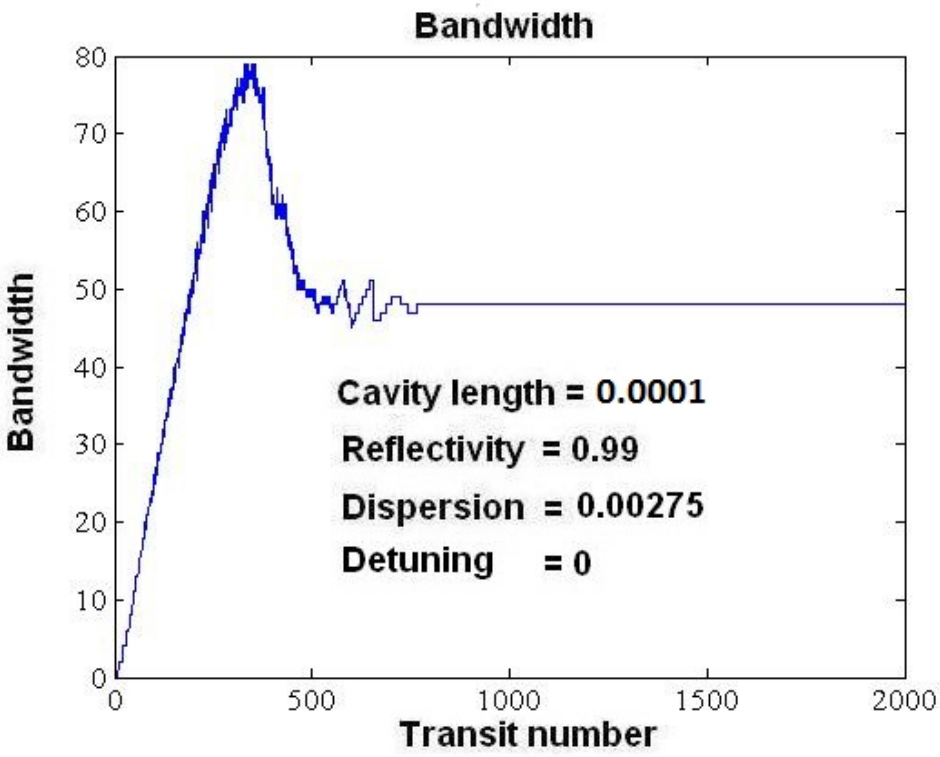


**Figure 6k – At very short cavity lengths and zero linear detuning we find that the cavity can generate bandwidths comparable to the non-cavity system.**

If the normalised cavity length is taken to be even shorter such as $Z_c = 0.0001$ and the linear detuning is zero the symmetrically pumped cavity can only generate a bandwidth that is comparable in size to the non-cavity results. However, when the normalised cavity length is very short, a small level of detuning can cause the generation of large levels of bandwidth. Very short cavity lengths are of particular interest because they can reduce the effects of finite levels of dispersion, and minimise levels of non-parametric sideband growth.

Figure 6l provides examples of bandwidth growth for several levels of detuning. These results show that the introduction of linear detuning can increase levels of bandwidth growth, even when the cavity length is extremely short.

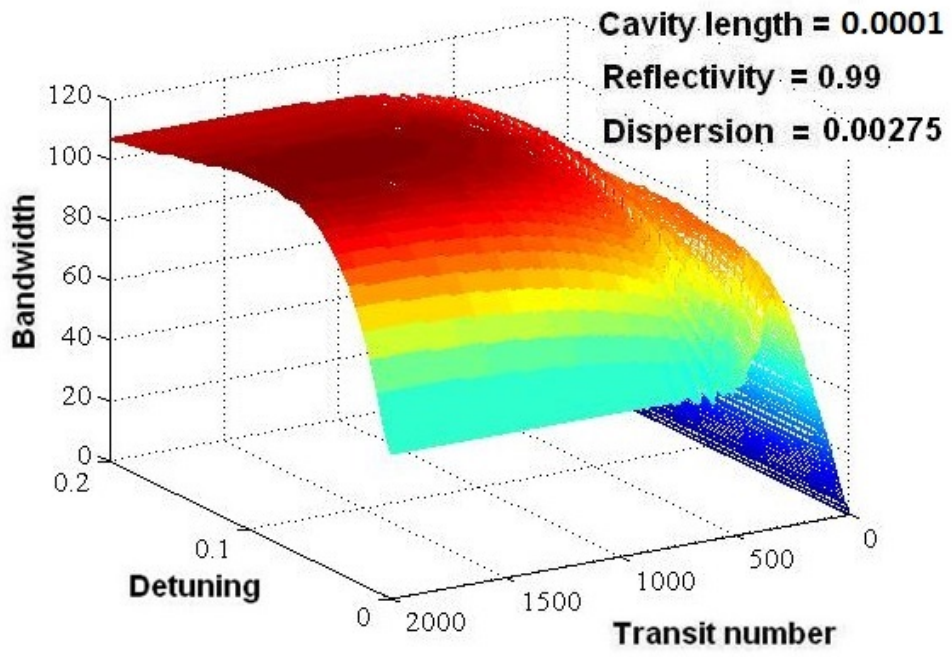


**Figure 6l – At very short cavity lengths we find that finite levels of detuning can optimise the level of bandwidth generated by the cavity system.**

Figure 6m gives the total intensity data of the multi-frequency spectrum corresponding to the bandwidth data given in figure 6l. There is a characteristic drop in the total intensity of the frequency spectrum which corresponds to the increased levels of sideband growth in the cavity.

The results from chapter 5, for the non-cavity system, showed that up to 30 sideband amplitudes could be generated over a normalised distance of $Z = 25$. The results given in figure 6l demonstrate that finite levels of detuning allow bandwidths of up to 100 frequency components can be generated in a cavity with a normalised length which is many orders of magnitude ($10^5$) shorter than the length of the example non-cavity system. The intensity of the multi-frequency spectrum can also be up to two orders of magnitude larger.

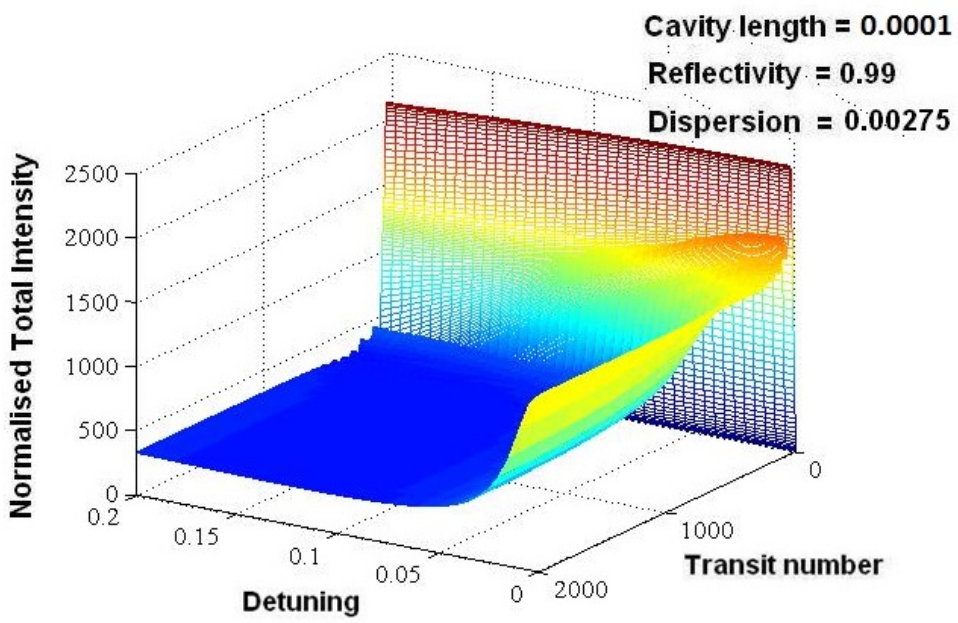


**Figure 6m – A drop in the total intensity contained within the frequency spectrum corresponds with the increased bandwidths generated by the cavity. After many cavity transits to total intensity reaches a fixed level, indicating that bandwidth growth has stopped and cavity pumping matches the intensity losses experienced by the spectrum.**

## 6.4 The pump ratio

So far the results have only covered symmetric pumping of the cavity system, therefore throughout this section the ratio of the pump amplitudes, $A_{-1}/A_0$, will be varied. In the case of the non-cavity system symmetric pumping is preferred because it provides the maximum medium excitation amplitude required for driving sideband growth. When the applied pump ratio is less than unity, peak levels of bandwidth are reduced significantly. Figure 6n demonstrates the change in bandwidth growth with respect to variations of the pump ratio, and shows unity pump ratios (symmetric pumping) to be optimal for the generation of bandwidth.

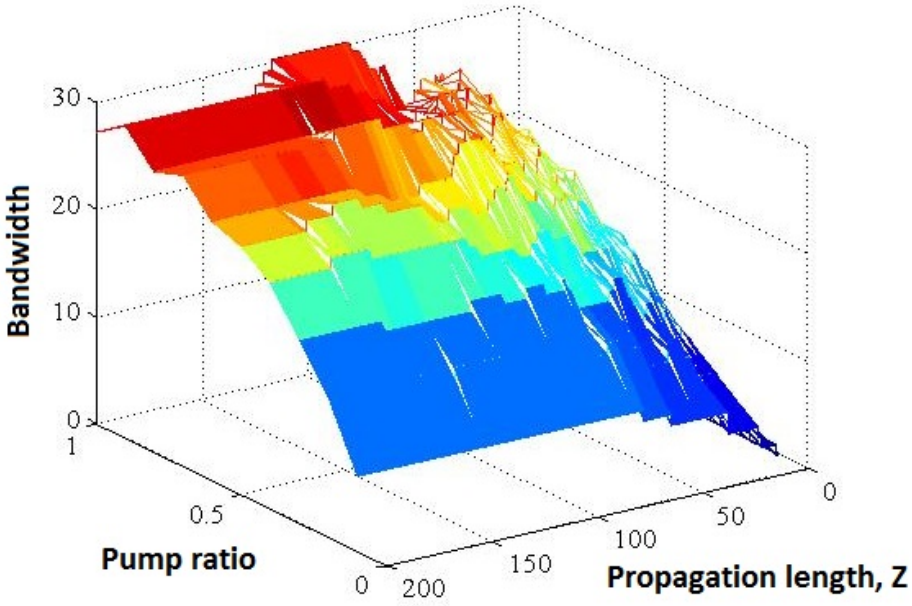


**Figure 6n – The non cavity system generates the largest levels of bandwidths when the level of pumping is symmetric.**

Symmetric pumping is not necessarily optimum for bandwidth generation in the cavity system. Simulations of the cavity demonstrate robustness with regard to changes in the pump ratio. Large levels of bandwidth can be produced for pump ratio's as small as 0.1, but the best results are achieved for pump ratios in the range 0.5 – 1. The results of figure 6o indicate that the cavity doesn't have to be pumped symmetrically to produce large bandwidths.

When small cavity lengths are considered, small pump ratios can be shown to be optimal for the generation of bandwidth. The use of a small pump ratio provides results which share similarities with the results for finite levels of detuning, in which the level of bandwidth can be optimised. Figure 6p give results obtained for a short cavity length of $Z_c = 0.0001$ for a range of pump ratios. At this cavity length the largest bandwidths are only generated when the pumping ratio is less than unity, and bandwidths of up to $\sim 90$ frequency components can be generated when an optimal pumping ratio of 0.5 is applied. Generally the results of figures 6o and 6p suggest that the pump ratio required to maximise bandwidth levels within the cavity depends on the length of the cavity.

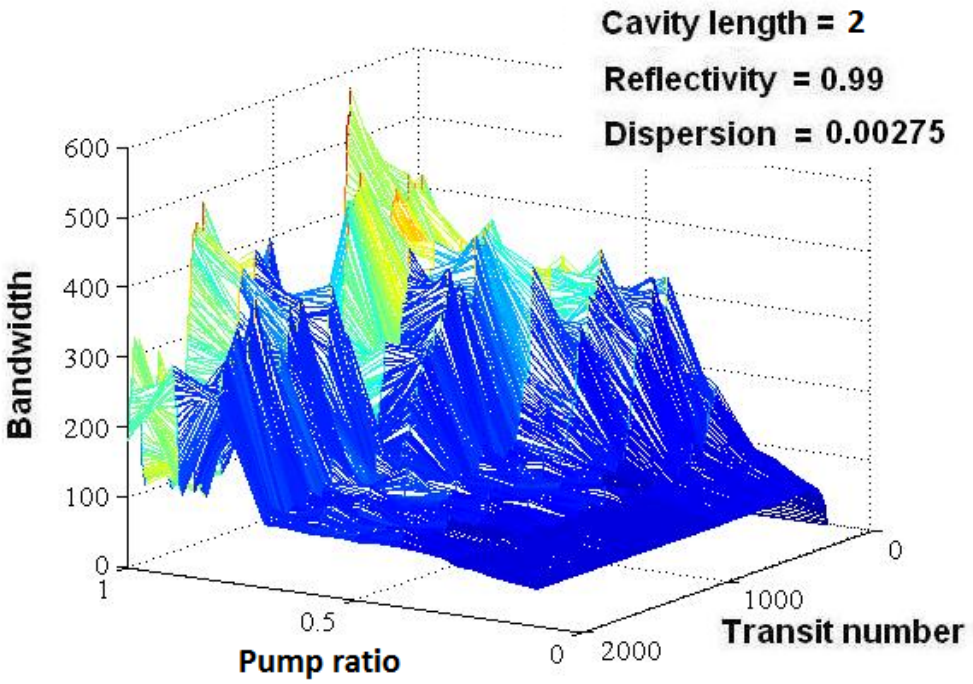


**Figure 6o – The cavity system can produce large bandwidths when non unity pump ratios are employed. This is unlike the non-cavity system where a unity pump ratio is preferred for bandwidth generation**

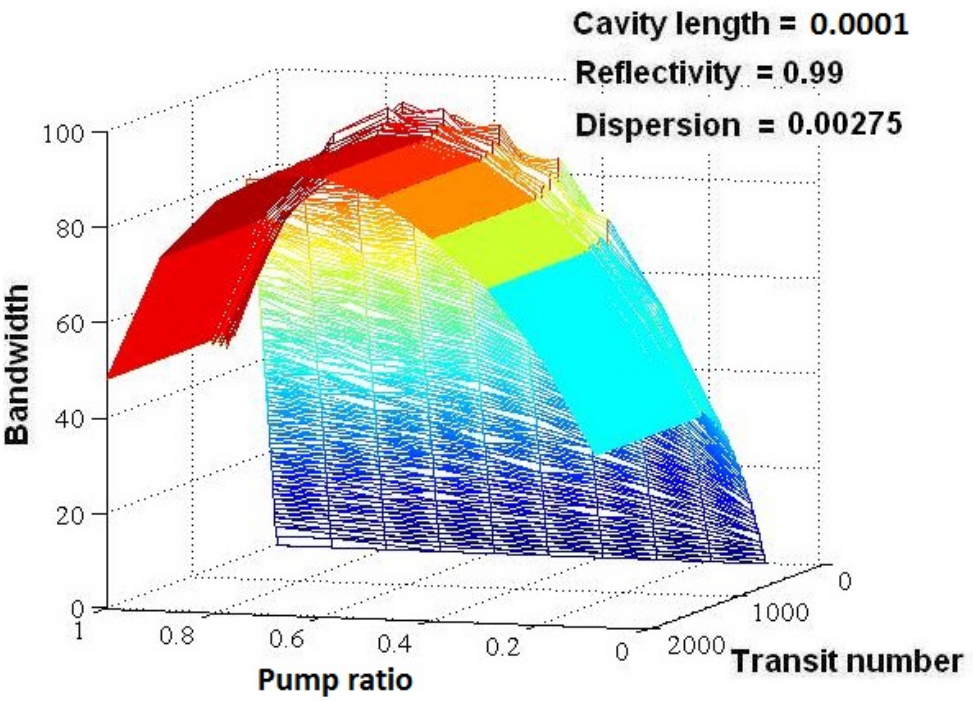


**Figure 6p - Large bandwidths can be generated in a very short cavity when a small pump ratio is employed. In this case a pump ratio of 0.5 allows the cavity to generate a bandwidth containing approximately 90 frequency components.**

## 6.4 Sideband intensities

The results presented in this chapter have thus far demonstrated that finite levels of detuning and non-unity pump ratios can increase the levels of bandwidth generated by the cavity system. The increased levels of bandwidth can be explained in a relatively simple manner by considering how the intensity levels at the pump and first Stokes amplitudes grow within the cavity.

The results of figure 6k, for a symmetrically pumped cavity of length $Z_c = 0.0001$, demonstrated that under certain parameter regimes, such as short cavity length and small levels of dispersion, the level of bandwidth growth can be restricted. If the growths of intensities at specific frequencies are taken into account, then the reasons for observing a reduced level of bandwidth can be attributed to the severe depletion of the pump amplitude.

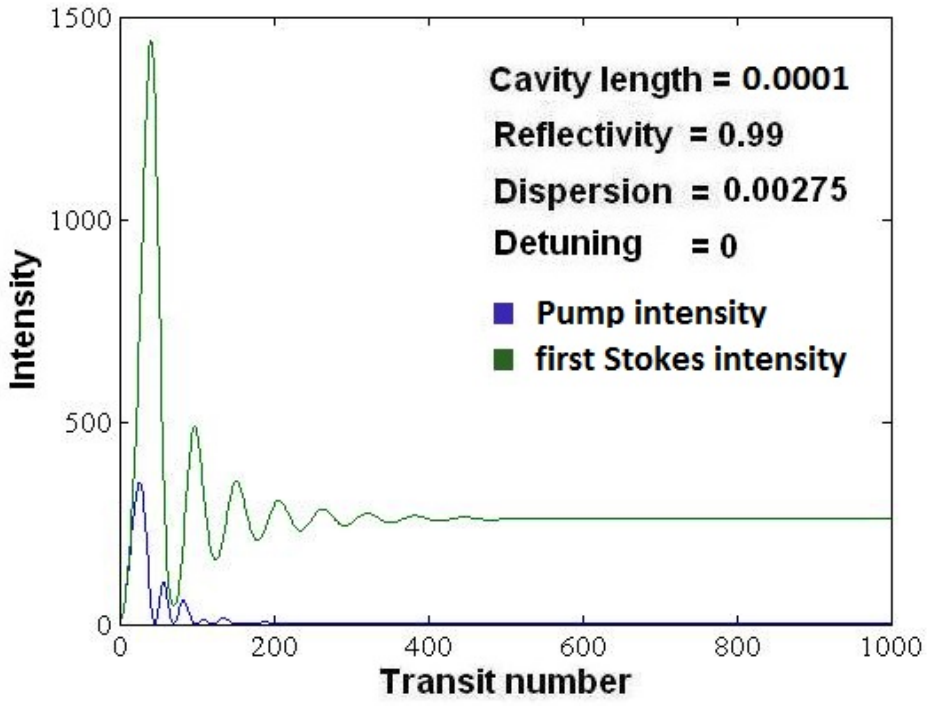


**Figure 6q - The pump is subject to large levels of depletion and the first Stokes intensity grows to a large level. After 200 cavity transits the pump intensity is approximately zero. This coincides with the restricted bandwidth shown in figure 6k.**

Figure 6q gives the intensity growth data for both the pump and first Stokes sideband and clearly shows that the Stokes sideband grows to a large intensity through the depletion of the pump, as well as pumping at the Stokes frequency.

Recalling the envelope equations (2.63) it can be recognised that each sideband grows in proportion to the amplitudes of the neighbouring sidebands.

$$\frac{\partial A_j}{\partial Z} = \frac{\omega_j}{2\omega_0}\left[P^* A_{j+1} e^{-i\gamma_{j+1}Z} - P A_{j-1} e^{i\gamma_j Z}\right].$$

If the first anti-Stokes sideband, $j = 1$, is chosen as an example and the pump considered to be severely depleted, such that $A_0 \approx 0$, then the envelope equation reduces to

$$\frac{\partial A_1}{\partial Z} = \frac{\omega_1}{2\omega_0}\left[P^* A_2 e^{-i\gamma_2 Z}\right].$$

Therefore, if the pump amplitude undergoes strong levels of depletion, and reduces to approximately zero we find that the first anti-Stokes sideband grows only in proportion to the second order anti-Stokes sideband. In this extreme limit no further energy is transferred into the anti-Stokes wing of the spectrum, therefore anti-Stokes sidebands do not contribute to the bandwidth.

If the equation for the medium excitation amplitude is also considered, it can be used to describe how finite levels of detuning and non-unity pump ratio's can produce the increased levels of bandwidth shown in figures 6l and 6p.

$$P = \frac{1}{(1+i\delta)} \sum_j A_j A_{j-1}^* \, e^{-i\gamma_j Z}.$$

The level of the medium excitation amplitude directly influences the rate at which new sidebands are generated, and in the case of the cavity system this amplitude can grow to be very large. The above formula indicates that a small pump ratio or finite level of linear detuning can reduce the level of the excitation amplitude, and therefore decrease the rate of sideband generation within the cavity.

Decreasing the rate of sideband generation also reduces pump depletion therefore allowing the pump intensity to grow to a level which is sufficient to support the generation of a large number of anti-Stokes sidebands (or bandwidth). Figure 6r gives an example of the intensity growth for both the pump and first Stokes sideband when a finite level of detuning is employed, and figure 6s gives intensity results for a non-unity pump ratio. Through comparison of figures 6q, 6r and 6s we can recognise that finite levels of detuning and non-unity pump ratios allow larger intensities to build up at the pump frequency, this allows the sustained growth of higher order anti-Stokes sidebands.

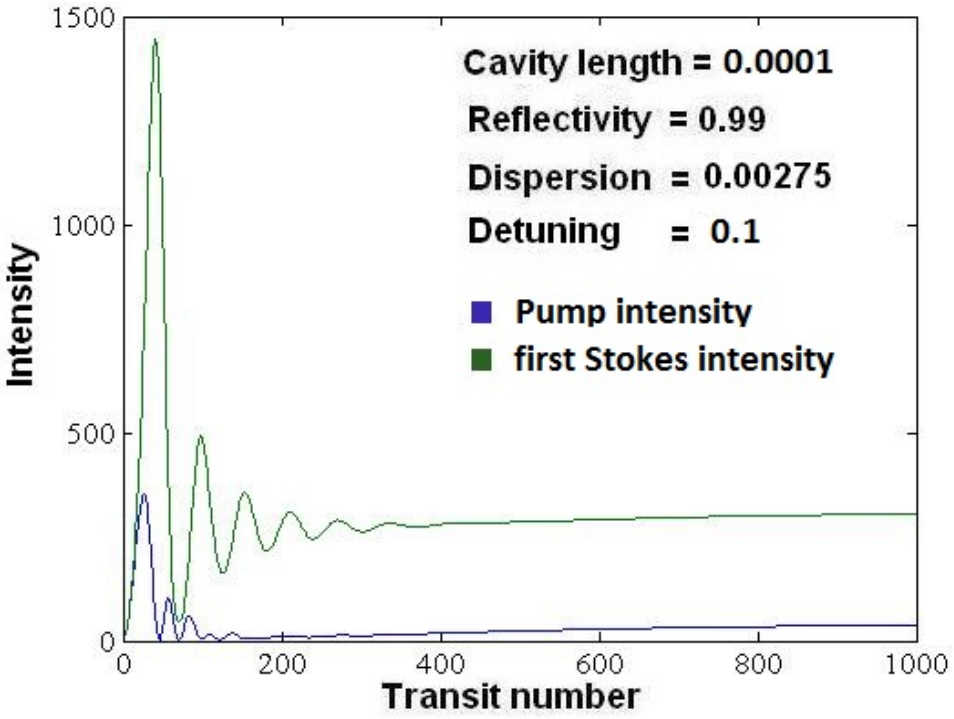


**Figure 6r - With the introduction of a finite level of detuning we find that the pump intensity stays at much larger level. This is required for driving anti-Stokes sideband growth.**

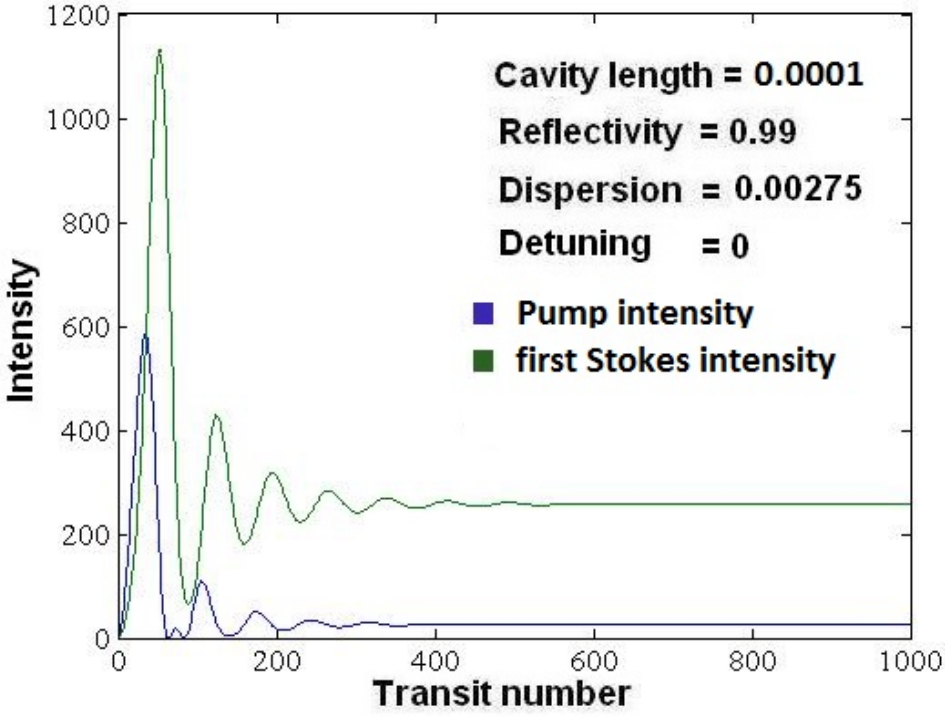


**Figure 6s - With the pump ratio set to 0.6 we find that the pump intensity stays at a relatively large level. This allows anti-Stokes sidebands to be maintained at an appreciable intensity.**

# CHAPTER 7

## Normalisation and pulse reconstruction

The results of previous chapters have been given in terms of normalised parameters. Normalisation has allowed results to be obtained without having to specify the level of pump intensity, $I_0$, or gain parameter, $g$, of the medium. This reduces the number of parameters which need to be considered when describing bandwidth growth within the cavity system. Normalisation has allowed large ranges of parameter regimes to be compared, and the processes limiting bandwidth growth to be quantified in terms of normalised parameters. The results of simulations are easily un-normalised when specific values of pump intensity and gain are specified.

Throughout this chapter examples of pulse profiles will be reconstructed from frequency data obtained by simulations of the cavity system, these results will also be un-normalised to obtain values for the peak power density, average power density and total energy density of the reconstructed pulses. An initial pump power density of $I_0 = 10^6\ Wcm^{-2}$ and a gain parameter of $g = 0.2\ cmGW^{-1}$ will be applied for each of the results (unless otherwise specified), and it will be assumed that the value of intensity occurs at the start of the first cavity transit, after transmission through the coupling mirror. The cavity length can be recovered in units of centimetres from the gain length product, $Z = gI_0z$ . By using the parameters specified above the intensity of each sideband, and therefore the synthesised pulses, can be recovered in units of $Wcm^{-2}$.

By first considering the non-cavity system, and employing the values for pump power and gain specified above, it can be recognised that specifying the gain length product also specifies the level of normalised dispersion, $\gamma_j = \frac{\Delta_j}{gI_0}$. The value of normalised dispersion employed in the following results is $\gamma_1 \approx 10$, unless otherwise specified. It can also be recognised, from the gain length product, that small levels of pump intensity imply that 'short' normalised distances can actually correspond to long un-normalised (physical) distances.

It has already been shown that large levels of normalised dispersion can limit bandwidth levels, see chapters 5 and 6. Large levels of normalised dispersion can also be shown to cause the generation of a spectrum with poor phase matching between sidebands. This corresponds to the synthesis of poor quality pulses in the time domain. The non-cavity system would require large pump intensities to generate a broad spectrum of phase-matched sidebands.

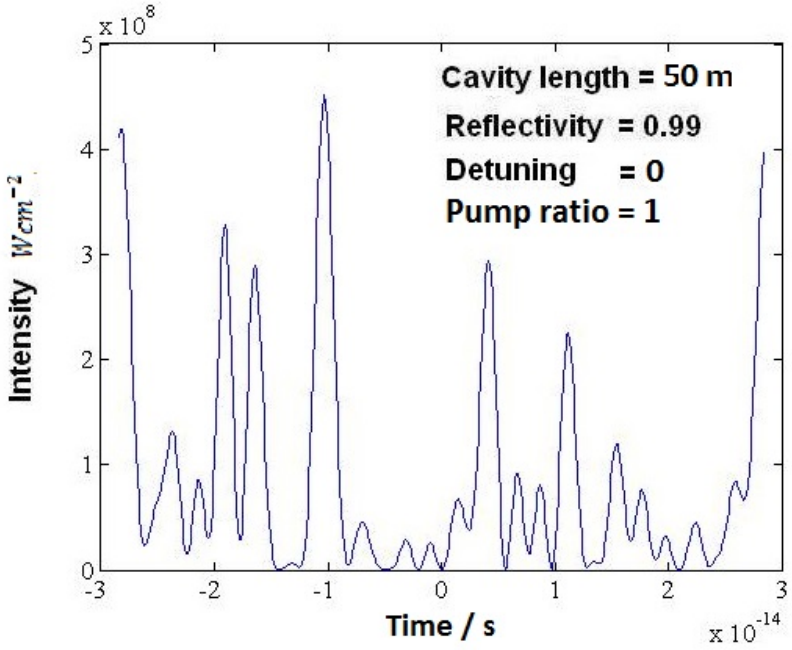


**Figure 7a – With a cavity length of $50\ m$ we find that poor phase matching between sidebands produces pulses with many peaks spread across the time domain.**

Pulses synthesised from spectra generated in the cavity system will now be considered. Figure 7a gives an example of a pulse generated by a cavity with a normalised cavity lengh of $Z_c = 1$ and, from the gain lengths product; this corresponds to a distance of $50$ metres. In the case of figure 7a the relatively low level of pump intensity implies that the system is subject to a large normalised dispersion (quoted earlier), hence the product of cavity length and dispersion ensures that only low levels of bandwidth can be obtained. The resulting spectrum also suffers from poor phase matching between sidebands, and gives rise to the synthesis of pulses with high average power densities and long durations.

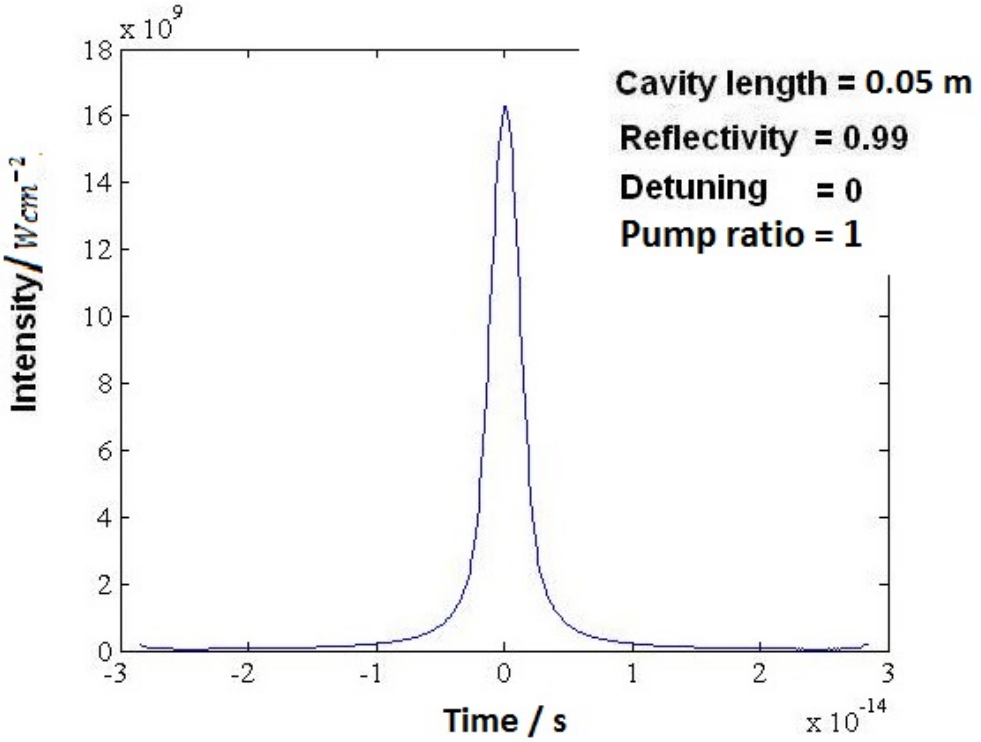


**Figure 7b – When the cavity length is short the cavity generates a sufficiently wide bandwidth which is capable of synthesising a $2.9\ fs$ pulse with a peak power of $16\ GWcm^{-2}$ and a total energy of $46\ \mu Jcm^{-2}$.**

The results of chapter 6 indicated that at high levels of normalised dispersion the largest levels of bandwidth can be produced at relatively short cavity lengths. The results have also indicated that finite levels of linear detuning or non-unity pumping ratios could be employed to optimise the level of bandwidth. By choosing to employ short normalised cavity lengths, $Z_c = 0.001$, corresponding to a distance of $0.05$ metres, pulses can be synthesised which have femtosecond duration and a high peak power density, such as the pulse given in figure 7b which has a duration of $2.9\ fs$, a peak power density of $16\ GWcm^{-2}$, average power density $0.8\ GWcm^{-2}$ and total energy density of $46\ \mu Jcm^{-2}$.

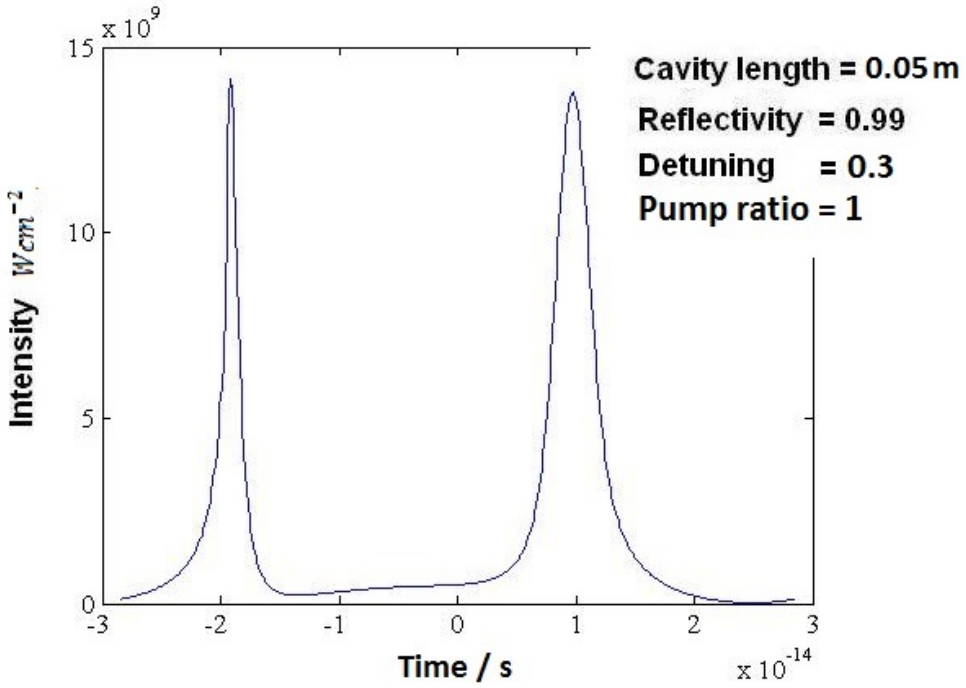


**Figure 7c– A finite level of linear detuning causes the generation of two pulses within one optical cycle and both pulses are of high peak power $\sim 14\ GWcm^{-2}$ with durations $1.3\ fs$ and $2.5\ fs$ (left to right).**

If the same length cavity is employed, with a finite level of linear detuning, the level of bandwidth is optimised. However, the introduction of a finite level of detuning changes the phase of each sideband; this causes two distinct pulses to be formed per optical cycle. Figure 7c provides an example of the pulses formed when linear detuning is employed. The pulses have durations of $1.3\ fs$ and $2.5\ fs$, each with a peak power of $14\ GWcm^{-2}$. The average power density is $0.47\ GWcm^{-2}$, and the total energy density contained within both pulses of 53 $\mu Jcm^{-2}$. These results indicate that a finite level of detuning can increase pulse energies whilst maintaining short pulse durations, but finite levels of detuning effectively lead to the doubling of the pulse repetition rate through the generation of two distinct femtosecond pulses per optical cycle.

The results provided in chapter 6 also indicated that non-symmetric pumping could produce large levels of bandwidth which can be greater than the levels generated by symmetric pumping. Figure 7d shows a $3.6\ fs$ pulse and a $1.4\ fs$ pulse generated for a pump ratio of $0.5$ in a $0.05$ metre long cavity, which is the same length as in figures 7b and 7c. The pulses have peak power densities of $9\ GWcm^{-2}$and $5\ GWcm^{-2}$ respectively. The average power density across the time domain is $0.69\ GWcm^{-2}$ and the total energy contained within the pulses is $39\ \mu Jcm^{-2}$. The results of figure 7b and 7d indicate that reducing the pump ratio leads to the synthesis of shorter pulses with slightly reduced peak powers. It is also apparent that non-unity pumping ratios can cause the formation of two distinct pulses per optical cycle, much like the results given in figure 7c for finite linear detuning.

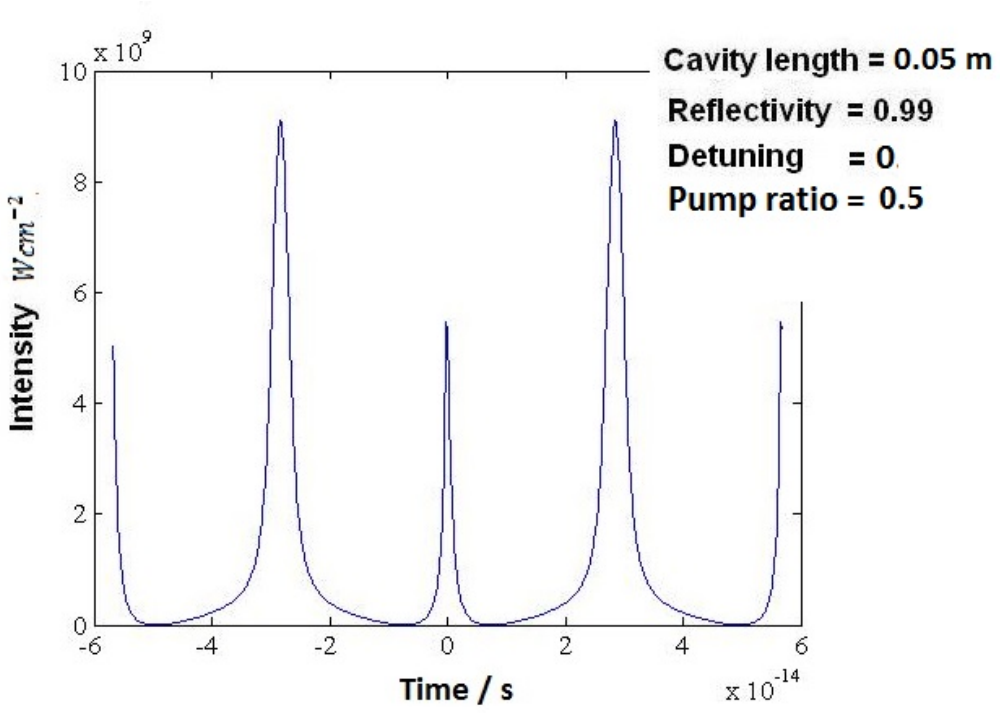


**Figure 7d – Employing a non unity pump ratio produces two pulses per optical cycle. The first pulse has a higher peak power density of $9\ GWcm^{-2}$ and duration of $3.6\ fs$ and the second pulse has a lower peak power density of $5\ GWcm^{-2}$ but a much shorter duration of $1.4\ fs$. The time axis in this figure covers two optical cycles.**

## 7.1 A realistic cavity mirror reflection profile

Modelling the cavity output mirror as infinitely broad with a uniform reflectivity has so far proven useful for determining the characteristics and limitations of sideband generation within the cavity.

The cavity system will now be tested by considering realistic coupling mirror reflectivity profiles.The main two types of mirror suited to high power and broadband application are metallic and dielectric mirrors. Metallic mirrors generally have broad reflection bandwidths which are characterised by a high reflectivity, covering a broad spectrum, with a sharp cut-off at the edges of the reflection bandwidth. The three most common metallic mirrors include silver, gold and aluminium which have reflection bandwidths covering ranges from $450\ nm - 20\ \mu m$, $800\ nm - 20\ \mu m$ and $250\ nm - 20\ \mu m$ respectively with average reflectance ranging from $90\%$ to $\sim 98\%$ . The applications of metallic mirrors are restricted because of strong levels of absorption in the ultra-violet region of the spectrum, and relatively low damage thresholds.

Dielectric mirrors have smaller reflection bandwidths compared to a metallic mirror, but their reflection profile can be easily tailored to suit most applications because of the large selection of dielectric coatings available for use. Some ultra broadband dielectric mirrors have reflection bandwidths covering $350\ nm - 1100\ nm$ with a reflectance $> 99\%$. Dielectric mirrors also have the benefit of having much higher damage thresholds and find application in current Ti:Sapphire femtosecond lasers (5, 6).

Figure 7e provides an example reflection profile for a broadband dielectric output coupler with an average reflectivity of $0.95$ over a reflection bandwidth $450\ nm - 1100\ nm$. This reflection offers a more realistic example from which the input / output coupling mirror of the Raman ring cavity can be modelled. Other commercially available coupling mirrors cover a wide range of different bandwidths, with different levels of reflectivity. Some mirrors are also designed to have broad reflectivity profiles, with narrow transmission bands centred at a particular frequency.

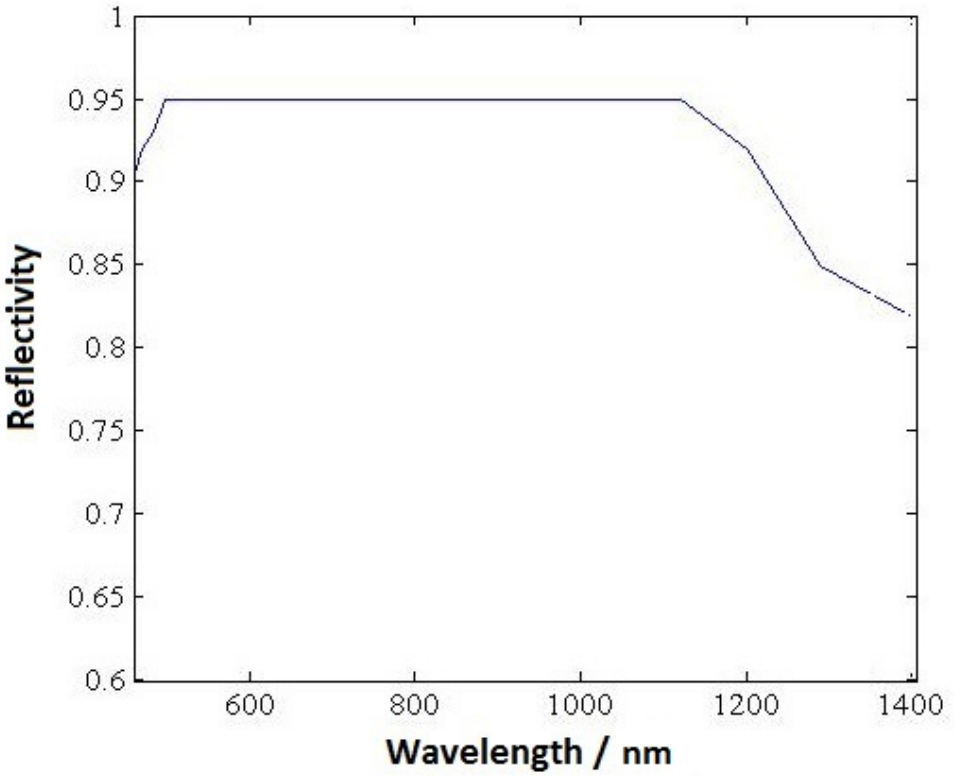


**Figure 7e - A realistic example of a commercially available input / output coupling mirror with a peak amplitude reflectivity of 0.95. It is clear that this reflectivity profile covers mostly Stokes wavelengths, and any wavelength falling outside of this range is subject to a reflectivity of 0 and is rejected from the cavity.**

Mirror profiles, such as the one given in figure 7e, restrict the maximum level of bandwidth which can be achieved by the cavity. The cavity length requires optimisation if pulses of femtosecond duration and of maximum possible intensity are to be achieved. This means that the cavity length has to be chosen such that

sidebands, with frequencies which fall within the reflection profile of the cavity mirror, reach their maximum possible intensity.

Figure 7f provides an example of a $3.9\ fs$ pulse generated in a $0.3\ m$ long cavity when employing the output mirror reflection profile provided in figure 7e. The pulse has a peak power density of $0.9\ GWcm^{-2}$, average power density $61\ MWcm^{-2}$ and energy density of $3.5\ \mu Jcm^{-2}$. The results given in figure 7f show that when employing realistic mirror reflection profiles the cavity can still support the synthesis of femtosecond pulses.

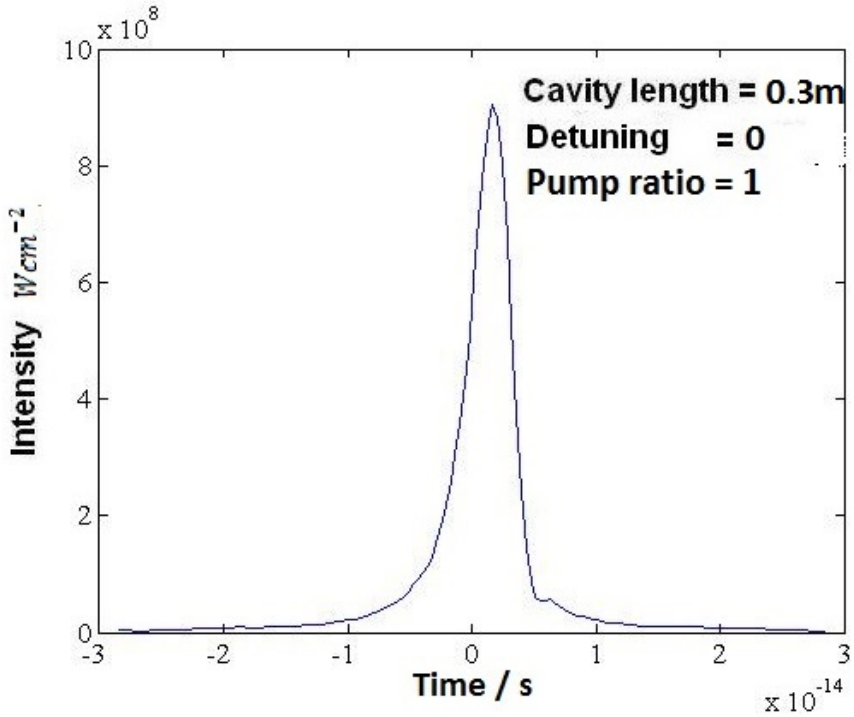


**Figure 7f - When the reflectivity profile given in figure 7e is employed we find that a pulse of $3.9\ fs$ with a peak power density of $0.9\ GWcm^{-2}$ can be generated. The duration and power of this pulse is optimised for a cavity length of $0.3\ m$.**

## 7.2 Atmospheric Nitrogen as the Raman medium

In 1997 McDonald et al (32) presented a paper regarding the generation of broadband light in air. The results indicated that large bandwidths could be generated in air by employing resonant symmetric pumping techniques, and exploiting the J = 8 - 10 rotational transition of atmospheric nitrogen. The Stokes shift and Raman gain coefficient of the exploited transition are given as $\omega_R = 78\ cm^{-1}$ and $g = 0.005\ cmGW^{-1}$ respectively (32, 43), and the initial pump intensity is again chosen to be $10^6\ Wcm^{-2}$. Using the levels of intensity and gain specified above, the level of normalised dispersion can be calculated using a Cauchy dispersion relation for air. The level of normalised dispersion is found to be large, $\gamma_j = \frac{\Delta_j}{gI_0} \approx 20$, and has a level which is approximately twice the value calculated for molecular hydrogen at atmospheric pressure. The increase in dispersion occurs because of the higher refractive index of atmospheric nitrogen.

Atmospheric nitrogen as a medium for use in UMRG has been well documented in references (32). Symmetric pumping allows large numbers of sidebands to be generated (32). Reference (32) also indicated that bandwidth can be optimised by a particular value of normalised medium dispersion, and showed how the optimal level of dispersion can vary between different Raman media, such as molecular hydrogen and atmospheric nitrogen, by an order of magnitude.

It can be recognised that the width of the exploited Raman transition dictates the number of Stokes and anti-Stokes sidebands required for the generation of a femtosecond pulse. For example, if the Raman transition frequencies of molecular hydrogen and nitrogen are compared, then the transition frequency of hydrogen is found to be roughly 7.5 times larger the transition of nitrogen. The Fourier bandwidth theorem implies that, to support a single femtosecond pulse, atmospheric nitrogen would need to support 7.5 times more bandwidth than hydrogen. Sideband phases also become important when such a large number of sidebands are required for the synthesis of a pulse, because poor phase matching between sidebands can lead to pulses being synthesised with durations which are longer than their theoretical Fourier limit.

The underlying processes that control bandwidth growth within the ring cavity, such as parametric and non-parametric growth, remain the same regardless of the choice of Raman medium. Therefore the maximum bandwidth can be optimised by the choice of cavity length, linear detuning, pumping ratio and cavity mirror reflectivity. Examples of pulses, synthesised from spectra generated in cavity confined atmospheric nitrogen, will now be presented. The cavity mirror reflectivity profile used in the simulations is the given in figure 7e.

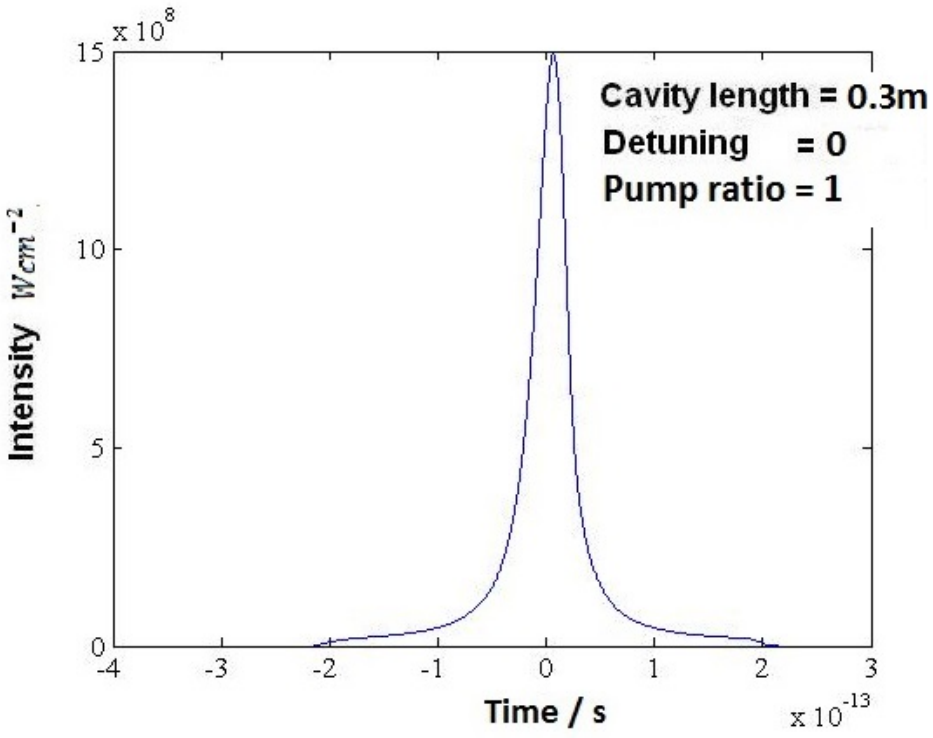


**Figure 7g - With atmospheric nitrogen as the medium we find that the cavity is capable of generating sufficient bandwidth to support the synthesis of $35\ fs$ pulses, with a peak power density of $1.5\ GWcm^{-2}$, in a $0.3\ m$ long cavity.**

As with the previous results, for molecular hydrogen, when employing an example of a realistic coupling mirror the cavity length can be chosen as to optimise the duration and power of the synthesised pulses. Figure 7g provides an example of a $35\ fs$ pulse generated in a $0.3\ m$ long cavity with a peak power density of $1.5\ GWcm^{-2}$, average power density $0.12\ GWcm^{-2}$ and pulse energy density of $53\ \mu J$. If figure 7g is compared to figure 7f it is apparent that pulses synthesised from spectra generated in atmospheric nitrogen, are approximately one order of

magnitude longer in duration than pulses produced in hydrogen and possess greater peak power and pulse energy density.

The relatively long pulse duration of figure 7g corresponds to a frequency bandwidth that is narrower than the reflection bandwidth of the cavity mirror. The lack of frequency bandwidth generated by the cavity can be attributed to large level of normalised dispersion, and losses at the cavity mirror. Therefore, to reduce coupling losses and obtain the maximum possible bandwidth, a higher reflectivity profile must be employed, like the one given in figure 7e, with a higher reflectivity of $0.99$ over a reflection bandwidth of $450\ nm - 1100\ nm$ .

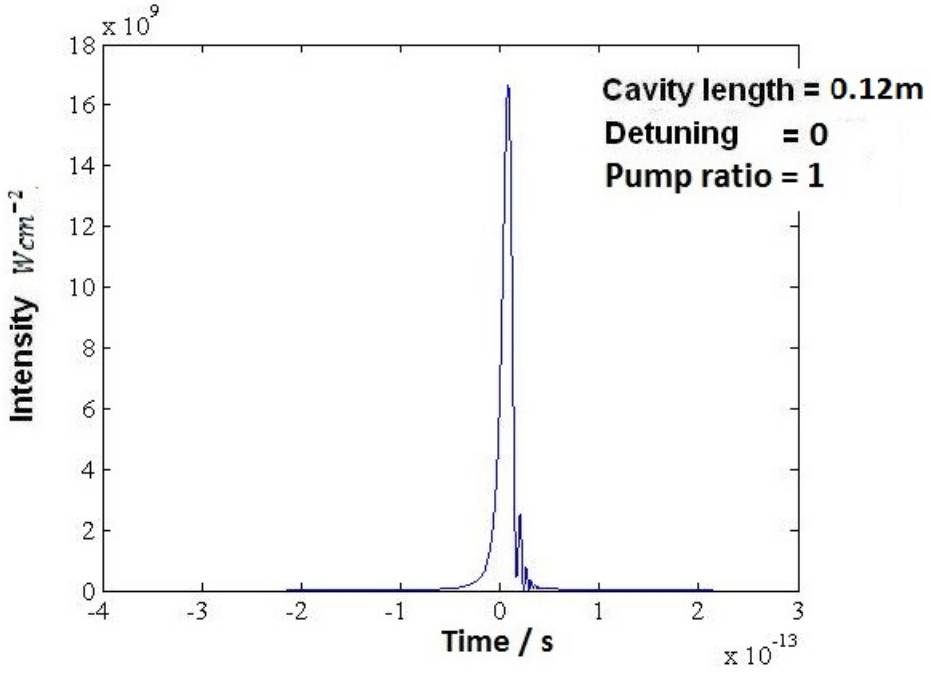


**Figure 7h - With atmospheric nitrogen as the medium and by employing a cavity mirror of higher reflectivity the cavity is found to be capable of generating sufficient bandwidth to support the synthesis of $11\ fs$ pulses with a peak power density of $16\ GWcm^{-2}$ in a $0.12\ m$ long cavity.**

Increasing the coupling mirror reflectivity leads to the generation of a broadband frequency spectrum with a much higher intensity, and corresponds to a high intensity femtosecond pulse in the time domain.

Figure 7h shows an example of a $11\ fs$ pulse generated in a $0.12\ m$ long cavity with a peak power density of $16.5\ GWcm^{-2}$, average power density of $0.4\ GWcm^{-2}$ and energy density of $181\ \mu Jcm^{-2}$. The duration of the pulse given in figure 7h is over three times shorter than that of figure 7g and carries over three times as much energy. The pulse given in figure 7h has a duration which is just over twice that of the pulse given in figure 7f for molecular hydrogen but with a much higher peak power density.

To obtain shorter pulse durations and higher peak power densities much greater pump intensities would need to be employed to increase the gain length product, $Z = gI_0z$. The benefits of employing higher power pump beams will now be discussed.

## 7.3 High power pump beams and attosecond pulses

Throughout this chapter, pumping has been defined by relatively low intensity pump beams, $I_0 = 10^6\ Wcm^{-2}$, such as those produced by CW lasers. The process of UMRG has also been modelled using the steady state UMRG equations (2.63). The steady state equations are derived from equations (2.62) by specifying that the width of the pump pulse is greater than the dephasing time of the medium, $t_p \gg T_2$. The time taken for light to traverse the cavity also needs to be considered so that it can be compared to pulse times, $t_p$, of possible pump lasers.

The time taken for light to travel through the cavity is given as:

$$T_{cav} = \frac{z_c}{c}\ , \tag{7.1}$$

where $c$ is the speed of light. By specifying that $z_c = 0.05\ m$ we find the transit time to be:

$$T_{cav} \approx 0.16\ ns$$

hence the time taken for a wave to complete $m$ cavity transits is:

$$T_m = T_{cav}.m. \tag{7.2}$$

Defining the pump beam as a square pump pulse provided by a diode pumped Nd:YAG laser, with a $10\ ns$ duration carrying $3\ J$ of energy and a $15\ mm$ spot size, the peak power can be calculated to be approximately $0.3\ GW$ and therefore the peak intensity of $0.17\ GWcm^{-2}$ is achieved. High intensity pump pulses can be achieved with a relatively large beam diameter, thereby reducing the level of beam diffraction, as will be discussed in chapters 8 and 9.

Through the comparison of the transit time and the pulse, $t_p \gg T_{cav}$, and using equation (8.2) it can be shown that multiple cavity transits can occur over the duration of the pump pulse. When $t_p \gg T_{cav}$ and $t_p \gg T_2$ the steady state UMRG equations given by (2.63) offer a suitable description of the system.

Using the quoted intensity, $I_0 = 0.17\ GWcm^{-2}$, and cavity length, $0.05\ m$, the gain length product yields a normalised cavity length $Z_c = 0.17$ and the normalised level of dispersion as $\gamma_1 = 6.5 \text{ x } 10^{-2}$. If these parameters are applied to a simulation, and the reflection profile given in figure 8e is specified, the inverse Fourier transform of the resulting frequency spectrum yields a near Fourier limited $2.5\ fs$ pulse with a peak power density of $42.5\ GWcm^{-2}$, average power density of $2\ GWcm^{-2}$and pulse energy density of $0.16\ mJcm^{-2}$, as shown in figure 7i.

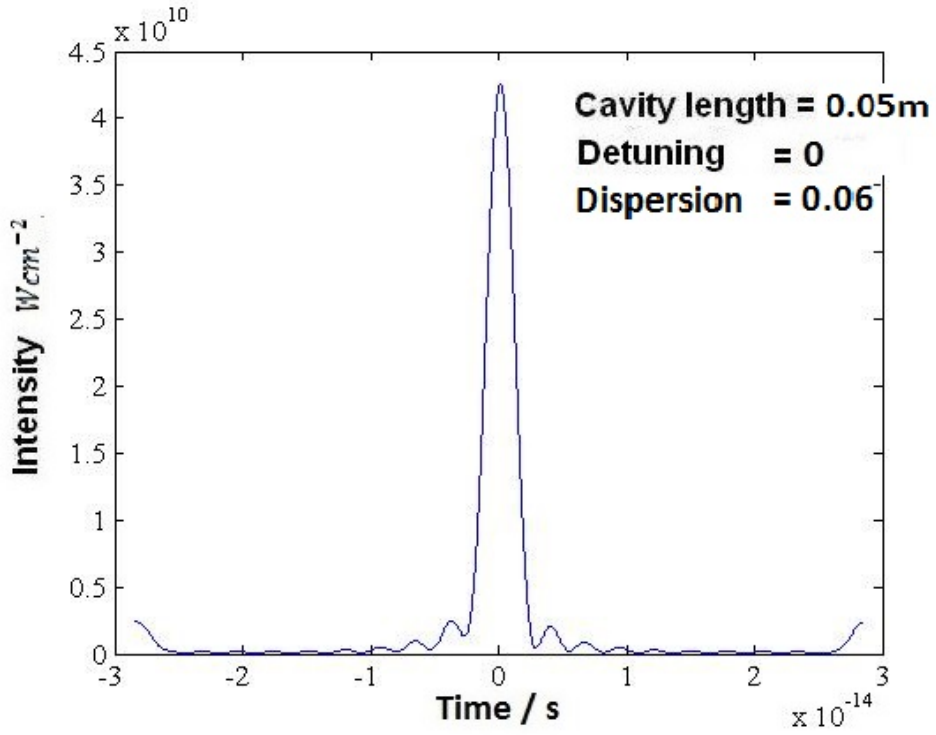


**Figure 7i – When a large level of pump intensity is employed a cavity length can be chosen such that the cavity can support the synthesis of a $2.5\ fs$ pulse with a peak power density of $42.5\ GWcm^{-2}$ and a total energy of $0.16\ mJcm^{-2}$.**

The results of figure7i demonstrate that increasing the level of pump intensity also increases the peak intensity of synthesised pulses. Large pump intensities also allow bandwidth generation to be achieved at shorter cavity lengths, therefore leading to the generation of a spectrum containing phase matched sidebands which can allow the synthesis of the shortest possible pulses. It is clear that an increased level of pump intensity is beneficial for the generation of high intensity few-femtosecond pulses.

If atmospheric nitrogen is used as the Raman medium, together with the reflection profile given in figure 7e and a pump intensity of $I_0 = 0.17\ GWcm^{-2}$results are achieved which show the cavity to be capable of generating sufficient bandwidth to support a $8.5\ fs$ pulse with a peak power density of $155\ GWcm^{-2}$, average power density of $3\ GWcm^{-2}$ and energy density of $1.3\ mJcm^{-2}$, as given in figure 7j.

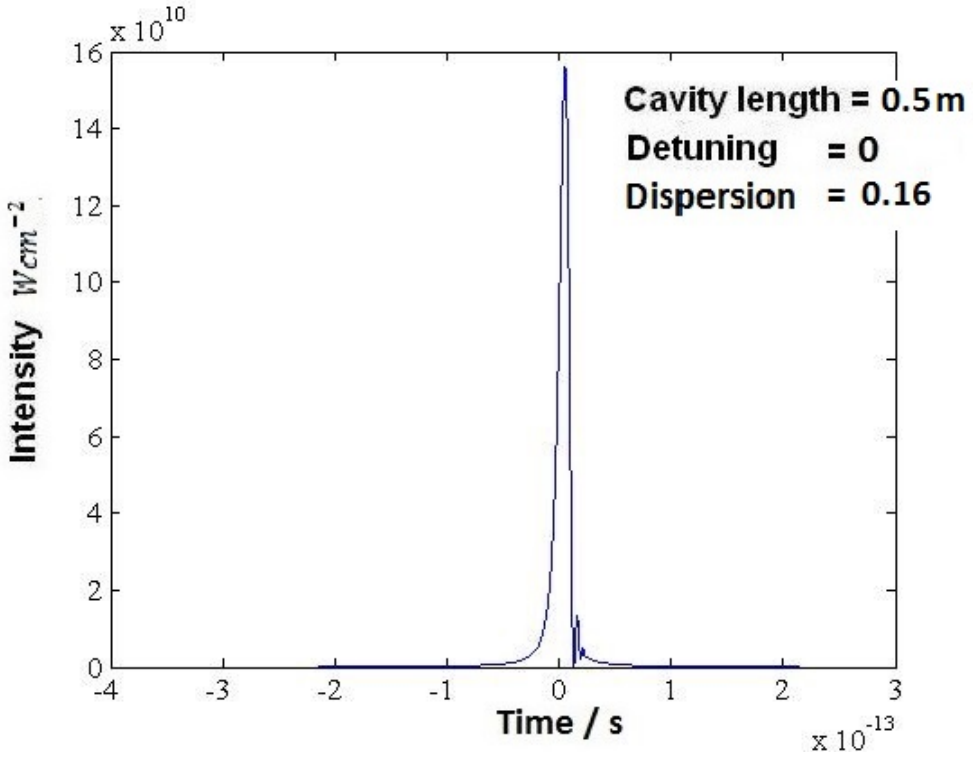


**Figure 7j – When a high level of pump intensity is employed, and atmospheric Nitrogen is the chosen Raman medium, the cavity can generate bandwidths suitable for the synthesis of a $8.5\ fs$ pulse with a peak power density of $155\ GWcm^{-2}$ and a total energy density of $1.3\ mJcm^{-2}$.**

Figures 7g and 7j both indicate that pulses generated in atmospheric nitrogen have longer durations, greater peak intensities and greater levels of pulse energy density than pulses generated in molecular hydrogen at atmospheric pressure. Higher intensity pulses are generated in atmospheric nitrogen because the Raman transition frequency of nitrogen is much smaller. This means that the repetition rate of the synthesised pulse train is smaller, and therefore more energy is contained within each pulse cycle.

It is also worth noting that the peak power densities given figures 7i and 7j are calculated assuming that the multi-frequency beam, generated by the cavity, has a spot diameter of $15\ mm$. However, most applications of femtosecond pulses require beams with much smaller spot sizes. If the multi-frequency beam of figure 7i were focussed onto a spot size of $1\mu m$ there would be a substantial increase in the level of peak power density, which would be approaching levels of $\sim 10^{19}\ Wcm^{-2}$ which implies pulses with energy densities $\sim 10^{5}\ Jcm^{-2}$.

## 7.4 Band pass mirror

Thus far the intensities of the applied pump lasers have been quoted as occurring at the start of the first cavity transit at $Z = 0$. Any rejection of the incident pump, through reflection at the cavity mirror, has been ignored. This obviously represents a large loss of the incident pump energy and makes cavity pumping incredibly inefficient.

To avoid reflection losses from the coupling mirror we could choose to employ a mirror with a narrow transmission band centred at the pump frequency. Such mirrors are employed in Ti:Sapphire laser oscillators as pump mirrors, and as mirrors for the selection of specific cavity modes. These types of mirrors have reflection bandwidths which can cover the entire gain bandwidth of the Ti:Sapphire medium.

The reflection profile given in figure 7e will now be considered, but with a transmission band centred at the pump and first Stokes wavelengths. Hence a reflection profile is achieved that is highly transmitting at only the pumped wavelengths. Employing the modified reflectivity profile, a pump intensity of $1\ GWcm^{-2}$ and a normalised level of dispersion of $\gamma_1 = 1 \text{ x } 10^{-2}$ yields a high intensity bandwidth that supports the synthesis of few-femtosecond pulses.

An example of the $2.2\ fs$ intra-cavity pulse, generated whilst employing the modified mirror profile and hydrogen as the medium, is given in figure 7k. The pulse has a peak power density of $90\ GWcm^{-2}$, average power density $3.49\ GWcm^{-2}$ and energy density $0.2\ mJcm^{-2}$. This result implies that the synthesis of pulses becomes more efficient when the coupling mirror allows transmission of the applied pump beams.

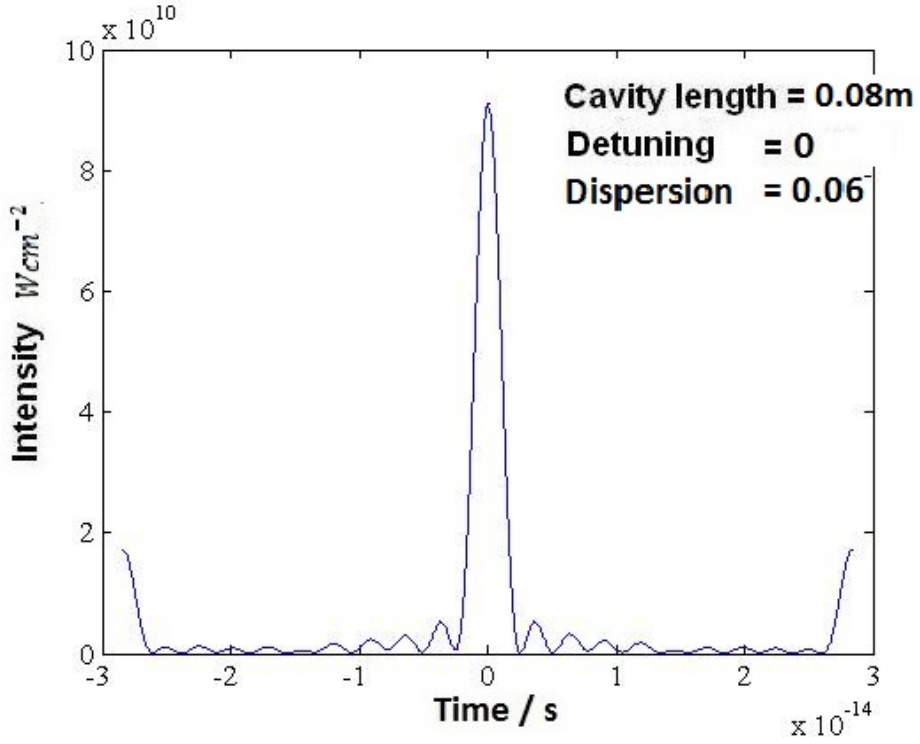


**Figure 7k – When $100\%$ transmission at the pump and first Stokes frequency is employed the cavity can maintain bandwidth suitable for the synthesis of a $2.2\ fs$ pulse with a peak power density of $90\ GWcm^{-2}$ and a total energy density of $0.2\ mJcm^{-2}$ .**

## 7.5 The ideal cavity

The ideal case of a coupling mirror with a very broad reflection bandwidth, with $100\%$ transmission at the pump and first Stokes frequencies, and no medium dispersion will now be considered. The chosen medium is hydrogen and the applied pump intensity is taken to be $1\ GWcm^{-2}$. Simulations show that, for this selection of parameters, very large bandwidths can be generated which contain approximately $\sim 600$ sidebands of comparable intensity. Such spectra can be shown

to be suitable for the synthesis of pulses as short as $60$ attoseconds. An example of such a pulse is given in figure 7l and has a peak power density of $70\ TWcm^{-2}$, average power density of $73\ GWcm^{-2}$ and energy density of $4.2\ mJcm^{-2}$.

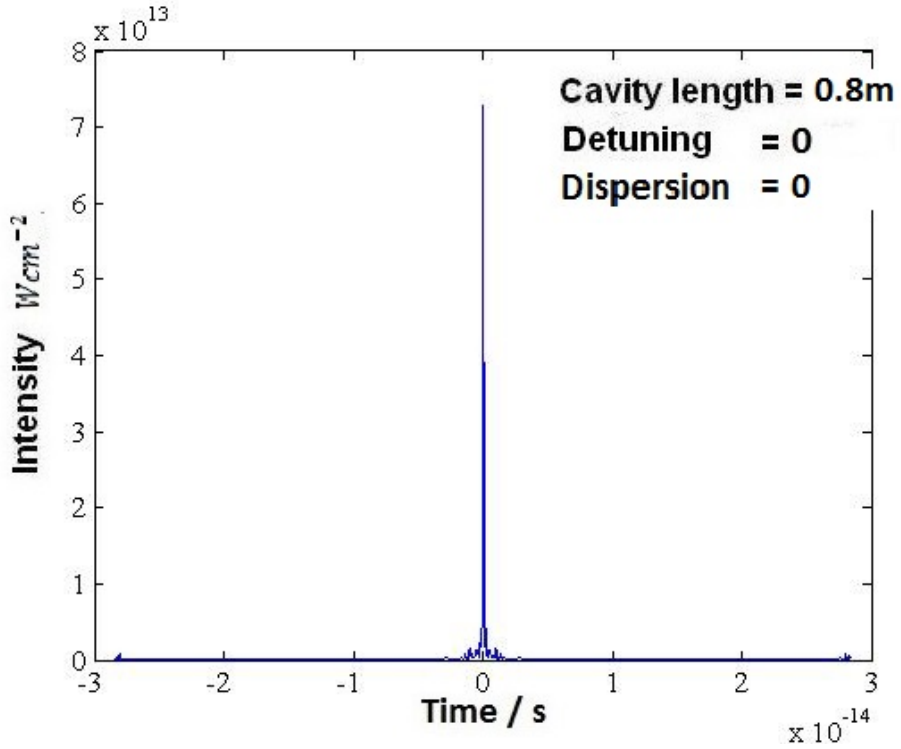


**Figure 7l – When the level of dispersion is negligible and the reflection bandwidth of the coupling mirror is broad (covering over $600$ sidebands) a pulse of 60 attosecond duration can be synthesised.**

The results presented in this chapter demonstrate the generation of few-femtosecond pulse trains. The duration and power of such pulses depends on the applied pump intensity and the reflectivity profile of the chosen cavity mirror. The optimal choice of cavity mirror possesses a reflection profile with a transmission band centred at the pumping frequencies.

The results presented in this chapter show that reflection bandwidths available to current dielectric mirrors restricts the level of bandwidth generated by cavity. Mirrors with broader reflection bandwidths could enable the synthesis of pulse trains, of attosecond duration, with peak powers of tens of terawatts, and focussing of such pulses could lead to power densities approaching $10^{20}Wcm^{-2}$.

# CHAPTER 8

## (1+1)D Cavity UMRG

At the end of chapter 2 the transverse UMRG equations were stated, and the diffraction terms discussed and normalised. The following chapters are devoted to the analysis of transverse UMRG with cavity boundary conditions in both one and two transverse dimensions (and the longitudinal coordinate). To begin, the full complexity of the transverse equations will be restricted by confining the spatial structure of the fields to only a single transverse dimension.

The transverse UMRG equations in the non-cavity context have been thoroughly analysed and documented in reference (78) for both one and two transverse dimensions. The results indicated that the development of spatial structure of each frequency component is most rapid at the centre of the beam. This occurs because frequency conversion is driven by higher levels of light intensity at the beam centre; therefore the rate of frequency conversion at the edges of the beam is much lower. The variation of intensity across the transverse axis gives rise to a range of conversion rates which drive the formation of complex transverse structures at each of the sideband frequencies.

These results also indicated that in the limit of zero dispersion and zero diffraction ($\gamma_j = b_j = 0$) bandwidths could be achieved which matched the bandwidth predicted by the dispersionless steady state plane wave UMRG equations (2.63), and that the combination of finite dispersion and relatively strong diffraction can be shown to decrease the maximum bandwidth (though the bandwidth is still close to one octave). Another important characteristic highlighted by reference (78) is the quality of the multi-frequency beams generated by UMRG which have a reasonably smooth and axially confined multi-frequency transverse energy distribution.

The introduction of transverse dimensions substantially increases the demands on both computational power and simulation time. Even when restricting the analysis to only one transverse dimension, solving the equations remains computationally expensive. This is not only because of the number of frequency components

modelled by the simulations but also because of the cavity boundary conditions and the large number of cavity transits.

When considering (1+1)D transient UMRG with cavity boundary conditions in the limit of zero dispersion and zero diffraction, we find that the results strongly agree with the dispersionless plane wave results. Extremely large bandwidths can be generated which are only restricted by the reflectivity profile of the coupling mirror, and the level of medium dispersion. The results given throughout this chapter are achieved from simulations which model the cavity mirror reflection profile given in figure 7e.

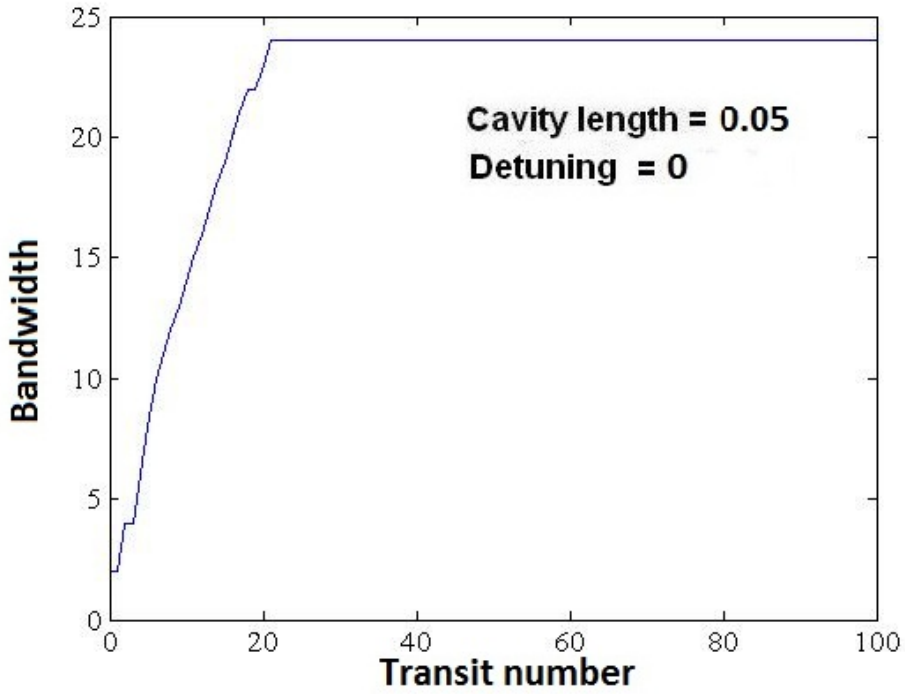


**Figure 8a – Cavity confined transverse UMRG can generate stable bandwidths which cover the reflection bandwidth of the cavity mirror. The diffraction length is, $L_D = 20$.**

The results of simulating the (1+1)D transverse UMRG can be shown to be in agreement with the plane wave results given in previous chapters. Bandwidth growth responds to various types of parameter changes, such as increasing levels of dispersion and finite levels of linear detuning, in a way which is analogous to the plane wave system. With the introduction of transverse structure, the effects of finite levels of beam diffraction (recall equation 2.69) also need to be considered.

This has been found to have an effect on bandwidth growth which is analogous to that of longitudinal dispersion (78) and can have a strong impact on the levels of bandwidth generated in relatively long cavities.

The following simulations model molecular hydrogen as the cavity medium. The pump and first Stokes beams are taken to be Gaussian and focused into a small spot size, $15\ mm$, with a central peak intensity of $I_0 = 10^6 W cm^{-2}$. Each result presented in this chapter will be obtained for a chosen normalised cavity length of $Z_c = 0.05$ with zero detuning, $\delta = 0$, zero dispersion, $\gamma_1 = 0$, and a normalised diffraction length of, $L_D = 20$, unless otherwise specified. Because the chosen reflectivity profile is that of figure 7e, it is clear that the maximum level of bandwidth is dictated by the spectrum of the cavity mirror. Figure 8a shows how the bandwidth can grow to its maximum level, which covers the spectral bandwidth of the cavity mirror, and reaches a fixed level after $30$ cavity transits. Figure 8b shows the corresponding growth of the total multi-frequency intensity. The results of figures 8a and 8b imply that a fixed spectrum with a large intensity could be coupled out of the cavity.

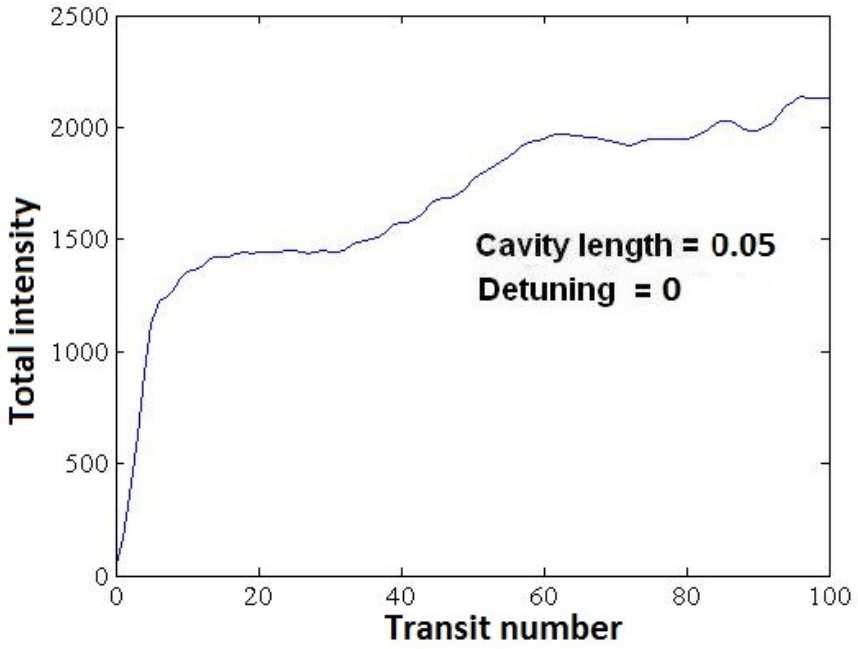


**Figure 8b – The total intensity of the multi-frequency spectrum reaches a large level which is almost stable. The diffraction length is, $L_D = 20$.**

To gain insight into the process of transverse UMRG, the intensity profiles of specific Raman sidebands should be considered. Figure 8c represents the normalised transverse intensity distribution for the first Stokes sideband, pump and first anti-Stokes sidebands after $100$ cavity transits. The simulation employed the same parameter regime as the results given in figures 8a and 8b. Each sideband has intensity much greater than the initial Gaussian pump beam.

It is apparent from the results of figure 8c that each sideband amplitude (after 100 cavity transits) carries a much larger intensity than the initially applied pump beam. Each profile is symmetric with respect to the beam centre and can have sharp, highly intense peaks.

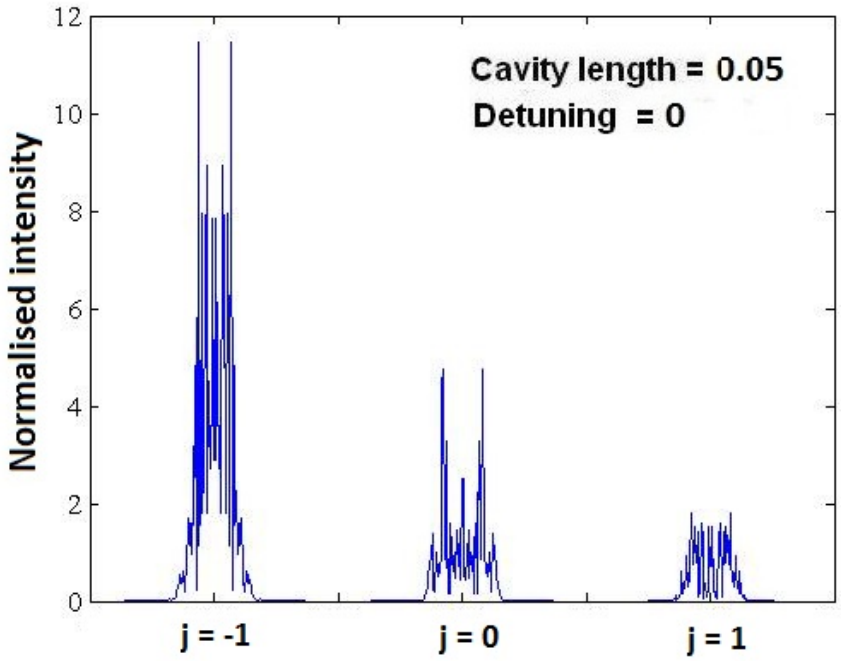


**Figure 8c – The transverse intensity profiles of the first Stokes (j = -1), pump (j = 0) and first anti- Stokes (j = 1) sidebands. Each of the frequency components carries a large intensity. The diffraction length is, $L_D = 20$.**

The medium excitation amplitude also possesses transverse structure and causes varying levels of growth across the transverse plane. It can be recognised just from the sideband profiles given in figure 8c that the medium excitation will carry large amplitude with a steep sided transverse profile.

The transverse distribution of the medium excitation plays a vital role in the shaping of each sidebands transverse intensity profile. This will be demonstrated in chapter 11 when nonlinear detuning is discussed in terms of the non-cavity system.

## 8.1 RMS width of the multi-frequency beam

It is useful to conduct the analysis of transverse UMRG in terms of the root mean square width of the total transverse intensity profile (78). Figure 8d explores the broadening of the transverse profile for a range of diffraction lengths (input beam radii). This is of particular importance when tightly focussed laser beams are required to achieve the high peak power densities required for efficient sideband generation.

The results of figure 8d are generalised by assuming that the combination of laser power and beam radius are chosen in a way which maintains the peak pump power density at a level of $I_0 = 10^6 W cm^{-2}$ . Doing this ensures that the results obtained from each simulation are subject to the same level of gain length product.

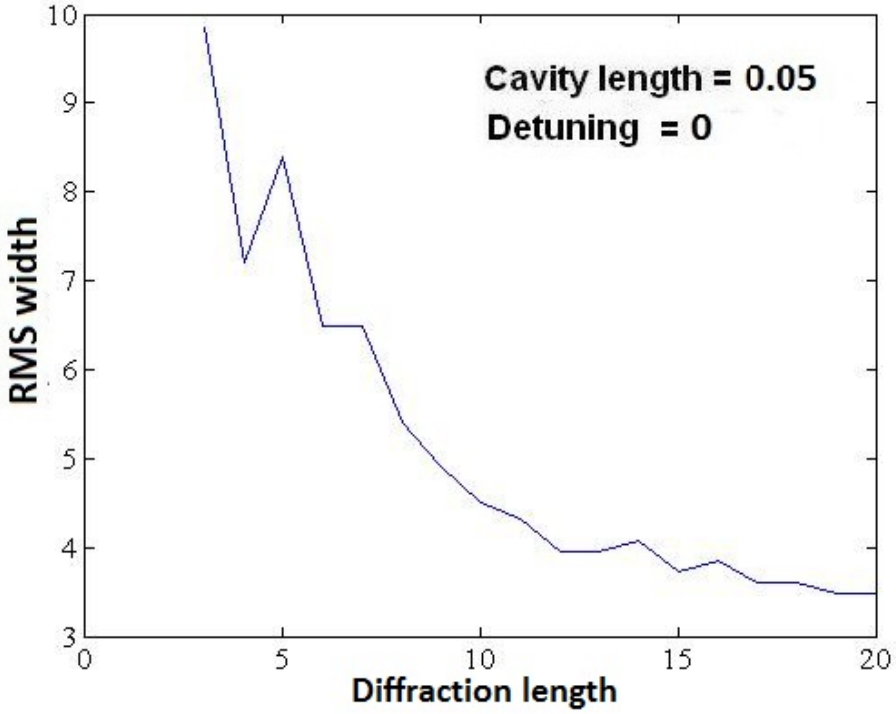


**Figure 8d – The RMS width of the total multi-frequency beam taken at 200 cavity transits for a range of diffraction lengths. The widest beams are achieved for the shortest diffraction lengths, and can be several times wider than the initial Gaussian pump beam.**

It is already known from the results given in reference (78) that, when the diffraction length is short, the total transverse intensity profile becomes significantly broadened to the point where bandwidth growth is strongly inhibited. Figure 8d represents the RMS width of the multi-frequency beams transverse intensity profile, for a range of diffraction lengths. Each of the results has been taken after 200 cavity transits and corresponds to the point after which each simulation reaches a stable bandwidth, and a stable level of intensity.

The results of figure 8d indicate that a large degree of beam diffraction can occur at the shortest diffraction lengths. The change in RMS width, with respect to increasing levels of beam diffraction, shows a similar trend to that of the non-cavity system, where the RMS width of the multi-frequency beam increases as the diffraction length is decreased. The overall trend is expected because applying boundary conditions does not directly influence beam diffraction.

Figures 8e and 8f represent the bandwidth and total multi-frequency intensity data, corresponding to the data given in figure 8d. The comparison of figures 8d and 8e shows that whilst the RMS width can vary significantly between chosen diffraction lengths, the bandwidth level remains constant (at its maximum).

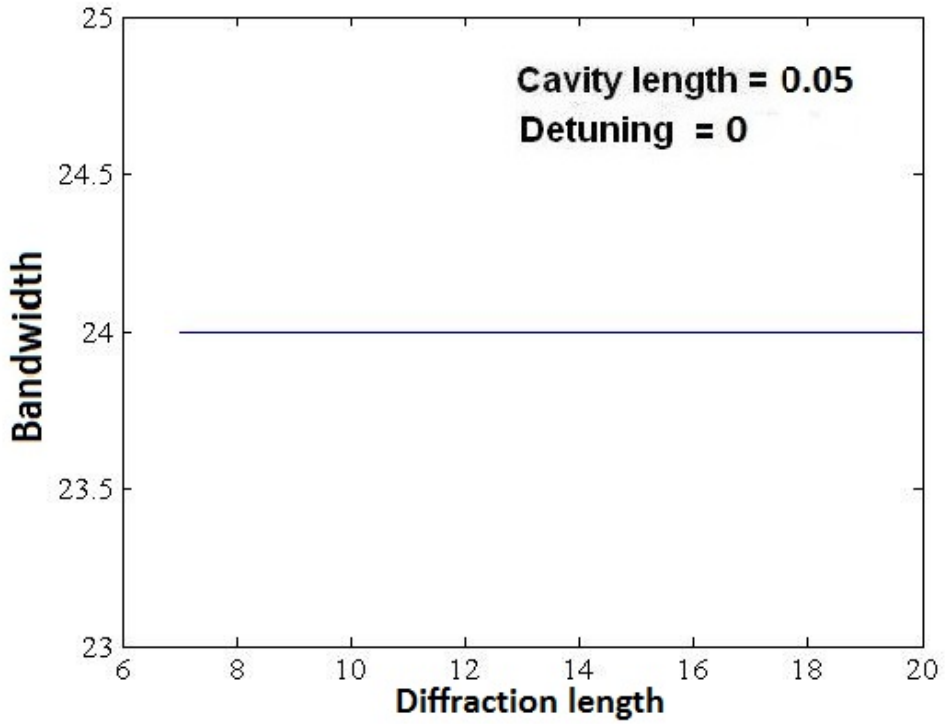


**Figure 8e – The cavity achieves its maximum level of bandwidth regardless of the level of diffraction length.**

The comparison of figures 8c and 8f indicate that the total intensity of the multi-frequency beam changes as a function of diffraction length in a way which is opposite to that of the RMS width. The largest levels of intensity occur at the longest diffraction lengths, and correspond to the narrowest RMS beam widths.

Significantly lower levels of intensity occur for shorter diffraction lengths because beam diffraction leads to diffractive spreading of the pump beam. Strong levels of diffraction decrease the overall growth rate of the sidebands, and leads to each sideband possessing a decreased level of intensity.

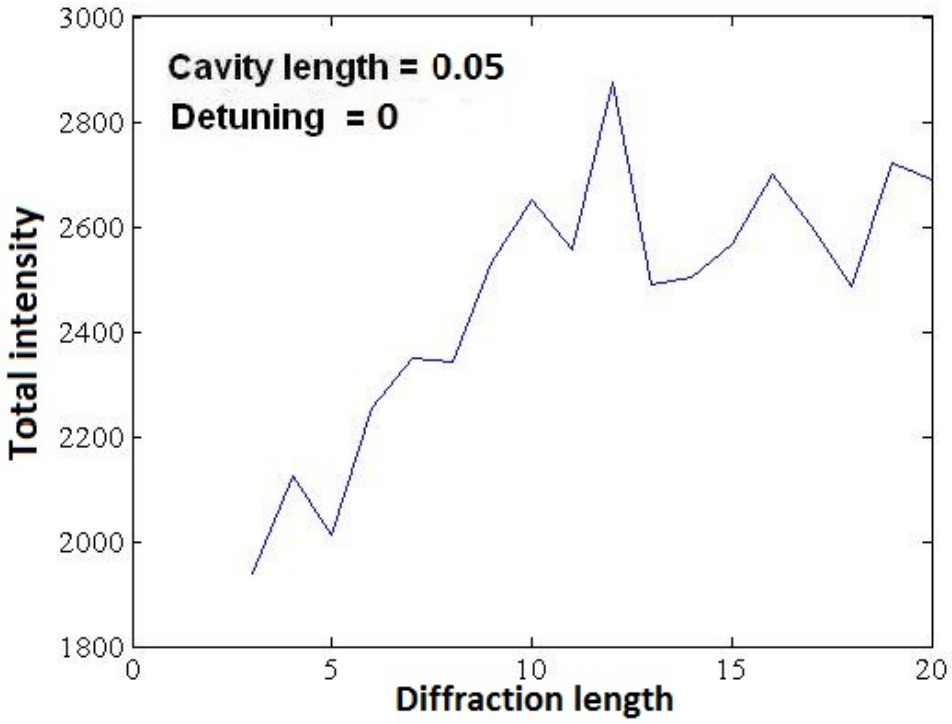


**Figure 8f– Very short diffraction lengths leads to a decreased level of normalised intensity contained within the cavity. When longer diffraction lengths are applied the spectrum contains much larger intensities.**

## 8.2 Transverse beam separation

When considering realistic cavity mirrors, the damage threshold also needs to be considered. Throughout this thesis, pump powers have been deliberately specified to fall within the damage threshold limits of dielectric and metallic mirror coatings. The transverse analysis allows a possible method of reducing mirror and medium damage to be considered.

The transition from a plane wave analysis to that of transverse UMRG allows the transverse separation of the applied pump lasers to be considered. This is achieved by ensuring that the peak intensities of the applied pump and first Stokes lasers do not fully overlap in the transverse plane when incident on the cavity mirror, or when travelling through the medium.

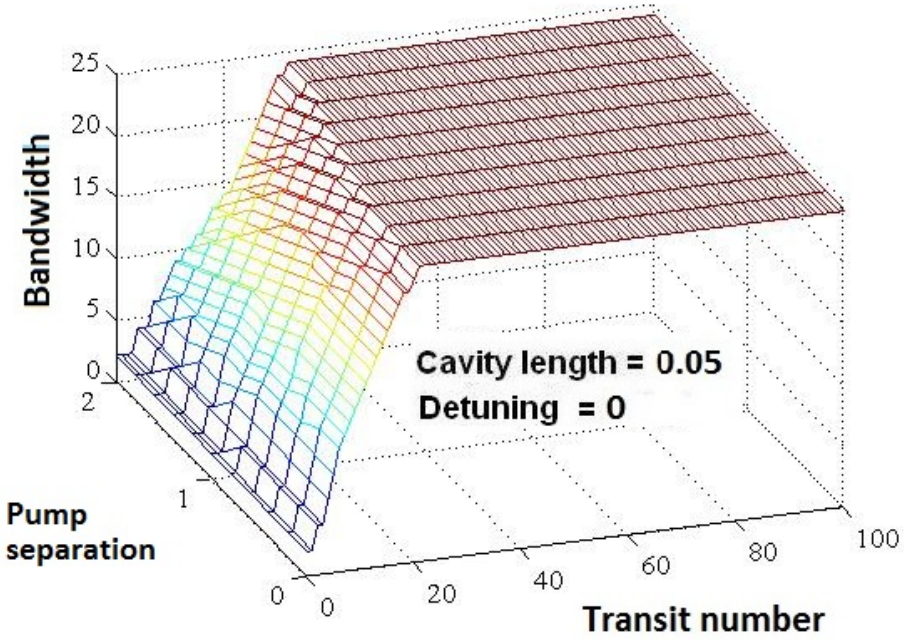


**Figure 8g – The maximum bandwidth of the cavity can be generated for a very broad range of beam separations. The diffraction length is, $L_D = 20$.**

The combined effect of beam separation and beam diffraction decreases the peak level of the multi-frequency intensity incident on the cavity mirror surface. This occurs because beam separation increases the RMS width of the multi frequency beam and decreases beam overlap. Including finite levels of beam separation could therefore decrease the chances of cavity mirror damage, whilst also preventing the breakdown of the Raman medium.

The results given in figure 8g represent the bandwidth levels obtained when employing varying levels of transverse beam separation. The results imply that large transverse beam separations, up to the width of the pump, can be employed with little adverse effects on the level of bandwidth generated by the cavity. However, the rate of bandwidth growth does decrease slightly as larger beam separations are applied.

At large beam separations, the peak intensities of the applied pump beams are separated by an appreciable distance, beam diffraction is therefore necessary to produce the beam overlap required and drive sideband growth.

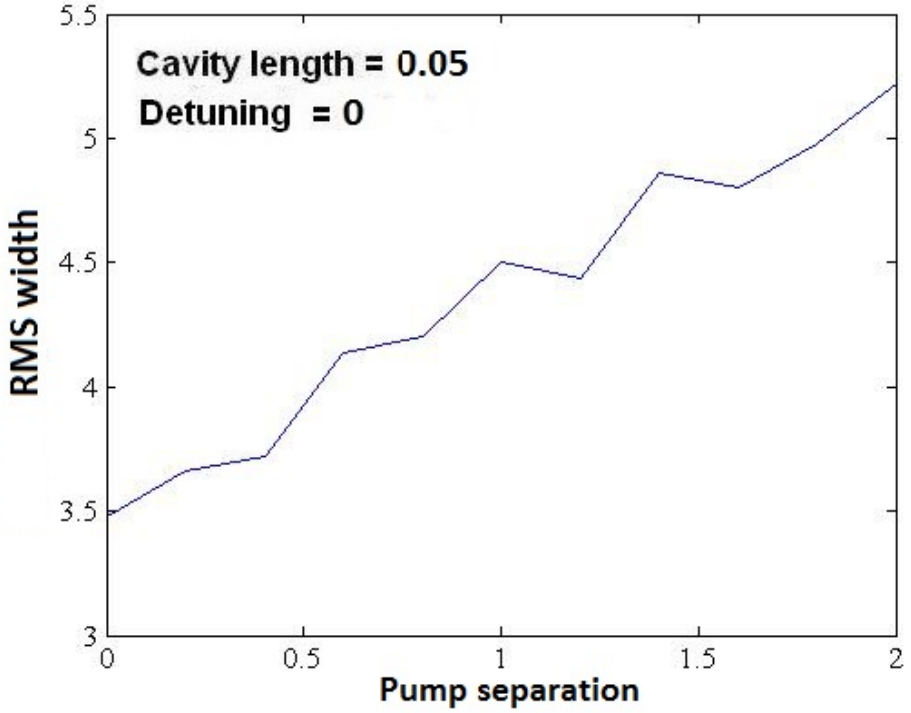


**Figure 8h –The RMS width of multi-frequency beam generated after $200$ cavity transits varies linearly with increasing levels of pump separation. The diffraction length is, $L_D = 20$.**

Measuring the RMS width of beam profiles generated by the cavity, for a range of beam separations, yields the results given in figure 8h. These results, coinciding with the bandwidth results given in figure 8g, demonstrate a linear relationship between the final RMS width of the multi-frequency beam and the applied level of beam separation. The results of figures 8g and 8h imply that large beam separations can be applied (equal to the pump width), without any adverse effects on the final level of bandwidth.

# CHAPTER 9

## (1+2)D Cavity UMRG

The analysis of (1+1)D transverse UMRG in the previous chapter yielded some interesting results in terms of beam diffraction and transverse separation of the applied pump lasers . Very few experimental situations arise in which modelling only a single transverse dimension is applicable. This chapter will extend the analysis further and provide results obtained from the simulation of transverse UMRG in two transverse dimensions.

The (1+2)D UMRG equations (2.66) are simulated with cavity boundary conditions. Each of the results has been obtained for a chosen normalised cavity length of $Z_c = 0.05$ , zero detuning, $\delta = 0$ ,and zero dispersion $\gamma_1 = 0$. The normalised diffraction length is relatively short, $L_D = 20$. The addition of a further transverse dimension significantly increases computational requirements. Solution of the equations requires the use of very large multi-dimensional arrays which can occupy vast amounts of a computer systems virtual memory. To reduce computational requirements, the number of sidebands computed by the simulation has been reduced by simulating the reflection profile given in figure 7e.

The results of the previous chapter have already shown that a combination of transverse structure and beam diffraction can produce complex transverse intensity profiles at each sideband frequency. Such intensity profiles arise from a lack of intensity confinement at the beam centre, where the peak intensity at the centre of the beam diffuses out across the transverse axis. This is in contrast to the plane wave analysis where the intensity is confined to a single point. The re-distribution of the pump intensity causes each point on the transverse axis to experience a different level of driving amplitude. Hence the level of sideband growth varies along the transverse axis. When the extension is made to include two transverse dimensions we find that a combination of transverse beam effects and cavity boundary conditions can produce complex transverse intensity profiles which can exhibit multiple ring structures of alternating high and low intensity.

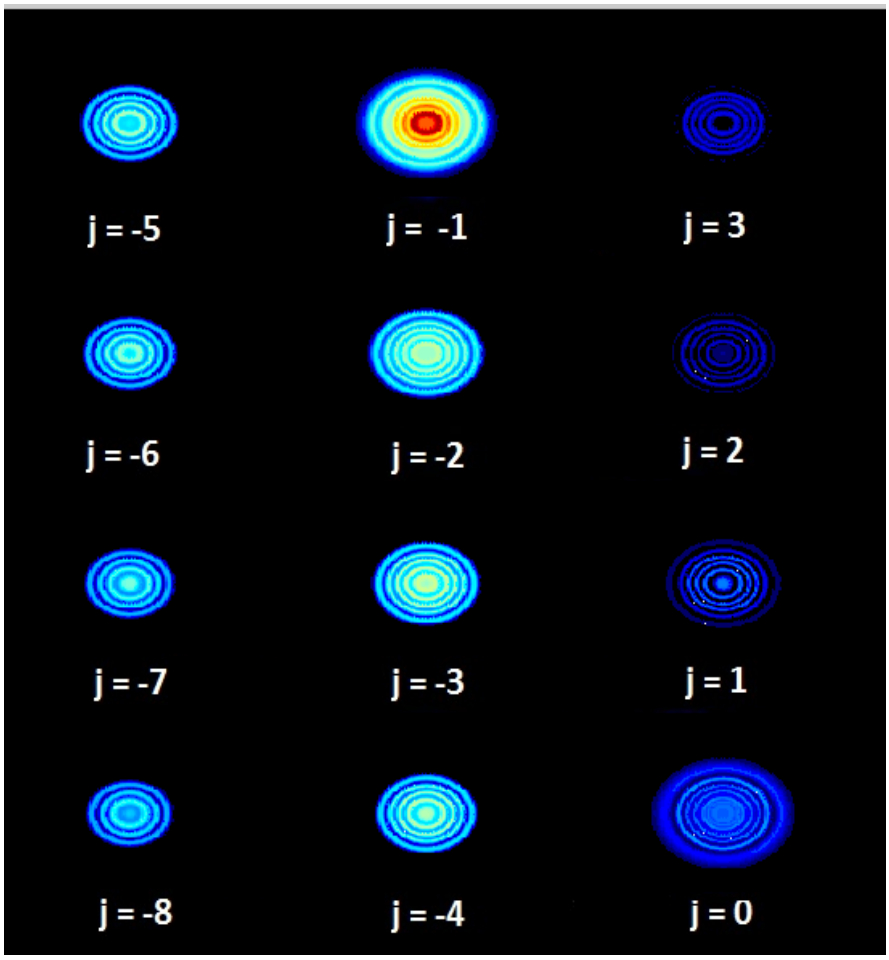


**Figure 9a – Transverse intensity profiles for sidebands ranging from the 8th order Stokes to the 3rd order anti-Stokes sideband. These results were taken after 50 cavity transits with the parameters specified as $Z_c = 0.05$, $L_D = 20$ and $\delta = 0$. It must be noted that the beam profiles are symmetric.**

Figure 9a provides examples of intensity profiles for a range of sideband amplitudes ranging from the 8th order Stokes sideband to the 3rd order anti-Stokes sideband. It is immediately apparent from these results that the Stokes wing of the spectrum carries the most intensity, signified by the brighter rings at the Stokes orders. Each Stokes sideband also possesses a wider beam profile than its anti-Stokes counterpart, the difference in beam diameters occurs because of a combination of the higher intensities present in the Stokes wing of the spectrum, and the frequency dependence of beam diffraction.

Each component of the spectrum shown in figure 9a exhibits multiple rings of alternating high and low intensity which are approximately symmetric around the centre of the transverse axes.

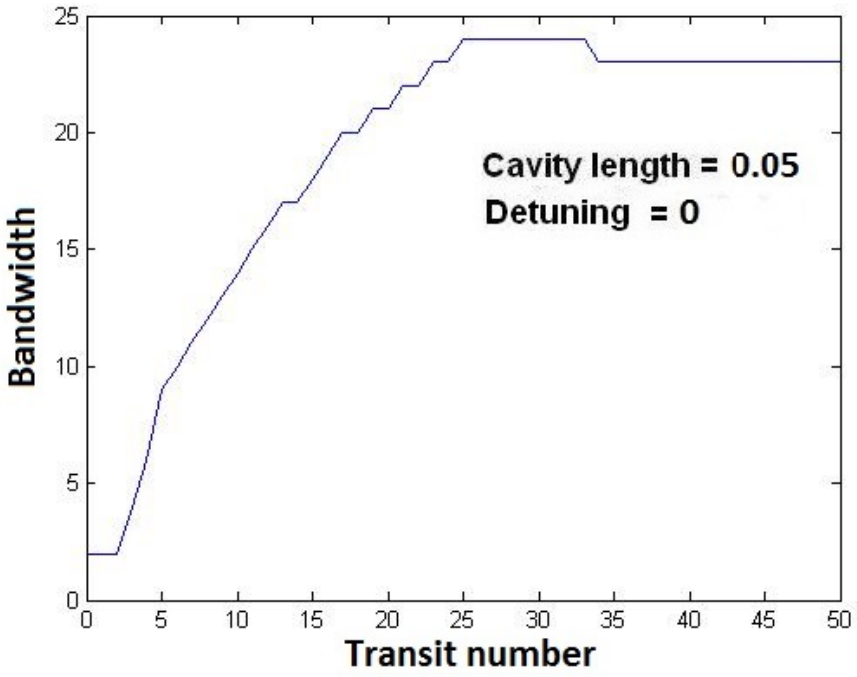


**Figure 9b – The bandwidth reaches a fixed level much like the results given for the plane wave and (1+1)D analysis.**

Figure 9a only shows a limited selection of the sidebands contributing to the level of bandwidth, however, the actual spectrum includes 23 sidebands of comparable intensity. Figure 9b shows the bandwidth generated by the cavity reaching a stable level, of 23 sidebands, after approximately $35$ cavity transits. Comparing the results of figures 9b and 8a, from the previous chapter, shows that the same levels of bandwidth are achieved for (1+1)D and (1+2)D simulations. These results indicate that the addition of a further transverse dimension has very little effect on the overall level of bandwidth growth.

Figures 9c and 9d provide results for the intensity of the multi-frequency beam, generated by the cavity, and its RMS width. Both figures indicate that a high intensity multi-frequency beam, many orders of magnitude larger than the initial pump beam, can be generated, and that the resulting beam reaches a fixed RMS width. These results imply that when the cavity length is much shorter than the beam diffraction length, such that $\frac{Z_c}{L_D} \ll 1$, a multi-frequency beam of fixed intensity and transverse profile can be generated by the cavity.

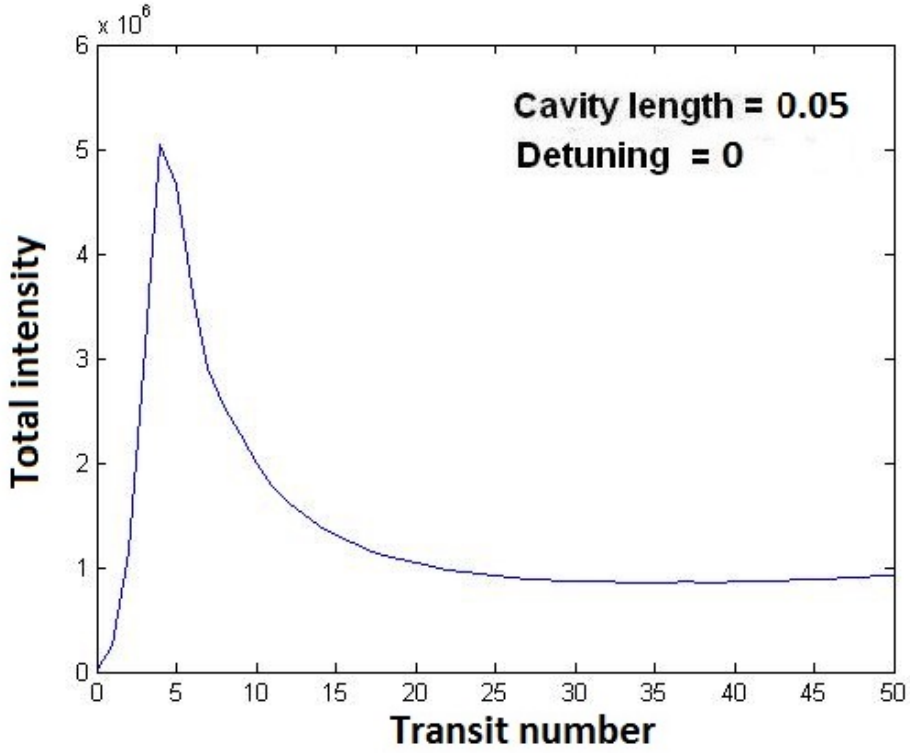


**Figure 9c – The total intensity contained within the multi-frequency beam is far greater than the applied pump intensity and reaches a stable level after 25 cavity transits.**

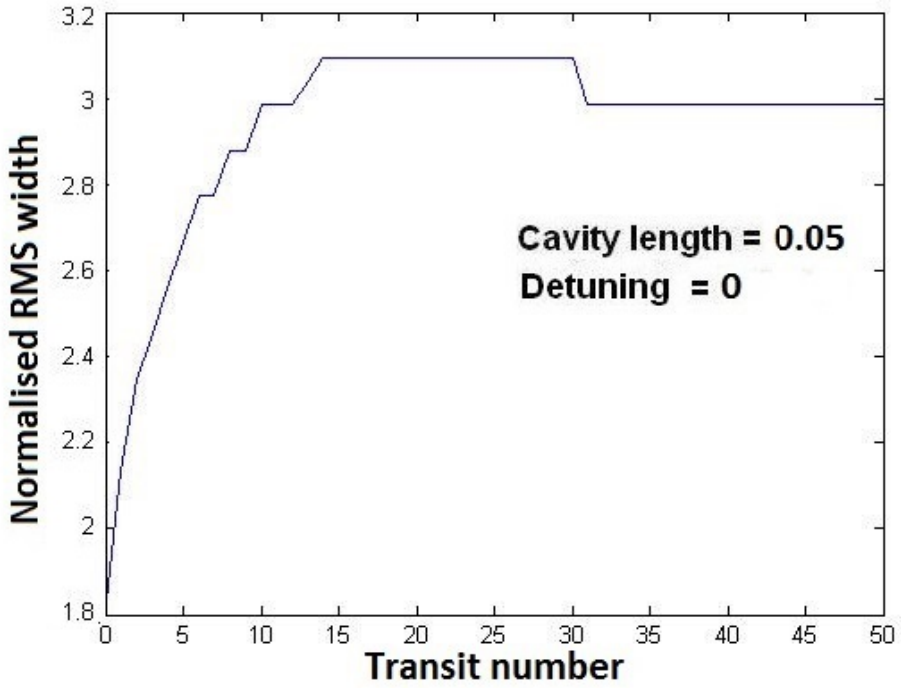


**Figure 9d – The RMS width of the multi-frequency beam reaches a stable level, implying that no further beam diffraction occurs after 35 cavity transits.**

## 9.1 Transverse beam separation

The notion of transverse beam separation was introduced in the previous chapter as a possible way of allowing higher intensity pump beams to be applied whilst avoiding possible damage to the coupling mirror of the cavity.

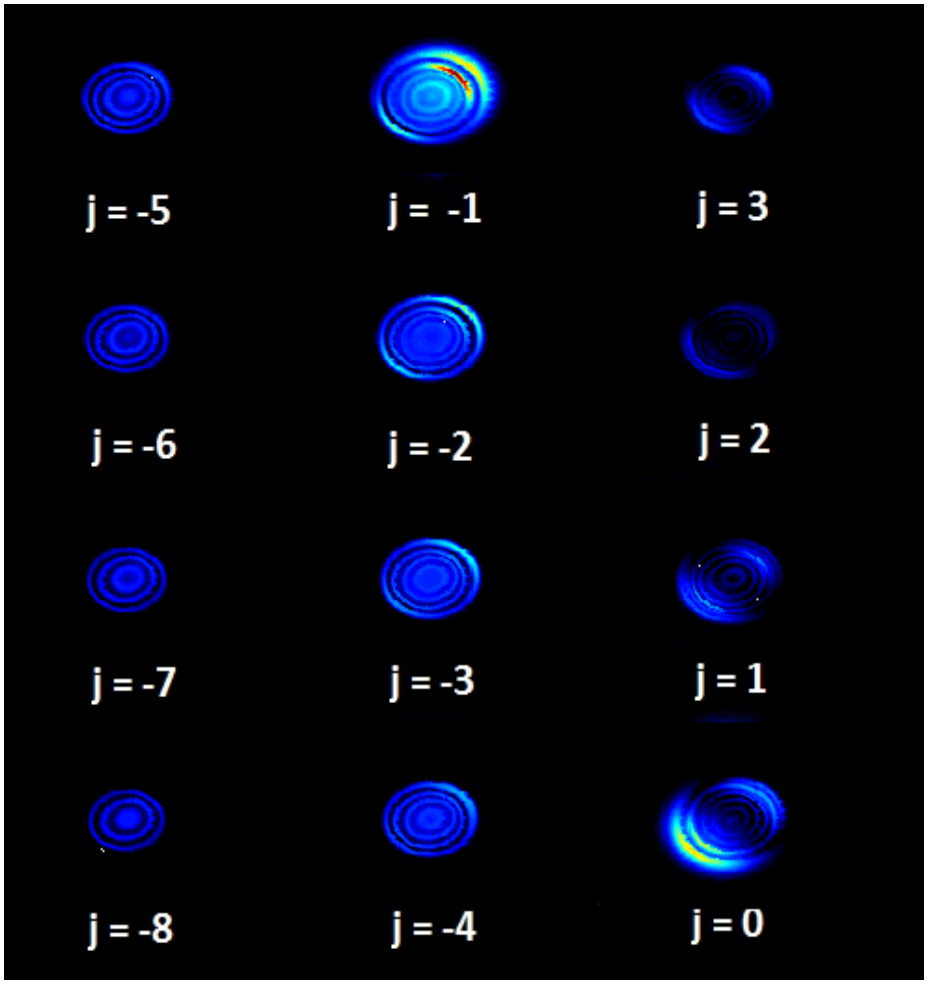


**Figure 9e – Transverse intensity profiles for a range of sidebands ranging from the 8th order Stokes to the 3rd order anti-Stokes sideband. These results were taken after 50 cavity transits with the chosen parameters given as $Z_c = 0.05$, $L_D = 20$ and $\delta = 0$ and an applied beam separation of $0.70$ between the pump and first Stokes beams.**

The results presented in this section are achieved for a relatively large value of beam separation, $L_S = 0.70$. In the case of two transverse dimensions the beam separation corresponds to a radial distance between the peaks of the Gaussian shaped pump beams. Figure 9e includes intensity profiles for a range of sideband amplitudes ranging from the 8$^{th}$ order Stokes sideband to the 3$^{rd}$ order anti-Stokes sideband. These results were achieved using the same parameter regime as the results of figure 9a with the addition of transverse beam separation.

There are some immediately apparent differences between figures 9e and 9a. The results imply that employing finite beam separations produces spectra in which the sideband beam profiles are no longer symmetric, with respect to the centre of the beam axis. Sidebands, such as the first Stokes sideband at $j = -1$, can possess high intensity peaks at the edge of the beams, however, the peaks of each sidebands transverse profile do not overlap, such that the resulting multi-frequency beam has a smoother transverse intensity profile

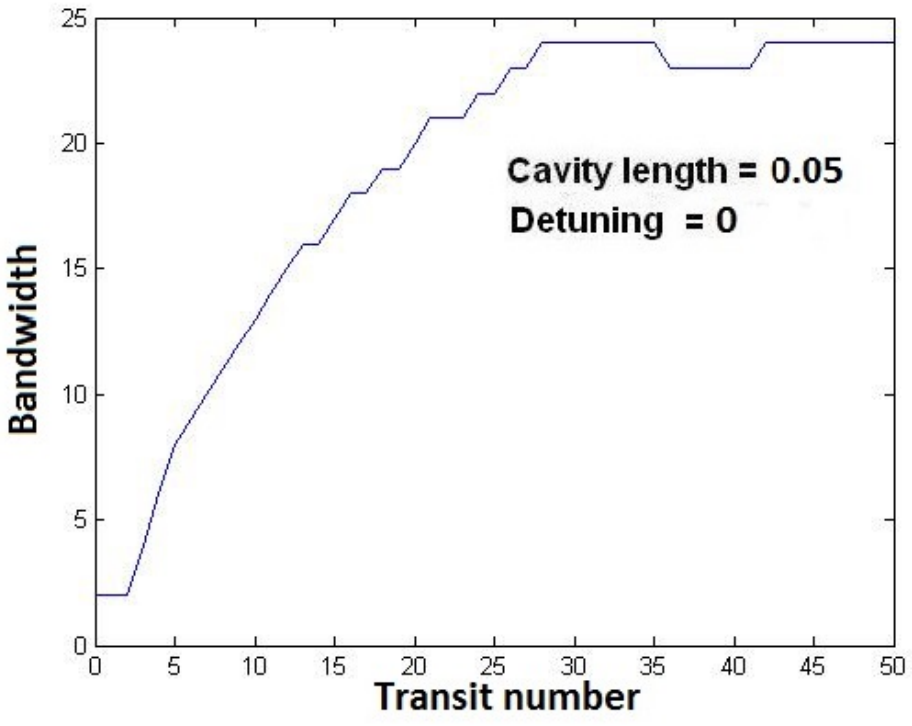


**Figure 9f – With an applied beam separation of $0.70$ the bandwidth still reaches a stable level which is slightly larger than the bandwidth shown in figure 9b.**

Figure 9f shows bandwidth growth within the cavity when the above beam separation is applied and, for the chosen parameter regime, the results show that the introduction of finite levels of beam separation does not affect the overall bandwidth growth rate or final level of bandwidth.

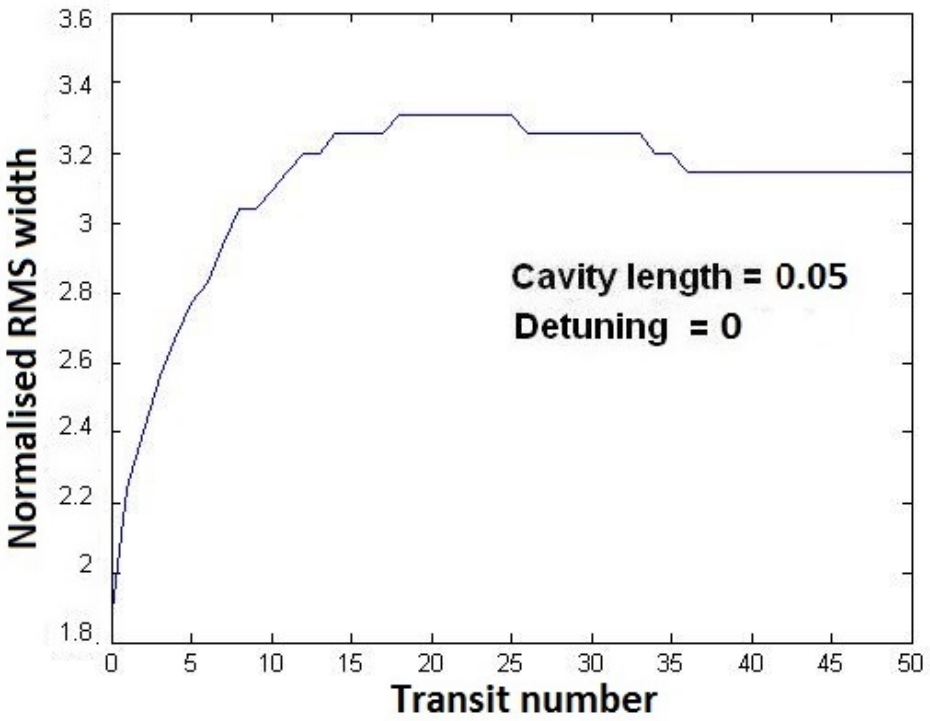


**Figure 9g – With an applied beam separation of $0.70$ the RMS width of the multi-frequency beam reaches a stable level. The final beam width is increased in proportion to the applied beam separation and remains wider than the beam width given in figure 9d.**

The multi-frequency beam generated by the cavity also reaches a maximum RMS width, which depends on the level of beam diffraction and level of applied beam separation. The comparison of figures 9d and 9g shows that beam separation increases the final RMS width in a way which appears to follow the linear increase shown in figure 8h, for the (1+1)D transverse UMRG equations.

# CHAPTER 10

## Linear and nonlinear detuning

The results of previous chapters have not included the effects of nonlinear detuning (Stark shift). Nonlinear detuning, or Stark shift, occurs when the intensities of the pump lasers (and resulting Raman spectra) are large enough to broaden/shift the Raman transition of the medium. This results in non-resonant excitation of the medium, therefore reducing the rate at which Raman scattering events occur.

Throughout the following chapter, the effects of linear and nonlinear detuning will be explored, with specific emphasis on plane wave and transverse non-cavity UMRG.

The detuning, including the nonlinear detuning, is given by the normalised UMRG equations (2.63) as

$$\delta = T_2 \left( \mathrm{I}_0 \left( \frac{\alpha_{22} - \alpha_{11}}{4\hbar} \right) \sum_j A_j A_j^* + \delta\omega \right).$$

The nonlinear component of the detuning is proportional to total multi-frequency intensity, and is scaled by a factor which contains the on-diagonal polarizability tensor components

$$T_2 \mathrm{I}_0 \left( \frac{\alpha_{22} - \alpha_{11}}{4\hbar} \right).$$

An approximate value for the above scaling term can be calculated by using approximate values for the tensor components (which need to be inferred experimentally).

In the case of hydrogen we will choose to specify the value of the polarizability as:

$$\left(\frac{\alpha_{22}-\alpha_{11}}{4\hbar}\right) \approx 3 \times 10^{-4}\, kg^{-1}s^{2}$$

and specifying the level of intensity as $\mathrm{I}_0 = 1\ GWm^{-2}$ and the dephasing time as $T_2 = 2\ ns$ gives the scaling factor for the nonlinear detuning as

$$T_2 \mathrm{I}_0 \left(\frac{\alpha_{22}-\alpha_{11}}{4\hbar}\right) \approx 6 \times 10^{-3}.$$

The nonlinear detuning is a unitless quantity and dimensionally consistent with the UMRG equations.

From the scaling factor and the equation for the total detuning defined above it can be recognised that, for the choice of pump intensity, the nonlinear contribution to the detuning is significantly smaller than the linear contribution. It must be noted that for larger applied pump intensities the level of nonlinear detuning will reach a significant level.

The nonlinear detuning influences the level of medium excitation,

$$P = \frac{1}{(1+i\delta)} \sum_j A_j A_{j-1}^{*}\, e^{-i\gamma_j Z}\ ,$$

such that large levels of detuning reduce the absolute level of medium excitation.

## 10.1 The non-cavity system ($\gamma_1 = 0, \delta\omega = 0$)

The non-cavity system will now be considered in the case of zero dispersion and zero linear detuning. The medium excitation becomes:

$$P = \frac{1}{\left(1 + i\mathrm{T}_2\mathrm{I}_0\left(\frac{\alpha_{22} - \alpha_{11}}{4\hbar}\right)\sum_j A_j A_j^*\right)}\sum_j A_j A_{j-1}^*$$

$$P(Z = 0) = \frac{1}{1+i6\times10^{-3}}.$$

therefore the medium excitation is initially subject to a small level of nonlinear detuning at $Z = 0$. Figure 10a shows that, under the influence of weak nonlinear detuning, the medium excitation amplitude grows as though the total level of detuning is zero. Hence, the data in figure 10a is indistinguishable from the zero dispersion, zero detuning data given earlier in chapter 6.

The matching data for the total intensity, provided in figure 10b, also indicates that small levels of nonlinear detuning have a negligible effect on the non-cavity system.

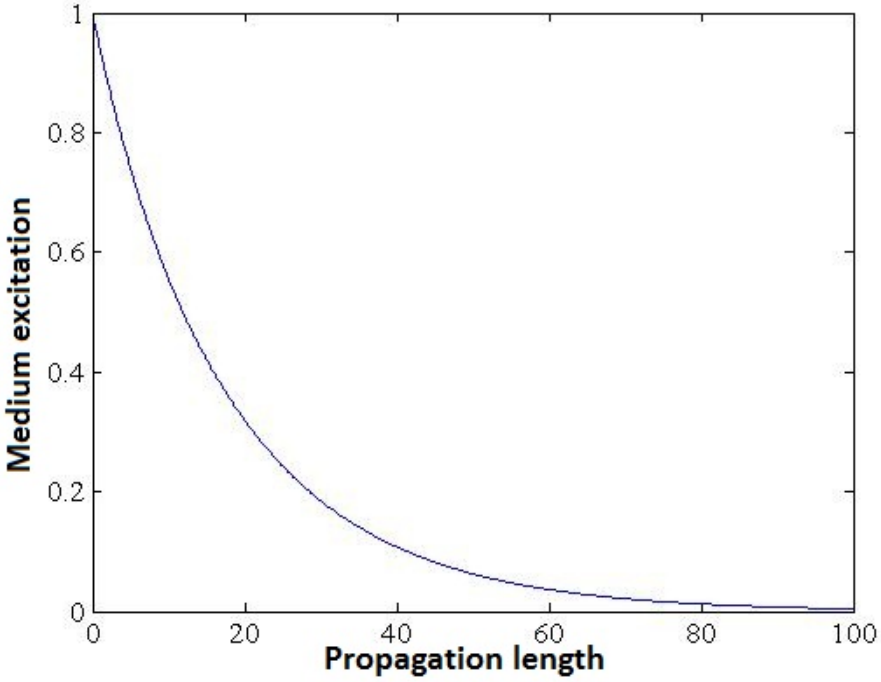


**Figure 10a – The medium excitation amplitude is depleted as sidebands are generated. Although the simulation incorporated a finite level of nonlinear detuning, the results are indistinguishable from the zero detuning results.**

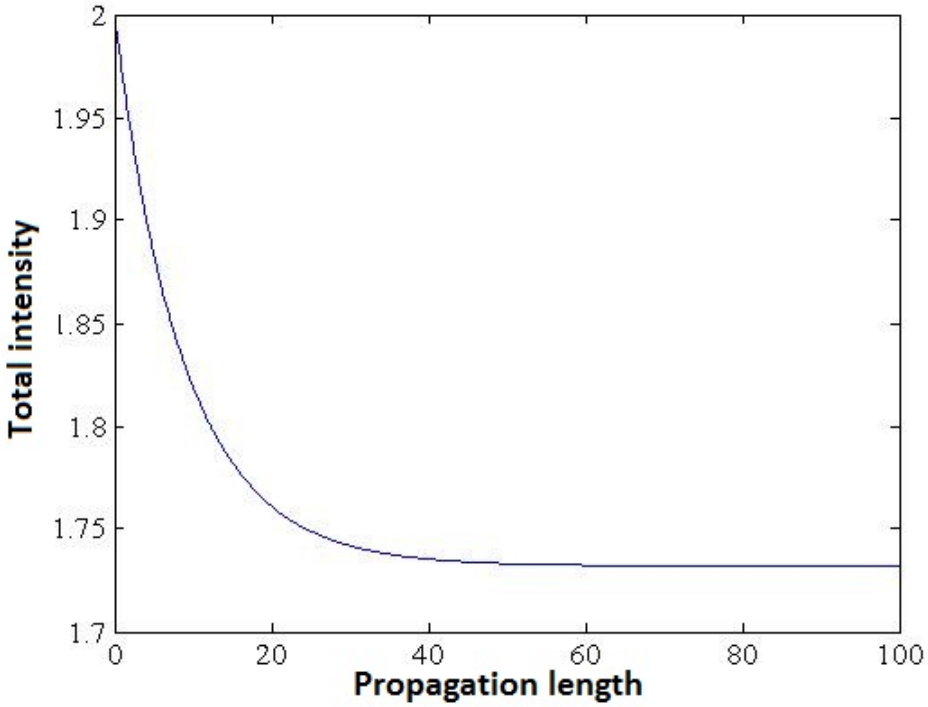


**Figure 10b – The total level of intensity decreases as sidebands are generated. This data is also indistinguishable from the zero detuning results.**

## 10.2 Finite linear and nonlinear detuning

In the absence of nonlinear detuning the medium excitation can be shown to change symmetrically with respect to the sign of the applied level of linear detuning. Figure 10c shows the initial value of the medium excitation, $P(Z = 0)$, for a range of applied linear detuning, varying symmetrically about $T_2\delta\omega = 0$.

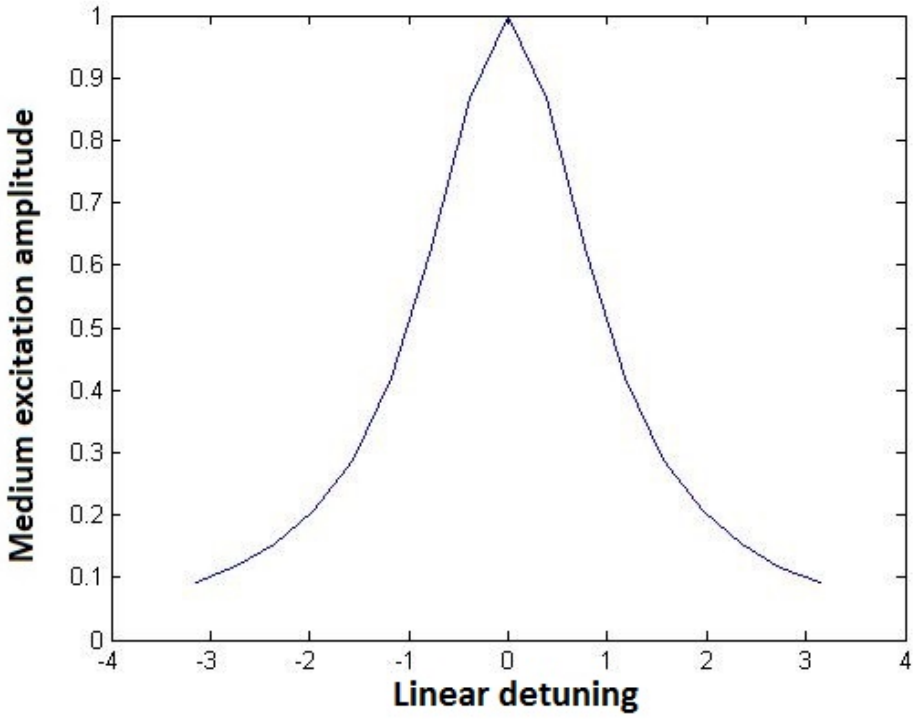


**Figure 10c – The initial level of medium excitation, at $Z = 0$, varies symmetrically with respect to the sign of linear detuning.**

When nonlinear detuning is taken into account the medium excitation can be shown to change asymmetrically with respect to the sign of detuning. Figure 10d shows the variation of $P(Z = 0)$, for much smaller values of linear detuning than those shown in figure 10c.

Asymmetry arises from the positive contribution made by the nonlinear detuning. In other words the maximum level of medium excitation is achieved for a negative value of detuning, $T_2\delta\omega = -6 \times 10^{-3}$, which is equal in magnitude to the nonlinear contribution.

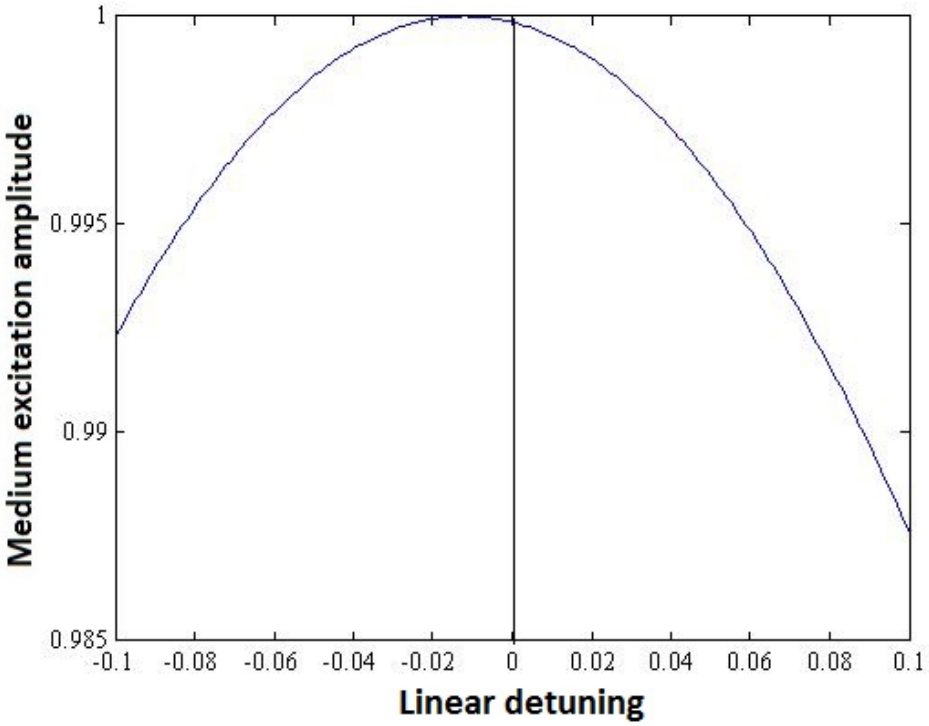


**Figure 10d – The medium excitation amplitude varies asymmetrically with respect to the sign of detuning. The vertical line represents the position of zero linear detuning.**

The maximum rate of sideband growth is also achieved for a linear detuning of $T_2\delta\omega = -6 \times 10^{-3}$ . Therefore specific levels of linear detuning can be chosen to optimise the level of bandwidth, and do so by cancelling out the contributions of the nonlinear detuning. Employing the correct level of linear detuning ensures that the total detuning is close to zero during the initial stages of sideband growth. However, the actual difference in sideband growth rate is almost negligible for weak levels of nonlinear detuning.

Although relatively weak levels of nonlinear detuning have been shown to provide a near negligible contribution to sideband growth, it will be shown throughout the following section that stronger levels of nonlinear detuning, and large intensities, can significantly affect bandwidth growth in the cavity system.

## 10.3 Nonlinear detuning and the cavity system

The nonlinear component of the detuning provides a relatively small contribution to the total level of detuning when compared to the linear component (at least for the chosen level of pump intensity). This means, in terms of the non-cavity results, that nonlinear detuning has an almost negligible effect on bandwidth growth.

This is not the case in the cavity system where large intra-cavity intensities can give rise to a large nonlinear detuning. It is therefore important to consider nonlinear detuning and its effects on bandwidth growth within the cavity. The following results are gathered from simulations which model a cavity mirror with an infinitely broad reflection bandwidth and a uniform value of reflectivity, such that

$$R_j = 0.99,$$

$$j = -\infty, .., -1, 0, 1, \ldots, \infty \, .$$

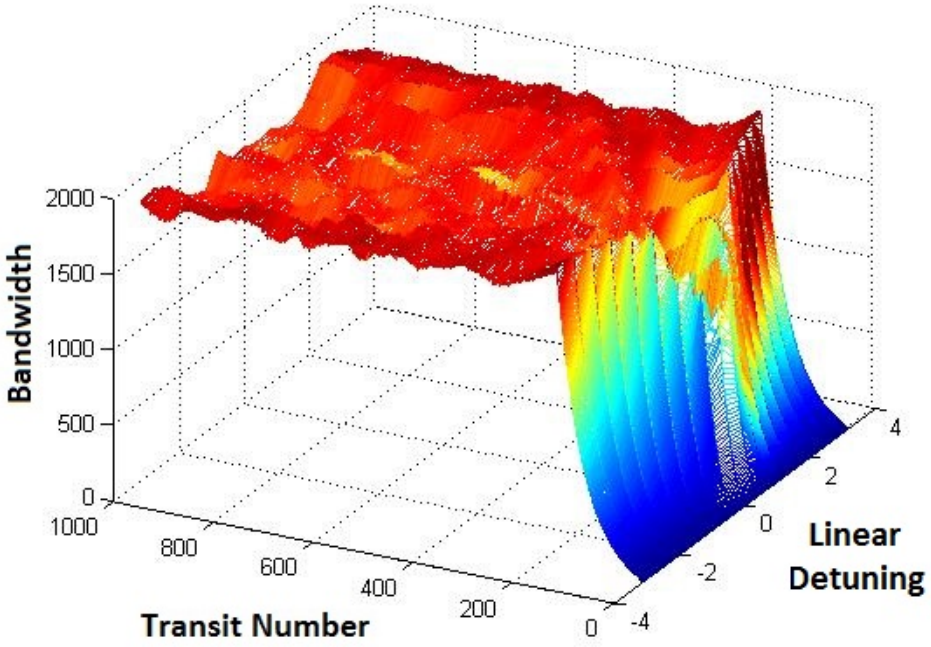


**Figure 10e – Very large bandwidths can be achieved in the cavity for a range of linear detuning. The normalised cavity length is $Z_c = 0.1$, the level of dispersion is zero, $\gamma_1 = 0$. A finite level of nonlinear detuning ($6 \times 10^{-3}$) is also employed.**

It can be shown that large bandwidths can still be generated by the cavity, even under the influence of nonlinear detuning. Figure 10e provides an example of the levels of bandwidth generated in a cavity, with a normalised cavity length of $Z_c = 0.1$, zero dispersion, $\gamma_1 = 0$ and a finite level of nonlinear detuning for a range of applied linear detunings.

The bandwidths shown in figure 10e are similar to results achieved by simulations without nonlinear detuning (recall figure 6a). The levels of bandwidth, and the rate of bandwidth growth, have a slight asymmetric variation with respect to the sign of the applied linear detuning. However, in the case of figure 10e, it is clear that linear detuning has the strongest contribution to the total level of detuning, and therefore determines the rate of sideband growth.

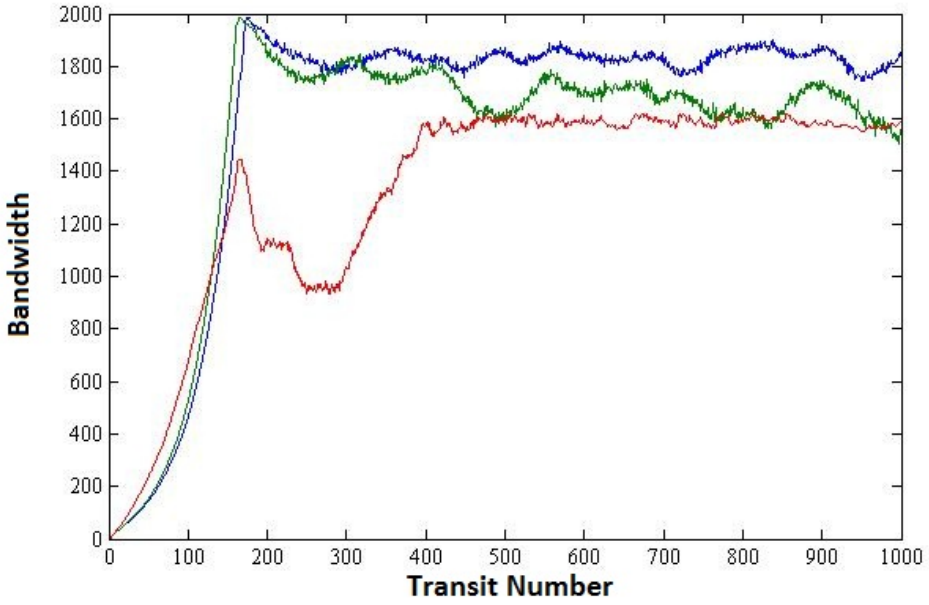


**Figure 10f – Bandwidth growth for three levels of nonlinear detuning, $6 \times 10^{-4}, 6 \times 10^{-3}, 6 \times 10^{-2}$, given as the blue, green and red traces, respectively. The normalised cavity length is $Z_c = 0.1$, and the linear detuning is $T_2 \delta\omega = -3$.**

When greater levels of nonlinear detuning are considered (higher levels of pump intensity) the effects of nonlinear detuning become more pronounced. Figure 10f provides examples of bandwidth growth curves for three levels of nonlinear

detuning, $6 \times 10^{-4}, 6 \times 10^{-3}, 6 \times 10^{-2}$ with a fixed level of linear detuning, $T_2\delta\omega = -3$.

When the levels of nonlinear detuning are increased, the sideband growth rates are attenuated, and the maximum levels of bandwidth are also decreased. This is mirrored in the results of figure 10f which show that the largest levels of bandwidth, and fastest bandwidth growth rates, occur for weaker levels of nonlinear detuning.

As with the non-cavity case, the attenuated bandwidth can be linked with a decreased level of medium excitation amplitude.

## 10.4 Nonlinear detuning and gain suppression

The gain suppression analysis derived in chapter 4, for finite linear detuning, $T_2\delta\omega \neq 0$, can be modified to include nonlinear detuning. This can be achieved by re-defining the detuning parameters, such that

$$\delta = T_2\delta\omega \rightarrow \delta_m = T_2\left(\mathrm{I}_0\left(\frac{\alpha_{22}-\alpha_{11}}{4\hbar}\right)\sum_j A_{j,m}(0)\,A^*_{j,m}(0) + \delta\omega\right),$$

$$D = (1+\delta)^2 \rightarrow D_m = (1+\delta_m)^2 .$$

The re-definition ensures that the detuning depends on the level of multi-frequency intensity defined at the start of each cavity transit. Employing these parameters also redefines the gain parameter, $K^{\pm}$, such that

$$K^{\pm}_m = -\frac{(1+i\delta_m)\left|A_{0,m}\right|^2\varepsilon}{D_m} \pm (\propto_R + i \propto_I) .$$

The real and imaginary contributions, $\propto_R$ and $\propto_I$, to the gain parameter are given as

$$\propto_R = \frac{1}{\sqrt{2}}\left[\left(\frac{(1-\delta_m^2)|A_{0,m}|^4\varepsilon^2}{D_m^2}+\frac{2\gamma_1|A_{0,m}|^2\delta_m}{D}-\gamma_1^2\right)+\sqrt{\left(\frac{(1-\delta_m^2)|A_{0,m}|^4\varepsilon^2}{D_m^2}+\frac{2\gamma_1|A_{0,m}|^2\delta_m}{D_m}-\gamma_1^2\right)^2+\frac{4|A_{0,m}|^4\left(\varepsilon^2|A_{0,m}|^2\delta_m-D_m\gamma_1\right)^2}{D_m^4}}\right]^{\frac{1}{2}},$$

$$\propto_I = \frac{1}{\sqrt{2}}\left[-\left(\frac{(1-\delta_m^2)|A_{0,m}|^4\varepsilon^2}{D_m^2}+\frac{2\gamma_1|A_{0,m}|^2\delta_m}{D_m}-\gamma_1^2\right)+\sqrt{\left(\frac{(1-\delta_m^2)|A_{0,m}|^4\varepsilon^2}{D_m^2}+\frac{2\gamma_1|A_{0,m}|^2\delta_m}{D_m}-\gamma_1^2\right)^2+\frac{4|A_{0,m}|^4\left(\varepsilon^2|A_{0,m}|^2\delta_m-D_m\gamma_1\right)^2}{D_m^4}}\right]^{\frac{1}{2}}.$$

The re-defined gain parameter, given above, now depends on the total intra-cavity multi-frequency intensity of the spectrum. This ensures that the level of gain is directly influenced by intra-cavity sideband growth.

The intensities of the Stokes and anti-Stokes sidebands can suppress exponential Stokes gain by increasing the level of nonlinear detuning. This is in addition to the strong levels of gain suppression already induced by cavity pumping (as discussed in chapters 3 and 4).

However, for relatively weak pump intensities, $I_0$, the nonlinear detuning provides a negligible contribution to the gain parameter, which means that under most parameter regimes it is acceptable to discard the nonlinear component of the detuning altogether.

## 10.5 Linear and nonlinear detuning in transverse UMRG

The above results have shown that nonlinear detuning can influence sideband growth (bandwidth growth), particularly when large initial pump intensities are applied. However, the most interesting aspects of linear and nonlinear detuning are only made apparent when transverse UMRG is considered.

The remainder of this chapter considers the effects of linear and nonlinear detuning on non-cavity (1+1)D transverse UMRG.

When the electric field components possess a finite transverse structure, it can be shown that the nonlinear component of the detuning also takes on a transverse structure, which is proportional to the total multi-frequency intensity, such that

$$\delta_{nonlinear}(x, Z = 0) = 6 \times 10^{-4} J(x, Z = 0)$$

where $J(x, Z = 0)$ is the transverse intensity profile of the multi-frequency beam defined at the beginning of the Raman medium.

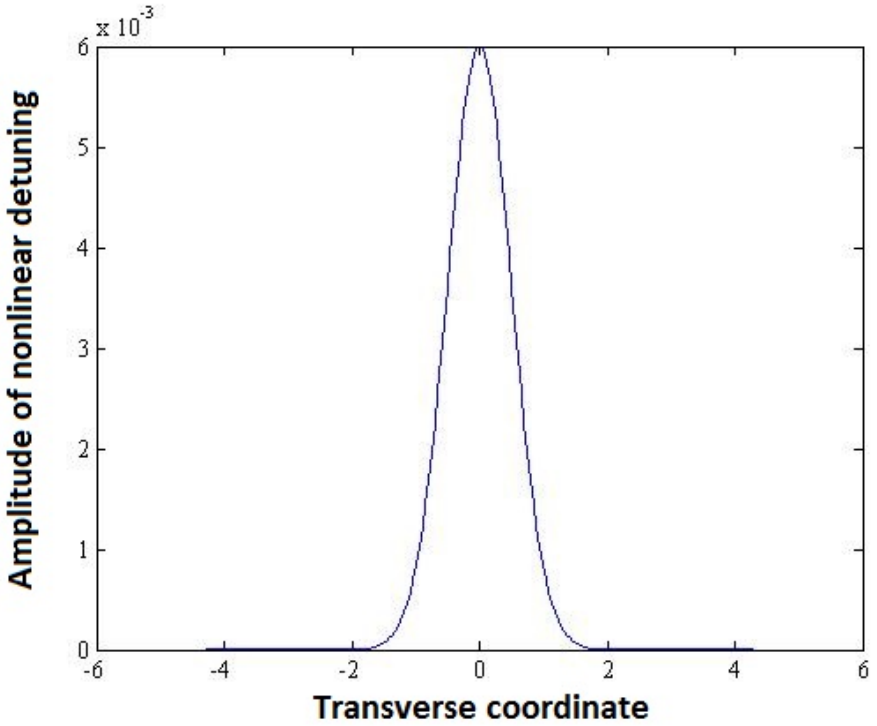


**Figure 10g – The nonlinear detuning has a small magnitude but possesses a finite transverse structure.**

Figure 10g gives an example of the transverse profile of the nonlinear detuning at $Z = 0$, and figure 10h provides an example of the transverse profile possessed by the total detuning when a positive linear detuning is specified.

The results of figures 10g and 10h demonstrate that the nonlinear detuning possesses a finite transverse structure which matches that of the total multi-frequency intensity (but with a much smaller amplitude). The transverse structure also depends on the sign of the applied linear detuning.

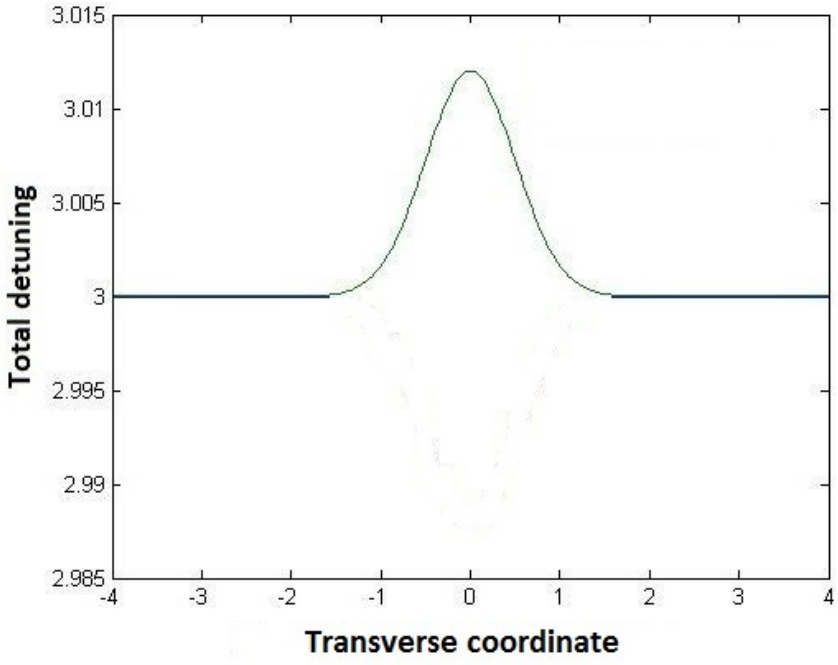


**Figure 10h – This figure provides the magnitude of the total detuning, for a positive level of linear detuning. It is clear that the nonlinear detuning contributes to the transverse structure of the detuning profile.**

When nonlinear detuning is excluded from simulations, the transverse structure of the medium excitation depends entirely on the structure of the sideband amplitudes. However, when nonlinear detuning is taken into account, the medium excitation is also scaled by a term proportional to the total transverse intensity. In this case the medium excitation takes on a transverse structure which can be modified by changing the value of the linear detuning.

The medium excitation at the beginning of the Raman medium is defined as

$$P(Z=0) = \frac{A_0(x,Z=0)A^*_{-1}(x,Z=0)}{1+i(\delta\omega+6\times10^{-4}J(x,Z=0))}.$$

The above equation indicates that the overall structure of the medium excitations transverse profile depends on the total level of detuning. Using the above equation we can calculate the transverse profile of the medium excitation, the results of this are given in figure 10i.

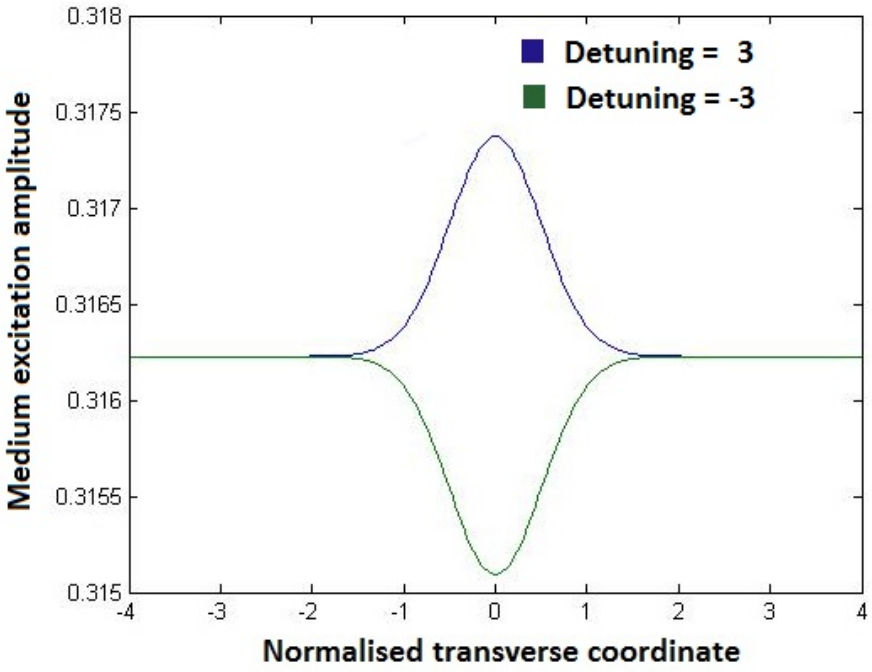


**Figure 10i – The medium excitation shares a profile similar to that of the total detuning given in figure 10h. It is clear that a negative linear detuning can decrease the level of the medium excitation around the centre of the beam axis.**

The results of figure 10i indicate that specifying levels of linear detuning with different signs can alter the shape of the medium excitations transverse profile. A positive level of linear detuning produces a flat transverse profile with a positive peak at the centre of the axis, and a negative detuning produces a flat profile with a depression around the centre of the beam axis.

The nonlinear component of the detuning provides a relatively small contribution to the transverse profile of the total detuning. However, the overall level of detuning can be shown to influence the growth of multi-frequency beam profiles.

Figure 10j gives three examples of transverse multi-frequency beam profiles, for a negative detuning, $T_2\delta\omega = -0.4$, zero detuning, $T_2\delta\omega = 0$, and a positive detuning, $T_2\delta\omega = 0.4$, taken after a normalised propagation distance of $Z = 25$. The normalised level of dispersion and diffraction length, specified for each simulation, are $L_D = 200$, and $\gamma_1 = 0$.

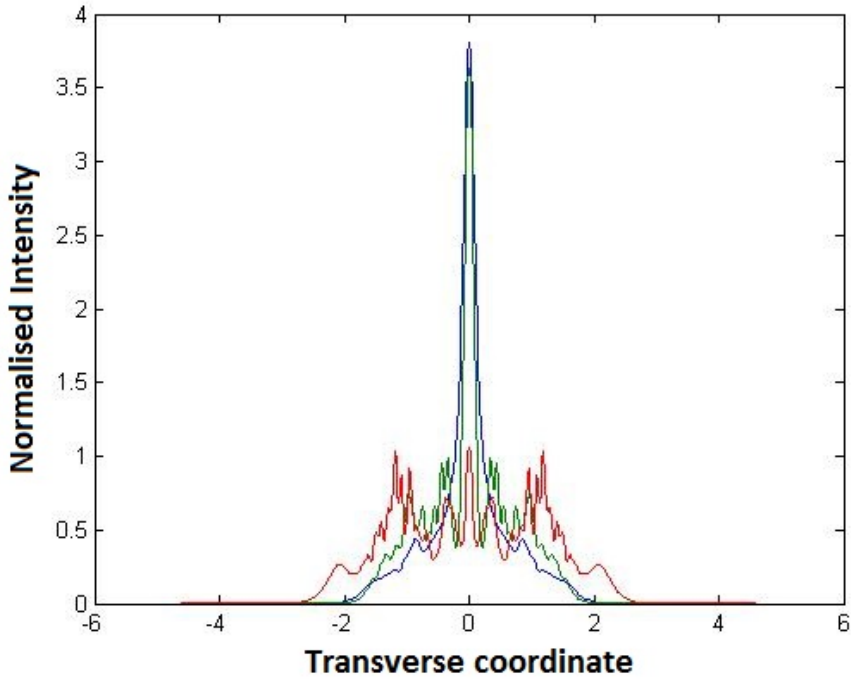


**Figure 10j – This figure presents, multi-frequency, transverse intensity profiles for three levels of detuning, $T_2\delta\omega = -0.4$ (blue trace), $T_2\delta\omega = 0$ (green trace) and $T_2\delta\omega = 0.4$ (red trace). The narrowest and broadest profiles occur for negative and positive detuning, respectively.**

The three specified levels of detuning, given above, result in the generation of multi-frequency beams with vastly different transverse intensity profiles. The results show that a level of negative detuning produces a beam profile which is narrower than the zero detuning case, and conversely, a positive detuning produces a multi-frequency beam with a much broader transverse profile.

The three profiles given in figure 10j have RMS widths of 2.7840 (blue trace, $T_2\delta\omega = -0.4$), 2.9760 (green trace, $T_2\delta\omega = 0$) and 4.4640 (red trace, $T_2\delta\omega = 0.4$). The profiles beam widths indicate an asymmetric relationship between the sign of the applied linear detuning and the width of the multi-frequency beam.

The effects of detuning can be explored further by considering the transverse intensity distribution of sidebands contributing to the total multi-frequency beam. Figures 10k, 10l and 10m represent the transverse intensity distribution of the spectra which contribute to the multi-frequency intensity profiles given in figure 10j. Hence, figures, 10k, 10l and 10m represent sideband spectra generated after a propagation distance of $Z = 25$ for a negative detuning, $T_2\delta\omega = -0.4$, zero detuning, $T_2\delta\omega = 0$, and a positive detuning, $T_2\delta\omega = 0.4$.

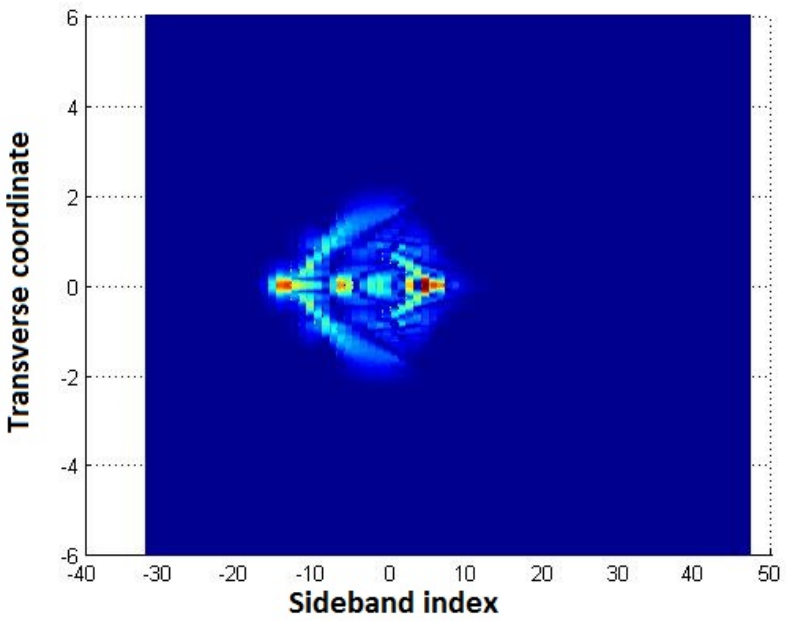


**Figure 10k – This figure represents the transverse intensity profile of each sideband. The sideband index represents each order of Stokes, $j < 0$, and anti-Stokes, $j > 0$, sideband. The results are taken after a normalised propagation distance of $Z = 25$, for a diffraction length of $L_D = 200$ and linear detuning, $T_2\delta\omega = -0.4$.**

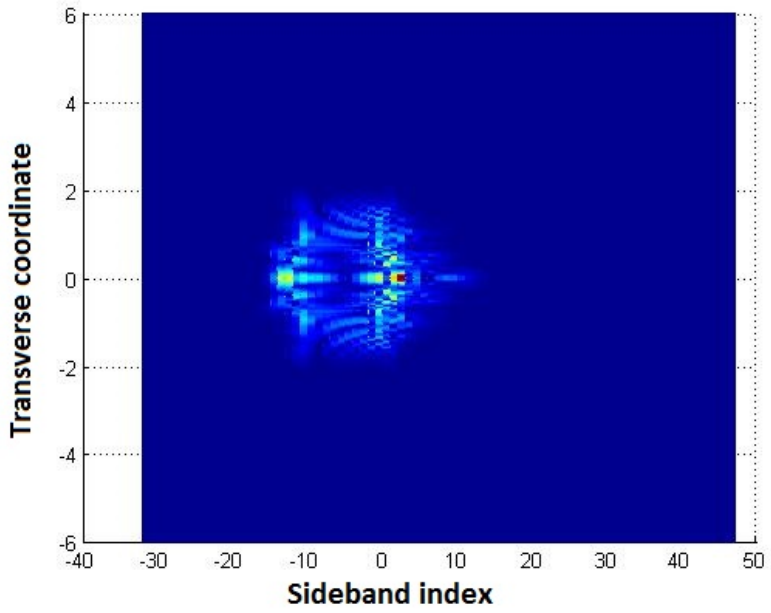


**Figure 10l – This figure represents the transverse intensity profile of each sideband. The sideband index represents each order of Stokes, $j < 0$, and anti-Stokes, $j > 0$, sideband. The results are taken after a normalised propagation distance of $Z = 25$, for a diffraction length of $L_D = 200$ and linear detuning, $T_2\delta\omega = 0$.**

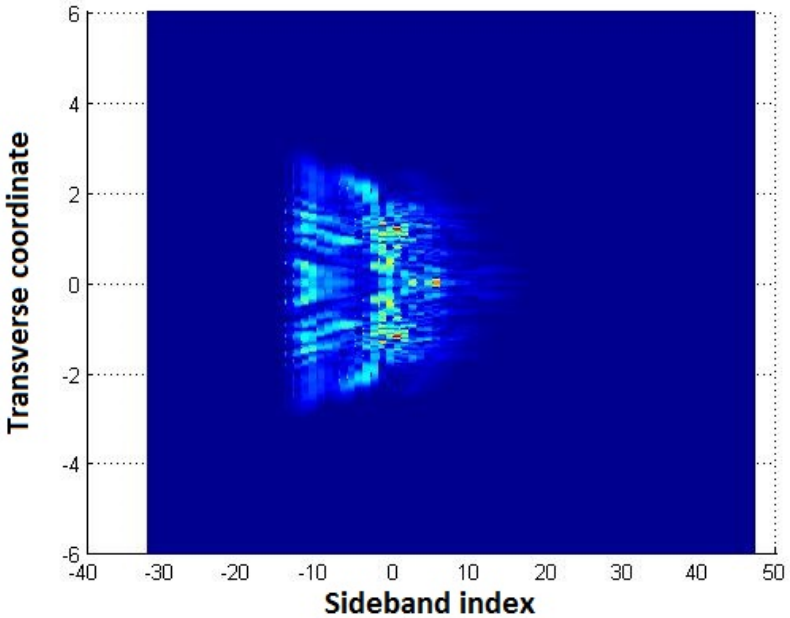


**Figure 10m – This figure represents the transverse intensity profile of each sideband. The sideband index represents each order of Stokes, $j < 0$, and anti-Stokes, $j > 0$, sideband. The results are taken after a normalised propagation distance of $Z = 25$, for a diffraction length of $L_D = 200$ and linear detuning, $T_2\delta\omega = 0.4$.**

The spectra shown in figures 10k, 10l and 10m contain roughly the same number of sideband components, however, each spectra has a unique shape which is determined by the sign of the applied linear detuning.

In the case of negative detuning, shown in figure 10k, the highest order sidebands have the narrowest transverse profiles with high intensity peaks located at the centre of the axis. The lower order sidebands have much wider beam profiles with a more even intensity distribution across the transverse plane.

When no linear detuning is employed the spectrum takes on a different form, shown in figure 10l. The results of figure 10l show an even distribution of energy between each wing of the sideband spectrum and that each sideband, except for sidebands located on the very edge of the spectrum, possesses a similar transverse intensity profile.

A positive detuning gives rise to a spectrum of sidebands with extremely broad transverse intensity profiles. The broadest profiles occur at high order Stokes sidebands and the narrowest occur at higher order anti-Stokes sidebands. In the specific case of figure 10m each sidebands transverse profile consists of several, evenly distributed, high intensity peaks.

## 10.6 Beam narrowing and beam broadening

Reference (85) presents theoretical and experimental results which indicate that Raman self focussing (and defocusing) can occur in an adiabatically pumped Raman medium. The results were achieved by employing two circularly, and oppositely, polarised pump beams (pump and first Stokes) to adiabatically pump the medium for a maximum level of coherence. The pump beams were chosen to be oppositely polarised to inhibit the generation of higher order Stokes and anti-Stokes radiation. The results, given in reference (85), show that beam narrowing (self focussing) occurs when positive levels of detuning are specified, and that beam broadening (self defocusing) also occurs for negative levels of linear detuning.

The authors attributed self focusing to the transverse structure and sign of the molecular excitation amplitude, which can be either in phase or in anti-phase with respect to the two photon driving amplitude (85), and contributes to the refractive index of each frequency component (which varies transversely).

Two-frequency simulations (including only the pump and first Stokes amplitudes) of the steady state transverse UMRG equations have been found to be in agreement with the experimental results given in reference (85). The results of such simulations show that positive (negative) levels of linear detuning can decrease (increase) the RMS width of a two-frequency beam during propagation through the Raman medium. Variation in the RMS width is demonstrated in figure 10n, where the RMS beam width is taken after a propagation distance of $Z = 25$, for a range of positive and negative linear detunings.

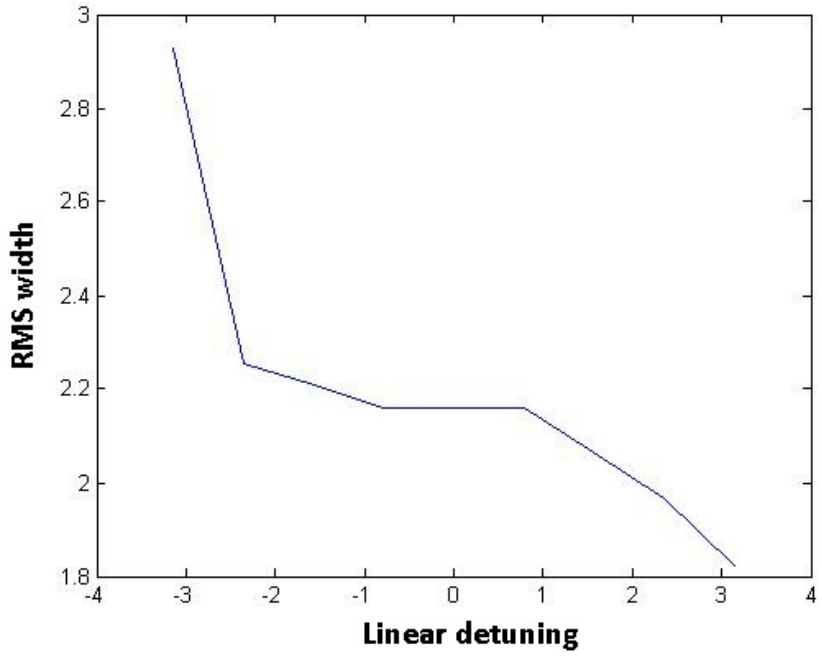


**Figure 10n – Two-frequency simulations yield results for the RMS width of a two-frequency beam taken, after a distance normalised distance of $Z = 25$, for a range of applied levels of linear detuning.**

The results of figure 10n show a variation with respect to detuning which is in agreement with the results given in reference (85). If the multi-frequency results of section 10.5 are considered, it can be recognised that levels of positive and negative detuning have opposite effects on two-frequency (pump, and first Stokes) and multi-frequency beams.

The above statement can be clarified further by considering the RMS widths of multi-frequency beams, achieved in multi-frequency simulations of transverse UMRG. Figure 10o covers a smaller parameter regime than figure 10n but demonstrates that a negative (positive) detuning causes the generation of a multi-frequency beam which is narrower (wider) than a beam achieved for zero detuning.

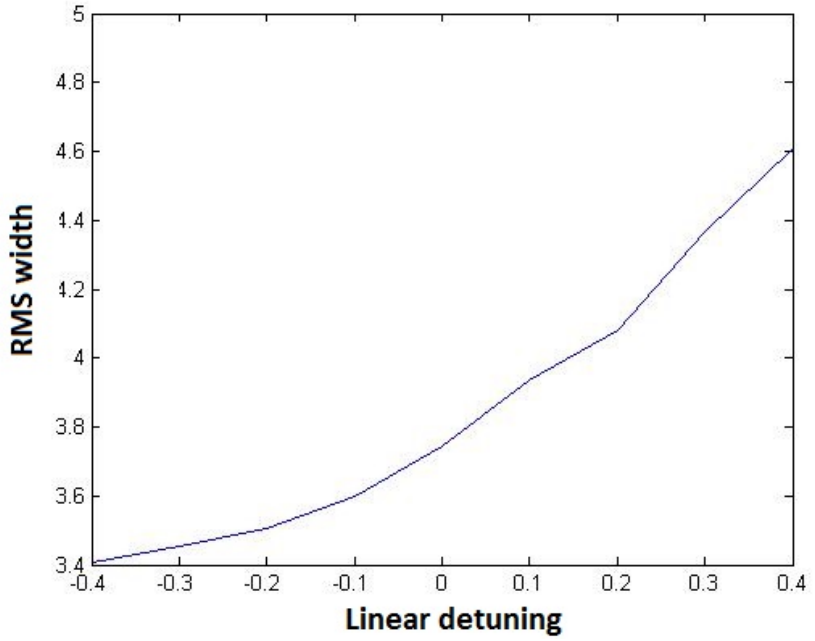


**Figure 10o – Multi-frequency simulations yield results for the RMS width of the multi-frequency beam, taken after a normalised distance of $Z = 25$, for a range of applied levels of linear detuning.**

The difference in results between the two-frequency and multi-frequency beams arises from phase contributions of each sideband to the medium excitation. When positive and negative levels of detuning are employed, the medium excitation amplitude evolves to have substantially different transverse profiles, such that a negative (positive) detuning causes large intensities build up at the centre (edge) of the beams transverse profile.

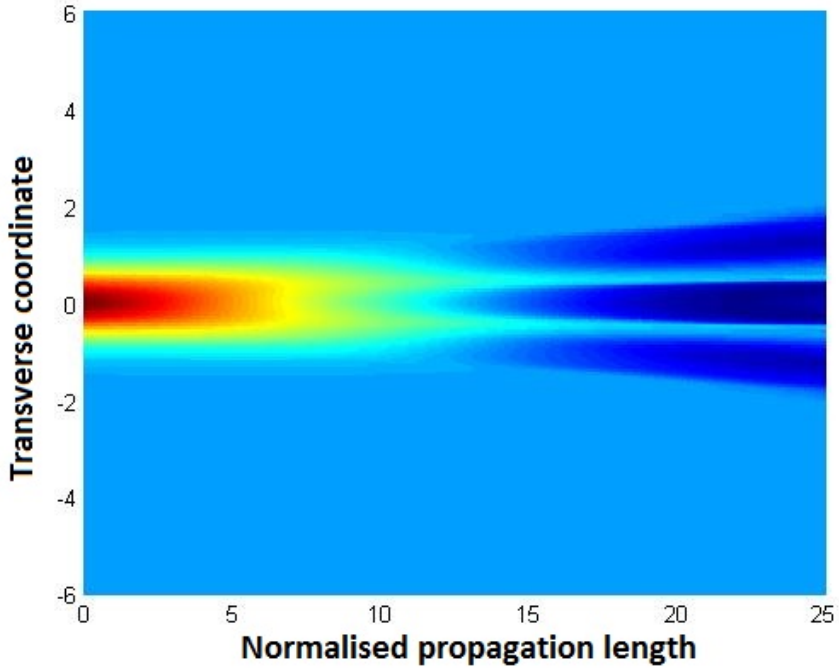


**Figure 10p – When a negative linear detuning, $T_2\delta\omega = -0.4$, is employed the medium excitation amplitude remains axially confined during propagation, over a normalised distance of $Z = 25$.**

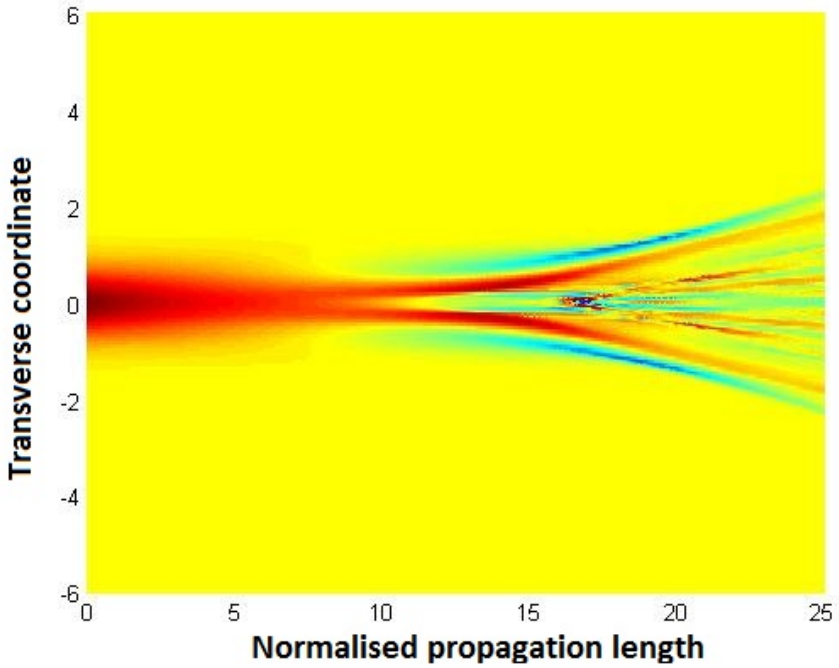


**Figure 10q – When a positive linear detuning, $T_2\delta\omega = 0.4$, is employed the medium excitation amplitude carries large peaks at the edge of the transverse beam, over a normalised distance of $Z = 25$.**

Figures 10p and 10q show how the transverse profile of the medium excitation amplitude (real component) evolves over a normalised propagation distance of $Z = 25$ for $T_2\delta\omega = -0.4$ and $T_2\delta\omega = 0.4$, respectively.

A positive value of detuning causes the generation of a medium excitation with large peaks at the edge of its transverse structure, and therefore drives the generation of sidebands with large transverse profiles

A negative value of detuning causes the generation of a medium excitation with a peak centred on the transverse axis. In this case, the medium excitation drives the generation of sidebands with peak intensities which are confined to the centre of the transverse axis.

The results given above show a strong level of agreement with the experimental results of reference (85) and indicate that beam focussing and defocusing can occur in the steady state regime (as well as the adiabatic regime (85)). The results also show that beam focusing and defocusing can influence sideband growth and the RMS width of the resulting multi-frequency beam.

The closing sections of this chapter represent the foundations for further work to be carried out in the area of transverse UMRG and cavity enhanced transverse UMRG, which will now be discussed in the concluding chapter.

# CHAPTER 11

## Conclusion

To conclude this thesis two questions will be answered: what are the main achievements of this thesis, and what further work can be achieved.

In answer to the first question we can begin by listing the main achievement in the order in which they occur throughout this thesis.

1) The normalised plane wave steady state UMRG equations have been derived in Bloch form, resulting in a set of coupled (parametric and non-parametric coupling) envelope equations. The envelope equations are accompanied by medium equations which describe the strength of the medium excitation, which drives sideband growth, and the population dynamics of the Raman transition.

   The transverse Raman equations are stated and the accompanying, frequency dependent, diffraction lengths specified and normalised in terms of the gain length product of the Raman transition.

2) Advanced numerical methods have been applied for the solution of the UMRG equations. Detailed descriptions of the methods have been provided in appendix B, they have been left out of the main thesis to save space and allow continuity between chapters.

   The numerical methods required for the simulation of the transverse (1+1)D and (1+2)D equations have been discussed in detail. Specific emphasis has been placed on the 3$^{rd}$ order Runge-Kutta method, Crank-Nicolson finite difference method and the alternating direction implicit (ADI) finite difference method.

The splitting of the transverse UMRG equations into their linear and nonlinear components has been described in detail. Each finite difference method, required for the integration of the linear components of the UMRG equations, has been derived in the form of tridiagonal matrix equations.

An example of the 3rd order Runge-Kutta and ADI integration routines have also been provided in appendix B, together with a discussion on their implementation regarding the full (1+2)D transverse integration code.

3) A gain suppression analysis has been derived which captures the growth of a three wave subsystem of the UMRG equations in terms of parametric gain. The analysis constitutes a set of linear solutions the subset of the UMRG equations involving the pump, first Stokes and first anti-Stokes sidebands. The gain parameter is found to be a function of medium and cavity parameters, and defines the level of sideband amplification within the cavity.

   An approximate form of the gain suppression equations has been found in the small dispersion regime, which yields a set of recurrence relations. The approximate solutions can be used to describe how parametric Stokes gain and sideband growth are suppressed in the cavity boundary conditions. In the limit of $R_0 = 1$ the Stokes amplitude has been shown, analytically and numerically, to reach a steady state. In the limit $R_0 < 1$ the Stokes intensity has also been shown to reach peak value, after which the intensity decreases as a function of reflectivity, to zero intensity.

   The limits of the gain suppression analysis have been studied in terms of a range of parameters. The analysis has been shown to break down for parameter regimes which produce high intensity sidebands, specifically in the regimes of large levels of normalised dispersion, long cavity lengths and large Stokes seed amplitudes. The breakdown of the analysis has been described in terms of the nonlinearity of UMRG and non-parametric growth mechanisms.

4) The cavity gain suppression analysis has been extended to include finite levels of linear detuning and captures the affect of detuning on the gain parameter. An approximate solution has been derived for the small dispersion regime which exhibits similar results to the zero detuning derivation, except for a scaling factor proportional to the inverse of the detuning squared.

   The form of the gain parameter suggests that Stokes gain can be optimised by the choice of specific levels of linear detuning. However, it has been shown that, in the case of the cavity system, pumping drives the gain parameter off its optimum level within a few cavity transits.

5) Multi-frequency simulations of the cavity system, with only a single pump beam, have been discussed. Results have been presented which show the single pump system to be incapable of generating sufficient bandwidth to support the synthesis of femtosecond pulses. The gain suppression analysis has been shown, for certain parameter regimes, to accurately describe some of the main results of the multi-frequency simulations.

6) Multi-frequency simulations of UMRG in a symmetrically pumped cavity have shown that very large bandwidths can be achieved which can cover many octaves.

   The choice of cavity mirror reflectivity and the product of normalised dispersion and cavity length have been shown to be the main parameters which limit the maximum level of bandwidth. Results have also been presented which indicate that the bandwidth, and intensity of the resulting spectrum, can be optimised by finite levels of linear detuning and non-unity pumping ratios (non-symmetric pumping).

7) Realistic cavity mirror profiles have been modelled, and the results of multi-frequency simulations have shown the cavity to be capable of generating a spectrum of high intensity sidebands (covering the reflection bandwidth of

the mirror). The best results have been achieved for cavities of with relatively short normalised cavity lengths, where the cavity length can be several orders of magnitude shorter than typical non-cavity Raman experiments.

Spectra generated by the cavity have been shown to be suitable for the synthesis of trains of pulses with gigahertz repetition rates. Examples of pulses have been provided which have durations ranging from tens of attoseconds in duration to a few femtoseconds. Such pulses can have peak powers, ranging from tens of gigawatts to a few terawatts, and low average powers. The duration and power of such pulses have been shown to depend on the level of applied pump intensity, normalised dispersion, linear detuning and pumping ratio. It has been shown that limited reflection bandwidths of current commercially available coupling mirrors restricts the minimum achievable duration and intensity of pulses generated by the cavity.

In the ideal case, with a coupling mirror with an ultra-broadband reflectivity profile and zero medium dispersion, the cavity has been shown to be capable of generating sufficient bandwidth to support the synthesis of ultra-short pulses, $\sim 60$ attoseconds, with very high peak power densities $70\ TWcm^{-2}$.

8) A hybrid Runge-Kutta / finite difference method has been employed for the simulation of the (1+1)D and (1+2)D transverse UMRG equations. Results of simulations have demonstrated the generation of stable frequency spectra, with each sideband possessing a complex transverse structure and a large total intensity.
   The structure of each sideband's transverse profile has been shown to occur as a result of the transverse variation of the medium excitation variable, and the level of diffraction experienced by the multi-frequency beam.

The results have also demonstrated that in particular parameter regimes, such as long diffraction lengths and short cavity lengths, the resulting multi-frequency beam can reach a fixed RMS width and intensity profile. This has been shown to occur because of pumping and losses at the coupling mirror, which results in the largest levels of intensity occurring at the centre of the beam axis.

9) Nonlinear detuning has been shown to have little effect on the levels of bandwidth generated by the non-cavity and cavity systems, unless very large pump intensities are employed (nonlinear detuning is proportional to the pump intensity, $I_0$).

   Results of simulations of non-cavity transverse UMRG have demonstrated that beam narrowing and broadening can be induced by finite levels of linear detuning. Simulations which include only two frequency components (pump and first Stokes) show that beam narrowing (broadening) occurs for positive (negative) levels of linear detuning, whereas, multi-frequency simulations demonstrate a relationship which is opposite to the two-wave case.

In summary the plane wave analysis of cavity enhanced UMRG has been shown to be capable of generating bandwidths suitable for the synthesis of ultra-short pulses of high peak power and gigahertz repetition rates (equal to the Raman transition frequency). The results of transverse UMRG have been shown to offer agreement with the plane wave results, even when moderate levels of beam diffraction are considered.

Possible further work in extension to the work presented in this thesis includes

1) Further characterisation of non-cavity and cavity transverse UMRG in terms of medium and cavity parameters, diffraction and transverse beam separation. The effects of curved cavity mirrors and the resulting beam focusing and defocusing also need to be considered.

2) Nonlinear and linear detuning also needs further consideration in terms of Raman self focusing and defocusing effects. The effects of detuning on cavity enhanced transverse UMRG is of particular interest, where beam focusing could offset the diffraction of the resulting multi-frequency beam.

3) The plane wave results could be extended to cover various Raman media, or other discrete transitions in hydrogen and atmospheric nitrogen. The aim is to further generalise the conclusions made in this thesis. A broad selection of suitable Raman media would enable peak pulse powers, repetition rates and pulse durations to be tailored, and optimised, for specific applications. Femtosecond pulses could be made available which have central wavelengths ranging from the infra-red to the ultra-violet regions of the electromagnetic spectrum.

4) Transient UMRG in the ring cavity context could also be analysed with specific emphasis on the highly transient regime $t_p \ll T_2$ where few nanosecond pulses are used to pump the Raman medium. The analysis could also then be extended to include population dynamics of the exploited Raman transition, therefore capturing dynamical medium effects.

As a final note, it has been made clear throughout this thesis that to achieve the shortest possible pulses using cavity confined UMRG (possibly of attosecond duration), cavity mirror technology requires further developments to produce dielectric cavity mirrors with much broader reflectivity profiles.

Such developments have been made to produce optical components suitable for use with other femtosecond laser systems, such as the Ti:sapphire laser. If similar efforts are placed on the development of mirror coatings suitable for cavity enhanced UMRG then the synthesis of trains of high power pulses, of attosecond duration, could be made possible.

# APPENDIX A

Equations (2.61) are more easily integrated in their dimensionless form.

Choosing:

$$F_j(z,t) = F_0(0,0)A_0(z,t) = F_0A_0\,, \tag{A.1}$$

$$\beta = \frac{\omega_0 \pi N \alpha_{12}}{c}\,, \tag{A.2}$$

and defining the gain length product as:

$$Z = \mathrm{g}|F_0|^2 z = \mathrm{gI_0 z}\,. \tag{A.3}$$

The field equation from equations (2.61) can be re-written in terms of A.2 and A.3 as:

$$\mathrm{gI_0}\frac{\partial A_j}{\partial Z} = \beta\frac{\omega_j}{\omega_0}\left[q^* A_{j+1}e^{-i\frac{\Delta_{j+1}}{\mathrm{gI_0}}Z} - qA_{j-1}e^{i\frac{\Delta_j}{\mathrm{gI_0}}Z}\right], \tag{A.4}$$

where the normalised mistuning can be defined as:

$$\gamma_j = \frac{\Delta_j}{\mathrm{gI_0}}\,, \tag{A.5}$$

$$\mathrm{gI_0}\frac{\partial A_j}{\partial Z} = \beta\frac{\omega_j}{\omega_0}\left[q^* A_{j+1}e^{-i\gamma_{j+1}Z} - qA_{j-1}e^{i\gamma_j Z}\right]. \tag{A.6}$$

Through the selection of:

$$q = CP(Z,t) \tag{A.7}$$

and using equations A.1-A.5 the equation for the medium dynamics of the system (2.61) can be re-written as:

$$\left(\frac{T_2}{t_p}\right)\frac{\partial P}{\partial \tau} = -(1+i\delta)P + \frac{\alpha_{12}T_2\mathrm{I_0}}{2\hbar C}\sum_j A_j A_{j-1}^*\, e^{-i\gamma_j Z}\,, \tag{A.8}$$

and if the units are chosen such that $\frac{\alpha_{12}T_2\mathrm{I_0}}{2\hbar C} \equiv 1$ hence $C = \frac{\alpha_{12}T_2\mathrm{I_0}}{2\hbar}$ and equations A.6 and A.8 become:

$$\mathrm{gI}_0 \frac{\partial A_j}{\partial Z} = \beta C \frac{\omega_j}{\omega_0}\left[P^* A_{j+1} e^{-i\gamma_{j+1}Z} - P A_{j-1} e^{i\gamma_j Z}\right], \qquad \text{A.9}$$

$$\left(\frac{T_2}{t_p}\right)\frac{\partial P}{\partial \tau} = -(1+i\delta)P + \sum_j A_j A_{j-1}^* \, e^{-i\gamma_j Z} \, . \qquad \text{A.10}$$

Choosing the units such that $\mathrm{gI}_0 \equiv 2\beta C$ so that the field equation takes its final dimensionless form:

$$\frac{\partial A_j}{\partial Z} = \frac{\omega_j}{2\omega_0}\left[P^* A_{j+1} e^{-i\gamma_{j+1}Z} - P A_{j-1} e^{i\gamma_j Z}\right] \, . \qquad \text{A.11}$$

# APPENDIX B

This appendix contains a description of the numerical methods employed for the simulation of the UMRG equations. Basic versions of the one dimensional plane wave and (1+2)D MATLAB codes are provided. For the sake of saving space the initially specified parameters of the simulation have been removed.

## Numerical Methods

The code written to simulate a Raman ring cavity in one dimension was produced using the MathWorks matlab programming environment. The system of steady state, plane wave coupled multi-frequency Raman equations, (2.63), can be solved using built in matlab integration functions such as ODE45 and ODE113.

ODE45 is a one step solver which uses the explicit Runge-Kutta $4^{th}$ /$5^{th}$ order formula to solve ordinary differential equations to both $4^{th}$ and $5^{th}$ order accuracy. The solver is adaptive and can choose an appropriate step size to control the error in the $4^{th}$ order solution, and does so by comparing the $4^{th}$ and $5^{th}$ order solutions.

If the measured error of a solution is greater than the tolerances specified by the user, then the solver will reduce its step size to control the error. The step size can also be increased if the solution has higher accuracy than the specified tolerance (80).

ODE113 is a variable order Adams-Bashforth-Moulton solver which can be more efficient than ODE45 at stringent tolerances, or when the systems of equations are computationally expensive to evaluate. This solver gives solutions which can be up to $13^{th}$ order accurate and can also vary its step size to maintain error tolerances.

The overall accuracy of the solutions given by these solvers depends on both the relative and absolute error tolerance specified for the Integration. The absolute error tolerance defines the maximum allowable error of a solution, and the relative error tolerance defines how large the error can be relative to the correct value of the solution.

At stringent error tolerances ODE113 is more efficient than ODE45 and in the case of the plane wave UMRG equations used throughout this thesis both methods offer similar levels of accuracy and speed.

The inbuilt Matlab ODE solvers offer levels of accuracy and computational efficiencies which are hard to achieve with home built ODE solving software (without great difficulty). Therefore the Matlab ODE solvers are to provide extremely accurate solutions for the plane wave UMRG equations.

## The plane wave code

This section of code generates the initial input vector containing the initial amplitudes of each frequency component:

```
Ain = zeros(length(n),1);
Ain(ipump) = Apump;
Ain(iStokes) = AStokes;
Aout(1,:) = Ain.';
```

A vector containing the frequency of each sideband is generated, the units of frequency are in $cm^{-1}$:

```
omega      =   omega0 + n*omegaR;
C          =   omega/2/omega0/epsilon;
```

The dispersion coefficients for each frequency component can be calculated using a simple Cauchy type equation or a Sellmeier type equation:

```
gamma = (n*gamma1.*(1 + (n-1)*epsilon/2));
Gamma1 = zeros(size(gamma));
Gamma1(1:length(gamma)-1) = gamma(2:length(gamma))/epsilon;
Gamma2 = gamma/epsilon;
```

The tolerances of the integration routine are defined before the routine is performed, through the inbuilt function "**options**":

```
err = ones(nmax+nmin+1,1)*1e-10;
options = odeset('RelTol',1e-6,'AbsTol',err);%,'MaxStep',1e-6);
```

The main loop integrates the set of UMRG equations defined by "**ODEcwUMRG**" over the specified cavity length and repeats for a number of cavity transits specified by "**Ntrans**". After the integration is performed the resulting set of amplitudes are subject to the cavity boundary conditions, such as cavity mirror losses and pumping at the pump and first Stokes frequencies.

The function to be integrated '**ODEcwUMRG.m**' is given at the end of this section.

```
for j = 1:Ntrans+1
(u,A) = ode45('ODEcwUMRG',u,Ain,options,nwave,Delta,C,Gamma1,Gamma2);
Aout(j+1,:) = A(3,:);
Aout(j+1,:) = R*Aout(j+1,:);
Aout(j+1,ipump) = exp(i*phiP)*Aout(j+1,ipump) + Apump;
Aout(j+1,iStokes) = exp(i*phiS)*Aout(j+1,iStokes) + AStokes;
Ain = Aout(j+1,:).';
end
```

The set of amplitudes which occur at the end of a cavity transit can be used to calculate the frequency bandwidth of the Raman spectra. The calculated frequency bandwidth is a good comparative measure for how the frequency spectrum grows over each cavity transit, and provides a standard which can be used to compare different parameter regimes.

We have chosen to define the bandwidth as the number of frequency components which have intensities $\geq \frac{|A_0(Z=0)|^2}{100}$, where $|A_0(Z\ =\ 0)|^2$ is the initial normalised pump intensity at the start of the first cavity transit:

```
for k = 1:Ntrans+1
s1 = find(abs(Aout(k,:)).^2 >= 1/100);
BW(k) = length(s1);
end
```

The wave vector mismatch (dispersion) parameters described above can be determined from a Cauchy type dispersion equation (74). The levels of dispersion experienced by each frequency component can be determined from the fundamental dispersion between the pump and first Stokes components.

An alternative approach to the Cauchy type equation is to employ a Sellmeier type equation (78), this can provide a more accurate representation of the levels of dispersion at high order anti-Stokes sideband frequencies. The increased accuracy arises from correction terms for absorption resonances of the medium.

In the case of Sellmeier dispersion the refractive index is modelled using:

$$\mu_j = 1 + \delta_0 \Omega_0 \mathrm{d}/(\Omega_0^2 - \omega_j^2)\ ,$$

where $\delta_0 = 1.4\ x\ 10^{-4} amagat^{-1}$, $\frac{\Omega_0}{2\pi c} = 1.17\ x\ 10^{-5} cm^{-1}$ (78) is a resonant frequency of the medium, $d$ is the gas density of the medium and $\omega_n$ is the frequency of the Raman sideband. Both types of dispersion equation are available for use within the plane wave code and, when considering limited bandwidths, both offer similar levels of accuracy.

The function ODEcwUMRG.m which is called by the main plane wave cavity code is integrated using an inbuilt Matlab integration routine such as ODE45 (as described at the start of the appendix).

```
function dAdu = ODEcwUMRG(u,A,flag,nwave,Delta,C,Gamma1,Gamma2)

%   Initialize dAdu, which represents dA/du, as a matrix of
zeros with nmax
%   + nmin + 1 entries...

dAdu = zeros(nwave,1);

%   Set up field matrices F1 and F2

F1 = zeros(nwave,1);
F1(1:nwave-1) = A(2:nwave);

F2 = zeros(nwave,1);
F2(2:nwave) = A(1:nwave-1);

%   Calculate the polarization P

P = sum(A.*conj(F2).*exp(-i*Gamma2*u))/(1+i*Delta);

%   Specify the UMRG equations in matrix form...

dAdu = C.*(conj(P).*F1.*exp(-i*Gamma1*u) - P.*F2.*exp(i*Gamma2
*u));
```

## Solving the transverse UMRG equations

The transverse Raman (UMRG) equations (2.65) are to be solved using a hybrid split step Runge Kutta / finite difference scheme. The transverse components of the (1+1)D equations are solved by employing a Crank-Nicolson scheme (82, 83), and the (1+2)D equations are to be solved using an alternating direction (ADI) implicit finite difference approach (84).

The Runge Kutta integration method (79, 80, 81), employed in the transverse simulations, is third order accurate in the propagation direction, and the finite difference schemes are second order accurate in each set of coordinates.

The hybrid method requires the UMRG envelope equations to be split into both their linear and nonlinear components. The linear components form a set of 1D or 2D equations, given as

$$\frac{\partial A_j}{\partial Z} = id_j \nabla_{\mathrm{T}}^2 A_j \,, \tag{B3.1}$$

where equation (B3.1) is just a wave equation and can be solved using numerous integration methods of varying accuracy and efficiency.

The hybrid method requires that the integration be split into two steps, where the first step deals with the integration of the nonlinear components of the UMRG equations. The solution is then propagated over the transverse coordinates using a finite difference scheme, and the output is used as initial conditions, for the solution of the nonlinear components, over the final half step. The total process results in the linear and nonlinear components of the UMRG equations being propagated over a full step in the longitudinal coordinate.

## Crank-Nicolson

Finite difference methods approximate partial derivatives of a function, $u_{ij}^n$, on a set of grid points in terms of finite difference expressions: defining a three dimensional grid $(i \times j \times n)$ where $i$, $j$ and $n$ correspond to units of $X$, $Y$ and Z forming the spatial grid.

By first focussing on the (1+1)D form of equation (B3.1) and choosing an arbitrary initial grid point, the derivatives can be defined as:

$$\frac{du}{dZ} = \frac{u_i^{n+1} - u_i^n}{\Delta z},$$

$$\frac{d^2u}{dX^2} = \frac{u_{i+1}^n - u_{i-1}^n}{\Delta x^2}.$$

Where $\Delta z$ and $\Delta x^2$ are the step sizes in the Z and X directions, respectively.

The above differences are centred on an arbitrary grid point to a second order accurate approximation. Substituting the above differences into equation (B3.1) results in an explicit expression for $u_i^{n+1}$ in terms of known $u_i^n$'s. The resulting expression is easy to implement but has an unstable solution unless the ratio, $\frac{\Delta z}{\Delta x^2}$, is small.

The instability problem can be overcome by instead considering implicit finite difference scheme such as the Crank-Nicolson scheme, which happens to be unconditionally stable (for all selections of $\frac{\Delta z}{\Delta x^2}$) and is second order in both the $Z$ and $X$ directions.

The expressions defining the finite differences in the Crank-Nicolson scheme are given as:

$$\frac{du}{dZ} = \frac{u_i^{n+1} - u_i^n}{\Delta z},$$

$$\frac{d^2u}{dX^2} = \frac{u_{i+1}^n - 2u_i^n + u_{i-1}^n + u_{i+1}^{n+1} - 2u_i^{n+1} + u_{i-1}^{n+1}}{2\Delta x^2}.$$

The above difference approximations are centred about an intermediate spatial step, $Z + \Delta z$ and therefore provide an average value for the derivatives.

Substituting the above expressions into equation (3.1) results in a system of linear equations which can be expressed in terms of a tridiagonal matrix (82):

$$\begin{bmatrix} B_0 & C_0 & 0 & 0 & \cdots & 0 \\ A_1 & B_1 & C_1 & 0 & \cdots & 0 \\ 0 & A_2 & B_2 & C_2 & 0 & \\ \vdots & & \ddots & \ddots & \ddots & \vdots \\ 0 & \dots & 0 & A_i & B_i & C_i \end{bmatrix} \begin{bmatrix} u_0^{n+1} \\ u_1^{n+1} \\ u_2^{n+1} \\ \vdots \\ u_i^{n+1} \end{bmatrix} = \begin{bmatrix} D_0 \\ D_1 \\ D_2 \\ \vdots \\ D_i \end{bmatrix},$$

$$A_i = -\frac{id_j}{2\Delta x^2},$$

$$B_i = \frac{1}{\Delta z} + \frac{id_j}{2\Delta x^2},$$

$$C_i = -\frac{id_j}{2\Delta x^2},$$

$$D_i = \frac{id_j}{2\Delta x^2}u_{i+1}^n + \frac{id_j}{2\Delta x^2}u_{i-1}^n + \left(\frac{1}{\Delta z} + \frac{id_j}{2\Delta x^2}\right)u_i^n \,.$$

Solutions to equation (3.1) can be found by solving the above tridiagonal matrix problem. Tridiagonal matrix problems can be solved efficiently using the methods of Gaussian elimination and back substitution.

## ADI finite difference method

When considering the solution of the (1+2)D form of equation (B3.1) the Crank-Nicolson method is found to be unsuitable. Although a naive generalisation of the Crank-Nicolson scheme could be used to find solutions, the computation of such solutions is highly inefficient and requires a very large number of operations to be performed to solve the resulting 'block' tridiagonal matrix.

The alternating direction implicit method (ADI) offers a computationally efficient alternative. The ADI method is implemented in two steps, with each step being implicit in one transverse direction and explicit in the other (alternating the transverse coordinate between steps).

Equation (B3.1) can be written in terms of the two-step ADI scheme (84) as:

$$\frac{u_{i,j}^{n+1/2} - u_{i,j}^n}{\Delta z/_2} = id_j\left[\frac{u_{i+1,j}^{n+1/2} - 2u_{i,j}^{n+1/2} + u_{i-1,j}^{n+1/2}}{\Delta x^2} + \frac{u_{i,j+1}^n - 2u_{i,j}^n + u_{i,j-1}^n}{\Delta y^2}\right],$$

$$\frac{u_{i,j}^{n+1} - u_{i,j}^{n+1/2}}{\Delta z/_2} = id_j\left[\frac{u_{i+1,j}^{n+1/2} - 2u_{i,j}^{n+1/2} + u_{i-1,j}^{n+1/2}}{\Delta x^2} + \frac{u_{i,j+1}^{n+1} - 2u_{i,j}^{n+1} + u_{i,j-1}^{n+1}}{\Delta y^2}\right],$$

where the first equation is implicit in $X$ and explicit in the $Y$ coordinate, and the second equation is implicit in Y and explicit in $X$. Each difference equation forms a tridiagonal matrix problem which can be solved by Gaussian elimination, like the

Crank-Nicolson scheme described above, and performing both steps results in a solution given at the point $Z + \Delta z$.

The implementation of the ADI method requires the solution of a dual tridiagonal matrix problem (given above) to be performed twice for each Raman frequency component during each time step $Z + \Delta z$.

An example of the ADI integration routine used to solve the (1+2)D UMRG is provided in the final section of this appendix. The full integration routine requires a large number of calculations to be performed. The number of calculations can be estimated by defining the number of frequency components and an example grid, such that the $X$ and $Y$ axes contain $500$ points each, the $Z$ coordinate is split into $1000$ steps and the number of frequency components is $j = 100$.

Starting with the ADI section of the code, each step in the longitudinal direction requires that the tridiagonal matrix solver is called $j(X + Y)$ times (which in itself performs a large number of calculations).

The Runge-Kutta code is performed $2j$ times per longitudinal step, therefore the total number of calculations per step is $2j + j(X + Y) = 200{,}400$, and multiplying by the number of $Z$ steps results in a total number of calculations for the simulation, $\approx 2e^8$.

Although large numbers of calculations can increase simulation times the main disadvantage is the vast memory requirements of multi-dimensional simulations. Most desktop machines can run out of memory very quickly when performing simulations of (1+1)D and (1+2D) equations

Using the above values for grid size we can calculate the size of the matrix required, for storing the transverse amplitudes, of each Raman frequency component, in a typical (1+2)D simulation (non-cavity). The resulting four dimensional matrix has a large number of components, $(X \times Y \times Z \times j) = 4e^9$, which can take up a large amount of virtual memory, up to 4 gigabytes, when being used to perform calculations.

To reduce computational requirements simulations will be performed with the smallest possible grid size (without sacrificing accuracy) for the least number of frequency components. This will be achieved by only considering realistic examples of cavity mirrors (with limited restricted reflection bandwidths).

## The (1+2)D code

This section of the appendix contains the integration routines used in the (1+2)D UMRG code, which are written in the Matlab syntax.

The third order Runge Kutta routine is defined as:

```
        B0(1:Nx,1:Ny) = A1(1,1:Nx,1:Ny);
        B1(1:Nx,1:Ny) = A1(2,1:Nx,1:Ny);

f1 = ((omega(1))/(2*omega0))*conj(P).*B1.*exp(-
i*gamma(2)*z(j-1));

f2 = ((omega(1))/(2*omega0))*conj(P).*(B1).*exp(-
i*gamma(2)*(z(j-1)+dz/4));

f3 = ((omega(1))/(2*omega0))*conj(P).*(B1).*exp(-
i*gamma(2)*(z(j-1)+dz/2));
A1(1,1:Nx,1:Ny) = B0 + (dz/6)*(f1 + 4*f2 + f3);

for jj = 2:nwave - 1
        B0(1:Nx,1:Ny) = A1(jj,1:Nx,1:Ny);
        B1(1:Nx,1:Ny) = A1(jj+1,1:Nx,1:Ny);
        B2(1:Nx,1:Ny) = A1(jj-1,1:Nx,1:Ny);
f1 = ((omega(jj))/(2*omega0))*(conj(P).*B1.*exp(-
i*gamma(jj+1)*z(j-1)) - P.*B2.*exp(i*gamma(jj)*z(j-1)));
```

```
f2 = ((omega(jj))/(2*omega0))*(conj(P).*(B1).*exp(-
i*gamma(jj+1)*(z(j-1)+dz/4)) -
P.*B2.*exp(i*gamma(jj)*(z(j-1)+dz/4)));

f3 = ((omega(jj))/(2*omega0))*(conj(P).*(B1).*exp(-
i*gamma(jj+1)*(z(j-1)+dz/2)) -
P.*B2.*exp(i*gamma(jj)*(z(j-1)+dz/2)));

A1(jj,1:Nx,1:Ny) = B0 + (dz/6)*(f1 + 4*f2 + f3);
end
        B0(1:Nx,1:Ny) = A1(nwave,1:Nx,1:Ny);
        B1(1:Nx,1:Ny) = A1(nwave-1,1:Nx,1:Ny);

f1 = -
(omega(nwave))/(2*omega0))*P.*B1.*exp(i*gamma(nwave)*z(j
-1));

f2 = -
((omega(nwave))/(2*omega0))*P.*(B1).*exp(i*gamma(nwave)*
(z(j-1)+dz/4));

f3 = -
((omega(nwave))/(2*omega0))*P.*(B1).*exp(i*gamma(nwave)*
(z(j-1)+dz/2));

A1(nwave,1:Nx,1:Ny) = B0 + (dz/6)*(f1 + 4*f2 + f3);
```

The above Runge-Kutta routine propagates the nonlinear components of the UMRG equations over half a step, $Z + \frac{\Delta z}{2}$. The equations are solved "**nwave"** times, with the first and last envelopes being solved outside of the main integration loop.

The resulting solution is then propagated in the transverse coordinates (linear component of the UMRG equation) using the ADI scheme described above.

An example of the ADI code is given as:

```
Ldif = i*(1/((omega(jj)/omega0)*4*LD));

TL = dz;
TR1(1:Nx) = -TL;
TR2(1:Nx) = (((4*dx^2)/Ldif)+2*TL);
TR3(1:Nx) = -TL;

for jjj = 2:Ny-1
for jjjj = 1:Nx

TR4(jjjj) = A1(jj,jjjj,jjj)*(((4*dx^2)/Ldif)-2*TL) +
A1(jj,jjjj,jjj+1)*TL + A1(jj,jjjj,jjj-1)*TL;

end
[A2(jj,1:Nx,jjj)] = TDMAsolver(TR1,TR2,TR3,TR4);
end

for jjjj = 1:Nx
TR44(jjjj) = A1(jj,jjjj,1)*(((4*dx^2)/Ldif)-2*TL) +
A1(jj,jjjj,2)*TL;

TR444(jjjj) = A1(jj,jjjj,Ny)*(((4*dx^2)/Ldif)-2*TL) +
A1(jj,jjjj,Ny-1)*TL;
end

[A2(jj,1:Nx,1)] = TDMAsolver(TR1,TR2,TR3,TR44);
[A2(jj,1:Nx,Ny)] = TDMAsolver(TR1,TR2,TR3,TR444);
```

**T**he above section of the ADI code deals with the first half step (implicit in $X$) of the full transverse solution. This means that the $Y$ coordinate are held stationary whilst the $X$ coordinate is varied.

The code begins by defining the constants, "**TR1, TR2, TR3**", which correspond to $A_i$ , $B_i$ and $C_i$ from the tridiagonal matrix problem. The parameter $D_i$ ,"**TR4**", is then calculated for each point on the 2D transverse grid. The resulting sets of parameters are passed into the tridiagonal matrix solver, "**TDMAsolver**".

The matrix solver returns the solution for the transverse amplitude at $Z + \frac{\Delta z}{2}$ which serves as the initial values for the second half step, where the second step feeds the solution back into a similar piece of code which is implicit in $Y$. Performing both transverse steps results in a solution for the transverse amplitude at $Z + \Delta z$.

# APPENDIX C

This appendix contains results for the gain suppression analysis derived in chapter 3. Each of the figures compares the depleted and un-depleted pump models to results given by numerical integration of the UMRG equations.

Each figure shows the growth of Stokes intensity within the cavity as predicted by the depleted pump model, un-depleted pump model and the numerical results as blue, green and red traces respectively.

## Cavity length

Two different levels of boundary mirror reflectivity will be considered $R_0 = 0.90$, $R_0 = 0.95$ and results are given in increasing increments of cavity length.

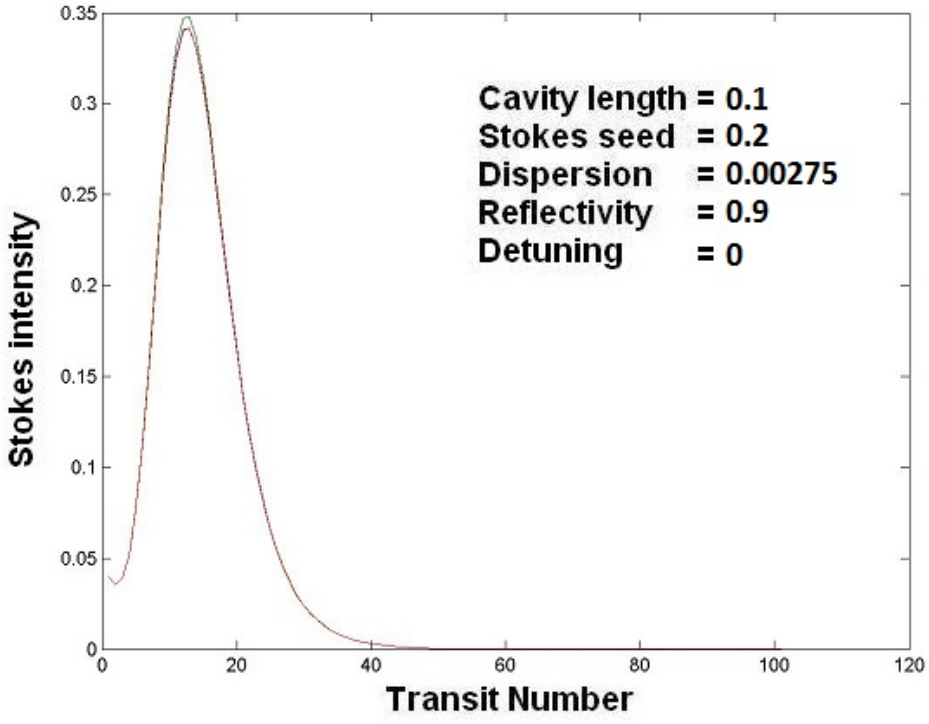


**Figure C1 - At short cavity lengths the results of each gain suppression analysis model are in agreement with the results of the numerical simulation.**

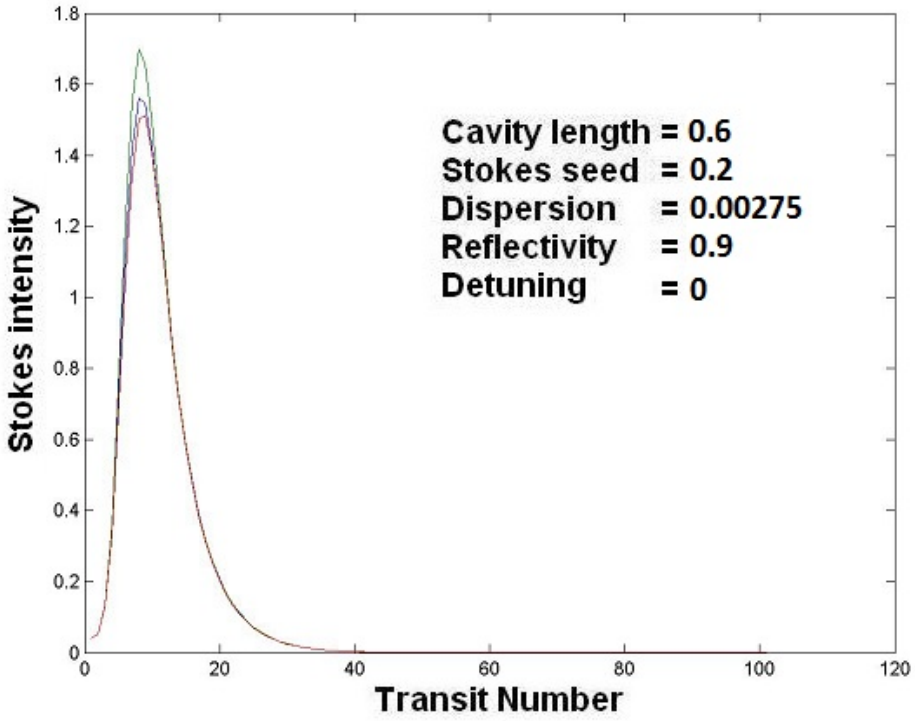


**Figure C2 - As the cavity lengths is increased we find that the un-depleted model fails to reproduce the numerical results**

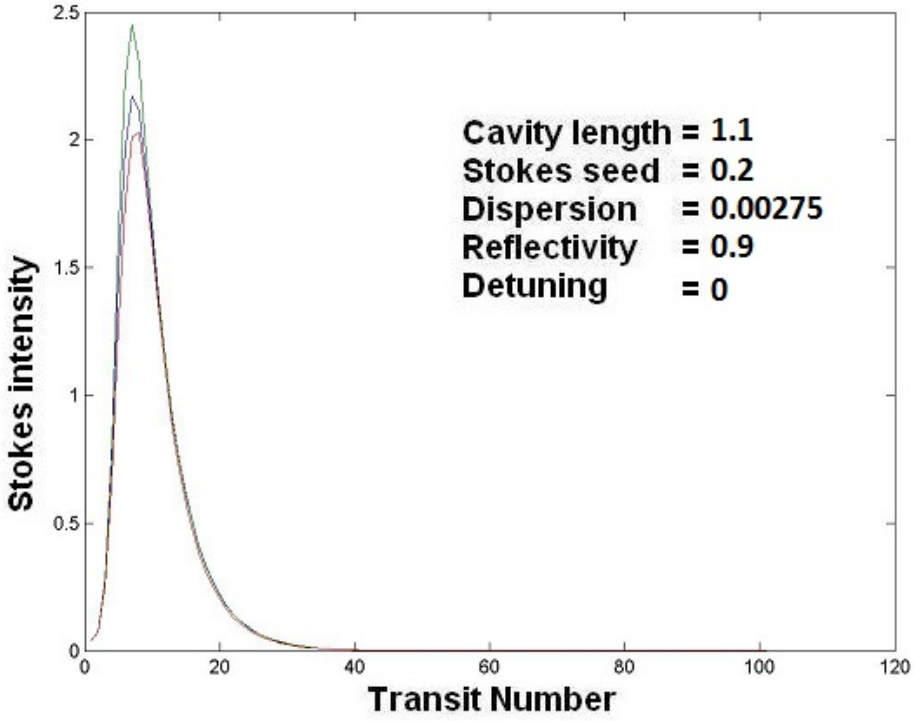


**Figure C3 - As the cavity lengths is increased we find that the un-depleted model fails to reproduce the numerical results**

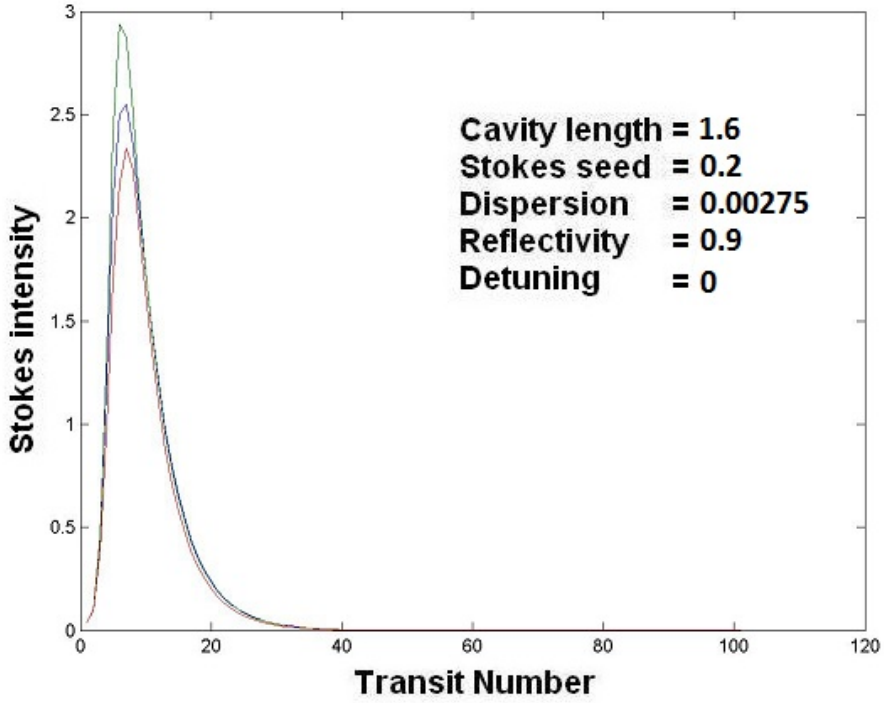


**Figure C4 - As the cavity lengths is increased we find that the un-depleted model fails to reproduce the numerical results**

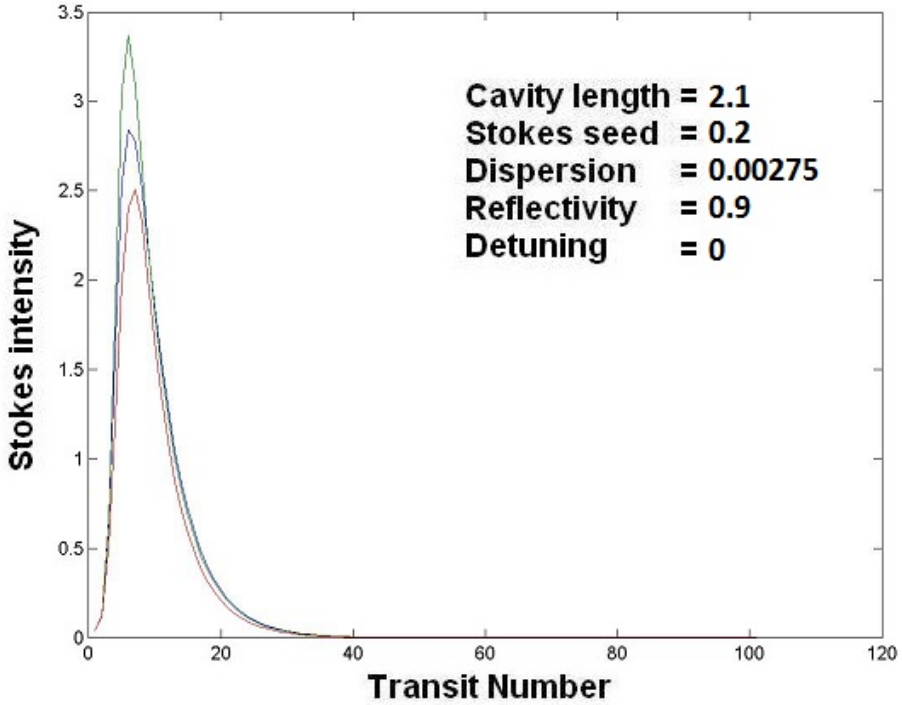


**Figure C5 - As the cavity lengths is increased we find that the un-depleted model fails to reproduce the numerical results**

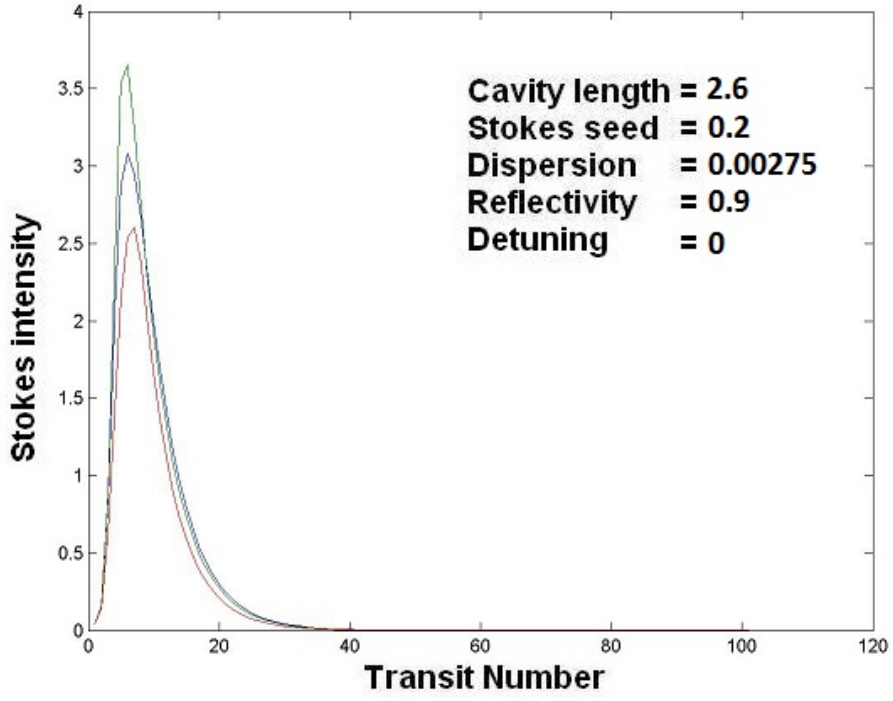


**Figure C6 - At long cavity lengths both the un-depleted and depleted gain suppression models fail to accurately capture the numerical results.**

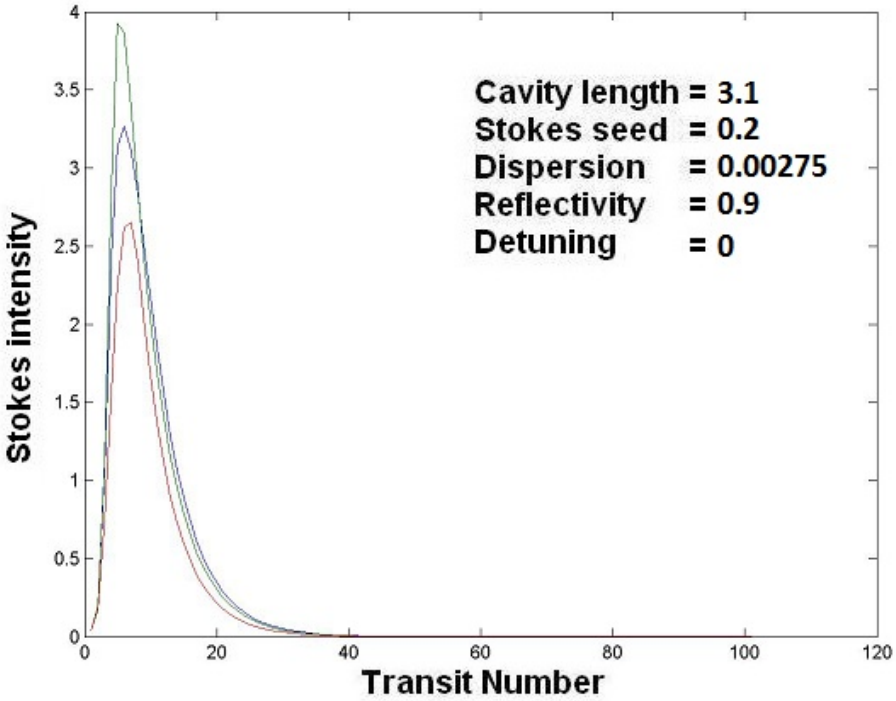


**Figure C7 - At long cavity lengths both the un-depleted and depleted gain suppression models fail to accurately capture the numerical results.**

The above figures ranging from figure C1 to C7 show that for a reflectivity of $R_0 = 0.9$ the depleted and un-depleted gain suppression models accurately model the growth of Stokes intensity within the cavity. At short cavity lengths both models provide the same level of accuracy, but as the cavity length is increased we find that the depleted pump model provides a more accurate result which is closer the results produced by the numerical integration of the UMRG equations.

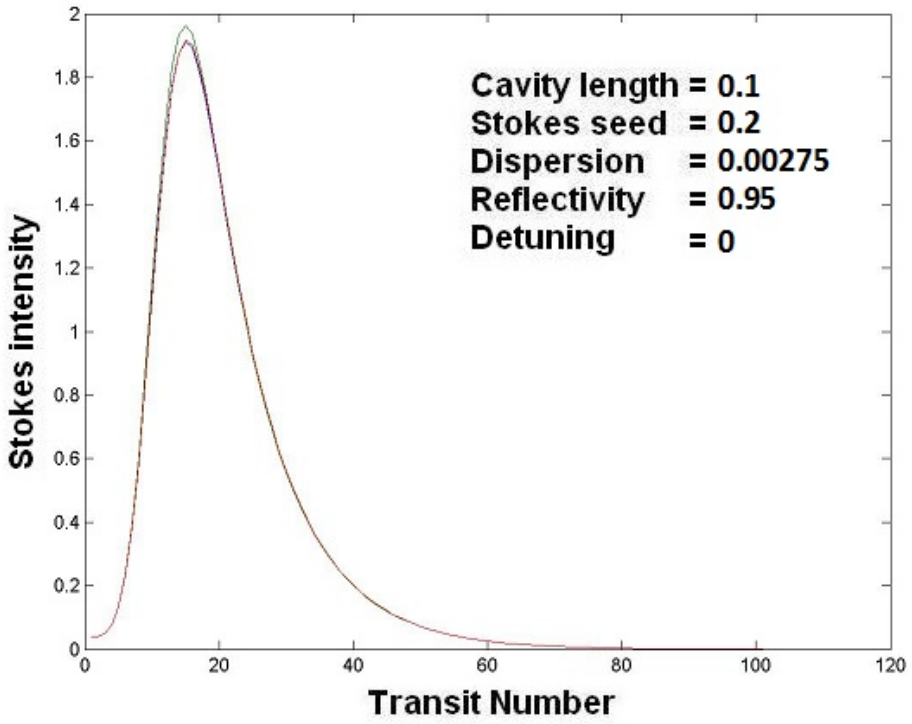


**Figure C8 - As with the results given for $R = 0.9$ both gain suppression models provide similar levels of accuracy at short cavity lengths.**

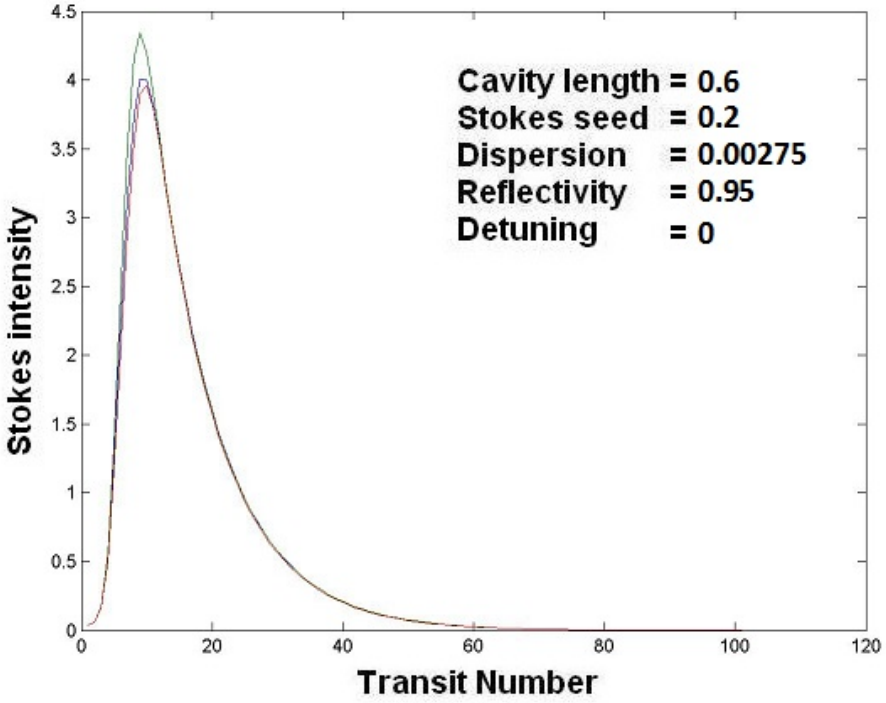


**Figure C9 - As with the results given for $R = 0.9$ both gain suppression models provide similar levels of accuracy at short cavity lengths.**

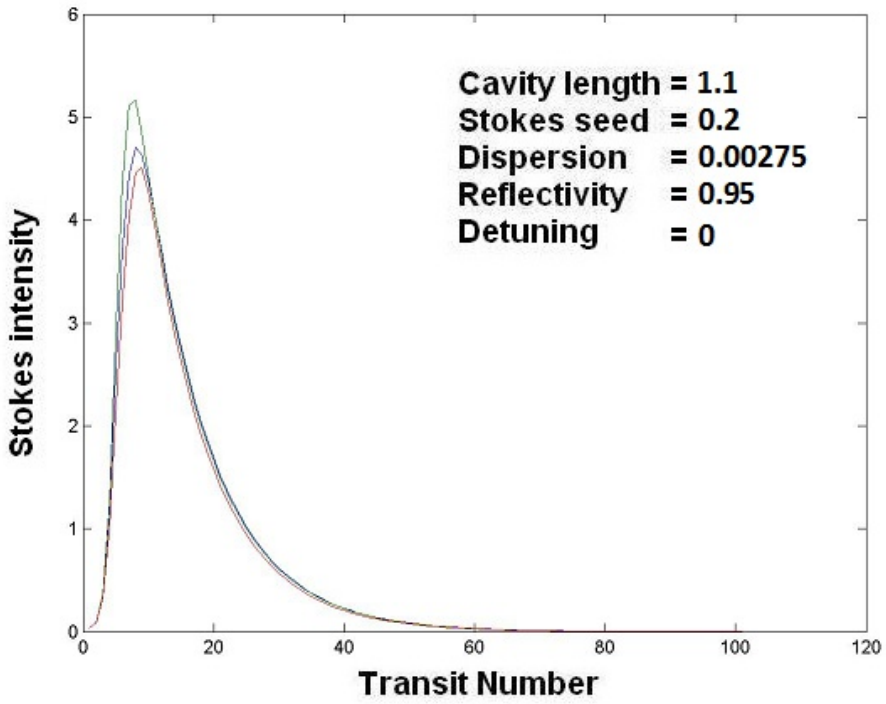


**Figure C10 - As the cavity length is increased we find that the un-depleted model begins to provide less accurate results.**

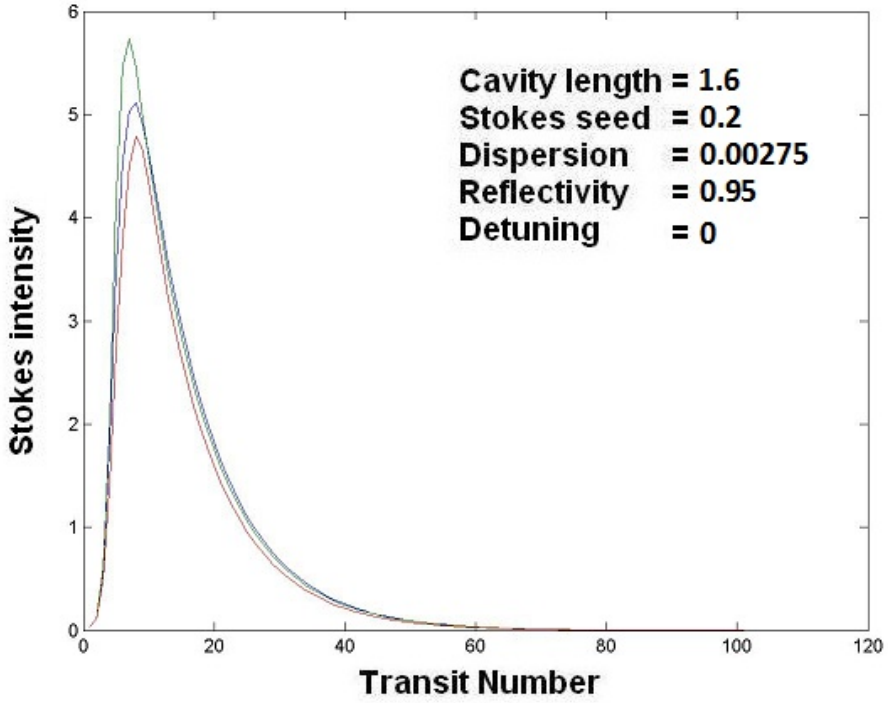


**Figure C11 - As the cavity length is increased we find that the un-depleted model begins to provide less accurate results**

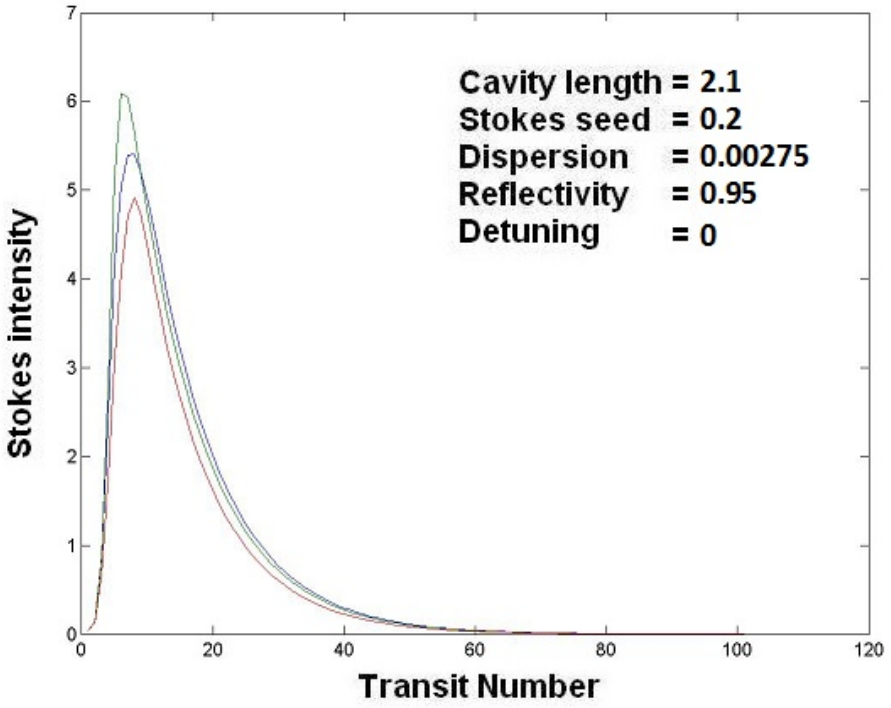


**Figure C12 - As the cavity length is increased we find that the un-depleted model begins to provide less accurate results**

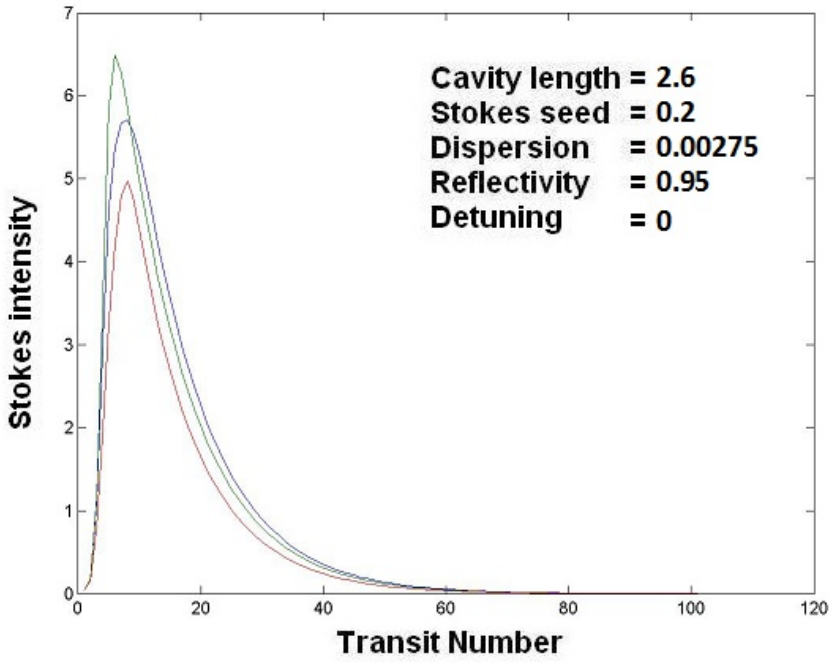


**Figure C13 - At long cavity lengths we find that both gain suppression models provide less accurate results. The depleted model still offers results which follow the general shape of the numerical results but over predicts the maximum intensity achieved in the cavity.**

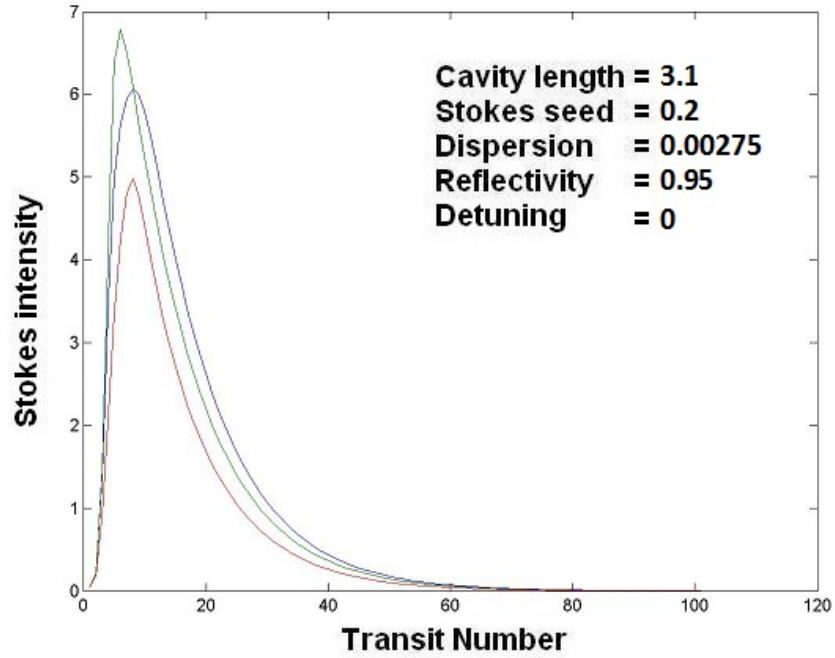


**Figure C14 - At long cavity lengths we find that both gain suppression models provide less accurate results. The depleted model still offers results which follow the general shape of the numerical results but over predicts the maximum intensity achieved in the cavity.**

When a higher level of reflectivity is chosen, $R_0 = 0.95$, we again find that both the depleted and un-depleted models offer similar levels of accuracy at shorter cavity lengths, but at longer cavity lengths we find that the differences between the results are much more pronounced. The depleted pump model provides more accurate results for a greater range of parameters. The shapes of the intensity curves generated by each analysis are vastly different at longer cavity lengths and the depleted pump model offers a curve with a similar shape to the numerical results.

## Initial Stokes seed

We now present results when varying the initial Stokes seed and the results will be given for the two levels of cavity mirror reflectivity given above. The cavity length will be kept at a fixed value of $Z_c = 0.1$ and the Stokes seed will be increased in increments of $0.1$ between each figure.

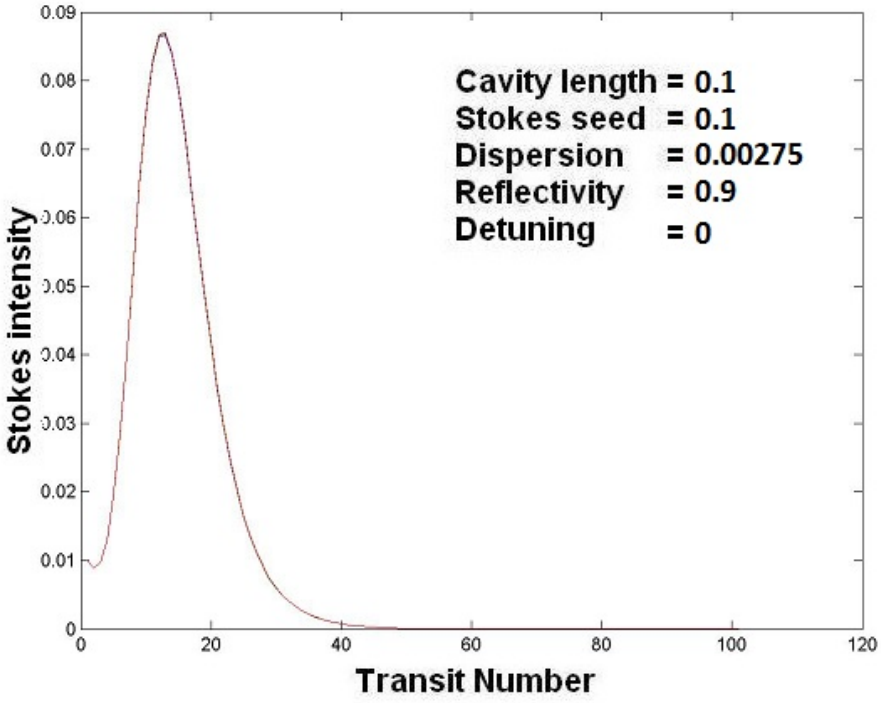


**Figure C15 - When a small level of initial Stokes seed is employed we find that both the depleted and un-depleted models provide results which match the numerical results.**

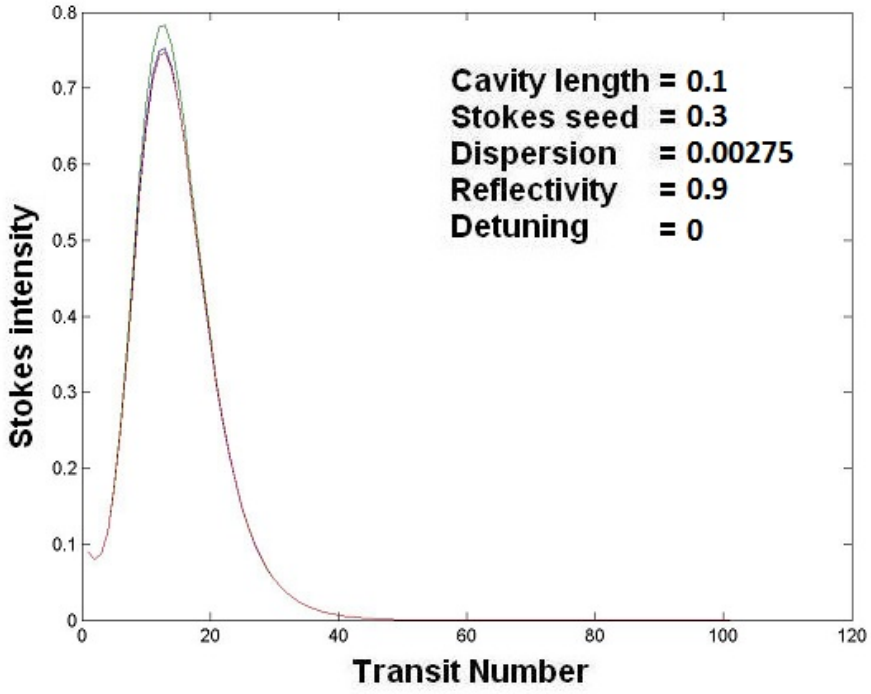


**Figure C16 - With only a small increase in the level of initial Stokes seed we find that the un-depleted model begins to produce inaccurate results.**

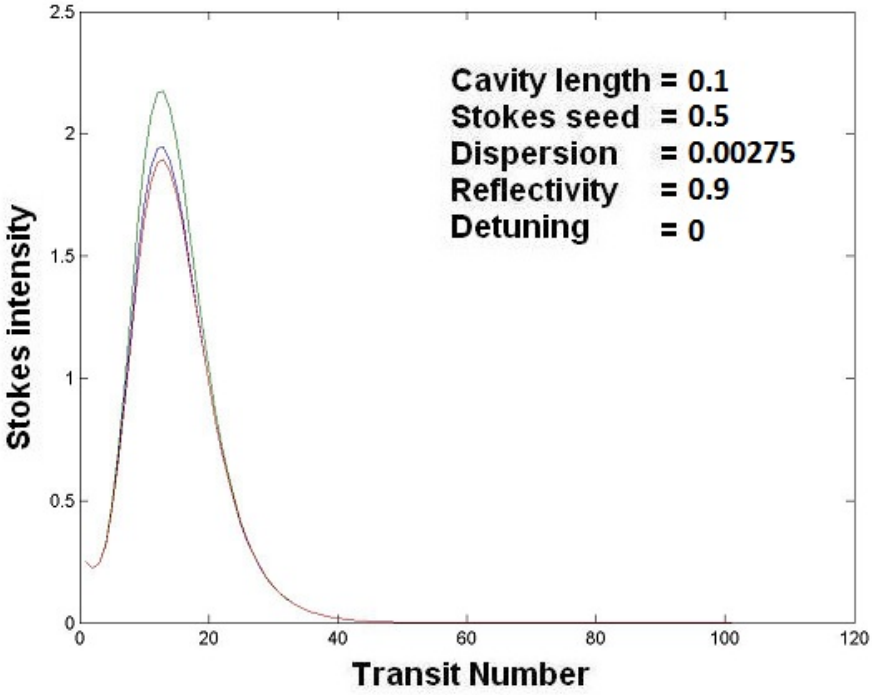


**Figure C17 - The depleted pump model provides accurate results for a broad range of initial Stokes seeds.**

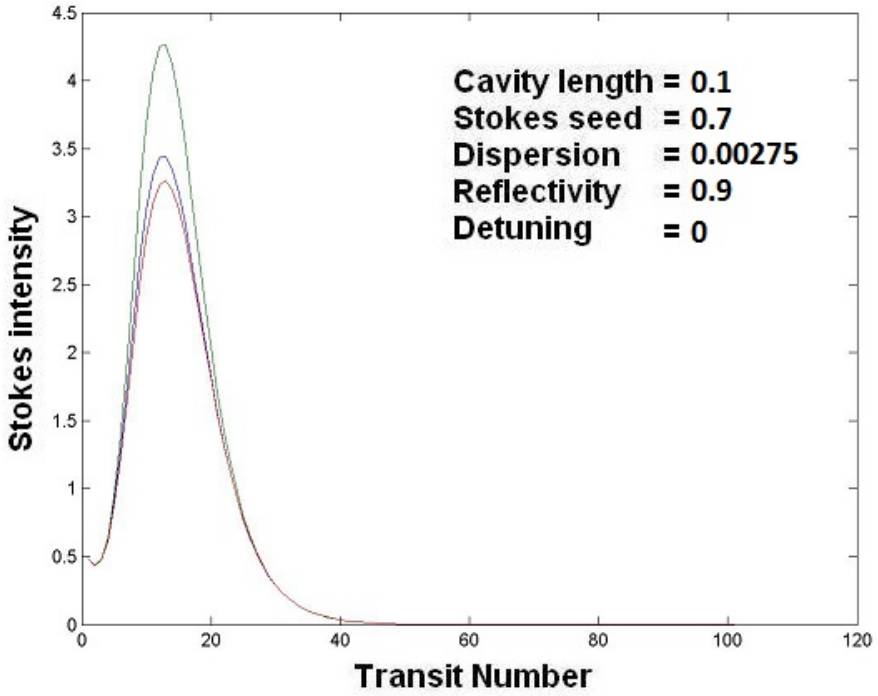


**Figure C18 - The depleted pump model provides accurate results for a broad range of initial Stokes seeds.**

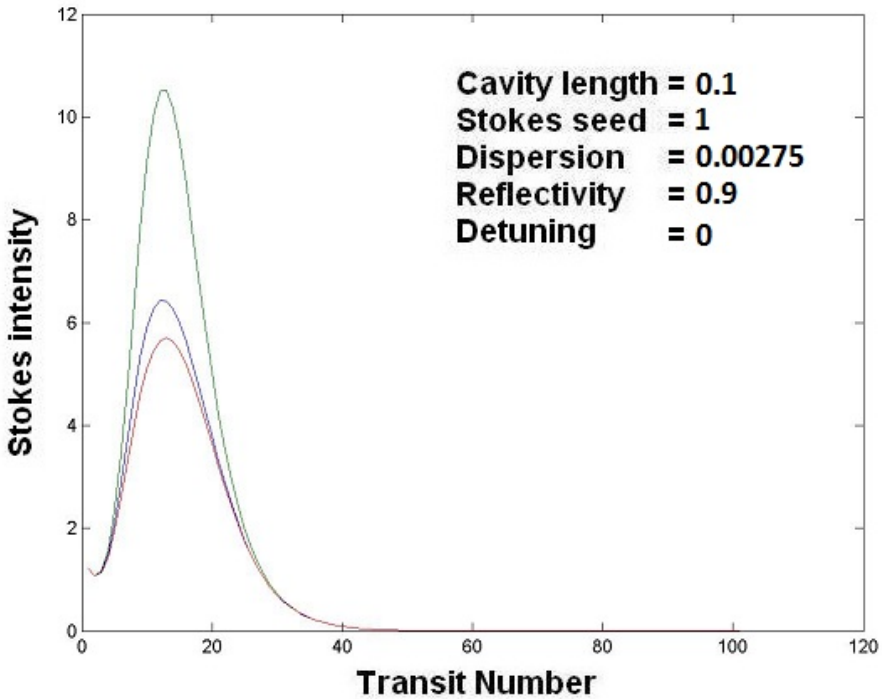


**Figure C19 - When the applied Stokes seed has the same intensity as the pump beam we find a significant difference between the depleted and un-depleted models.**

The results for a reflectivity of $R_0 = 0.9$ show that as the level of initial Stokes seed is increased the depleted pump model more accurately describes the growth of the Stokes intensity over a greater number of cavity transits and produces results which closely resemble the results of the numerical analysis.

When the reflectivity is increased to $R_0 = 0.95$ we find that the depleted pump model still offers the most accurate results and that the difference in results between the depleted pump and un-depleted pump gain suppression models are much more pronounced, where the un-depleted pump model can predict Stokes intensities up to $3$ times larger than that of the numerical data and depleted pump model.

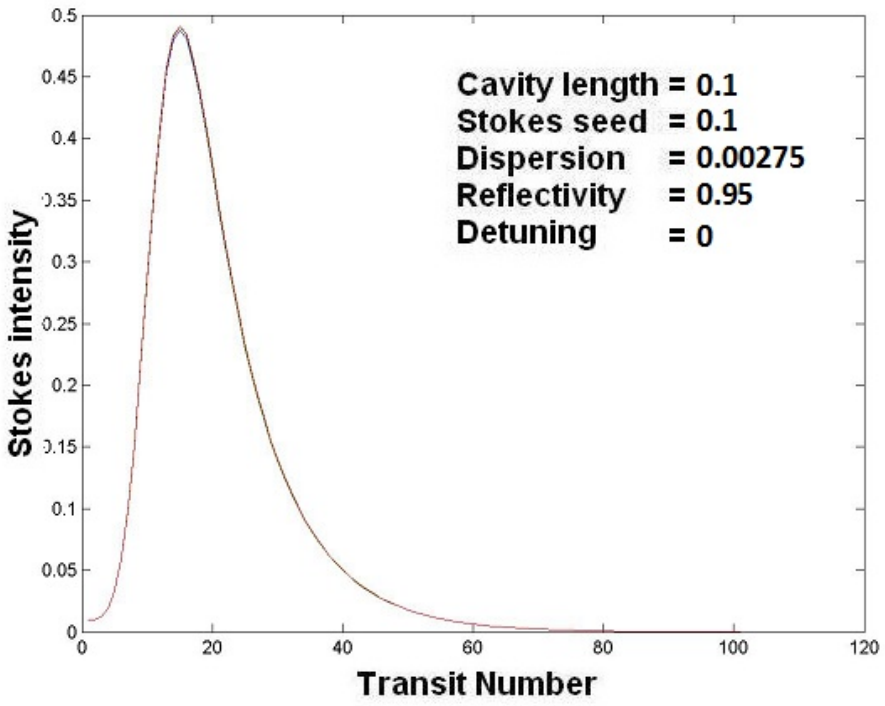


**Figure C20 - When a small level of initial Stokes seed is employed we find that both the depleted and un-depleted models provide results which match the numerical results.**

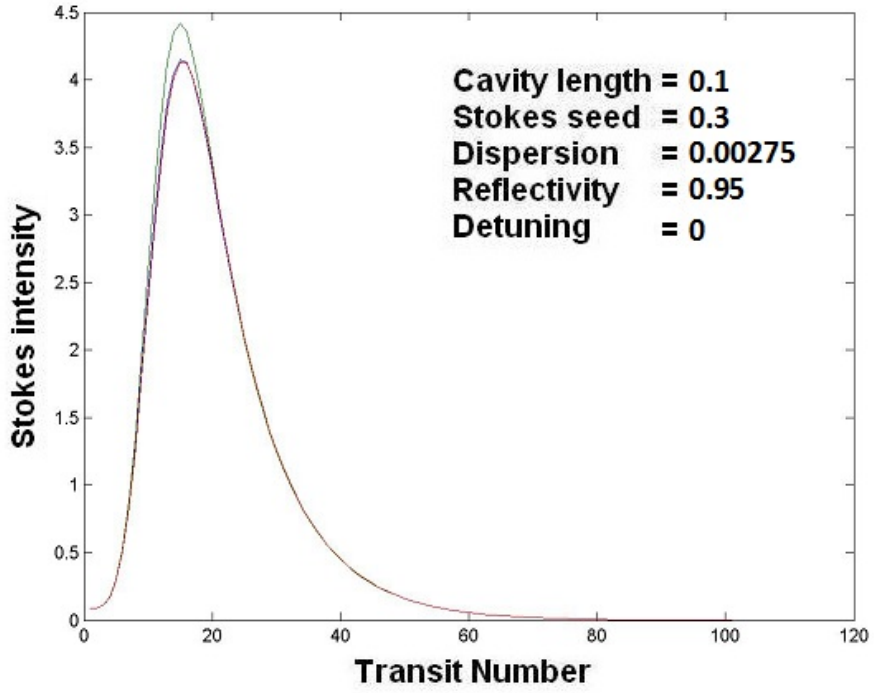


**Figure C21 - With only a small increase in the level of initial Stokes seed we find that the un-depleted model begins to produce inaccurate results.**

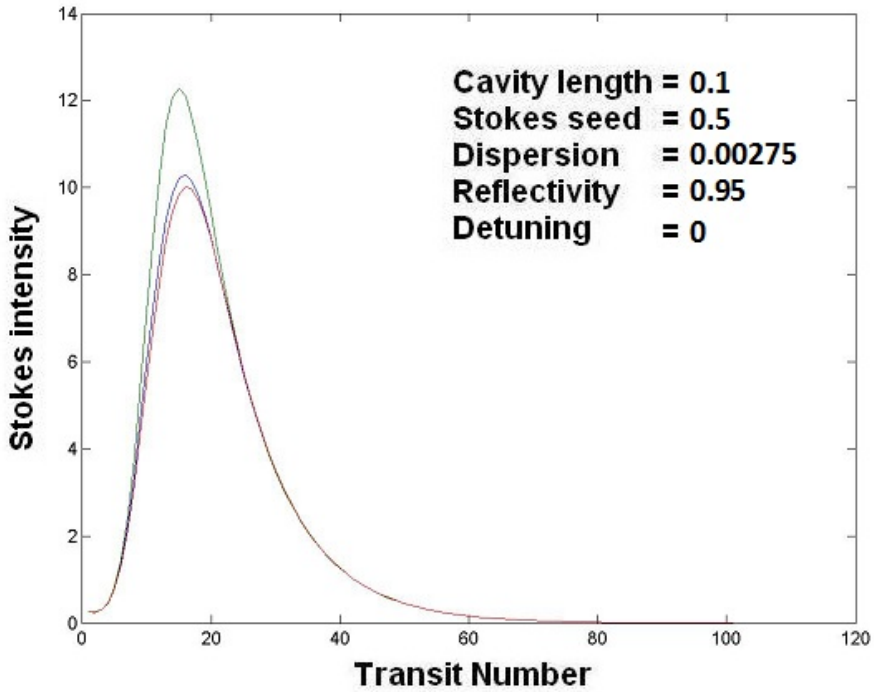


**Figure C22 - The depleted pump model provides accurate results for a broad range of initial Stokes seeds.**

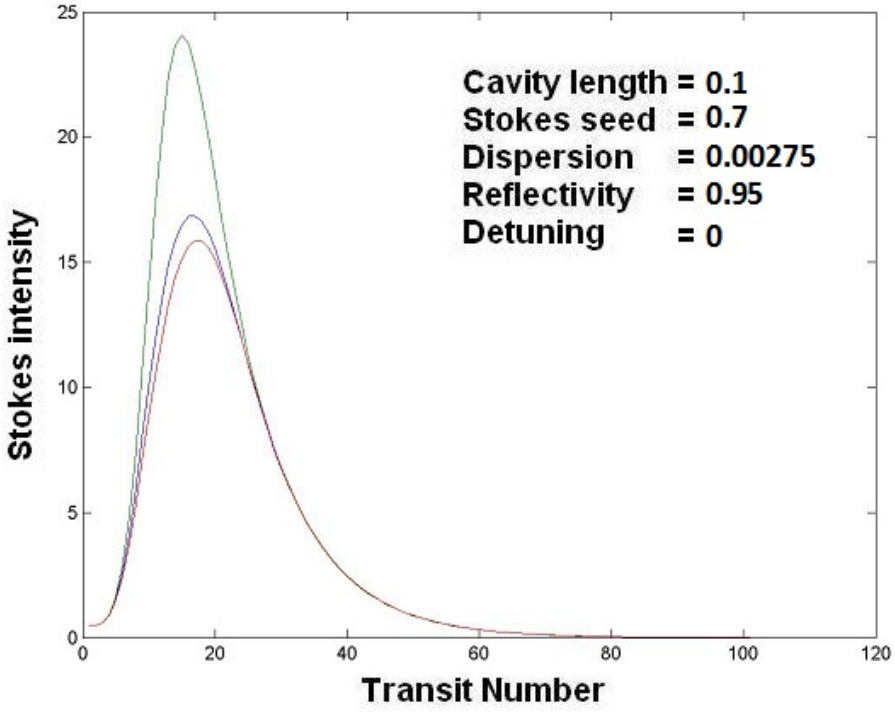


**Figure C23 - The depleted pump model provides accurate results for a broad range of initial Stokes seeds**

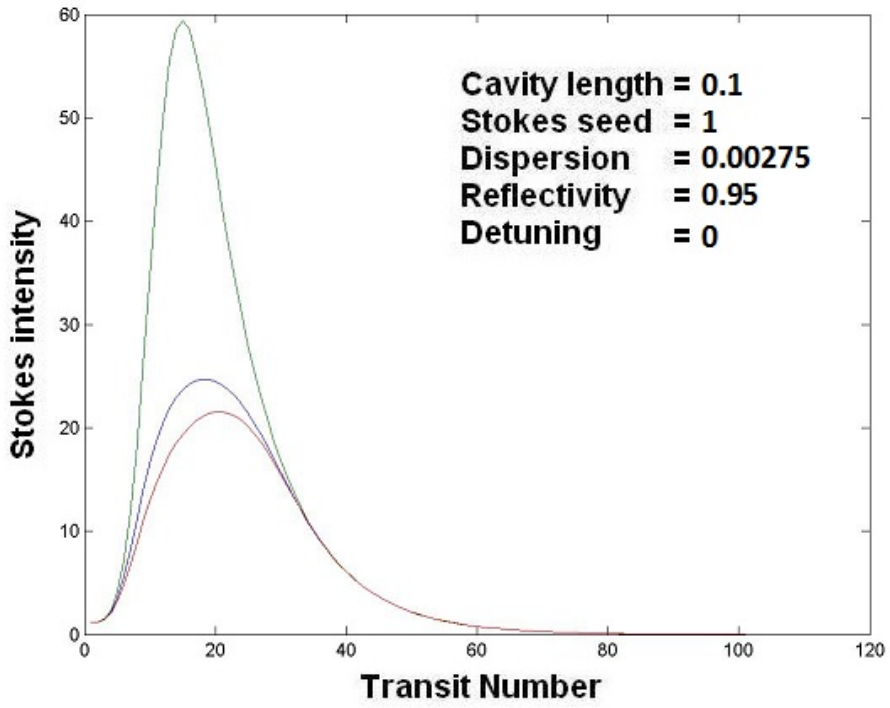


**Figure C24 - When the applied Stokes seed has the same intensity as the pump beam we find a significant difference between the depleted and un-depleted models.**

# APPENDIX D

This appendix contains the derivation of the finite dispersion gain suppression analysis.

The governing envelope equations for the 3-wave Raman system are obtained from equations (2.63):

$$\frac{dA_{-1}}{dZ} = \frac{(1-\varepsilon)}{2(1-i\delta)}\left[|A_0|^2 A_{-1} + A_0^2 A_1^* e^{i\gamma_1 Z}\right] \tag{D.1}$$

$$\frac{dA_0}{dZ} = \frac{1}{2(1-i\delta)}\left[A_0^* A_{-1} A_1 e^{-i\gamma_1 Z} + |A_1|^2 A_0\right] - \frac{1}{2(1+i\delta)}\left[A_0^* A_{-1} A_1 e^{-i\gamma_1 Z} + |A_{-1}|^2 A_0\right] \tag{D.2}$$

$$\frac{dA_1}{dZ} = -\frac{(1+\varepsilon)}{2(1+i\delta)}\left[|A_0|^2 A_1 + A_0^2 A_{-1}^* e^{i\gamma_1 Z}\right]. \tag{D.3}$$

The the Stokes shift parameter is $\varepsilon = \frac{\omega_R}{\omega_0}$ and the detuning is given as:

$$\delta = T_2\left(\mathrm{I}_0\left(\frac{\alpha_{22}-\alpha_{11}}{4\hbar}\right)\sum_j A_j A_j^* + \delta\omega\right).$$

Denoting for the m$^{\text{th}}$ cavity round trip in the medium $A_0^2 = A_{0,m}^2 = \left|A_{0,m}\right|^2 e^{i2\theta_m}$ ,

where $\theta_m = \arg\left[A_{0,m}\right]$, and similarly $A_{-1} = A_{-1,m}$ and $A_1 = A_{1,m}$, equations (D.1) and (D.3) become:

$$\frac{dA_{-1,m}}{dZ} = \frac{\left|A_{0,m}\right|^2}{2}\frac{(1-\varepsilon)}{(1-i\delta)}\left[A_{-1,m} + A_{1,m}^* e^{i\gamma_1 Z + i2\theta_m}\right] \tag{D.4}$$

$$\frac{dA_{1,m}}{dZ} = -\frac{\left|A_{0,m}\right|^2}{2}\frac{(1+\varepsilon)}{(1+i\delta)}\left[A_{1,m} + A_{-1,m}^* e^{i\gamma_1 Z + i2\theta_m}\right]. \tag{D.5}$$

The sidebands are subject to a loss at the coupling mirror in the form of the mirror reflectivity $R_j$, hence the boundary conditions are given as:

$$A_{-1,m+1}(Z=0) = R_{-1}A_{-1,m}(Z=L)$$

$$A_{1,m+1}(Z=0) = R_1 A_{1,m}(Z=L).$$

For the undepleted pump model one could model the intra-cavity pump field through

$$\text{Where} \quad A_{0,m+1} = A_0 + A_{0,m} R_0 e^{-\alpha L + i\emptyset} \quad , m = 1,2,3 \ldots \ , \tag{D.6}$$

and $\alpha$ includes any linear loss, $L = Z_c$ is the cavity length, $R_0$ is the pump (amplitude) cavity mirror reflectivity and $m$ is the transit number. $\alpha$ defines any linear loss within the cavity and $\emptyset$ defines any pump mistuning from cavity resonance.

For the undepleted model, evolution of the pump may be treated as a geometric series where:

$m = 1, \quad A_{0,m} = A_0$

$m = 2, \quad A_{0,m} = A_0 + A_0 R_0 e^{-\alpha L + i\emptyset} = A_0(1 + R_0 e^{-\alpha L + i\emptyset})$

$m = 3, \quad A_{0,m} = A_0 + R_0 e^{-\alpha L + i\emptyset} A_0\left(1 + R_0 e^{-\alpha L + i\emptyset}\right) = A_0\left(1 + R_0 e^{-\alpha L + i\emptyset} + (R_0 e^{-\alpha L + i\emptyset})^2\right)$ .

Therefore the series can be defined as:

$$A_{0,m} = \sum_{j=1}^{m} A_0 (R_0 e^{-\alpha L + i\emptyset})^{j-1} = \frac{A_0(1 - R_0^m e^{-m(\alpha L + i\emptyset)})}{(1 - R_0 e^{-\alpha L + i\emptyset})} .$$

There are two cases of interest defined by this model, the resonant high-finesse limit where $R_0 e^{-\alpha L} = 1$ and the case of $R_0 e^{-\alpha L} < 1$. The high finesse case causes the pump to grow as $mA_0$ while for any value of finite cavity loss the series converges, convergence depends on the inequality $\left|R_0 \ e^{-(\alpha L + i\emptyset)}\right| < 1$ (the modulus is less than unity).

It is convenient to conjugate the Stokes field equation so that, the model now takes the form:

$$\frac{dA_{-1,m}}{dZ} = \frac{|A_{0,m}|^2}{2} \frac{(1-\varepsilon)}{(1-i\delta)} \left[A_{-1,m} + A_{1,m}^* e^{i\gamma_1 Z + i2\theta_m}\right] \tag{D.7}$$

$$\frac{dA_{1,m}^{*}}{dZ} = -\frac{|A_{0,m}|^2}{2}\frac{(1+\varepsilon)}{(1-i\delta)}\left[A_{1,m}^{*} + A_{-1,m}e^{-i\gamma_1 Z - i2\theta_m}\right], \tag{D.8}$$

These equations pose an eigenvalue problem with a periodic set of eigenfunctions, $A_{-1,m}$, $A_{1,m}^{*}$, and eigenvalues $K_m^{\pm}$ , which permit general solutions to be constructed.

We seek trial eigensolutions of the form:

$$A_{-1,m}(Z) = a_{-1,m}e^{\left[\left(K_m + i\frac{\gamma_1}{2}\right)Z + i\theta_m\right]} \tag{D.9}$$

$$A_{1,m}^{*}(Z) = a_{1,m}^{*}e^{\left[\left(K_m - i\frac{\gamma_1}{2}\right)Z - i\theta_m\right]}. \tag{D.10}$$

Introducing the trial eigensolutions into equations (D.7) and (D.8) gives:

$$a_{-1,m}\left(K_m + i\frac{\gamma_1}{2}\right) = \frac{|A_{0,m}|^2}{2}\frac{(1-\varepsilon)}{(1-i\delta)}\left[a_{-1,m} + a_{1,m}^{*}\right], \tag{D.11}$$

$$a_{1,m}^{*}\left(K_m - i\frac{\gamma_1}{2}\right) = -\frac{|A_{0,m}|^2}{2}\frac{(1+\varepsilon)}{(1-i\delta)}\left[a_{1,m}^{*} + a_{-1,m}\right]. \tag{D.12}$$

This can be expressed in matrix form:

$$\begin{bmatrix} K_m + i\frac{\gamma_1}{2} - \frac{|A_{0,m}|^2}{2}\frac{(1-\varepsilon)}{(1-i\delta)} & -\frac{|A_{0,m}|^2}{2}\frac{(1-\varepsilon)}{(1-i\delta)} \\ \frac{|A_{0,m}|^2}{2}\frac{(1+\varepsilon)}{(1-i\delta)} & K_m - i\frac{\gamma_1}{2} + \frac{|A_{0,m}|^2}{2}\frac{(1+\varepsilon)}{(1-i\delta)} \end{bmatrix} \begin{matrix} a_{-1,m} \\ a_{1,m}^{*} \end{matrix} = \begin{matrix} 0 \\ 0 \end{matrix} \tag{D.13}$$

Taking the determinant of the coefficient matrix, to determine non-trivial sideband solutions, gives:

$$K_m^2 + \left(|A_{0,m}|^2\varepsilon\right)K_m\frac{(1+i\delta)}{(1+\delta^2)} + \frac{{\gamma_1}^2}{4} + \frac{|A_{0,m}|^2\gamma_1}{2}\frac{(i-\delta)}{(1+\delta^2)} = 0, \tag{D.14}$$

which has complex solutions:

$$K_m^{\pm} = -\frac{(1+i\delta)|A_{0,m}|^2\varepsilon}{D} \pm (\propto_R + i \propto_I), \tag{D.15}$$

where $D = 1 + \delta^2$ and:

$$\propto_R$$

$$= \frac{1}{\sqrt{2}}\left[\left(\frac{(1-\delta^2)\left|A_{0,m}\right|^4\varepsilon^2}{D^2} + \frac{2\gamma_1\left|A_{0,m}\right|^2\delta}{D} - \gamma_1^2\right)\right.$$

$$\left. + \sqrt{\left(\frac{(1-\delta^2)\left|A_{0,m}\right|^4\varepsilon^2}{D^2} + \frac{2\gamma_1\left|A_{0,m}\right|^2\delta}{D} - \gamma_1^2\right)^2 + \frac{4\left|A_{0,m}\right|^4\left(\varepsilon^2\left|A_{0,m}\right|^2\delta - D\gamma_1\right)^2}{D^4}}\right]^{\frac{1}{2}},$$

$$\propto_I$$

$$= \frac{1}{\sqrt{2}}\left[-\left(\frac{(1-\delta^2)\left|A_{0,m}\right|^4\varepsilon^2}{D^2} + \frac{2\gamma_1\left|A_{0,m}\right|^2\delta}{D} - \gamma_1^2\right)\right.$$

$$\left. + \sqrt{\left(\frac{(1-\delta^2)\left|A_{0,m}\right|^4\varepsilon^2}{D^2} + \frac{2\gamma_1\left|A_{0,m}\right|^2\delta}{D} - \gamma_1^2\right)^2 + \frac{4\left|A_{0,m}\right|^4\left(\varepsilon^2\left|A_{0,m}\right|^2\delta - D\gamma_1\right)^2}{D^4}}\right]^{\frac{1}{2}}.$$

(D.16)

Splitting equation (D.15) into its real and imaginary components yields:

$$K_{\bar{m}}^{\pm} = Re[K_{\bar{m}}^{\pm}] + iIm[K_{\bar{m}}^{\pm}]\ ,$$

$$Re[K_{\bar{m}}^{\pm}] = \frac{1}{2}\left[-\frac{\left|A_{0,m}\right|^2\varepsilon}{D} \pm \propto_R\right] \tag{D.17}$$

$$Im[K_{\bar{m}}^{\pm}] = \frac{1}{2}\left[-\frac{\delta\left|A_{0,m}\right|^2\varepsilon}{D} \mp \propto_I\right]\ , \tag{D.18}$$

where $Re[K_{\bar{m}}^{\pm}]$ is linked to the growth (or attenuation) of the Raman sidebands within the cavity.

General solutions to the envelope equations can be written as a linear combination of eigensolutions with coefficients $C_{ks,m}$and $C_{ka,m}$ (where $k = 1,2$):

$$A_{-1,m}(Z) = \left(C_{1s,m}e^{K_{\bar{m}}^{+}Z} + C_{2s,m}e^{K_{\bar{m}}^{-}Z}\right)e^{i\frac{\gamma_1}{2}Z + i\theta_m} \tag{D.19}$$

$$A_{1,m}^{*}(Z) = \left(C_{1a,m}e^{K_{\bar{m}}^{+}Z} + C_{2a,m}e^{K_{\bar{m}}^{-}Z}\right)e^{-i\frac{\gamma_1}{2}Z - i\theta_m}\ . \tag{D.20}$$

The cavity boundary conditions then determine the form of the coefficients involved in the general solutions. Setting $Z = 0$ in equations (D.19) and (D.20) gives:

$$A_{-1,m}(0) = \left(C_{1s,m} + C_{2s,m}\right)e^{i\theta_m} \tag{D.21}$$

$$A^*_{1,m}(0) = \left(C_{1a,m} + C_{2a,m}\right)e^{-i\theta_m} \ . \tag{D.22}$$

Taking the $Z$-derivative of equations (D.19) and (D.20), equating the results to equations (D.7) and (D.8) respectively and setting $Z = 0$ gives:

$$\left(K_m^+ + i\frac{\gamma_1}{2}\right)C_{1s,m}e^{i\theta_m} + \left(K_m^- + i\frac{\gamma_1}{2}\right)C_{2s,m}e^{i\theta_m} = \frac{\left|A_{0,m}\right|^2}{2}\frac{(1-\varepsilon)(1+i\delta)}{D}\left[A_{-1,m}(0) + A^*_{1,m}(0)e^{i2\theta_m}\right] \tag{D.23}$$

$$\left(K_m^+ - i\frac{\gamma_1}{2}\right)C_{1a,m}e^{-i\theta_m} + \left(K_m^- - i\frac{\gamma_1}{2}\right)C_{2a,m}e^{-i\theta_m} = -\frac{\left|A_{0,m}\right|^2}{2}\frac{(1+\varepsilon)(1+i\delta)}{D}\left[A^*_{1,m}(0) + A_{-1,m}(0)e^{-i2\theta_m}\right]. \tag{D.24}$$

Substituting equation (D.21) into equation (D.23) and re-arranging gives:

$$\frac{\left[2K_m^+ + i\gamma_1 - \left|A_{0,m}\right|^2(1-\varepsilon)\frac{(1+i\delta)}{D}\right]}{\left|A_{0,m}\right|^2(1-\varepsilon)\frac{(1+i\delta)}{D}}\,C_{1s,m} + \frac{\left[2K_m^- + i\gamma_1 - \left|A_{0,m}\right|^2(1-\varepsilon)\frac{(1+i\delta)}{D}\right]}{\left|A_{0,m}\right|^2(1-\varepsilon)\frac{(1+i\delta)}{D}}\,C_{2s,m} = A^*_{1,m}(0)e^{i\theta_m}\ , \tag{D.25}$$

Likewise equations (D.22) and (D.24) also give:

$$\frac{\left[2K_m^+ - i\gamma_1 + \left|A_{0,m}\right|^2(1+\varepsilon)\frac{(1+i\delta)}{D}\right]}{\left|A_{0,m}\right|^2(1+\varepsilon)\frac{(1+i\delta)}{D}}\,C_{1a,m} + \frac{\left[2K_m^- - i\gamma_1 + \left|A_{0,m}\right|^2(1+\varepsilon)\frac{(1+i\delta)}{D}\right]}{\left|A_{0,m}\right|^2(1+\varepsilon)\frac{(1+i\delta)}{D}}\,C_{2a,m} = -A_{-1,m}(0)e^{-i\theta_m}\ . \tag{D.26}$$

Taking the derivatives of equations (D.19) and (D.20), and equating them to equations (D.7) and (D.8) respectively gives:

$$\left(K_m^+ + i\frac{\gamma_1}{2}\right)C_{1s,m}e^{K_m^+ + i\frac{\gamma_1}{2}Z + i\theta_m} + \left(K_m^- + i\frac{\gamma_1}{2}\right)C_{2s,m}e^{K_m^- + i\frac{\gamma_1}{2} + i\theta_m} = \frac{|A_{0,m}|^2}{2}\frac{(1-\varepsilon)(1+i\delta)}{D}\left[A_{-1,m} + A_{1,m}^* e^{i\gamma_1 Z + i2\theta_m}\right]$$

(D.27)

$$\left(K_m^+ - i\frac{\gamma_1}{2}\right)C_{1a,m}e^{K_m^+ - i\frac{\gamma_1}{2}Z - i\theta_m} + \left(K_m^- - i\frac{\gamma_1}{2}\right)C_{2a,m}e^{K_m^- - i\frac{\gamma_1}{2} - i\theta_m} = -\frac{|A_{0,m}|^2}{2}\frac{(1+\varepsilon)(1+i\delta)}{D}\left[A_{1,m}^* + A_{-1,m}e^{-i\gamma_1 Z - i2\theta_m}\right].$$

(D.28)

The substitution of equations (D.19) and (D.20) into both equations (D.27) and (D.28) gives:

$$\left[\left(K_m^+ + i\frac{\gamma_1}{2}\right)C_{1s,m} - \frac{|A_{0,m}|^2}{2}\frac{(1-\varepsilon)(1+i\delta)}{D}\left(C_{1s,m} + C_{1a,m}\right)\right]e^{(K_m^+ - K_m^-)Z} = \frac{|A_{0,m}|^2}{2}\frac{(1-\varepsilon)(1+i\delta)}{D}\left(C_{2s,m}C_{2a,m}\right) - \left(K_m^- + i\frac{\gamma_1}{2}\right)C_{2s,m}$$

(D.29)

$$\left[\left(K_m^+ - i\frac{\gamma_1}{2}\right)C_{1a,m} + \frac{|A_{0,m}|^2}{2}\frac{(1+\varepsilon)(1+i\delta)}{D}\left(C_{1s,m} + C_{1a,m}\right)\right]e^{(K_m^+ - K_m^-)Z} = -\frac{|A_{0,m}|^2}{2}\frac{(1+\varepsilon)(1+i\delta)}{D}\left(C_{2s,m} + C_{2a,m}\right) - \left(K_m^- - i\frac{\gamma_1}{2}\right)C_{2a,m}\ .$$

(D.30)

Taking the derivative of equation (D.29) and (D.30) and setting Z = 0 gives:

$$(K_m^+ - K_m^-)\left[\left(K_m^+ + i\frac{\gamma_1}{2}\right)C_{1s,m} - \frac{|A_{0,m}|^2}{2}\frac{(1-\varepsilon)(1+i\delta)}{D}\left(C_{1s,m} + C_{1a,m}\right)\right] = 0$$

(D.31)

$$(K_m^+ - K_m^-)\left[\left(K_m^+ - i\frac{\gamma_1}{2}\right)C_{1a,m} + \frac{|A_{0,m}|^2}{2}\frac{(1+\varepsilon)(1+i\delta)}{D}\left(C_{1s,m} + C_{1a,m}\right)\right] = 0\ .$$

(D.32)

When $K_m^+ \neq K_m^-$ re-arranging equation (D.31) or (D.32) gives the ratio:

$$\frac{C_{1a,m}}{C_{1s,m}} = \frac{\left(2K_m^+ + i\gamma_1\right)D}{\left|A_{0,m}\right|^2(1-\varepsilon)(1+i\delta)} - 1 \quad , \tag{D.33}$$

and by comparing equation (D.33) to equation (D.26) and using equation (D.21) one also finds the corresponding ratio:

$$\frac{C_{2a,m}}{C_{2s,m}} = \frac{\left(2K_m^- + i\gamma_1\right)D}{\left|A_{0,m}\right|^2(1-\varepsilon)(1+i\delta)} - 1 \quad . \tag{D.34}$$

Using the relation (D.21), equation (D.26) can be re-arranged to give equations for, $C_{1s,m}$, $C_{2s,m}$:

$$C_{1s,m} = \frac{\left|A_{0,m}\right|^2\left(\frac{(1-\varepsilon)(1+i\delta)}{D}\right)A_{1,m}^*(0)e^{i\theta m} + \left[\left|A_{0,m}\right|^2\left(\frac{(1-\varepsilon)(1+i\delta)}{D}\right) - 2K_m^- - i\gamma_1\right]A_{-1,m}(0)e^{-i\theta m}}{2\left(K_m^+ - K_m^-\right)} \tag{D.35}$$

$$C_{2s,m} = \frac{\left|A_{0,m}\right|^2\left(\frac{(1-\varepsilon)(1+i\delta)}{D}\right)A_{1,m}^*(0)e^{i\theta m} + \left[\left|A_{0,m}\right|^2\left(\frac{(1-\varepsilon)(1+i\delta)}{D}\right) - 2K_m^+ - i\gamma_1\right]A_{-1,m}(0)e^{-i\theta m}}{2\left(K_m^- - K_m^+\right)} \quad . \tag{D.36}$$

These equations fully define the gain suppression analysis for an undepleted pump with finite detuning.

Setting the Stokes shift $\varepsilon = 0$, transit number $m = 0$, detuning $\delta = 0$ and $\left|A_{0,m}\right|^2 = 1$ retrieves the gain suppression analysis of Shen and Bloembergen [69].

# APPENDIX E

This appendix contains the finite detuning gain suppression code. Setting $\delta = 0$ retrieves the zero detuning gain suppression analysis. Each stage of the code is described so the code can be easily compared to the gain suppression analysis derived in chapter 4.

The gain suppression code is repeated for **N** cavity transits.

**for m = 1:N**

**M = A(ipump,m);**

The real and imaginary components $\alpha_R$ and $\alpha_I$ are calculated using the pump amplitude, **M**, given at the start of the cavity transit. **Delta** defines the level of detuning, **D** = 1+**Delta**$^2$, **gamma1** defines the level of dispersion and **epsilon** is the Stokes shift.

```
alphaR(m) = (1/2)*(((M.^4)*(epsilon^2)*(1-Delta^2)/(D^2) +
(2*gamma1*(M.^2)*Delta/(D)) - (gamma1^2)) + sqrt((((M.^4)*(epsilon^2)*(1-
Delta^2)/(D^2) + (2*gamma1*(M.^2)*Delta/D) - (gamma1^2)).^2) +
(4*(M.^4)*(Delta*(M.^2)*(epsilon^2) - D*gamma1)^2)/(D^4)));

alphaR(m) = sqrt(alphaR(m));

alphaI(m) = (1/2)*(-((M.^4)*(epsilon^2)*(1-Delta^2)/(D^2) +
(2*gamma1*(M.^2)*Delta/(D)) - (gamma1^2)) + sqrt((((M.^4)*(epsilon^2)*(1-
Delta^2)/(D^2) + (2*gamma1*(M.^2)*Delta/D) - (gamma1^2)).^2) +
(4*(M.^4)*(Delta*(M.^2)*(epsilon^2) - D*gamma1)^2)/(D^4)));

alphaI(m) = sqrt(alphaI(m));
```

The gain parameters $K_m^{\pm}$ are calculated from the real and imaginary components $\alpha_R$ and $\alpha_I$.

```
Kneg(m) = (1/2)*(-((1+i*Delta)*(M.^2)*epsilon/D) - (alphaR(m) + i*alphaI(m)));

Kpos(m) = (1/2)*(-((1+i*Delta)*(M.^2)*epsilon/D) + (alphaR(m) + i*alphaI(m)));
```

The constants required for the general solution of the Stokes and anti-Stokes components can now be calculated using the gain parameter.

```
C1s(m) = (((1-epsilon)*conj(A(iAStokes,m))*(M.^2)*DD/D) + (((M.^2)*(1-epsilon)*(DD/D)) - i*gamma1 -2*Kneg(m))*A(iStokes,m))/(2*(Kpos(m) - Kneg(m)));

C2s(m) = (((1-epsilon)*conj(A(iAStokes,m))*(M.^2)*DD/D) + (((M.^2)*(1-epsilon)*(DD/D)) - i*gamma1 -2*Kpos(m))*A(iStokes,m))/(2*(Kneg(m) - Kpos(m)));


C1a(m) = C1s(m)*(((2*(Kpos(m) + (i*gamma1/2))*D)/((M.^2)*(1-epsilon)*DD)) - 1);

C2a(m) = C2s(m)*(((2*(Kneg(m) + (i*gamma1/2))*D)/((M.^2)*(1-epsilon)*DD)) - 1);


Az(iStokes,:) = (C1s(m).*exp(Kpos(m)*Z)
+C2s(m).*exp(Kneg(m)*Z)).*exp(i*Z*(gamma1/2));

Az(iAStokes,:) = conj((C1a(m).*exp(Kpos(m)*Z) + C2a(m).*exp(Kneg(m)*Z)).*exp(-i*Z*(gamma1/2)));
```

The general solutions for the first Stokes and first anti-Stokes amplitudes are now calculated and the boundary conditions applied. The initial conditions for the next cavity transit are now saved in a 3 by **N** matrix.

```
A(ipump,m+1)=Apump+A(ipump,m)*R;

A(iStokes,m+1)=Az(iStokes,ndZ)*R;

A(iAStokes,m+1) = Az(iAStokes,ndZ)*R;

end
```

# References

[1] A. Zewail, “Laser Femtochemistry”, Science 242, 1645–1653 (1988).

[2] M. Uiberacker et al, “Attosecond real-time observation of electron tunnelling in atoms”, Nature 446, 627–632 (2007).

[3] P.F. Moulron, "Ti-doped Sapphire Tunable Solid State Laser", Opt. News 8, 9 1982.

[4] J. D. Kafka, M. L. Watts, D. J. Roach, M.S. Keirstead, H.W. Schaaf, and T Baer, "Pulse Compression of a Mode-Locked Ti:Sapphire Laser", Postdeadline paper, CLEO '90, Anaheim, CA, 21-25 May 1990, CPDP8.

[5] J. Goodberlet, J. Wang, J. G. Fujimoto, and P. A. Schulz,"Femtosecond Passively Mode-Locked Ti:Al20 3 Laser with a Nonlinear Exrernal Caviry", Opt. Lett. 14, 1125 1989.

[6] D.E. Spence, P.E. Kean, and W. Sibbett, "Sub-100fs Pulse Generarion from a Self-Modelocked Titanium-Sapphire laser," Postdeadline paper, CLEO '90, Anaheim, CA, 21-25 May 1990, CPDPIO.

[7] K. F. Wall and A. Sanchez, “Titanium Sapphire Lasers”, The Lincoln Laboratory Journal 3, 3 1990.

[8] G. T. Nogueira, B. Xu, Y. Coello, M. Dantus and F. C. Cruz, “Broadband 2.12 GHz Ti:sapphire laser compressed to 5.9 femtoseconds using MIIPS”, Optics Express 16, 14 2008.

[9] S. A. Diddams, L. Hollberg, and V. Mbele, “Molecular fingerprinting with the resolved modes of afemtosecond laser frequency comb”, Nature 445, 627-630 2007.

[10] S. T. Cundiff and J. Ye, “Colloquium: Femtosecond optical frequency combs”, Rev. Mod. Phys. 75, 325-342 2003.

[11] P. M. Paul, E. S. Toma, P. Breger, G. Mullot, F. Augé, Ph. Balcou, H. G. Muller, P. Agostini, “Observationof a Train of Attosecond Pulses from High Harmonic Generation”, Science 292, 1689 - 1692 2001.

[12] E. Goulielmakis et al, “Single-Cycle Nonlinear Optics”, Science 320, 1614 - 1617 (2008).

[13] T. Brabec & F. Krausz, "Intense few-cycle laser fields: frontiers of nonlinear optics”, Rev. Mod. Phys. 72, 545–591 (2000).

[14] F. Krausz & M. Ivanov, “Attosecond Physics”, Rev. Mod. Phys. 81, 163–234 (2009).

[15] F. Calegari et al, “Efficient continuum generation exceeding 200 eV by intense ultrashort two-color driver”, Opt. Lett. 34, 3125–3127 (2009).

[16] K. J. Schafer et al, "Above threshold ionization beyond the high harmonic cutoff”, Phys. Rev. Lett. 70, 1599 (1993).

[17] P. B. Corkum, “Plasma perspective on strong field multiphoton ionization”, Phys. Rev. Lett. 71, (1994).

[18] J. L. Krause, K. J. Schafer and K. C. Kulander, “High-Order Harmonic Generation from Atoms and Ions in the high Intensity Regime”, Phys. Rev. Lett. 68, 3535 (1992).

[19] P. B. Corkum, N. H. Burnett & M. Y. Ivanov, “Subfemtosecond pulses”, Opt. Lett. 19, 1870–1872 (1994).

[20] O. Tcherbakoff, E. Mevel, D. Descamps, J. Plumridge & E. Constant, “Time-gated high-order harmonic generation”, Phys. Rev. A. 68, 043804 (2003).

[21] J. Mauritsson et al. Phys, “Attosecond Pulse Trains Generated Using Two Color Laser Fields”, Rev. Lett. 97, 013001 (2006).

[22] H. Mashiko, S. Gilbertson, C. Li, E. Moon & C. Zenghu, “Optimizing the photon flux of double optical gated high-order harmonic spectra”, Phys. Rev. A. 77, 063423 (2008).

[23] H. Merdji et al, “Isolated attosecond pulses using a detuned second-harmonic field”, Opt. Lett. 32, 3134–3136 (2007).

[24] E. Takahashi, T. Kanai, Y. Nabekawa & K. Midorikawa, “10 mJ class femtosecond optical parametric amplifier for generating soft x-ray harmonics”, Appl. Phys. Lett. 93, 041111 (2008).

[25] T. Popmintchev et al, “Extended phase matching of high harmonics driven by mid-infrared light”, Opt. Lett. 33, 2128–2130 (2008).

[26] E. J. Takahashi,P. Lan, O. D. Mucke, Y. Nabekawa & K. Midorikawa, “Infrared Two-Color Multicycle Laser Field Synthesis for Generating an Intense Attosecond Pulse”, Phys. Rev. Lett. 104, 233901 (2010).

[27] P. Lan, E. J. Takahashi & K. Midorikawa, "Wavelength scaling of efficient high-order harmonic generation by two-color infrared laser fields”, Phys. Rev. A. 82, 053413 (2010).

[28] E. Takahashi, Y. Nabekawa, T. Otsuka, M. Obara & K. Midorikawa, “Generation of highly coherent submicrojoule soft x rays by high-order harmonics”, Phys. Rev. A. 66, 021802 (2002).

[29] D. Eimerl, W. L. Kruer, and E. M. Campbell, “Ultrabroad Bandwidth for ICF Applications”, Comm. Plasma Phys. Controlled Fusion 15, 85 (1992).

[30] G. S. McDonald, G. H. C. New, L. L. Losev and A. P. Lutsenko, "On the Generation of Ultrabroad Bandwidth Light for Inertial Confinement Fusion", IOP Conference Series, 140, 85-88 (1995).

[31] G. S. McDonald, G. H. C. New, L. L. Losev A. P. Lutsenko and M. Shaw, "Ultrabroad Bandwidth Multi-frequency Raman Generation", Opt. Lett, 19, 18 (1994).

[32] G. S. McDonald, G. H. C. New, L. L. Losev and A. P. Lutsenko, "On the generation of ultra-broad bandwidth light in air at atmospheric pressure", J. Phys. B: At. Mol. Opt. Phys. 30, L719-L725 (1997).

[33] C. V. Raman & K. S. Krishnan, **"**A new type of secondary radiation", Nature 121, 501–502 (1928).

[34] E. J. Woodbury & W. K. Ng, "Ruby operation in the Near IR", Proc. Inst. Radio Eng. 50, 2367 (1962).

[35] E. Garmire, F. Pandarese & C. H. Townes, "Coherently Driven Molecular Vibrations and Light Modulation**",** Phys. Rev. Lett. 11, 160–163 (1963).

[36] T. Imasaka, S. Kawasaki, and N. Ishibashi,"Generation of more than 40 laser emission lines from the ultraviolet to the visible regions by two-color stimulated Raman effect", Appl. Phys. B. 49, 389 (1989).

[37] A. E. Dangor, A. K. L. Dymoke-Bradshaw, A. Dyson, T. Garvey, S. Karttunen, J. Partanen, R. R. E. Salomaa, A. J. Cole, C. Danson, C. B.Edwards, and R. G. Evans, "Forced Raman scattering in air by a two-frequency laser beam", J. Phys. B 22, 797 (1989).

[38] A. Z. Grasyuk, L. L. Losev, A. P. Lutsenko, and S. N. Sazonov, "Raman parametric generation of anti-Stokes radiation under conditions of

amplification of an external Stokes signal", Kvantovaya Elektron. (Moscow) 17, 599 (1990) [Sov. J. Quantum Electron.
20,529 (1990)].

[39] S. Yoshikawa & T. Imasaka, "New approach for the generation of ultrashort optical pulses", Opt. Commun. 96, 94–98 (1993).

[40] S. E. Harris & A. V. Sokolov, "Broadband spectral generation with refractive index control", Phys. Rev. A 55, R4019–R4022 (1997).

[41] F. L. Kien et al., "Subfemtosecond pulse generation with molecular coherence control in stimulated Raman scattering ", Phys Rev. A 60, 1562–1571 (1999).

[42] T. Suzuki, M. Hirai & M. Katsuragawa, "Octave-Spanning Raman Comb with Carrier Envelope Offset Control", Phys. Rev. Lett. 101, 243-602 (2008).

[43] L. L. Losev and A. P. Lutsenko, "Parametric Raman laser with a discrete output spectrum equal in width to the pump frequency", Kvantovaya Electron. (Moscow) 20, 1054 (1993).

[44] G. S. McDonald, G. H. C. New, L. L. Losev, A.P. Lutsenko and M.J. Shaw, "Ultrabroad Bandwidth Multiline Stimulated Raman Scattering", Annual Report of the Central Laser Facility, Rutherford Appleton Laboratories, RAL-94-0 42 (1994) 140.

[45] S. W. Huang, W. Chen & A. H. Kung, "Vibrational molecular modulation in hydrogen", Phys. Rev. A 74, 063825 (2006).

[46] A. V. Sokolov, D. R. Walker, D. D. Yavuz, G. Y. Yin & S. E. Harris, "Light Modulation at Molecular Frequencies", Phys. Rev. Lett. 85, 562–565 (2000).

[47] D. R. Walker, D. D. Yavuz, G. Y. Yin & S. E. Harris, “Rotational Raman Generation with Near Unity Conversion Efficiency”, Opt. Lett. 27, 769–771 (2002).

[48] J. R. Murray, Julius Goldhar, David Eimerl, and Abraham Szoke, “Raman pulse compression of excimer lasers for application to laser fusion”, IEEE. J. Quantum Electron. 15, 5 (1979).

[49] S. A. Diddams, D. J. Jones, J. Ye, S. T. Cundiff, J. L. Hall, J. K. Ranka, R. S. Windeler, R. Holzwarth, T. Udem, and T. W. Hansch, “Direct link between microwave and optical frequencies with a 300 THz femtosecond laser comb”, Phys. Rev. Lett. 84, 5102– 5105 (2000).

[50] S. A. Diddams, T. Udem, J. C. Bergquist, E. A. Curtis, R. E. Drullinger, L. Hollberg, W. M. Itano, W. D. Lee, C.W. Oates, K. R. Vogel, and D. J.Wineland, “An Optical Clock Based on a Single Trapped $^{199}Hg^{+}$ Ion”, Science. 293, 825–828 (2001).

[51] M. J. Thorpe, K. D.Moll, R. J. Jones, B. Safdi, and J. Ye, "Broadband cavity ringdown spectroscopy for sensitive and rapid molecular detection”, Science. 311, 1595– 1599 (2006).

[52] S. A. Diddams, L. Hollberg, and V. Mbele, “Molecular fingerprinting with the resolved modes of a femtosecond laser frequency comb”, Nature. 445, 627–630 (2007).

[53] V. Lefevre-Seguin, “Whispering-gallery mode lasers with doped silica microspheres”, Opt. Mater. 11, 153-165 (1999).

[54] D. K. Armani et al, “Ultra-high-Q toroid microcavity on a chip”, Nature. 421, 905-908 (2003).

[55] T. Baba. et al, “Photonic crystals and microdisk cavities based on GaInAsP-InP system”, IEEE Photon. Technol. Lett. 9, 878-880 (1997).

[56] C. Gmachl. et al, “High-power directional emission from microlasers with chaotic Resonances”, Science. 280, 1556-1564 (1998).

[57] G.S. Solomon et al, “Single-mode spontaneous emission from a single quantum dot in a three-dimensional microcavity”, Phys. Rev. Lett. 86, 3903 – 3906 (2001).

[58] O.J. Painter et al, ”Room temperature photonic crystal defect lasers at near-infrared wavelengths in InGaAsP”, IEEE. J. Lightwave Technol. 17, 2082-2088 (1999).

[59] T. J. Kippenberg, S. M. Spillane, and K. J. Vahala, “Ultralow-threshold microcavity Raman laser on a microelectronic chip”, Phys. Rev. Lett. 93, 083904 (2004).

[60] R. H. Stolen and J. E. Bjorkholm, “Parametric amplification and frequency conversion in optical fibers”, IEEE. Journal Of Quantum Electronics. 18, 1062–1072 (1982).

[61] K. J. Vahala, “Optical microcavities”, Nature. 424, 839–846 (2003).

[62] P. Del’Haye, A. Schliesser, O. Arcizet, T. Wilken, R. Holzwarth, and T.J. Kippenberg, “Optical frequency comb generation from a monolithic microresonator”, Nature. 450, 1214-1217 (2007).

[63] D. K. Armani, T. J. Kippenberg, S. M. Spillane, and K. J. Vahala, “Ultra-high-*Q* toroid microcavity on a chip”, Nature. 421, 925–928 (2003).

[64] M. Pollinger et al, **"**Ultrahigh-Q Tunable Whispering-Gallery-Mode Microresonator**",** Phys. Rev. Lett. 103, 053901 (2009).

[65] S. M. Spillane, T. J. Kippenberg and K. J. Vahala, "Ultralow-threshold Raman laser using a spherical dielectric microcavity", Nature. 415, 621 (2002).

[66] A. P. Hickman and W. K. Bischel, "Theory of Stokes and anti-Stokes generation by Raman frequency conversion in the transient limit", Phys. Rev. A 37, 2516 (1988).

[67] A. Smekal, "Zur Quantentheorie der Dispersion", In: Die Naturwissenschaften. 11, Nr. 43, S. 873-875 (1923).

[68] C. V. Raman, "A new class of spectra due to secondary radiation", Indian J. Phys. 2, 387 (1928).

[69] Y. R. Shen and N. Bloembergen, "Theory of Stimulated Brillouin and Raman Scattering", Phys. Rev. 137, 6A (1965).

[70] D. Eimerl, R. S. Hargrove, and J. A. Paisner, "Efficient Frequency Conversion by Stimulated Raman Scattering", Phys. Rev. Lett. 46, 651–654 (1981).

[71] N. Bloembergen, "The Stimulated Raman Effect", Am. J. Phys. 35, 989 (1967).

[72] V. Wilke, W. Schmidt, "Broadly tuneable UV-source based on stimulated Raman scattering", J.Opt. Soc. Am. 68, 1626 (1978).

[73] A. P. Hickman, J. A. Paisner, and W. K. Bischel, "Theory of multiwave propagation and frequency conversion in a Raman medium", Phys. Rev. A 33, 1788 (1986).

[74] G. S. McDonald, G. H. C. New, Yuk-Ming Chan, “Competing Nonlinear Effects in Multifrequency Raman Generation”, J. Mod. Opt. 45, 6 1099-1110 (1998).

[75] R. P. Feynman, F. L. Vernon and R. W. Hellwarth, “Geometrical Representation of the Schroedinger Equation for Solving Maser Problems”, J. Appl. Phys. 28, 49 (1957).

[76] R. W. Boyd. Nonlinear Optics. Third edition. Academic Press, London (2008).

[77] A. V. Sokolov, M. Y. Shverdin, D. R. Walker, D. D. Yavuz, A. M. Burzo, G. Y. Yin and S. E. Harris,” Generation and control of femtosecond pulses by molecular modulation”, J. Mod. Opt. 52, 2 285-304 (2005).

[78] K. S. Syed, G.S. McDonald and G. H. C. New, “Transverse Effects in Multifrequency Raman Generation”, J. Opt. Soc. Am. B 17, 8 (2000).

[79] L. F. Shampine, I. Gladwell, S. Thompson, "Solving ODEs with matlab , Cambridge university press, 48 - 57 (2003).

[80] M. Abramowitz and I. A. Stegun, "Handbook of mathematical functions", U.S. Department of Commerce, National Bureau of standards, 896 1972 (1964).

[81] L. F. Shampine, I. Gladwell and S. Thompson, "Solving ODEs with matlab", Cambridge university press, 46 - 48 (2003).

[82] R. J. LeVeque, "Finite difference methods for ordinary and partial differential equations", Society for industrial and applied mathematics, 181-183 (2007).

[83] L. F. Shampine, I. Gladwell and S. Thompson, "Solving ODEs with matlab", Cambridge university press, 49 - 165 (2003).

[84] M. D. Duncan, R. Mahon, J. Reintjes and L.L. Tankersley, “Parametric Raman gain suppression in $D_2$ and $H_2$”, Opt. Lett. 11, 12 803-805 (1986).

[85] D. R. Walker, D. D. Yavuz, M. Y. Sheverdin, G. Y. Yin, A. V. Sokolov and S. E. Harris, "Raman self-focusing at maximum coherence", Optics letters. 27, 23 2094 - 2096 (2002).